Optimisation of superconducting thin film growth for next generation superconducting detector applications

Archan Banerjee

A thesis presented for the degree of
Doctor of Philosophy
School of Engineering
University of Glasgow
Scotland
October, 2017

Abstract

There is a growing demand for superconducting detectors with single photon sensitivity from near- to far infrared wavelengths. Emerging application areas include imaging, remote sensing, astronomy and free space communications. Two superconducting device technologies, superconducting nanowire single-photon detectors (SSPDs/SNSPDs) and microwave kinetic inductance detectors (MKIDs) have the potential to outperform off-the-self semiconductor technologies and offer scalability to large arrays. Fabrication of high efficiency superconducting detectors strongly depends on the quality of superconducting thin films. The original work presented in this thesis has explored the growth and optimization of several superconducting thin film materials for next generation superconducting detectors. Films have been grown in an ultra-high vacuum sputter deposition system and an atomic layer deposition system.

Since its initial demonstration, NbN and NbTiN have been predominantly used as the base material for SNSPDs. In this work, we have explored the optimization of both the materials with an emphasis on NbTiN. NbTiN is optimized by heating the substrates to 800℃ achieving a T_c of 10.4 K for a film thickness of 5.5 nm on silicon substrate. Due to their crystalline nature superconducting properties of NbN or NbTiN thin films are strongly correlated with the lattice parameters of substrate properties. This causes a restriction on the substrate choice and integration of SNSPD devices with complex circuits. Amorphous superconducting materials can be promising alternatives for this purpose. We have explored growth and optimization of amorphous MoSi and MoGe thin films. Both the materials are co-sputtered to tune the composition. For 5 nm thick MoSi film on silicon substrate we obtain T_c of 5.5 K. For MKID fabrication, TiN can be an useful base material due to its high sheet resistance and widely tuneable superconducting properties. TiN thin films have been sputtered on heated (500℃) silicon substrates with a T_c of 3.9 K for a 90 nm thick film. The dielectric constants of the thin films as a function of wavelength (270-2200 nm) have been determined via variable angle spectroscopic ellipsometry (VASE). Atomic structure and stoichiometry of the films have been characterized in high resolution transmission electron microscopy (HRTEM). This study enables us to precisely control film properties and thus tailor superconducting films to the requirements of specific photon-counting applications.

Contents

Chapter 6

Chapter 7

Foreword

This thesis gives an account of the original research work which I have carried out as a PhD student since November, 2013 in the Quantum Sensors group at the School of Engineering, University of Glasgow. In course of pursuing my PhD research I have benefitted greatly from the guidance and the advice that I have received from various sources. At first, I wish to record my gratitude to my supervisor, Professor Robert Hadfield, for his constant encouragement and guidance. His enthusiasm, inspiration, and guidance played a significant role in improving my skills as a scientist and individual, while making the PhD experience enjoyable. I thank all my colleagues in Quantum Sensors group. We had numerous interesting and stimulating discussions in our office or during carrying out experiments. (Especially, I worked closely with Kleanthis Erotokritou, Dr. Alessandro Casaburi, Dr. Robert Heath, Dr. Chandra mouli Natarajan and Dr. Dmtry Morozov.) I am grateful to them for their help, support and contribution.

I acknowledge late Dr Patrick Smutek of Plassys Bestek France for expert support in the design and delivery of the sputter deposition tool. I am thankful to all the stuff members of James Watt Nanofabrication Centre, University of Glasgow for their technical support during my research work in clean room. (David Gourlay deserves a special mention among them.) Dr. Dave Bosworth and Dr. Zoe Barber (both from Department of Materials Science & Metallurgy, University of Cambridge) gave some crucial advice regarding superconducting thin film deposition at the beginning of my thesis work.

I would like to thank Dr. Ian MacLaren, Alastair Doye, Samuel McFadzean and other stuff members of School of Physics and Astronomy, University of Glasgow for their help in carrying out transmission electron microscopy analysis of superconducting thin film samples.

I would like to express my humble gratitude to stuff members of mechanical and electronics workshops at School of Engineering (especially Steven Mckernan, Denis Kearns and Thomas Dickson) for their support in machining the parts for the cryogen free thin film testing set up for this thesis work.

Finally, I would like to thank my parents for their enthusiasm and support during my time in Scotland.

Author's Declaration

I declare that, except where explicit reference is made to the contribution of others, this thesis is the result of my own work and has not been submitted for any other degree at the University of Glasgow or any other institution.

List of Acronyms and Symbols

Included as an useful reference guide rather than an exhaustive list.

Abbreviations:

AC: Alternate current

AFM: Atomic force microscopy

ALD: Atomic layer deposition

BCS: Bardeen, Cooper and Schrieffer (theory)

DC: Direct current

EBL: Electron beam lithography

EDX: Energy dispersive x-ray

EELS: Electron energy loss spectroscopy

FEM: Fluctuation electron microscopy

FFT: Fast Fourier transform

FIB: Focussed ion beam

GM: Gifford-McMahon

HRTEM: High resolution transmission electron microscopy

HTS: High temperature superconductor

MKID: Microwave Kinetic Inductance Detector

MKID: Microwave Kinetic Inductance Detector

MoGe: Molybdenum Germenium

MoSi: Molybdenum Silicide

MRO: Medium range order

NbN: Niobium Nitride

NbTiN: Niobium Titanium Nitride

NEP: Noise equivalent power

NEP_{G-R}: Generation-recombination noise equivalent power

RF: Radio frequency

RIE: Reactive Ion beam etching

rpm: Rotations per minute

RRR: Residual resistivity ratio

sccm: Standard cubic centimetre per minute

SEM: Scanning electron microscopy

SNSPD: Superconducting Nanowire single photon detector

SRO: Short range order

STES: Superconducting transition edge sensor

STJ: Superconducting tunnel junction

TiN: Titanium Nitride

TM: Transition metal

UHV: Ultra high vacuum

VASE: Variable angle spectroscopic ellipsometry

Symbols:

$\vec{E}$: Applied electric field

$\vec{J}$: Superconducting current density

A,B: Fitting parameters for Ivry Model

d_c: Critical thickness

D_{CR}: Dark count rate

e: electronic charge

E: Energy

eV: Electron volt

h: Planck's constant

$\hbar$: Reduced Planck's constant

I: Intensity

I_c: Critical current

j_c: Critical current density

k: Extinction co-efficient

K: Kelvin

k_B: Boltzmann's Constant

k_f : Fermi wavenumber

k_s: Scattering vector

l:Mean fee path

L_k: Kinetic inductance

m_e= mass of electron

N(0): Density of states of electron at absolute zero

n: Refractive index

n_e= electron density

N_2: Nitrogen

N_{qp}: Number of quasi particles

R_s : Sheet resistance

Si: Silicon

T: Temperature

T_c: Superconducting Transition Temperature

T_{co}: Bulk superconducting transition temperature

V_{BCS}: BCS interaction potential

V: Variance

W: Watt

υ: Frequency

Δ(0): Superconducting energy gap at absolute zero

λ: London penetration depth

ξ: Coherence Length

Δ: Superconducting energy gap

η: Detection efficiency

$\eta_{Coupling}$: Coupling Efficiency

$\eta_{Absorption}$: Absorption Efficiency

$\eta_{Registering}$: Registering Efficiency

γ: Fitting parameter for Finkel'stein Model

Δt: Timing jitter

η_{quasi}: Efficiency of MKID devices to generate quasi particles

σ: Conductivity

μ : Mobility

τ: Mean scattering time

λ_M: McMillan's parameter

ρ_n: Room temperature resistivity

ΔE: Energy resolution

List of Figures

List of Tables

Chapter 1

Introduction

Single photon detection plays a significant role in a wide range of fields in science and technology. Sensitive photon detection at the quantum level is immensely important in the fields of quantum information processing [1], astronomy [2], remote sensing [3], deep space communication [4] or biotechnology [5]. The detection of infrared photons also has a huge importance in the development of next generation communication technology. On the other hand, low noise infrared – sub millimetre wavelength photon detection has a crucial impact on astronomical instrumentation and terahertz imaging [6], [7].

In 2001, a new single photon detector was demonstrated by Gregory Gol'tsman and his colleagues based on superconducting niobium nitride nanowire [8]. This type of device, known as the superconducting nanowire single-photon detector (SNSPD/SSPD), is single-photon sensitive at visible and infrared wavelengths. The spectral range of an SNSPD extends far into the infrared, with photon energies of just a fraction of an electron volt. Thus, SNSPDs can operate at telecom wavelengths (1310 nm or 1550 nm) providing compatibility with the fibre optic communications technology whereas the spectral range of traditional semiconductor single photon detectors is limited due to the band gap of semiconductor materials. That is why SNSPDs have been recognised as a promising technology for ultra-weak optical signal detection. They operate at a temperature of ~4 K which is within the reach of rapidly improving closed cycle cooling technology. Hence, the operation of SNSPDs does not involve the use of expensive and hazardous cryogenics.

SNSPDs, nowadays, play a significant role as an enabling technology in advanced photon counting applications. Its applications include quantum key distribution (QKD) [9], optical quantum computing [10], characterisation of quantum emitters [11], space-to-ground communication [12], integrated circuit testing [13], fibre sensing [14] and time-of-flight ranging [15] etc.

The process of SNSPD fabrication starts with superconducting thin film deposition on appropriate substrates. The quality of the superconducting films is crucial to the fabrication of state-of-the-art SNSPDs. Understanding and controlling film quality holds the key to realising next generation SNSPD devices like large area multipixel arrays and waveguide

integrated devices. DC magnetron sputtering is the most widely used technique for depositing high quality superconducting thin films. NbN films are deposited by reactive sputtering. The superconducting properties of NbN thin films are strongly influenced by their crystalline structure. Their lattice constant should match well with that of the substrate to achieve ultrathin high quality films. Thus, the crystalline nature of NbN puts a strong constraint on the substrate choice. This problem sometimes restricts their range of applications and potential device architectures. Polycrystalline NbTiN shows good superconducting properties on a wider range of substrates including silicon. Recently some research groups have started working on the possibility of SNSPD fabrication on amorphous superconducting films (e.g. MoSi, MoGe or WSi). Amorphous films do not set strict requirements on substrate choice as the problem of lattice matching does not arise here.

The concept of the kinetic inductance detector was first proposed by Jonas Zmuidzinas and his group members [16]. This specific category of cryogenic detectors gained attention due to the ability to detect photons with extreme sensitivity and suitability to multiplex in a large array [17]. Although, initially aluminium was the conventional base material for MKIDs – many groups have explored how various other thin films materials can be used to tune detector properties according to specific requirements.

This thesis focuses on the growth and optimisation of superconducting thin films for next generation superconducting detector applications.

Chapter 2 presents an in depth discussion on the various aspects of superconducting detectors particularly in terms of thin film materials with an emphasis on SNSPDs and MKIDs. An introductory discussion on superconductivity and superconducting materials has been presented here. This chapter also elaborates on the theoretical models that correlate superconducting property and materials parameters and the influence of deposition parameters on the structural properties of superconducting thin films.

Chapter 3 describes all the experimental techniques employed for this study. Superconducting thin films have been grown in a newly commissioned ultra-high vacuum sputter deposition system (manufactured by Plassys Bestek, France (http://www.plassys.com)) that is installed in the James Watt Nanofabrication Centre, University of Glasgow. A cryogen free thin film testing station has been set up to determine superconducting transition temperature of the films. Structural and optical properties of the

films have been analysed by high resolution transmission electron microscopy (HRTEM) and variable angle spectroscopic ellipsometry (VASE).

Chapter 4 describes optimisation of Niobium (Nb), Niobium Nitride (NbN) and Niobium Titanium Nitride (NbTiN) thin films. As a part of the acceptance test of the sputter deposition system, the transition temperature of a 300 nm thick Nb film (9.1 K) has been reported. NbTiN films have been grown by co-sputtering Nb and Ti in an Ar/N_2 environment. Following the optimised process, a T_c of 7.2 K has been achieved for a 5.5 nm thick NbTiN film grown on silicon substrate. When we heat the substrate to 800°C, a NbTiN film with the same thickness shows a transition temperature of 10.4 K. HRTEM analysis demonstrates the polycrystalline nature of the NbTiN thin films. It also shows that substrate heating has a positive impact on the structural property of the films.

Chapter 5 describes the growth and optimisation of amorphous MoSi and MoGe films. All the films have been deposited by co-sputtering in an Ar environment. Variation of T_c with film thickness and sheet resistance has been compared using theoretical models. Material parameters extracted from the fit indicate the amorphous nature of the film. A detailed investigation has been carried out on the local structural ordering and stoichiometry of MoSi films using a suite of HTEM techniques. Fluctuation electron microscopy (FEM) studies reveal that the films assumed an A15-like medium range order. Electron energy loss spectroscopy (EELS) indicates that the film stoichiometry was close to $Mo_{83}Si_{17}$. Optical properties from ultraviolet (270 nm) to infrared (2200 nm) wavelengths were measured via spectroscopic ellipsometry for 5 nm thick MoSi films indicating improved long wavelength absorption relative to NbN or NbTiN. We also measured the current density as a function of temperature for nanowires patterned from these films. The current density at 3.6 K is 3.6 x $10^5 A/cm^2$ for the widest wire studied (2003 nm), falling to 2 x $10^5 A/cm^2$ for the narrowest (173 nm).

Chapter 6 describes the optimisation of TiN films by sputtering and atomic layer deposition for microwave kinetic inductance detector (MKID) applications. For a 90 nm thick film grown on a hydro fluoric (HF) acid cleaned silicon substrate in the sputter system, we have obtained a T_c of 2.9 K. When we heat the substrate before deposition up to 500°C, an improved T_c of 4 K has been achieved. A 30 nm thick TiN film grown in the ALD system following the optimised process shows a T_c of 2.4 K.

Chapter 7 reviews the main advances made in this thesis and gives an outlook on future developments.

References

[1] R. H. Hadfield, “Single-photon detectors for optical quantum information applications,” *Nat. Photonics*, vol. 3, no. 12, pp. 696–705, Dec. 2009.

[2] J. M. Beckers, “Adaptive Optics for Astronomy: Principles, Performance, and Applications,” *Annu. Rev. Astron. Astrophys.*, vol. 31, no. 1, pp. 13–62, Sep. 1993.

[3] A. Kirmani, D. Venkatraman, D. Shin, A. Colaço, F. N. C. Wong, J. H. Shapiro, and V. K. Goyal, “First-photon imaging.,” *Science*, vol. 343, no. 6166, pp. 58–61, Jan. 2014.

[4] J. A. Mendenhall, L. M. Candell, P. I. Hopman, G. Zogbi, D. M. Boroson, D. O. Caplan, C. J. Digenis, D. R. Hearn, and R. C. Shoup, “Design of an Optical Photon Counting Array Receiver System for Deep-Space Communications,” *Proc. IEEE*, vol. 95, no. 10, pp. 2059–2069, Oct. 2007.

[5] D. Elson, J. Requejo-Isidro, I. Munro, F. Reavell, J. Siegel, K. Suhling, P. Tadrous, R. Benninger, P. Lanigan, J. McGinty, C. Talbot, B. Treanor, S. Webb, A. Sandison, A. Wallace, D. Davis, J. Lever, M. Neil, D. Phillips, G. Stamp, and P. French, “Time-domain fluorescence lifetime imaging applied to biological tissue.,” *Photochem. Photobiol. Sci.*, vol. 3, no. 8, pp. 795–801, Aug. 2004.

[6] M. Tonouchi, “Cutting-edge terahertz technology,” *Nat. Photonics*, vol. 1, no. 2, pp. 97–105, Feb. 2007.

[7] G. H. Rieke, “Infrared Detector Arrays for Astronomy,” *Annu. Rev. Astron. Astrophys.*, vol. 45, no. 1, pp. 77–115, Sep. 2007.

[8] G. N. Gol’tsman, O. Okunev, G. Chulkova, A. Lipatov, A. Semenov, K. Smirnov, B. Voronov, A. Dzardanov, C. Williams, and R. Sobolewski, “Picosecond superconducting single-photon optical detector,” *Appl. Phys. Lett.*, vol. 79, no. 6, p. 705, Aug. 2001.

[9] R. J. Collins, R. H. Hadfield, V. Fernandez, S. W. Nam, and G. S. Buller, “Low timing jitter detector for gigahertz quantum key distribution,” *Electron. Lett.*, vol. 43, no. 3, p. 180, Feb. 2007.

[10] J. Chen, J. Altepeter, M. Medic, K. Lee, B. Gokden, R. Hadfield, S. Nam, and P. Kumar, “Demonstration of a Quantum Controlled-NOT Gate in the Telecommunications Band,” *Phys. Rev. Lett.*, vol. 100, no. 13, p. 133603, Apr. 2008.

[11] M. A. Jaspan, J. L. Habif, R. H. Hadfield, and S. W. Nam, “Heralding of telecommunication photon pairs with a superconducting single photon detector,” *Appl. Phys. Lett.*, vol. 89, no. 3, p. 31112, Jul. 2006.

[12] M. E. Grein, A. J. Kerman, E. A. Dauler, O. Shatrovoy, R. J. Molnar, D. Rosenberg, J. Yoon, C. E. DeVoe, D. V Murphy, B. S. Robinson, and D. M. Boroson, “Design of a ground-based optical receiver for the lunar laser communications

demonstration," *Space Optical Systems and Applications (ICSOS), 2011 International Conference on*. pp. 78–82, 2011.

[13] J. Zhang, N. Boiadjieva, G. Chulkova, H. Deslandes, G. N. Gol'tsman, A. Korneev, P. Kouminov, M. Leibowitz, W. Lo, R. Malinsky, O. Okunev, A. Pearlman, W. Slysz, K. Smirnov, C. Tsao, A. Verevkin, B. Voronov, K. Wilsher, and R. Sobolewski, "Noninvasive CMOS circuit testing with NbN superconducting single-photon detectors," *Electron. Lett.*, vol. 39, no. 14, p. 1086, 2003.

[14] S. D. Dyer, M. G. Tanner, B. Baek, R. H. Hadfield, and S. W. Nam, "Analysis of a distributed fiber-optic temperature sensor using single-photon detectors.," *Opt. Express*, vol. 20, no. 4, pp. 3456–66, Feb. 2012.

[15] J. B. Abshire, H. Riris, G. Allan, X. Sun, S. R. Kawa, J. Mao, M. Stephen, E. Wilson, and M. A. Krainak, "Laser Sounder for Global Measurement of CO_2 Concentrations in the Troposphere from Space," in *Laser Applications to Chemical, Security and Environmental Analysis*, 2008, p. LMA4.

[16] J. Zmuidzinas and P. L. Richards, "Superconducting detectors and mixers for millimeter and submillimeter astrophysics," *Proc. IEEE*, vol. 92, no. 10, pp. 1597–1616, 2004.

[17] P. K. Day, H. G. LeDuc, B. A. Mazin, A. Vayonakis, and J. Zmuidzinas, "A broadband superconducting detector suitable for use in large arrays," *Nature*, vol. 425, no. 6960, pp. 817–821, Oct. 2003.

Chapter 2

Background Review

The need for efficient low noise photon detection at the infrared wavelength is gaining importance in many fields of scientific endeavour. Single photon detectors based on superconducting nanowires (SNSPDs) offer a promising solution for this purpose. Microwave kinetic inductance detectors (MKIDs) are also gaining importance in the field of low noise infrared – sub millimetre wavelength photon detection. The fabrication process of SNSPD and MKID starts with the deposition of superconducting thin films. The growth and optimisation of superconducting thin films for next generation superconducting detectors are the main themes of this thesis. In this chapter, Section 2.1 presents an introduction to the theoretical background of superconductivity. Section 2.3 presents a brief review on the properties of superconducting thin films (including theoretical models correlating superconducting property & materials parameters and the influence of deposition parameters on film structures). The working principle, the main performance parameters, thin film materials and real life applications of SNSPDs and MKIDs have been reviewed in Section 2.5 and 2.6.

2.1 Superconductivity

Superconductivity was first observed by Dutch physicist Heike Kamerling Onnes in 1911 [1], [2] and was recognised by the award of the Nobel Prize. By 1908, Onnes had succeeded in producing liquid helium in his laboratory. Using liquid helium bath as a coolant, he proceeded to investigate the electrical resistance of metals at low temperature. He observed that the electrical resistance of mercury abruptly dropped to zero at 4.2 K. He reported that below a critical temperature (specific to the material), mercury underwent a transition to a new phase. The new phase was termed the superconducting state. Similar properties were revealed for many more materials.

The temperature at which this phase transition occurred was termed the critical temperature or superconducting transition temperature (T_c). It was also observed that there was a threshold value of current density which could be carried by a superconducting material. If the current exceeded this threshold, the material would return to the normal resistive state. This threshold was called critical current [3]. Besides current density, applied magnetic field

was also observed to have a significant influence on superconductivity. Superconducting properties would be destroyed if the applied field exceeded a threshold value. This threshold value of the magnetic field was termed the critical field [4]. Both critical current and critical field were function of temperature.

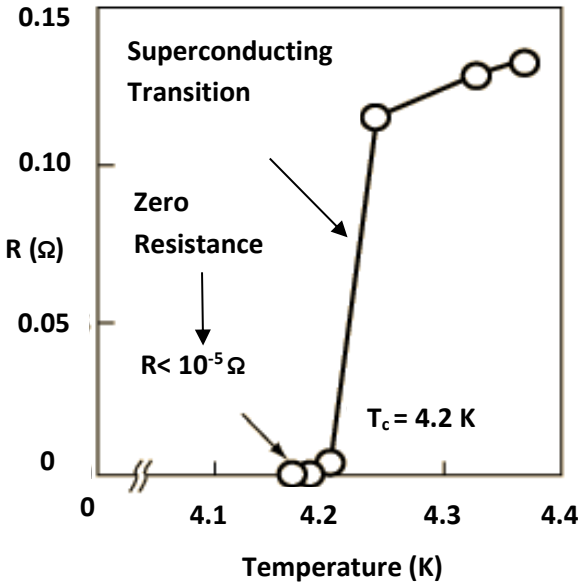

Fig. 2.1: The discovery of superconductivity: Resistance versus Temperature plot of mercury when it is cooled in liquid helium bath [1].

In 1933, Walther Meissner and Robert Ochsenfeld showed that apart from the perfect conductivity with zero resistance there was a further characteristic property of superconducting materials [5]. They observed that when a magnetic field was applied to a superconducting material it did not conserve magnetic field (contrary to what was expected of a perfectly conducting material). Instead, it expelled the magnetic flux. When the applied magnetic field was smaller than the critical field specific to the superconducting material under observation (i.e. when the magnetic field was not large enough to destroy the superconducting state), magnetic field density was essentially zero inside the material. Thus, the superconducting material was seen to be perfectly diamagnetic. This effect has come to be called the Meissner effect.

Due to these two unique characteristic properties (zero DC resistance and perfect diamagnetism), superconducting materials have immense technological potential for real world applications. Since both critical field and critical current gradually increase as the temperature of the superconductor is further lowered below its critical temperature, superconducting materials need to be cooled to at least around $0.6T_c$ (to maximize critical current density) in most of the engineering applications. Thus, real world technological applications of superconducting materials strongly depend on advancements in cryogenic technology [6].

2.1.1 Theoretical Background of Superconductivity

In 1935, Fritz and Heinz London proposed a pair of simple but useful equations to describe the electrodynamic behaviour of superconducting materials [7], [8]. Their equations are as follows:

$$\vec{E} = \frac{\partial}{\partial t}\left(\Lambda \vec{J}\right) \tag{2.1}$$

And,

$$\nabla \times \left(\Lambda \vec{J}\right) = -\vec{B} \tag{2.2}$$

[$\vec{E}$=Applied Electric Field; $\vec{J}$=Superconducting Current Density; $\Lambda = \frac{m_e}{n_e e^2}$ (m_e=Mass of Electron, n_e= Superconducting Electron Density and e= Electronic Charge)]

Equation (2.1) and (2.2) are called the London equations. It is to be noted that these two equations do not explain the physical mechanism behind superconductivity. They simply give a phenomenological description of the two characteristic properties of superconducting materials (perfect diamagnetism and zero dc resistance) in terms of electromagnetic theory.

From Maxwell's equations, we know that $\nabla \times \vec{B} = \mu_o \vec{J}$ [Since superconductors have zero resistance we may neglect charge accumulation.]

So, combining Maxwell's equation and the second London equation, we may write that:

$$\nabla \times \left(\nabla \times \vec{B}\right) = \mu_o\left(\nabla \times \vec{J}\right) = -\frac{\mu_o \vec{B}}{\Lambda} = -\frac{\vec{B}}{\lambda^2} \tag{2.3}$$

Using vector identity we can write:

$$\nabla^2 \vec{B} = \frac{\vec{B}}{\lambda^2} \tag{2.4}$$

Equation (2.4) indicates that the magnetic field inside a superconductor decays exponentially from its surface with a characteristic penetration depth of $\lambda = \sqrt{\frac{\Lambda}{\mu_o}}$. This is simply the Meissner effect. The parameter λ is called the London penetration depth.

Though the London equations give a very useful description of electromagnetic properties of superconductors, they do not include any physical explanation of superconductivity.

In 1957, Bardeen, Cooper and Schrieffer proposed a microscopic quantum mechanical model explaining superconductivity [9], [10]. According to their theory (called BCS theory), electrons in superconductors form collective quantum states (bosons) that are made up of a pair of electrons that have opposite momentum and spin. BCS theory predicts that there exists an attractive force between electrons [11]. This force originates from the electrostatic attraction between the electron and the crystal lattice. An electron in the lattice will cause a slight increase in positive charges around it. This increase in positive charge will, in turn, attract another electron. If the energy required to bind these electrons together remains greater than the energy from the thermal vibrations of the lattice attempting to break them apart, the pair will remain bound. Such electron pairs are called Cooper pairs. When a superconducting material is cooled down below its critical temperature, the thermal vibration of its lattice becomes small enough to allow the formation of Cooper pairs. In a superconductor, the current is made up of these Cooper pairs rather than of the individual electrons.

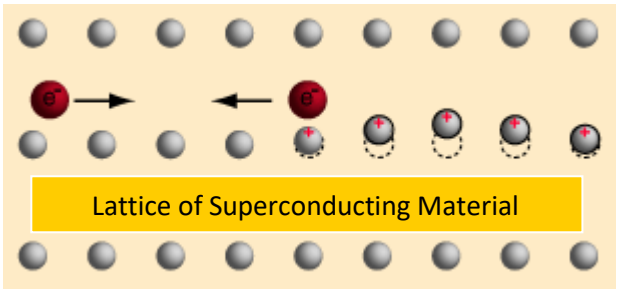

Fig. 2.2: A simple illustration of BCS Theory: Negatively charged electrons induce a polarisation in the neighbouring crystal lattice leading to a slight increment in positive charge. This positive charge attracts another electron (Image taken from *http://hyperphysics.phy-astr.gsu.edu/hbase/Solids/coop.html*).

The length scale of the Cooper pairs (called coherence length (ξ)) is much larger than the lattice spacing of the material. The interaction between a Cooper pair is transient. Each electron in the pair goes on to form a Cooper pair with another electron, and this process continues, with all the newly formed Cooper pairs. Thus, each electron is attracted to every other electron, resulting in the formation of a large network of Cooper pairs. This collective behaviour of all the electrons prevents any further collisions with the lattice and enables current to flow without any resistance.

In 1950, Ginzburg and Landau proposed a phenomenological theory describing superconductivity in terms of a complex order parameter [8]. Later on, Gor'kov showed that the Ginzburg and Landau (GL) theory can be derived from the microscopic description of the BCS theory [12]. The GL theory assumes that in the superconducting state, the current is carried by super electrons of mass m^*, charge e^* and density n_s^* [$m^*=2m_e$; $e^*=\pm 2e$ and $n_s^*=\frac{1}{2}n_s$]. They also proposed the existence of an order parameter given by the following equation:

$$\phi(r) = |\phi(r)|e^{i\Theta} \tag{2.5}$$

Here, $|\phi(r)|^2$ denotes the super electron density. The order parameter $\phi(r)$ has a zero value above T_c and continuously increases as the temperature falls below T_c. In presence of any external magnetic field, the order parameter would have spatial variation. According to this theory, near the transition temperature the Gibbs free energy per unit volume of the system can be expressed as a function of order parameter.

According to BCS theory, electrons in the Cooper pair network are bound to each other with energy (usually of the order of meV) specific to the material and operating temperature. This energy is referred to as superconducting gap energy (*2Δ*). Whenever it is necessary to split the Copper pairs in normal electrons to disrupt superconducting properties, it is imperative to supply more energy than the gap energy externally. The relationship between interaction potential of electrons and energy gap can be expressed by the following integral equation derived from BCS theory [8]:

$$\frac{1}{N(0)V_{BCS}} = \int_0^{\hbar\omega_c} \frac{tanh\frac{1}{2}\beta(\xi^2+\Delta^2)^{1/2}}{(\xi^2+\Delta^2)^{1/2}} \tag{2.6}$$

Here, *N(0)* is the density of states of electrons at absolute zero temperature, V_{BCS} denotes the interactional potential, ω_c is the cut-off frequency at which the lattice induced attraction of the electrons is cancelled by the Coulomb potential and β is the Boltzmann factor $1/k_BT$. From this integral, temperature dependence of superconducting gap energy *Δ(T)* can be computed numerically from equation (2.6) or from the approximate formula as discussed by Khasanov *et al.* or Carrington *et al*. [13], [14] :

$$\Delta(T) = \Delta(0)\tanh\{1.82[1.018(\frac{T_c}{T}-1)]^{0.51}\} \tag{2.7}$$

Dependence of critical current on temperature in the dirty limit can be described by the following relation:

$$I_c(T) = I_c(0)\frac{\Delta(T)}{\Delta(0)}\tanh\left[\frac{\Delta(T)}{2k_BT}\right] \tag{2.8}$$

$I_c(T)$ is the critical current measured at a specific measurement temperature.

The following figure shows the temperature dependence of superconducting energy gaps of niobium, tantalum & tin and how it matches with the numerical solution of equation (2.6) or (2.7).

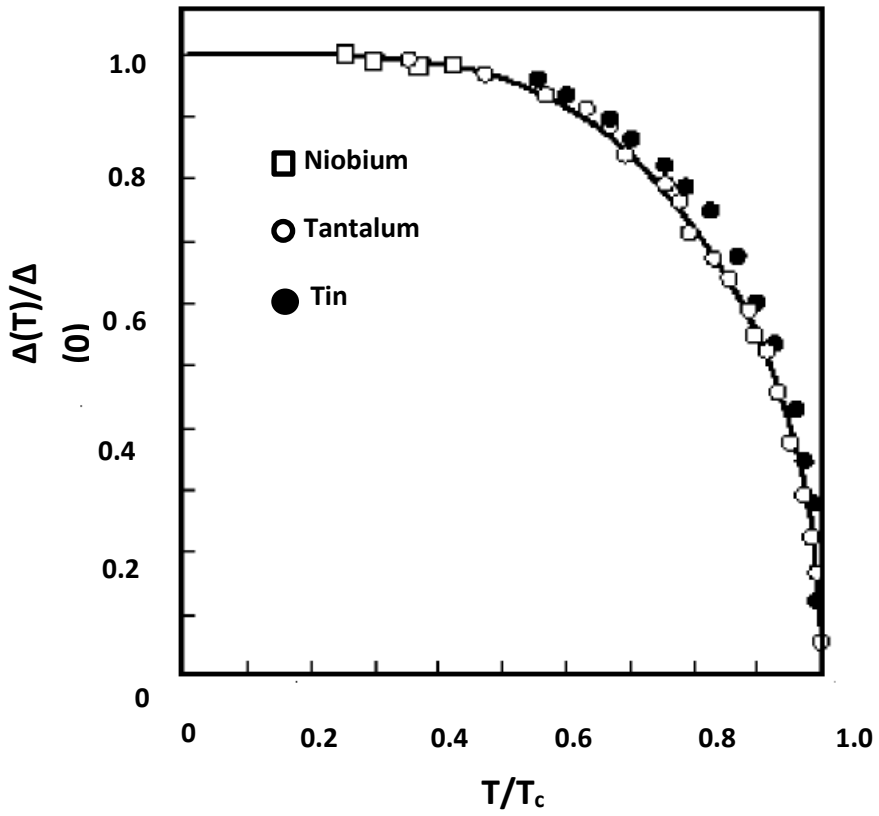

Fig. 2.3: Temperature dependence of superconducting energy gap computed numerically from the BCS theory and compared with experimental data of niobium, tin and tantalum [15].

For weakly coupled superconductors (where $N(0)V_{BCS} \ll 1$), the ratio of gap energy at absolute zero and T_c takes a simplified form:

$$2\Delta(0) = 3.53 k_B T_c \qquad (2.9)$$

2.2 Superconducting Materials

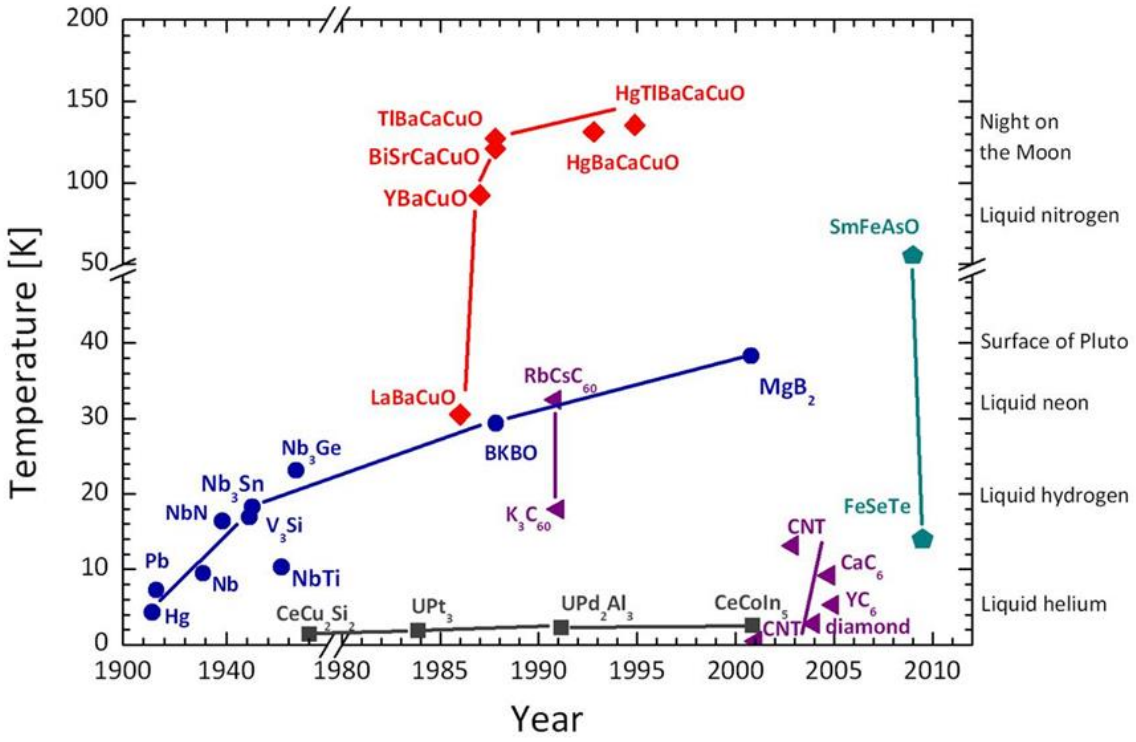

Fig. 2.4: Transition temperature (T_c) of superconducting materials discovered over time (Image taken from *http://www.ccas-web.org/superconductivity*).

The rapid advancement of cryogenic technology has enabled widespread research on superconducting materials. It has been found that many elements in the periodic table show superconductivity (tungsten, lead, niobium, mercury, etc.). Their critical temperatures vary from as low as 0.01 K (tungsten in the alpha phase crystalline structure) to 9.3 K (niobium) [16]. Typically, metals have transition temperatures below 10 K. It is also interesting to note that noble metals such as gold, silver or copper, which have very high electrical conductivity, do not exhibit superconductivity. Several elements also show superconductivity only under special conditions (e.g. Ba or Y under high pressure or Li, Mg or Fe in thin film conditions) [16], [17]. When a superconducting element has more than one isotope, T_c decreases with increasing isotopic mass. This is called the isotope effect [18]. Many metallic compounds and alloys show superconductivity with higher transition temperature [19], [20]. From the following table, it is evident that for binary compounds the T_c can span from 2.6 K (B_3Ru_7, $D10_2$) to 23 K (Nb_3Ge, A15) [16]. A15 structured superconducting materials have many commercial applications [21]. In 1987, Chu and Wu discovered that the alloy $YBa_2Cu_3O_7$

has a superconducting transition temperature of 95 K which can be achieved by liquid nitrogen [22]. Figure 2.4 illustrates the timeline of the discovery of successive classes of superconducting materials and their transition temperatures.

Table 2.1: Superconducting materials and their respective critical temperatures in bulk form [16]

Material	T_c (K)	$2\Delta(0)$ *(meV)*
Nb	9.1	2.77
Ti	0.4	0.12
Pb	7.2	2.19
Se	6.9	2.1
Nb_3Ge	23.2	7.06
B_3Ru_7	2.6	0.79
MoC	14.3	4.35
VRu	5.0	1.52
MgB_2	39.0	11.87
NbN	16	4.9
TiN	5	1.52
Al	1.2	0.36
$YBa_2Cu_3O_7$	95.0	28.91*

(*This value has been calculated from BCS theory. High temperature superconductors have complicated superconducting gap structure which is far from ideal BCS theory.)

2.3 Superconducting Thin Films

Thin film form of superconducting materials is the key to many nanoscale device applications [23]. Especially in the quantum sensor based technologies, superconducting thin films play a decisive role [24]. The relationship between low temperature and normal state material parameters is crucial to the exploration of the superconductivity of thin films. As is well documented in the literature, the superconducting property of thin films is tuned with film thickness and sheet resistance [16]. (The sheet resistance of a film is defined by $R_s = \frac{\rho}{d}$ where ρ is the resistivity of the film and d denotes film thickness [25].) Another important parameter relating to the normal state and cryogenic properties of thin films is the residual resistivity ratio (*RRR).* This is defined by the ratio of sheet resistance measured at room temperature to that at 20 K [26]. It can give an idea about the metallic or insulating

nature of the films. It can also provide a qualitative idea about impurities or crystal defects in the thin film. For metallic films (e.g. Nb) the higher value of RRR indicates higher metallic purity and high crystalline structure of the film. Hence, for the metallic superconducting materials, we should aim for high RRR values. For the semiconducting materials (e.g. NbN and NbTiN) a RRR value >1 indicates the metallic nature of the superconducting film. On the other hand, RRR value < 1 indicates the insulating nature.

2.3.1 Theoretical Models describing correlation of superconductivity and material parameters of Thin Films

Reduction in the film thickness results in the degradation of superconducting property. In particular, once the film thickness reaches a value comparable to the coherence length of the specific material, the superconducting property of the film rapidly decreases. Since, in this thesis, we aim to optimise ultrathin films (< 10 nm) for superconducting detectors, it is worth exploring the theoretical models which describe the correlation between T_c, thickness and sheet resistance and explain the thickness induced destruction of superconductivity. Several theoretical models have been reported in the literature for this purpose [27], [28], [29].

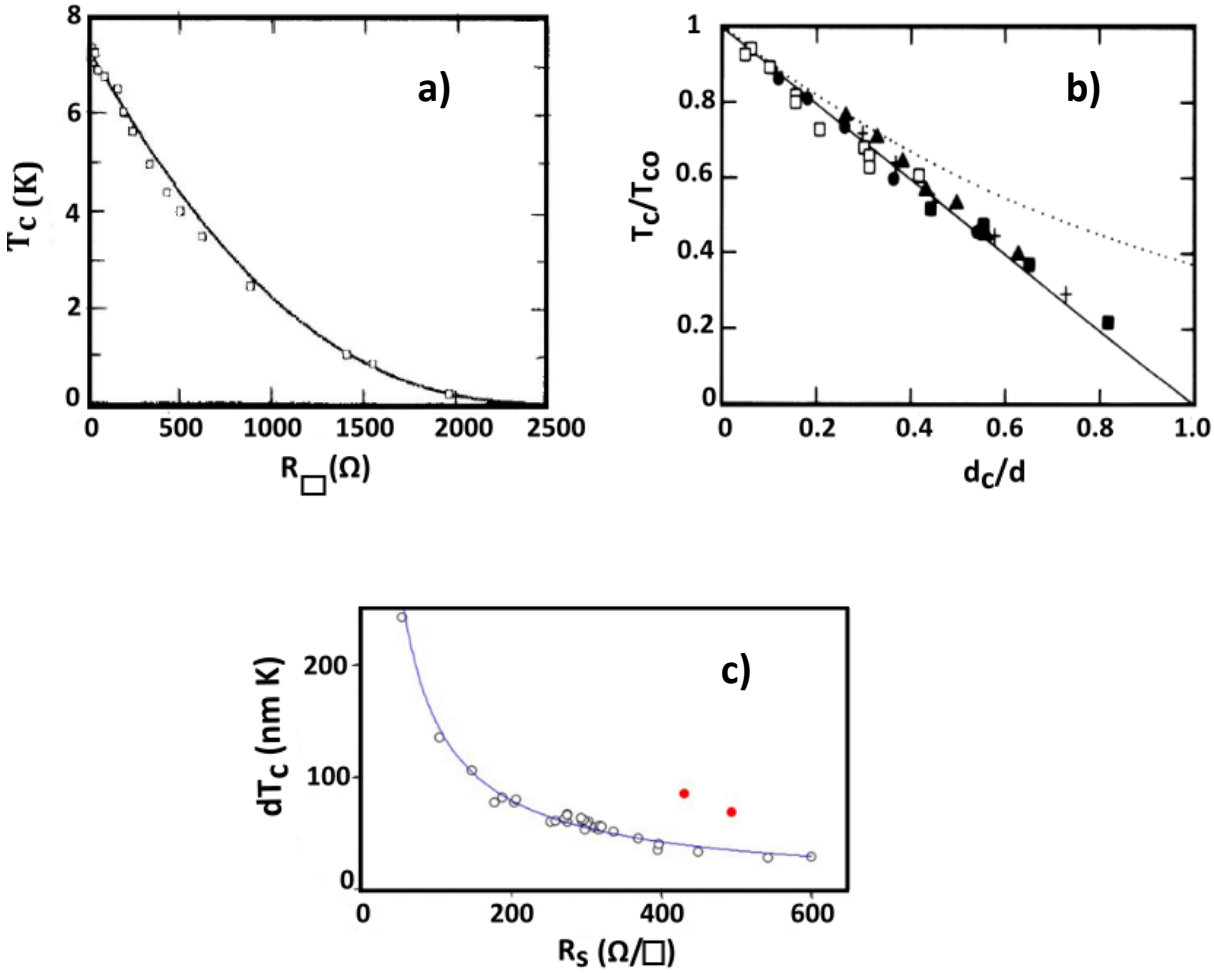

Fig. 2.5: Theoretical Models describing correlation of superconductivity and material parameters of thin films. (a) Finkel'stein Model: Comparison of the Finkel'stein model with the T_c versus R_s data collected from a series of $Mo_{79}Ge_{21}$ samples. According to this model, for homogeneously disordered materials suppression in T_c can be modelled as a function of R_s (*without considering thickness as a variable*) [29]. (b) Simonin Model: The figure shows how the Simonin model fits with the T_c vs d experimental measurements of niobium and lead films. Based on Ginzburg Landau theory, this model describes the correlation between T_c and thickness [28]. (c) Universal Scaling Law: Fitting of universal scaling law proposed by Ivry *et al*. to NbN films deposited on MgO substrates. This empirical law takes into consideration both thickness and sheet resistance dependence of superconducting properties [27].

Finkel'stein proposed a model using renormalisation group tools [29]. This derivation was based on a modified BCS equation. This model explains the destruction of superconductivity through the competition between Cooper-pair attraction and disorder enhanced Coulomb repulsion. According to this model, T_c can be expressed as a function of sheet resistance (R_s)

for homogeneously disordered superconducting materials. *(No direct mention of thickness dependence.)* According to this model,

$$\frac{T_c}{T_{co}}=\exp(\gamma)\left[\frac{1-x}{1+x}\right]^{1/\sqrt{2r}} \quad (2.10)$$

where $\gamma=Ln[\hbar/\tau T_{co}k_B]$; $x=\left(\frac{\sqrt{r/2}}{\frac{r}{4}+1/\gamma}\right)$ and $r=(e^2/2\pi^2\hbar)\,R_s$

Here, T_{co} denotes the bulk superconducting transition temperature of the specific material, ħ is the reduced Planck's constant, e is the elementary charge and γ is a fitting parameter. Finkel'stein analysed a set of amorphous $Mo_{79}Ge_{21}$ superconducting films and compared R_s vs T_c data of those films with his proposed model. They have shown that equation (2.10) fits reasonably well with MoGe data (shown in Fig. 2.5).

Simonin derived a simple model based on Ginzburg Landau theory to describe the correlation between T_c and film thickness resulting in the following equation [28]:

$$T_c=T_{co}[1-d_c/d] \quad (2.11)$$

Here, d_c is termed critical thickness. This can be defined as a threshold thickness for the specific material below which it will lose superconducting property. T_{co} denotes the bulk superconducting transition temperature in both the models.

Ivry *et al.* proposed an empirical universal scaling law which takes into account both the effects of d and R_s on T_c. Although this scaling law was established by analysing data from the past 50 year' of research on various superconducting materials, there was no theoretical derivation of this model [27]. Later, Tao *et al.* explored the theoretical foundation of this model using the renormalisation group method [30]. According to this law, film thickness, sheet resistance and the transition temperature scale as $T_cd(R_s)$ lead to the following power law:

$T_c d = A R_s^{-B}$ (2.12)

Here A and B are fitting parameters. Ivry *et al.* discussed that the numerical value of the exponent B can be related to structural disorder of the material. More disordered the thin film material is higher the value of B will be.

2.3.2 Influence of growth conditions on film microstructures

Superconducting properties are strongly influenced by microstructures and crystallographic orientation of thin films. Hence, a better understanding of the correlation between film microstructure and various growth parameters can be very helpful in order to design a thin film material for specific technological applications. Here, we have reviewed the model proposed by Thornton, which predicts how the structural properties of the film microstructure varies with the deposition parameters (e.g. substrate temperature and working gas pressure) in the case of any physical vapour deposition technique [31], [32]. According to the Thornton zone model, thin film deposition processes can be divided into three steps. First, the arriving atoms transfer their kinetic energy to the lattice and become loosely bonded adsorbed atoms (transport step). In the next step, they diffuse over the surface until they either are desorbed or become incorporated in the film (surface diffusion step). Finally, diffusion occurs within the bulk of the film and with the substrate (bulk diffusion step). The thermal motion of atoms in the growing film strongly depends on the ratio between substrate temperature T_s and the binding energy of atoms in the solid. As the melting point (T_m) of a solid depends largely on the binding energy of its atoms, thermal motion of atoms scales with the ratio of T_s to T_m (in K), (termed as the reduced temperature). Thus, each of the three basic processes (transport, surface diffusion and bulk diffusion) can be expected to dominate film growth over different ranges of T_s/T_m, which results in different film structures. The diffusion length Λ of the adsorbed atoms at the time t is given by $\Lambda = a\sqrt{k_d t}$ whereas k_d denotes the frequency at which an individual adsorbate atom jumps to another adjacent site and a is the distance between two sites [33]. As is shown in the Fig. 2.6, three structural zones (Zone 1, 2 & 3) and a transitional zone (zone T) can be identified in the sputter deposition process.

For room temperature deposition or deposition on the cooled substrate – i.e. low reduced temperature (T_s/T_m<0.3) – the thermal motion of the adsorbed material is negligible. [$\Lambda < a$ in this condition.] Hence, surface diffusion does not have time to occur before the deposition of the next atomic layer. In this regime, known as the quenched growth (QG)

regime, it is the transport process that dominates film growth, meaning that atoms become immobilised where they land. Films resulting from these quenched growth processes exhibit amorphous or poor crystalline microstructure (Zone 1 and zone T in Fig. 2.6):

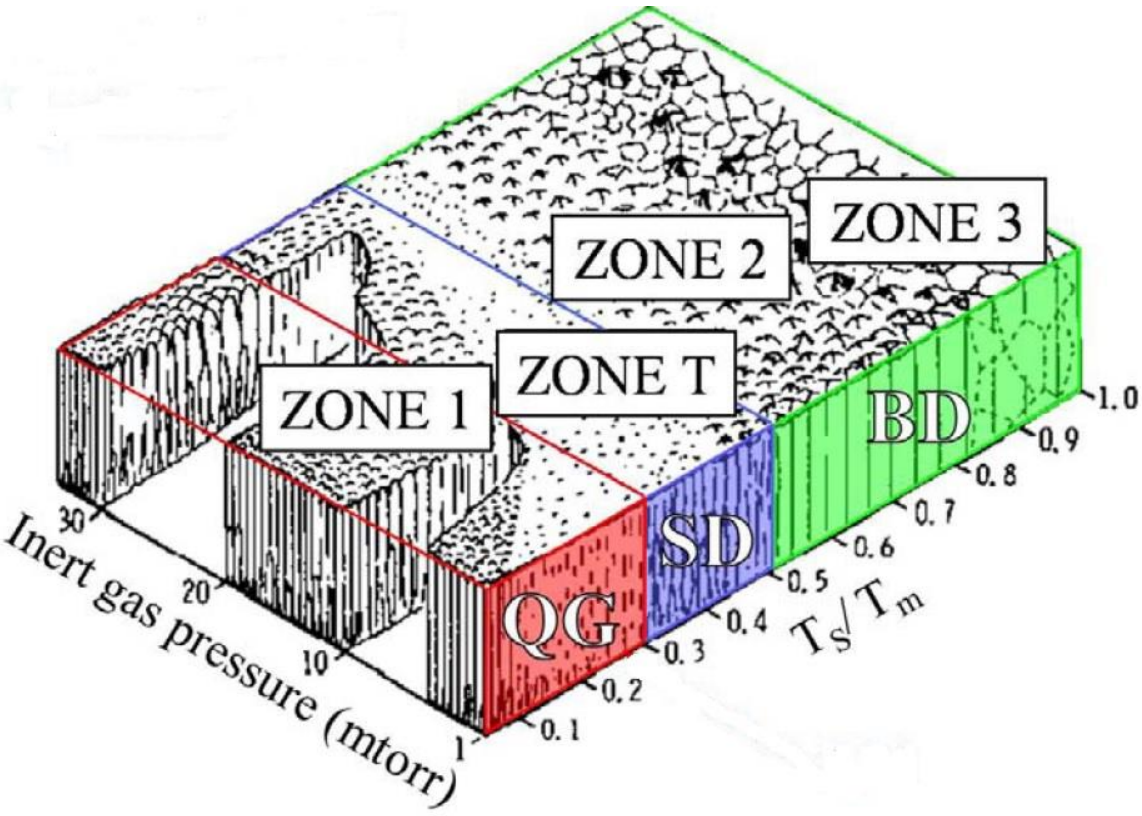

Fig. 2.6: Influence of deposition parameters on structural properties of thin films deposited by any physical vapour deposition technique as explained by Thornton's structure zone model [34].

When we start to heat the substrate during film deposition (i.e. at intermediate reduced temperatures ($0.3<T_s/T_m<0.5$)), film growth gradually becomes dominated by ad-atom surface diffusion. Films resulting from this growth regime consist of columns having tight grain boundaries between them (Zone 2 in Fig. 2.6). Grain sizes increase with T_s/T_m. Hence, films grown on the heated substrate have improved crystalline property in comparison to the films grown at room temperature. If we heat substrates further to higher temperature (i.e at high reduced temperatures ($T_s/T_m>0.5$)) bulk diffusion dominates the film growth and its structure is dominated by more isotropic and equiaxed grains (Zone 3 in Fig. 2.6). Zone 3 is rarely experimentally observed.

From the above general description of structures, it can be inferred that for amorphous films it would be useful to grow the films at low temperatures (at room temperature or even on cooled substrates). On the hand, for crystalline or polycrystalline materials substrate heating would improve the structural properties of the films.

2.4 Detection of electromagnetic energy in superconductors

Due to its unique properties, superconductivity can be utilised in the detection of electromagnetic energy. Based on Max Planck's mathematical formulation, Einstein postulated that electromagnetic radiation may be described as a collection of quantised particles called photons [35], [36]. According to Planck's law, the energy of each single photon is characterised by its frequency ($E=h\upsilon$). Photon detection is immensely important in many scientific and technological applications [37]. For instance, low energy, long wavelength photons are particularly relevant in cosmology and astrophysics where the Doppler shift has influenced the radiation across billions of light years [38]. In telecommunications, fibre optic cables are used to transmit information with low attenuation at infrared wavelength [39]. In quantum cryptography, secure cryptographic keys are created by encoding information on the phase or polarisation of single photons [40]. Thus, infrared photon detection is essential to the development of next generation communication technology. Photons in the mid and far infrared are also highly relevant in the field of atmospheric science and remote sensing [41]. In the following sections, we summarise how superconductivity has been used to develop novel photon detection technology.

2.4.1 Superconducting Tunnel Junction

A Superconducting Tunnel Junction (STJ) consists of a thin insulating barrier layer (e.g. Al_2O_3) sandwiched between two thin superconducting absorbers (e.g. Nb or Ta) [42]. When a photon is incident on the superconducting absorber, which is maintained well below its critical temperature (usually below 1 K), charge carriers (hot electrons) are generated as Cooper pairs are broken. These charge carriers tunnel across the thin barrier layer resulting in a measurable current. The magnitude of this tunnelling current depends upon the

tunnelling, recombination and scattering of charge carriers in the system. STJs have very high energy resolution. For photon energies between 1 eV and 1 keV, Nb based STJ has energy resolution between 0.13 eV and 4.3 eV full width half maximum (FWHM). Due to their high energy resolution, STJs are of interest in the field of infrared astronomy. However, since STJs need ultralow operational temperature and require an applied magnetic field to suppress other tunnelling effects (Josephson current), they are too expensive and impractical for widespread use in other applications.

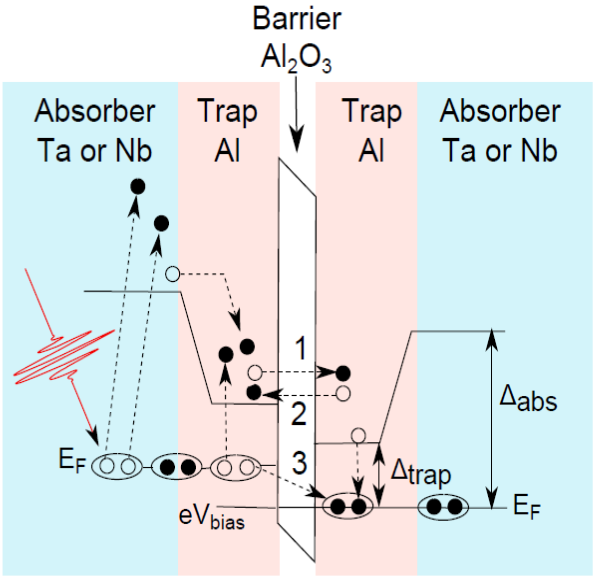

Fig. 2.7: Schematic Diagram of a Superconducting Tunnel Junction (STJ): incident photons generate quasi particles (hot electrons) in the superconducting absorber layer. They tunnel through the insulating Al_2O_3 barrier to generate a measurable current signal. Tunnelling of Cooper pairs (Josephson tunnelling) is suppressed by the application of a magnetic field [43].

2.4.2 Superconducting Transition-Edge Sensors

A Superconducting Transition-Edge Sensor (STES) consists of a thin layer of superconducting material (e.g. tungsten) placed on an insulating substrate. The STES operates near the transition temperature of the superconducting thin film [44], [45]. When a photon is incident on the sensor, the superconducting material absorbs the photon, and its temperature slightly increases above its transition temperature. Hence, it generates a sharp

change in resistance. Gradually, it cools down by dissipating heat to the weakly coupled heat sink and the STES returns to the superconducting state again. The resistance fluctuation is measured via electronics read-out and is recorded as a photon detection event. STES devices measure the energy deposited and hence have spectral and photon number resolving capability.

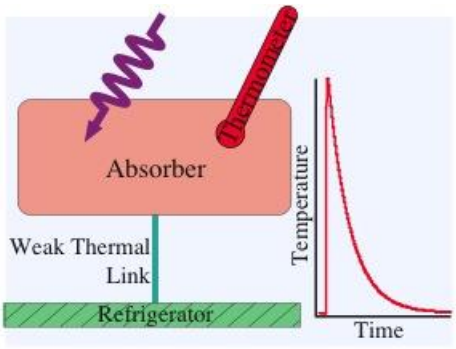

Fig. 2.8: Schematic of Superconducting Transition Edge Sensor (STES): superconducting absorber weakly coupled to refrigerator heat sink (Image taken from *http://space.mit.edu/micro-x/science/tes-science/tes-science.html).*

STESs have very high detection efficiency at visible and near infrared wavelengths. Lita *et al.* [45] have demonstrated detection efficiency of η= 95% at 1556 nm (with an energy resolution of 0.29 eV FWHM). They have used tungsten as a superconducting thin film and integrated it within an optimised optical structure to enhance optical absorption. The dark count rate of these devices is very low (1/1000 s). They also show excellent photon energy resolution. On the other hand, STESs have some crucial disadvantages. First, it is very difficult to match their noise to amplifiers (an STES's normal resistance is typically a few ohms or less). Secondly, there is the problem regarding the operation of the STES at very narrow superconducting to normal transition region. [Voltage biased operations with a SQUID (superconducting quantum interference device) electronic read-out have been introduced to eliminate these problems.] Thirdly, STESs need expensive electronics read-out and a weak link with a refrigerator operating at a very low temperature (40 to 300 mK). Finally, they are also susceptible to triggering by background black body radiation.

2.5 Infrared single photon detection: Superconducting Nanowire Single Photon Detector (SNSPD)

In 2001, Gol'tsman *et al.* first demonstrated that nano structures patterned on a superconducting thin film may be used for single photon detection [46], [47]. They used a bridge structure that was well below a micrometre in width and patterned via electron beam lithography and etching in a 5 nm thick NbN superconducting film. A nanowire patterned superconducting detector was cooled down well below its superconducting transition temperature, and it was DC-biased with a current close to its critical current.

The nanowire absorbs incident photons depending upon the optical properties of the superconducting material. If photons have sufficient energy (greater than the superconducting gap energy of the material) Cooper pairs will be broken, creating hot electrons or quasiparticles. For NbN at infrared wavelengths the absorbed photon will disrupt hundreds of Cooper pairs in the nanowire, resulting in the formation of a resistive region as the breaking of Cooper pairs will lead to the transition to a normal state. This small resistive region is called a 'hotspot' [48]. The hotspot resistance forces the super current in the superconducting nanowire to bypass this region. Since the width of the nanowire is very small (~100 nm), this diversion causes the local current density around the hotspot to increase quickly (within few picosecond) beyond the critical current density of the material, creating a resistive barrier across the nanowire. Thus, the bias current is diverted in a parallel path across shunt resistance [49]. As is shown in Fig. 2.10, the electrons in the hotspot region exchange their energy with phonons in the nanowire via electron-phonon scattering with a time a constant of τ_{e-ph} (~ 10 ps). Then, this energy is coupled to the substrate through phonon-phonon scattering with a time constant of τ_{ph-sub}. A small fraction of the energy is reflected back into the electron system of the nanowire due to the lattice mismatch between the superconducting nanowire and the substrate. Thus, the substrate (which is remained cold at $T_{substrate}$) acts as a heat sink for the 'hot' electrons absorbing their energy [50]. In this way, the hotspot region gradually cools down and recovers to a superconducting state and the wire starts carrying bias currents normally. Hence, we get a measurable output voltage pulse as a signal of the photon detection event. Recently, Engel *et al.* have compared the existing theoretical descriptions of the detection mechanism of the SNSPD with the experimental data, and they have predicted that a magnetic vortices based model may improve accuracy of theoretical description [51].

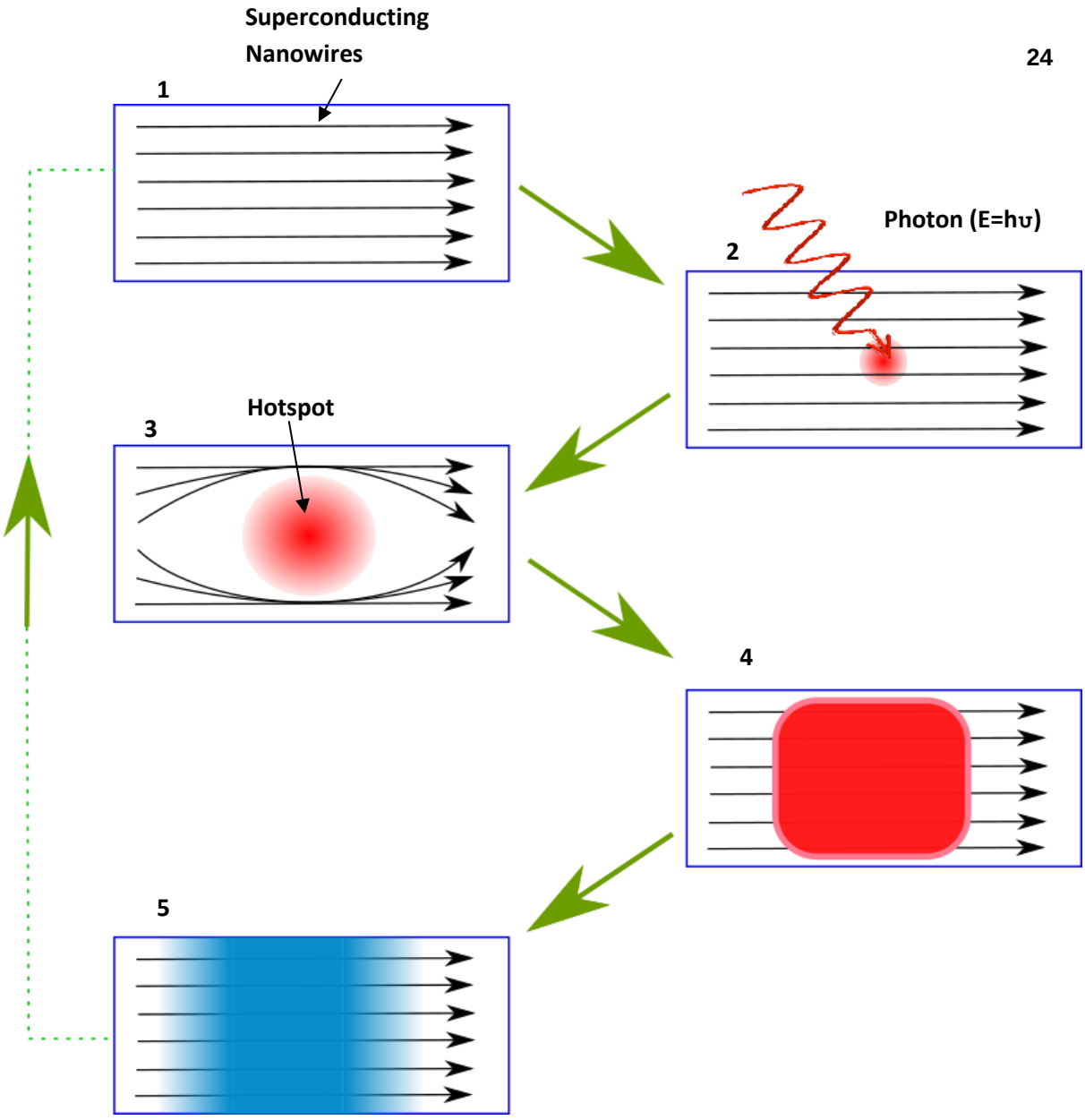

Fig. 2.9: The working principle of the Superconducting Nanowire Single Photon Detector (SNSPD): 1. The nanowire is cooled down below the superconducting transition temperature and externally DC biased just below the critical current specific to the device. 2. A photon is incident on the nanowire and a hotspot region is created as incident photons break the Cooper pairs inside the material. 3. The hotspot expands to the edges of the nanowire as supercurrent is diverted around the edges, increasing the local current density above the critical current level 4. This hotspot region grows in size due to Joule heating and eventually creates a resistive barrier across the nanowire. This resistive region causes the bias current to be diverted to the external shunt. 5. The nanowire is able to cool down below the superconducting transition temperature and the bias current returns to the nanowire at the same level as in 1 [47], [37].

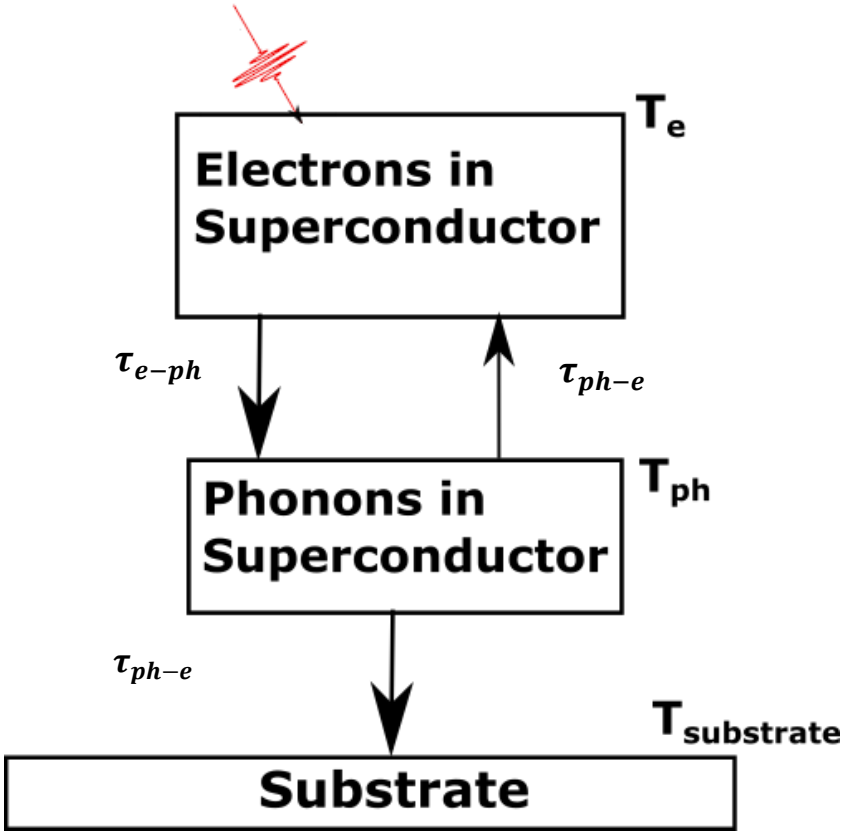

Fig. 2.10: Schematic of the energy dissipation process after photon absorption in a superconductor: T_e and T_{ph} denote the temperature of the electron system and phonon system of superconducting nanowires respectively. Electrons in the nanowire absorb energy from the incident photon and a hotspot is created there (T_e). The energy in the electron system is coupled to the phonons of the superconducting material via electron-phonon scattering, with a time constant of τ_{e-ph}. The phonons then couple the energy to the substrate (which remains cold at $T_{substrate}$) via phonon-phonon scattering, with a time constant of τ_{ph-sub} .

2.5.1 Performance Parameters for SNSPDs

An ideal single photon detector will generate an electrical signal whenever it absorbs a photon. In practical scenarios, SNSPDs have non-ideal performance characteristics. The following parameters benchmark the practical performance of SNSPD as a single photon detector.

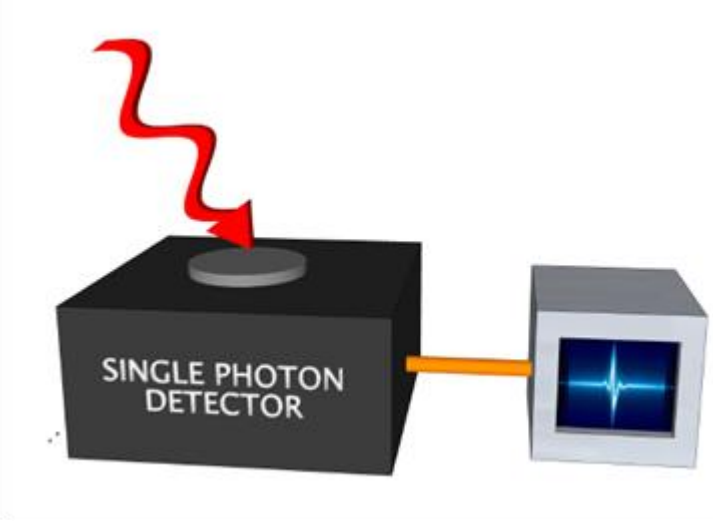

Fig. 2.11: An ideal single photon detector will generate a fast, well defined electrical signal for every photon incident on it.

(a) **Detection Efficiency**: Detection efficiency (η) is the most crucial performance parameter of an SNSPD. It is defined by the probability that a photon will be detected (by taking the photon all the way through the experimental system and generating an output signal in the read-out electronics) once a photon is incident on the detector system [52], [53]. In real life applications, η is usually less than 100% and strongly depends on device design, uniformity and the spectral wavelength of incident photons. Efficiency is usually measured by recording device counts per second and comparing that to the number of incident photons.

Detection efficiency can be broken into several constituent elements. First, in any real life application, photons can be lost before reaching the detector due to absorption, scattering or reflection within the experimental environment. Thus, the probability of coupling incident light with a detector is defined as the coupling efficiency ($\eta_{Coupling}$). Secondly, the optical absorption property of the detector (depending on wavelength, material and geometry) defines the number of photons which will actually be absorbed by the detector. Absorption efficiency ($\eta_{Absorption}$) gives the probability that an incident photon which is coupled with the detector is absorbed by the SNSPD. Finally, there may be a non-unity probability that the detector generates an output electrical signal at the read-out electronics after photon absorption. We define this as the registering probability ($\eta_{Registering}$).

Taking all these into account, we can write the following:

$$\eta = \eta_{Coupling} X \eta_{Absorption} X \eta_{Registering} \quad (2.13)$$

(b) **Dark Counts**: An SNSPD may produce spurious signal pulses in addition to photon detection signals due to stray light, black body radiation or electrical noise [37]. Since these detectors are highly sensitive, they can be triggered by stray light in the experimental environment and also by black body radiation of the experimental system. Dark counts can be reduced by encapsulating the detectors in a radiation shield and by eliminating as much light from the laboratory as possible. The dark count rate (D_{CR}) is measured in terms of counts per second (cps) or Hertz (Hz).

(c) **Dead Time**: During the generation of the voltage signal, superconducting nanowires are unable to register another incoming photon [47]. This time period is known as dead time. As discussed above, upon absorption of a photon, a small resistive hotspot is created in the nanowire. This grows very quickly to form a resistive barrier across the wire with a time constant of τ_1. This defines the rise time of the leading edge of the output voltage pulse. Then, the nanowire slowly cools down to a superconducting state, dissipating heat to the substrate with a time constant of τ_2. This time constant defines the trailing edge of the pulse. The total duration of (τ_1+τ_2) is defined as the dead time. After this time, the detector returns to superconducting state and becomes ready for photon detection.

(d) **Timing Jitter**: Timing jitter is the intrinsic timing resolution between the arrival of the photon at the SNSPD and the generation of the output pulse [54], [55]. The jitter of a detector is measured by calculating the Full Width at Half Maximum (FWHM) from the plot of the statistical distribution of time delay between the arrival of a photon at the detector and the observation of an output signal from the detector. The lower the timing jitter of a device, the better timing precision it has for the arrival of the photon. This sets a limit on the maximum count rate of the detector or the maximum possible clock speed that the device can be used

at. Low timing jitter enables high-clock-rate quantum communication experiments and leads to improved signal-to-noise ratio (SNR) in gated photon counting experiments.

Figure of Merit: Noise equivalent power (NEP) has been widely used as a figure of merit of photon detectors. It is measured by the input optical power, which is necessary to generate a signal-to-noise ratio of 1 Hz output bandwidth at a given data-signaling rate or modulation frequency, operating wavelength and effective noise bandwidth [56]. For single photon detectors, it is given by $\frac{h\nu}{\eta}\sqrt{2D_{CR}}$ (D_{CR} denotes dark count of the device). However, NEP does not take into account the timing jitter of the detector. Hadfield *et al.* proposed a dimentionless figure of merit of the SNSPD considering all the perforance paramters [37]. It is defined by $H=\frac{\eta}{D_{CR}\Delta t}$. (Δt denotes the timing jitter of the device.) It should be noted that if we operate the detector at a lower bias current we will get very low dark count leading to a low value of NEP. However, it will also reduce the detection efficiency of the device.

2.5.2 Evolution of Device Design

Since its initial demonstration, many research groups around the world have been working to improve the performance parameters of SNSPDs. Focussing an optical spot on a ~100-200 nm wide nanowire (well below the wavelength of infrared light) may not be feasible for practical experiments or will lead to very poor coupling efficiency. One approach used to solve this is to pattern the superconducting nanowire in a large square area (several microns along each side) meander in order to increase the coupling efficiency of the incoming light. To enhance the optical absorption in the detector, researchers have tried to integrate the device inside an optical cavity or waveguide circuit or to deposit an anti-reflection coating on top of the device (e.g. detectors have been fabricated on the top of SiO_2/Si or GaAs/AlGaAS distributed Bragg reflectors or Au mirrors have been used to form an optical cavity). This reduces optical losses due to transmission or reflection from the device and thereby increases the probability of photon absorption in the nanowire [57], [58]. Zhang *et al.* have shown that a 60% system detection efficiency at a wavelength of 940 nm can be achieved with a NbN based meander device fabricated on the top of a Si based DBR substrate. To enhance the device's active area so that detectors can be optically coupled through free space or using multi-mode fibres, the concept of large area multi pixel SNSPD array has been proposed. Allman *et al.* have reported the performance of free-space-coupled 64 pixel WSi based SNSPD array [59].

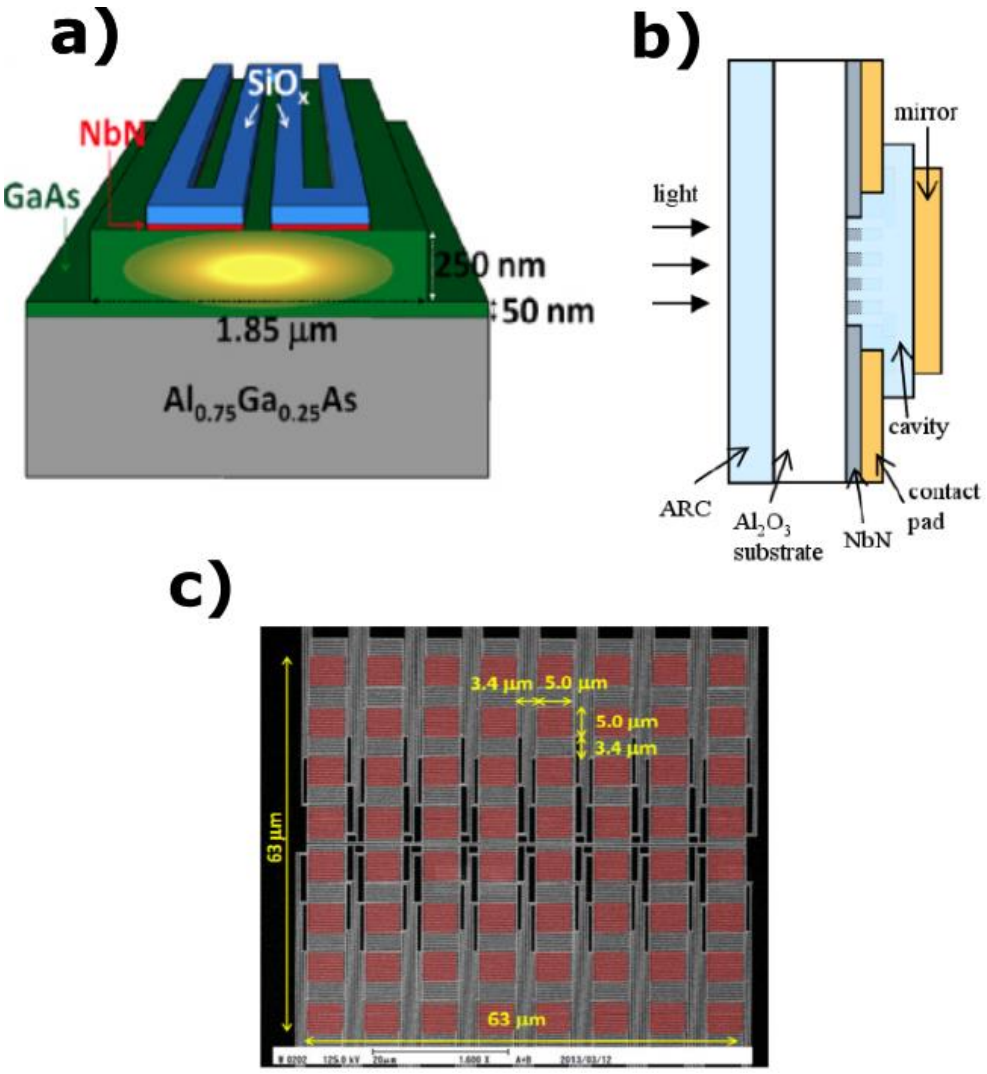

Fig. 2.12: Recent advances in SNSPD device designs from international groups (a) SNSPD fabricated on the top of GaAS based waveguide structure to to improve optical coupling efficency (TU Eindhoven) [60] (b) NbN based SNSPD integrated in optical cavity (MIT) [58] (c) 64 pixel SNSPD array based on NbTiN film (NICT Japan) [61].

2.5.3 Superconducting thin films for SNSPD

The first and the most crucial step in superconducting detector fabrication is to deposit superconducting thin film on appropriate substrates. For SNSPD operation we need ultrathin (< 10 nm) superconducting films which can be cooled down using refrigerators. For thicker films, the hotspot will not be able to create a resistive barrier across the nanowire. Rather, it will decay, dissipating heat in the surroundings. Hence, the device will not be able to generate a signal indicating photon detection. Gol'tsman *et al.* used 4 nm thick NbN in their initial detectors [46]. NbN has a crucial advantage of having a comparatively higher critical

temperature (17 K for bulk) and shorter coherence length (~ 5 nm) [62]. Thus, it is possible to deposit thin NbN (~ 6nm or 8nm) films which will superconduct even at 4 K [63]. Being a very hard refractory transition metal nitride, NbN has the advantage of having stability even over repeated thermal cycling between room temperature and cryogenic temperatures [64]. With subsequent development, SNSPDs with NbTiN (a polycrystalline material having properties similar to NbN) films have been evolved. NbTiN nanowire devices have been shown to possess a shorter dead time compared to NbN devices since they have lower kinetic inductance [65]. NbN and NbTiN have been widely employed as the base material for SNSPD fabrication.

Since NbN or NbTiN films used in SNSPDs are very thin, the crystalline quality of the films becomes a crucial issue. Poor crystalline quality may lead to non-uniformity in the film or to degradation of the film's superconducting property. The lattice structure of the film material should match well with that of the substrate to achieve ultrathin films with high crystalline properties. Since lattice parameters of MgO (0.421 nm) [66] or sapphire (0.471 nm) [67] are very close to that of NbN (0.439 nm) [68] and NbTiN (0.434 nm) [69], these are widely used substrates for SNSPD. Marsili *et al.* have reported a T_c of 8.6 K for a 3 nm NbN film deposited on an MgO substrate [63].

However, crystalline nature of NbN & NbTiN makes substrate choice of superconducting detectors very limited, which sometimes restricts their efficiency and range of applications. Especially, for integration in waveguide circuits or optical cavities we need to fabricate detectors on substrates like GaAs or silicon. Though enough research has been carried out to heat the substrate up to a few hundred degrees centigrade during the thin film deposition or to control film growth parameters, deposition of NbN or NbTiN on lattice mismatched substrates or complicated optical structures is still a challenging problem [70]. Miki *et al*. have demonstrated high efficiency fiber-coupled NbTiN based SNSPDs fabricated on thermally oxidised silicon substrates (the best performing device have an SDE of 74%) [71].

Recently, several amorphous transition metal (TM) based Type II superconducting materials (MoSi, MoGe or WSi) have been demonstrated to be highly promising alternatives for this purpose. These materials offer various advantages to SNSPD fabrication [72]. (Type II superconductors are a specific class of superconducting materials where there are two differenct critical magnetic fields. At the onset of the first one, the material enter a mixed region of normal and superconducting state, named as vortex state. At the second one, superconducting property is completely destroyed.) They do not have strict substrate

requirements and also have lower superconducting gap energies which give higher intrinsic single photon detection efficiency at long wavelengths [73]. Though they have lower critical current density compared to NbN due to lower free carrier concentration but that also leads to larger hotspot size during absorption of an incident photon [74].

From the eqn. 2.9 it is evident that the advantage of the lower superconducting gap ($2\Delta(0)$) comes with a lower superconducting transition temperature. Molybdenum silicide, with a composition of $Mo_{75}Si_{25}$, has a bulk T_c of ~7.5 K [62], which is comparatively much higher than what other transition metal based superconducting material allows. On the other hand, its bulk superconducting energy gap is ~ 2.28 meV [62] which is almost half of the energy gap of NbN (4.9 meV) [73]. The following table presents a comparison between superconducting properties of various TM based amorphous alloys and traditional SNSPD materials. Amorphous alloys such as WSi (which is until now the most commonly used amorphous thin film for high efficiency SNSPDs) or NbSi have very low bulk T_c. Hence, we need an expensive and complicated cooling system to run WSi based SNSPDs below 1 K to achieve high system detection efficiency (SDE) and low timing jitter. MoSi has a T_c > 4K even in the thin film form although its superconducting energy gap is comparable to that of WSi. So, it can be an ideal base material for high performance SNSPDs which can be operated at a temperature >2K with relatively cheap, less complex closed cycle cryogenic systems.

Table 2.2: Comparison of the superconducting properties of amorphous transition metal (TM) based alloy materials with conventional SNSPD material

	NbN	**MoSi**	**MoGe**	**WSi**	**NbSi**
Bulk T_c (K)	16 [73]	7.5 [73]	5 [62]	7.4 [62]	3.1 [75]
Thin Film T_c (K)	8.6 (3 nm) [63]	4.2 (4 nm) [73]	4.4 (7.5 nm) [62]	3.7 (4.5 nm) [62]	2 (10 nm) [76]
Energy Gap $2\Delta(0)$ (meV)	4.9 [73]	2.28 [62]	2.2 [62]	1.52 [62]	0.94

SNSPDs fabricated from WSi amorphous thin films have demonstrated better than 90% SDE. The first MoSi based SNSPD was reported by Korneeva *et al.* achieving 18% efficiency at 1200 nm wavelength [77]. Verma *et al.* have recently shown by integrating

detectors in an optical cavity, an enhanced efficiency of 87% at 1542 nm can be obtained with 76 ps timing jitter [78].

Though high temperature superconductors (HTS) could be interesting material for SNSPDs in terms of cryogenics, they have significant disadvantages. These materials have large superconducting energy gaps compared to low temperature superconductors [79]. (As shown by equation 2.9 superconducting energy gap is a linear function of T_c . Though HTSs are far from ideal BCS superconductors its energy gap is larger due to its comparetively higher T_c .) Hence, it is really difficult to design high efficiency SNSPDs for infrared single photon detection based on HTS films. Ultrathin films with optimal superconducting properties based on HTS materials are hard to produce and are subject to rapid degradation. Moreover, complicated crystal structure and grain boundaries lead to suppresion of critical current and formation of grain boundary based josphson junstions. It would be very challenging to deposit uniform HTS films over a large area and fabricate nanowire based devices on them [80].

2.5.4 Applications

SNSPDs have been demonstrated to be highly a promising alternative solution for advanced photon counting applications. Potential applications include quantum key distribution (QKD) [81], linear optical quantum computing [82], characterisation of quantum emitters [83], space-to-ground communications [84], integrated circuit testing [85] and single oxygen luminescence dosimetry for laser based cancer treatment [86]. As shown in the following figure, the spectral sensitivity of an SNSPD covers a wide range (200 nm - >> 2μm) due to smaller superconducting energy gap (meV instead of eV). At infrared wavelengths SNSPDs operate with high system detection efficiency, low dark count rate and tens of picoseconds timing jitter. On the other hand, the performance of semiconductor based single photon detectors is restricted by material properties (e.g. for infrared photon detection SPAD development is very complicated due to competing requirements of a material with good IR absorption and low noise gain). Though the requirement of cryogenic operation brings additional complexity to measurement set up, it is possible to design and fabricate high performance SNSPDs which can be operated at a temperature >2 K using relatively cheap, less complex closed cycle cryogenic systems. Hence, SNSPDs can be promoted as an attractive substitute technology for single photon detection especially in the infrared spectral domain.

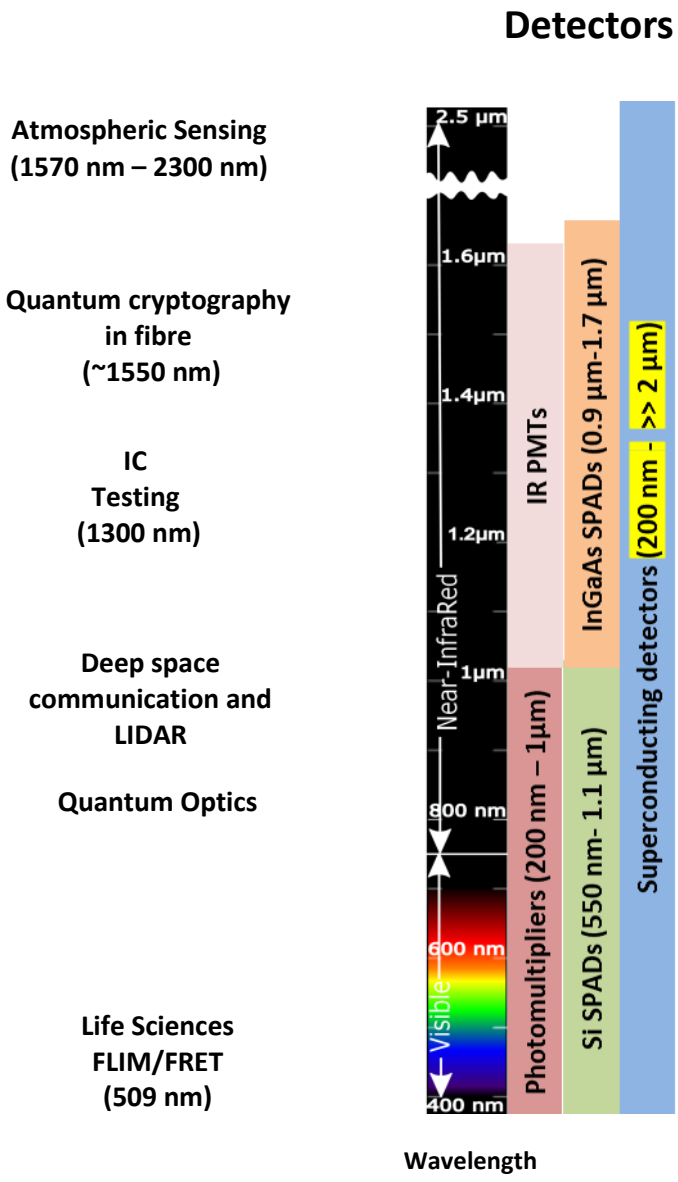

Fig. 2.13: The compatibility between single photon counting technologies and applications in terms of operating wavelength; the figure also demonstrates the advantage of superconducting detectors as an alternative choice for ultrasensitive photon detection due to its smaller energy gap (meV instead of eV).

2.6 Terahertz radiation detection: Microwave Kinetic Inductance Detector (MKID)

In spite of having zero DC resistance, superconductors have non-zero complex surface impedance for alternating current (AC). When an electric field is applied on a superconductor, Cooper pairs are accelerated storing kinetic energy in them. Energy may also be stored in the magnetic field inside the superconductor (within the short penetration depth). Thus, a superconductor has a complex surface impedance due to the energy flow between the superconductor and the applied electromagnetic field [87], [88]. Superconducting kinetic inductance sensors utilise this property. When a photon is incident on the sensor, some Cooper pairs are broken leading to the creation of a cascade of quasiparticles having energy slightly greater than the superconducting gap energy. The number of quasiparticles is given by $N_{qp}=\eta_{quasi}h\nu/\Delta$ (η_{quasi} is the efficiency of the device to generate quasiparticles.) These particles persist until two quasiparticles meet and emit a phonon, recombining into a Cooper pair again. These quasiparticles induce a change in the surface impedance of the superconducting thin film ($Z_s=R_s+i\omega L_s$) as the kinetic inductance of a superconductor is inversely proportional to the density of Cooper pairs. This change in surface impedance is detected through proper read-out electronics. The read-out is achieved by introducing the device in a microwave feed line and through the resonant frequency of the LC circuit as shown in the figure below. The absorption of a photon will cause the resonance centre frequency to shift to lower values and the resonance dip to decrease in depth. A crucial advantage of MKIDs is that they are easy to multiplex via a single microwave feed line and are thus scalable to large arrays.

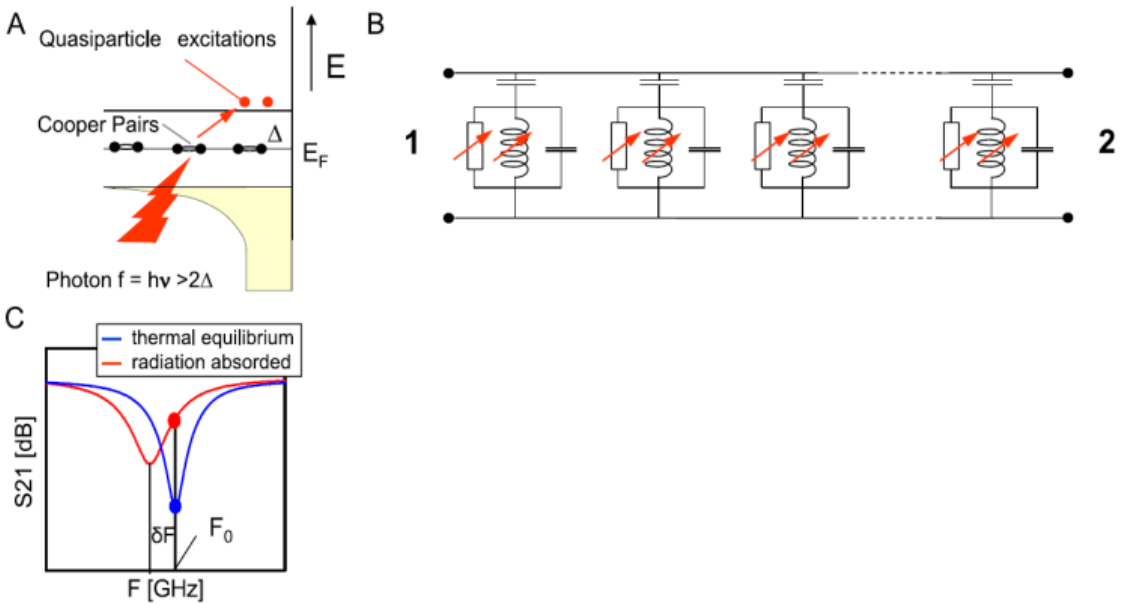

Fig. 2.14: MKID operation principle. A: Incident photons break Cooper pairs creating quasiparticles. B: By embedding a superconducting thin film device in a resonance circuit, it is possible to read out changes in the complex surface impedance and frequency division multiplexing can be achieved by coupling many resonator circuits to a single transmission feedline. C: Measured transmission from contact 1 to 2 in resonator circuit shown in B. The blue line represents the equilibrium situation and the red line the situation after photon absorption [89].

2.6.1 Performance Parameters for MKIDs

Noise Equivalent Power (NEP): Noise equivalent power (NEP) is an important parameter to measure the sensitivity of MKID detectors. In thermal equilibrium, the sensitivity of kinetic inductance detectors is limited by the random generation and recombinations of quasiparticles due to thermal noise. The generation-recombination noise equivalent power $NEP_{G\text{-}R}$ can be expressed as [89]:

$$NEP_{G-R} = \frac{2\Delta}{\eta_{quasi}}\sqrt{\frac{N_{qp}}{\tau_{qp}}} \propto \exp(-\frac{\Delta}{k_B T}) \tag{2.14}$$

Here, N_{qp} denotes the number of quasiparticles and τ_{qp} is the quasiparticle life time. Since, theoretically, both N_{qp} and τ_{qp} follow exponential dependency with temperature, NEP_{G-R} also follow similar scaling with temperature. For applications in next generation far infrared astronomoy projects , a NEP of the order of $10^{\wedge\text{-}19}$ is required. On the other hand, for passive teraherz imaging, a NEP ~$10^{\wedge\text{-}15}$ is sufficient [87].

Energy Resolution: For any photon detector which works on the concept of creation of quasiparticles upon absorption of photons, there is a fundamental limit on the energy resolution of the device called the Fano Limit. This limit arises because the number of quasiparticles created by absorbing a photon is a noisy process. Due to this noise or fluctuation, for a monochromatic incident signal, a gaussian like signal is generated instead of a sharp delta function like peak. The full width half maximum of this peak defines the energy resolution of the detector system. The following equation describes the energy resolution of MKID [89]:

$$\Delta E = 2.355\sqrt{E_{photon}\Delta F\eta_{quasi}{}^{-1}} \tag{2.15}$$

Here, F is the Fano factor and Δ denotes the energy gap. Since energy lower than this value cannot be detected by the specific detector, the relative energy resolution is defined by,

$$R=E/\Delta E \tag{2.16}$$

(*E* is energy of incident photons)

2.6.2 Base material for MKID

Since its first demonstration in 2003, there have been considerable research efforts made to develop microwave kinetic inductance detectors (MKIDs). This technology is widely employed in ground based astronomy and is under consideration for many other domains. In the first instance, thin Al films were used to fabricate MKIDs [90]. Recently, TiN has shown to have several advantageous properties in comparison to Al. The main benefit of TiN thin film is its tunable superconducting property, as the T_c of the sub stoichiometric TiN film can be tuned by changing its N_2 content (in the range of 0.5 K < T_c< 5 K). Hence, we can design the film property according to the desired frequency range to be detected or the operating temperature of the device [91]. Also, higher room temperature resistivity of TiN leads to higher kinetic inductance, which allows for much more straightforward and compact designs of lumped-element MKID devices (assuming the thicknesses of the superconducting thin films is much smaller than their London penetration depths; the correlation between kinetic inductance and room temperature sheet resistance can be interpreted from the following equation: $L_k = \frac{\hbar R_S}{\pi\Delta(0)}$ [92]).

2.6.3 Application of MKIDs

MKIDs enable the detection of single photons for the frequencies ranging from infrared to x-ray with high time resolution (~ μs) and with simultaneous energy resolution. They are gaining importance in millimetre wave astronomy. MKIDs do not suffer from the read noise or dark current like CCDs (charge coupled devices) or other standard detector for optical astronomy. The following Fig. 2.15 shows an image of an IRAM 30 m telescope located in Spain where there is an ongoing project of MKID based detector installations in this telescope. MKIDs can also provide a low noise, high sensitivity alternative in the field of passive terahertz imaging. There is a huge commercial market for terahertz imaging related applications. (Applications of terahertz imaging include defence assessment, the analysis of sub-surface features in historical art works, biomedical imaging, remote sensing in automatic navigation systems, etc. [93], [94]) Rowe has reviewed the comparison between the key specifications and the performance parameters of MKID based camera and other available terahertz imaging systems [95].

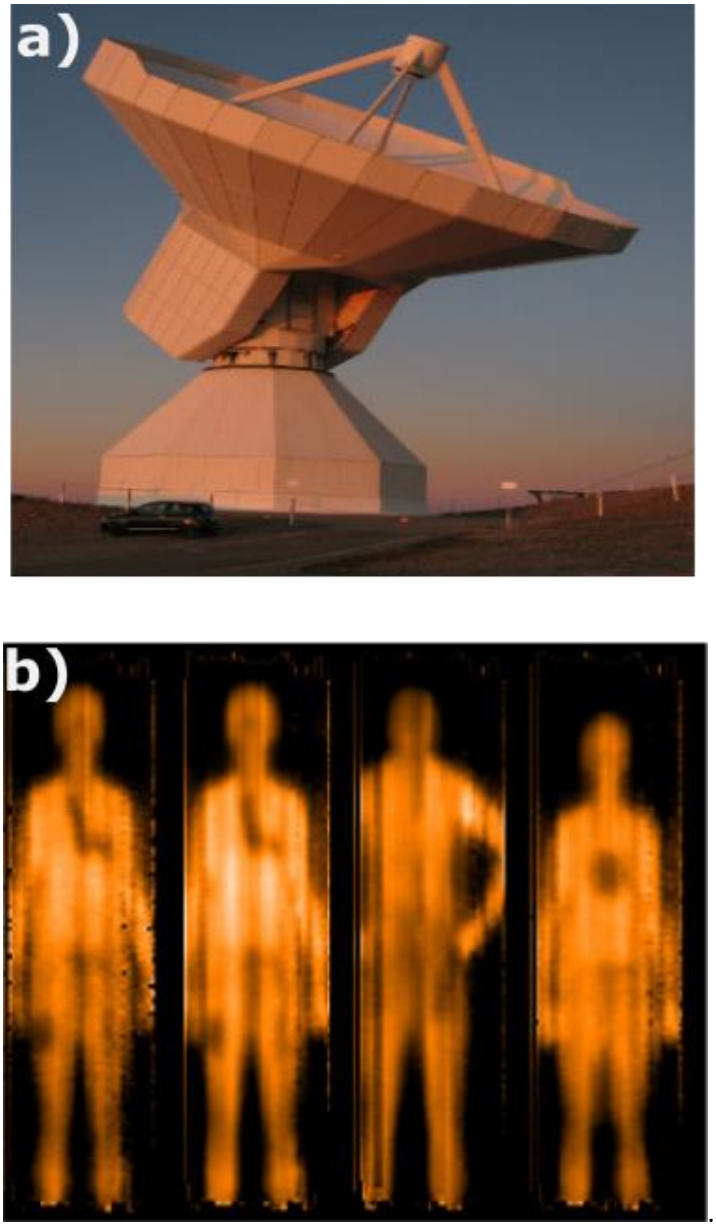

Fig. 2.15: Applications of MKIDs: (a) IRAM 30 m telescope located in Spain, there is an ongoing project of KID based detector installation (b) Passive terahertz imaging.

2.7 Summary

Detection of single photon is a crucial technology for many real life applications including quantum information processing, astronomy, remote sensing, deep space communication or biotechnology. Two superconducting device technologies (superconducting nanowire single photon detectors [SSPDs/SNSPDs]) and microwave kinetic inductance detectors (MKIDs) have the potential to outperform other existing technologies and offer scalability to large arrays due to their unique properties. Superconducting thin films are critical for the

development of high efficiency superconducting detectors. In this thesis, we have studied optimisation of NbTiN & NbN thin film growth for SNSPD fabrication. After that, amorphous superconducting thin films have been explored (with an emphasis on MoSi) for the same purpose. Finally, we have investigated TiN as a potential high transition temperature base material for MKIDs for passive Terahertz imaging.

References

[1] H. Kamerlingh Onnes, "Further experiments with liquid helium. D. On the change of electric resistance of pure metals at very low temperatures, etc. V. The disappearance of the resistance of mercury.," *Comm. Phys. Lab. Univ. Leiden; No. 122b*, 1911.

[2] D. van Delft and P. Kes, "The discovery of superconductivity," *Phys. Today*, vol. 63, no. 9, pp. 38–43, Sep. 2010.

[3] D. Dew-Hughes, "The critical current of superconductors: an historical review," vol. 27, pp. 967–979, 2001.

[4] C. Kittel, *Introduction to solid state physics*. Wiley, 2005.

[5] W. Meissner and R. Ochsenfeld, "Ein neuer Effekt bei Eintritt der Supraleitfähigkeit," *Naturwissenschaften*, vol. 21, no. 44, pp. 787–788, Nov. 1933.

[6] R. Radenbaugh, "Refrigeration for superconductors," *Proc. IEEE*, vol. 92, no. 10, pp. 1719–1734, Oct. 2004.

[7] F. London and H. London, "The Electromagnetic Equations of the Supraconductor," *Proc. R. Soc. A Math. Phys. Eng. Sci.*, vol. 149, no. 866, pp. 71–88, Mar. 1935.

[8] M. Tinkham, *Introduction to Superconductivity: Second Edition (Dover Books on Physics) (Vol i)*. Dover Publications, 2004.

[9] J. Bardeen, L. N. Cooper, and J. R. Schrieffer, "Theory of Superconductivity," *Phys. Rev.*, vol. 108, no. 5, pp. 1175–1204, Dec. 1957.

[10] J. Bardeen, L. Cooper, and J. Schrieffer, "Microscopic Theory of Superconductivity," *Phys. Rev.*, vol. 106, no. 1, pp. 162–164, Apr. 1957.

[11] L. Cooper, "Bound Electron Pairs in a Degenerate Fermi Gas," *Phys. Rev.*, vol. 104, no. 4, pp. 1189–1190, Nov. 1956.

[12] L. P. Gor 'kov, "MICROSCOPIC DERIVATION OF THE GINZBURG-LANDAU EQUATIONS IN THE THEORY OF SUPERCONDUCTIVITY," *J. Exptl. Theor. Phys.*, vol. 36, no. 36, pp. 1918–1923, 1959.

[13] R. Khasanov, P. W. Klamut, A. Shengelaya, Z. Bukowski, I. M. Savić, C. Baines, and H. Keller, "Muon-spin rotation measurements of the penetration depth of the $Mo_3 Sb_7$ superconductor," *Phys. Rev. B*, vol. 78, p. 14502, 2008.

[14] A. Carrington and F. Manzano, "Magnetic penetration depth of MgB_2," *Phys. C Supercond.*, vol. 385, no. 1, pp. 205–214, 2003.

[15] F. J. Blatt, *Modern physics*. McGraw-Hill, 1992.

[16] C. P. Poole, *Superconductivity*. Academic Press, 2007.

[17] B. Lorenz and C. W. Chu, “High Pressure Effects on Superconductivity,” in *Frontiers in Superconducting Materials*, Berlin/Heidelberg: Springer-Verlag, 2005, pp. 459–497.

[18] J. de Launay, “The Isotope Effect in Superconductivity,” *Phys. Rev.*, vol. 93, no. 4, pp. 661–665, Feb. 1954.

[19] B. Matthias, T. Geballe, and V. Compton, “Superconductivity,” *Rev. Mod. Phys.*, vol. 35, no. 1, pp. 1–22, Jan. 1963.

[20] T. H. Geballe, B. T. Matthias, V. B. Compton, E. Corenzwit, G. W. Hull, and L. D. Longinotti, “Superconductivity in Binary Alloy Systems of the Rare Earths and of Thorium with Pt-Group Metals,” *Phys. Rev.*, vol. 137, no. 1A, pp. A119–A127, Jan. 1965.

[21] J. Muller, “A15-type superconductors,” *Reports Prog. Phys.*, vol. 43, no. 5, pp. 641–687, May 1980.

[22] M. Wu, J. Ashburn, C. Torng, P. Hor, R. Meng, L. Gao, Z. Huang, Y. Wang, and C. Chu, “Superconductivity at 93 K in a new mixed-phase Y-Ba-Cu-O compound system at ambient pressure,” *Phys. Rev. Lett.*, vol. 58, no. 9, pp. 908–910, Mar. 1987.

[23] J. P. Pritchard, “Superconducting thin-film technology and applications,” *IEEE Spectr.*, vol. 3, no. 5, pp. 46–54, May 1966.

[24] T. Guruswamy, D. J. Goldie, and S. Withington, “Quasiparticle generation efficiency in superconducting thin films,” *Supercond. Sci. Technol.*, vol. 27, no. 5, p. 55012, May 2014.

[25] D. K. Schroder, *Semiconductor material and device characterization*. Wiley, 1998.

[26] N. W. Ashcroft and N. D. Mermin, *Solid state physics*. Brooks/Cole Cengage Learning, 2003.

[27] Y. Ivry, C. S. Kim, A. E. Dane, D. De Fazio, A. N. McCaughan, K. A. Sunter, Q. Zhao, and K. K. Berggren, “Universal scaling of the critical temperature for thin films near the superconducting-to-insulating transition,” *Phys. Rev. B*, vol. 90, no. 21, p. 214515, 2014.

[28] J. Simonin, “Surface term in the superconductive Ginzburg-Landau free energy: Application to thin films,” *Phys. Rev. B*, vol. 33, no. 11, pp. 7830–7832, Jun. 1986.

[29] A. M. Finkel’stein, “Suppression of superconductivity in homogeneously disordered systems,” *Phys. B Condens. Matter*, vol. 197, no. 1, pp. 636–648, 1994.

[30] Y. Tao, “Scaling Laws for Thin Films near the Superconducting-to-Insulating Transition,” *Sci. Rep.*, vol. 6, no. 2, p. 23863, March. 2016.

[31] J. A. Thornton, “Influence of apparatus geometry and deposition conditions on the structure and topography of thick sputtered coatings,” *J. Vac. Sci. Technol.*, vol. 11, no. 4, 1974.

[32] J. A. Thornton, “Influence of substrate temperature and deposition rate on structure of thick sputtered Cu coatings,” *J. Vac. Sci. Technol.*, vol. 12, no. 4, pp. 830–835, Jul. 1975.

[33] D. L. Smith, *Thin-film deposition : principles and practice*. McGraw-Hill, 1995.

[34] F.Marsili, “Single-photon and photon-number-resolving detectors based on superconducting nanowires,” *PhD Thesis* , Faculty of Science, École polytechnique fédérale de Lausanne EPFL, Switzerland, 2009.

[35] M. Planck, “Ueber das Gesetz der Energieverteilung im Normalspectrum,” *Ann. Phys.*, vol. 309, no. 3, pp. 553–563, 1901.

[36] A. Einstein, “Über einen die Erzeugung und Verwandlung des Lichtes betreffenden heuristischen Gesichtspunkt,” *Ann. Phys.*, vol. 322, no. 6, pp. 132–148, 1905.

[37] R. H. Hadfield, “Single-photon detectors for optical quantum information applications,” *Nat. Photonics*, vol. 3, no. 12, pp. 696–705, Dec. 2009.

[38] J. M. Beckers, “Adaptive Optics for Astronomy: Principles, Performance, and Applications,” *Annu. Rev. Astron. Astrophys.*, vol. 31, no. 1, pp. 13–62, Sep. 1993.

[39] B. Lee, “Review of the present status of optical fiber sensors,” *Opt. Fiber Technol.*, vol. 9, no. 2, pp. 57–79, Apr. 2003.

[40] W. Tittel, J. Brendel, H. Zbinden, and N. Gisin, “Quantum Cryptography Using Entangled Photons in Energy-Time Bell States,” *Phys. Rev. Lett.*, vol. 84, no. 20, pp. 4737–4740, May 2000.

[41] A. Kirmani, D. Venkatraman, D. Shin, A. Colaço, F. N. C. Wong, J. H. Shapiro, and V. K. Goyal, “First-photon imaging.,” *Science*, vol. 343, no. 6166, pp. 58–61, Jan. 2014.

[42] A. Peacock, P. Verhoeve, N. Rando, A. van Dordrecht, B. G. Taylor, C. Erd, M. A. C. Perryman, R. Venn, J. Howlett, D. J. Goldie, J. Lumley, and M. Wallis, “Single optical photon detection with a superconducting tunnel junction,” *Nature*, vol. 381, no. 6578, pp. 135–137, May 1996.

[43] S. Friedrich, “Superconducting Tunnel Junction Photon Detectors: Theory and Applications,” *J. Low Temp. Phys.*, vol. 151, no. 1–2, pp. 277–286, Jan. 2008.

[44] B. Cabrera, R. M. Clarke, P. Colling, A. J. Miller, S. Nam, and R. W. Romani, “Detection of single infrared, optical, and ultraviolet photons using superconducting transition edge sensors,” *Appl. Phys. Lett.*, vol. 73, no. 6, p. 735, Aug. 1998.

[45] A. E. Lita, A. J. Miller, and S. W. Nam, “Counting near-infrared single-photons with 95% efficiency,” *Opt. Express*, vol. 16, no. 5, p. 3032, 2008.

[46] G. N. Gol’tsman, O. Okunev, G. Chulkova, A. Lipatov, A. Semenov, K. Smirnov, B. Voronov, A. Dzardanov, C. Williams, and R. Sobolewski, “Picosecond superconducting single-photon optical detector,” *Appl. Phys. Lett.*, vol. 79, no. 6, p. 705, Aug. 2001.

[47] C. M. Natarajan, M. G. Tanner, and R. H. Hadfield, “Superconducting nanowire single-photon detectors: physics and applications,” *Supercond. Sci. Technol.*, vol. 25, no. 6, p. 63001, Jun. 2012.

[48] A. D. Semenov, G. N. Gol'tsman, and R. Sobolewski, “Hot-electron effect in superconductors and its applications for radiation sensors,” *Supercond. Sci. Technol.*, vol. 15, no. 4, pp. R1–R16, Apr. 2002.

[49] J. K. W. Yang, A. J. Kerman, E. A. Dauler, V. Anant, K. M. Rosfjord, and K. K.

Berggren, “Modeling the Electrical and Thermal Response of Superconducting Nanowire Single-Photon Detectors,” *IEEE Trans. Appl. Supercond.*, vol. 17, no. 2, pp. 581–585, Jun. 2007.

[50] A. J. Annunziata, “Single-Photon Detection, Kinetic Inductance, and Non-Equilibrium Dynamics in Niobium and Niobium Nitride Superconducting Nanowires,” *PhD Thesis*, Department of Physics, Yale University, U.S.A, 2010.

[51] A. Engel, J. J. Renema, K. Il ’in, and A. Semenov, “Detection mechanism of superconducting nanowire single-photon detectors.” *Supercond. Sci. Technol.* , vol. 28 , no. 11, p. 114003, Sept. 2015

[52] C. Silberhorn, “Detecting quantum light,” *Contemp. Phys.*, vol. 48, no. 3, pp. 143–156, May 2007.

[53] S. Cova, M. Ghioni, a. Lotito, I. Rech, and F. Zappa, “Evolution and prospects for single-photon avalanche diodes and quenching circuits,” *J. Mod. Opt.*, vol. 51, no. 9–10, pp. 1267–1288, Jan. 2004.

[54] E. A. Dauler, B. S. Robinson, A. J. Kerman, J. K. W. Yang, E. K. M. Rosfjord, V. Anant, B. Voronov, G. Gol’tsman, and K. K. Berggren, “Multi-Element Superconducting Nanowire Single-Photon Detector,” *IEEE Trans. Appl. Supercond.*, vol. 17, no. 2, pp. 279–284, Jun. 2007.

[55] S. S. Haykin, *Communication systems*. Wiley, 2009.

[56] P. L. Richards, “Bolometers for infrared and millimeter waves,” *J. Appl. Phys.*, vol. 76, no. 1, pp. 1–24, Jul. 1994.

[57] V. Anant, A. J. Kerman, E. A. Dauler, J. K. W. Yang, K. M. Rosfjord, and K. K. Berggren, “Optical properties of superconducting nanowire single-photon detectors,” *Opt. Express*, vol. 16, no. 14, p. 10750, Jul. 2008.

[58] K. M. Rosfjord, J. K. W. Yang, E. A. Dauler, A. J. Kerman, V. Anant, B. M. Voronov, G. N. Gol’tsman, and K. K. Berggren, “Nanowire single-photon detector with an integrated optical cavity and anti-reflection coating,” *Opt. Express*, vol. 14, no. 2, p. 527, 2006.

[59] M. S. Allman, V. B. Verma, M. Stevens, T. Gerrits, R. D. Horansky, a. E. Lita, F. Marsili, A. Beyer, M. D. Shaw, D. Kumor, R. Mirin, and S. W. Nam, “A near-infrared 64-pixel superconducting nanowire single photon detector array with integrated multiplexed readout,” *Appl. Phys. Lett.*, vol. 106, no. 19, p. 192601, 2015.

[60] J. P. Sprengers, A. Gaggero, D. Sahin, S. Jahanmirinejad, G. Frucci, F. Mattioli, R. Leoni, J. Beetz, M. Lermer, M. Kamp, S. Höfling, R. Sanjines, and A. Fiore, “Waveguide superconducting single-photon detectors for integrated quantum photonic circuits,” *Appl. Phys. Lett.*, vol. 99, no. 18, p. 181110, Oct. 2011.

[61] S. Miki, T. Yamashita, Z. Wang, and H. Terai, “A 64-pixel NbTiN superconducting nanowire single-photon detector array for spatially resolved photon detection,” *Opt. Express*, vol. 22, no. 7, p. 7811, Apr. 2014.

[62] A. E. Lita, V. B. Verma, R. D. Horansky, J. M. Shainline, R. P. Mirin, and S. Nam, “Materials Development for High Efficiency Superconducting Nanowire Single-Photon Detectors,” *MRS Proc.*, vol. 1807, pp. 1–6, 2015.

[63] F. Marsili, D. Bitauld, A. Fiore, A. Gaggero, F. Mattioli, R. Leoni, M. Benkahoul, F.

Lévy, “High efficiency NbN nanowire superconducting single photon detectors fabricated on MgO substrates from a low temperature process.” *Opt. Express*, vol. 16, no. 5, p. 3191, 2008.

[64] H. O. Pierson, *Handbook of refractory carbides and nitrides : properties, characteristics, processing, and applications*. Noyes Publications, 1996.

[65] S. Miki, M. Takeda, M. Fujiwara, M. Sasaki, A. Otomo, and Z. Wang, “Superconducting NbTiN Nanowire Single Photon Detectors with Low Kinetic Inductance,” *Appl. Phys. Express*, vol. 2, no. 7, p. 75002, Jun. 2009.

[66] “Magnesium oxide (MgO) crystal structure, lattice parameters, thermal expansion,” in *II-VI and I-VII Compounds; Semimagnetic Compounds*, Berlin/Heidelberg: Springer-Verlag, pp. 1–6.

[67] M. Lucht, M. Lerche, H.-C. Wille, Y. V Shvyd ’ko, H. D. Rüter, E. Gerdau, and P. Becker, “Precise Measurement of the Lattice Parameters of Sapphire in the Temperature Range 4.5 K -250 K Using the ossbauer Wavelength Standard,” *J. Appl. Cryst*, vol. 36, no. 4, pp. 1075–1081, 2003.

[68] G. Zou, M. Jain, H. Zhou, H. Luo, S. A. Baily, L. Civale, E. Bauer, T. M. Mccleskey, A. K. Burrell, and Q. Jia, “Ultrathin epitaxial superconducting niobium nitride films grown by a chemical solution technique.”

[69] M. C. Burton, M. R. Beebe, K. Yang, R. A. Lukaszew, A.-M. Valente-Feliciano, and C. Reece, “Superconducting NbTiN thin films for superconducting radio frequency accelerator cavity applications,” *J. Vac. Sci. Technol. A Vacuum, Surfaces, Film.*, vol. 34, no. 2, p. 21518, Mar. 2016.

[70] F. Marsili, A. Gaggero, L. H. Li, A. Surrente, R. Leoni, F. Lévy, and A. Fiore, “High quality superconducting NbN thin films on GaAs,” *Supercond. Sci. Technol.*, vol. 22, no. 9, p. 95013, Sep. 2009.

[71] S. Miki, T. Yamashita, H. Terai, and Z. Wang, “High performance fiber-coupled NbTiN superconducting nanowire single photon detectors with Gifford-McMahon cryocooler.,” *Opt. Express*, vol. 21, no. 8, pp. 10208–14, Apr. 2013.

[72] D. Bosworth, S.-L. Sahonta, R. H. Hadfield, and Z. H. Barber, “Amorphous Molybdenum Silicon Superconducting Thin Films,” *AIP Adv.*, vol. 5, no. 8, p. 87106, 2015.

[73] V. B. Verma, A. E. Lita, M. R. Vissers, F. Marsili, D. P. Pappas, R. P. Mirin, and S. W. Nam, “Superconducting nanowire single photon detectors fabricated from an amorphous $Mo_{0.75}Ge_{0.25}$ thin film,” *Appl. Phys. Lett.*, vol. 105, no. 2, pp. 0–5, 2014.

[74] B. Baek, A. E. Lita, V. Verma, and S. W. Nam, “Superconducting a-W_xSi_{1-x} nanowire single-photon detector with saturated internal quantum efficiency from visible to 1850 nm,” *Appl. Phys. Lett.*, vol. 98, no. 25, p. 251105, 2011.

[75] T. Proslier, J. A. Klug, J. W. Elam, H. Claus, N. G. Becker, and M. J. Pellin, “Atomic Layer Deposition and Superconducting Properties of NbSi Films,” *J. Phys. Chem. C*, vol. 115, no. 19, pp 9477–9485, May. 2011.

[76] S. N. Dorenbos, P. Forn-Díaz, T. Fuse, A. H. Verbruggen, T. Zijlstra, T. M. Klapwijk, *and* V. Zwiller, “Low gap superconducting single photon detectors for infrared sensitivity,” *Appl. Phys. Lett.*, vol. 98, no. 25, p. 251102, June. 2011.

[77] Y. P. Korneeva, M. Y. Mikhailov, Y. P. Pershin, N. N. Manova, A. V Divochiy, Y. B. Vakhtomin, A. A. Korneev, K. V Smirnov, A. G. Sivakov, A. Y. Devizenko, and G. N. Goltsman, "Superconducting single-photon detector made of MoSi film," *Supercond. Sci. Technol.*, vol. 27, no. 9, p. 95012, Sep. 2014.

[78] V. B. Verma, B. Korzh, F. Bussières, R. D. Horansky, S. D. Dyer, a E. Lita, I. Vayshenker, F. Marsili, M. D. Shaw, H. Zbinden, R. P. Mirin, and S. W. Nam, "High-efficiency superconducting nanowire single-photon detectors fabricated from MoSi thin-films," *Instrum. Detect.*, vol. 23, no. 26, pp. 343–348, 2015.

[79] M. Hashimoto, I. M. Vishik, R.-H. He, T. P. Devereaux, and Z.-X. Shen, "Energy gaps in high-transition-temperature cuprate superconductors," *Nat. Phys.*, vol. 10, no. 7, pp. 483–495, Jun. 2014.

[80] D. M. Ginsberg, Ed., *Physical properties of high temperature superconductors*. World Scientific, 1989.

[81] R. J. Collins, R. H. Hadfield, V. Fernandez, S. W. Nam, and G. S. Buller, "Low timing jitter detector for gigahertz quantum key distribution," *Electron. Lett.*, vol. 43, no. 3, p. 180, Feb. 2007.

[82] E. Knill, R. Laflamme, and G. J. Milburn, "A scheme for efficient quantum computation with linear optics.," *Nature*, vol. 409, no. 6816, pp. 46–52, Jan. 2001.

[83] M. A. Jaspan, J. L. Habif, R. H. Hadfield, and S. W. Nam, "Heralding of telecommunication photon pairs with a superconducting single photon detector," *Appl. Phys. Lett.*, vol. 89, no. 3, p. 31112, Jul. 2006.

[84] M. E. Grein, A. J. Kerman, E. A. Dauler, O. Shatrovoy, R. J. Molnar, D. Rosenberg, J. Yoon, C. E. DeVoe, D. V Murphy, B. S. Robinson, and D. M. Boroson, "Design of a ground-based optical receiver for the lunar laser communications demonstration," *Space Optical Systems and Applications (ICSOS), 2011 International Conference on*. pp. 78–82, 2011.

[85] J. Zhang, N. Boiadjieva, G. Chulkova, H. Deslandes, G. N. Gol'tsman, A. Korneev, P. Kouminov, M. Leibowitz, W. Lo, R. Malinsky, O. Okunev, A. Pearlman, W. Slysz, K. Smirnov, C. Tsao, A. Verevkin, B. Voronov, K. Wilsher, and R. Sobolewski, "Noninvasive CMOS circuit testing with NbN superconducting single-photon detectors," *Electron. Lett.*, vol. 39, no. 14, p. 1086, 2003.

[86] N. R. Gemmell, A. McCarthy, B. Liu, M. G. Tanner, S. D. Dorenbos, V. Zwiller, M. S. Patterson, G. S. Buller, B. C. Wilson, and R. H. Hadfield, "Singlet oxygen luminescence detection with a fiber-coupled superconducting nanowire single-photon detector," *Opt. Express*, vol. 21, no. 4, p. 5005, Feb. 2013.

[87] J. Zmuidzinas and P. L. Richards, "Superconducting detectors and mixers for millimeter and submillimeter astrophysics," *Proc. IEEE*, vol. 92, no. 10, pp. 1597–1616, 2004.

[88] B. A. Mazin, "Microwave kinetic inductance detectors," *PhD Thesis*, Department of Physcis, Mathematics and Astronomy, California Institute of Technology, U.S.A, 2005.

[89] J. Baselmans, "Kinetic Inductance Detectors," *J. Low Temp. Phys.*, vol. 167, no. 3–4, pp. 292–304, Jan. 2012.

[90] B. A. Mazin, "Microwave kinetic inductance detectors: The first decade," in *AIP*

Conference Proceedings, 2009, pp. 135–142.

[91] G. Coiffard, K.-F. Schuster, E. F. C. Driessen, S. Pignard, M. Calvo, A. Catalano, J. Goupy, and A. Monfardini, "Uniform Non-stoichiometric Titanium Nitride Thin Films for Improved Kinetic Inductance Detector Arrays," *J. Low Temp. Phys.*, vol. 184, no. 3–4, pp. 654–660, Aug. 2016.

[92] H. McCarrick, D. Flanigan, G. Jones, B. R. Johnson, P. Ade, D. Araujo, K. Bradford, R. Cantor, G. Che, P. Day, S. Doyle, H. Leduc, M. Limon, V. Luu, P. Mauskopf, A. Miller, T. Mroczkowski, C. Tucker, and J. Zmuidzinas, "Horn-coupled, commercially-fabricated aluminum lumped-element kinetic inductance detectors for millimeter wavelengths," *Rev. Sci. Instrum.*, vol. 85, no. 12, p. 123117, Dec. 2014.

[93] J. F. Federici, B. Schulkin, F. Huang, D. Gary, R. Barat, F. Oliveira, and D. Zimdars, "THz imaging and sensing for security applications?explosives, weapons and drugs," *Semicond. Sci. Technol.*, vol. 20, no. 7, pp. S266–S280, Jul. 2005.

[94] J. A. Zeitler and Y.-C. Shen, "Industrial Applications of Terahertz Imaging," Springer Berlin Heidelberg, 2012, pp. 451–489.

[95] S. Rowe, "Passive terahertz imaging with lumped element kinetic inductance detectors," *PhD Thesis*, Department of Physics and Astronomy, School of Physics and Astronomy, Cardiff University, U.K, 2015.

Chapter 3

Experimental Methods

In this chapter, we describe the experimental methods which have been employed to deposit and characterise superconducting thin films for this study. A newly installed ultra-high vacuum sputter deposition system has been used for the purpose of growth and process optimisation of superconducting thin films (Section 3.1). An atomic layer deposition tool has been used to grow TiN films (Section 3.1). Superconducting properties of the films have been characterised in a cryogen free thin film testing set-up (Section 3.2). Structural and optical properties have been analysed using high resolution scanning transmission electron microscopy (Section 3.4) and variable angle spectroscopic ellipsometry (Section 3.5).

3.1 Thin Film Growth

Thin films can be grown by various techniques such as atomic layer deposition, sputtering, electron beam evaporation, chemical vapour deposition or ion-implantation etc [1], [2]. Among these methods, sputtering is the most used technique for superconducting thin film growth for the purpose of nanoscale device applications. Magnetron sputtering can be used to grow all the materials we are interested in for superconducting detector fabrication, i.e. refractory metal nitrides (NbN, NbTiN or TiN) or TM based amorphous alloys (MoSi, MoGe or WSi). That is why we have used an ultra-high vacuum load-locked sputter deposition system for superconducting thin film growth. The atomic layer deposition (ALD) technique has also been explored to deposit superconducting TiN films.

3.1.1 Sputter Deposition System

A schematic of a sputter deposition process is shown in Fig. 3.1. During sputter deposition, a high voltage is applied between the cathode (target) and anode. This ignites a glow-discharge plasma. Positively charged plasma ions collide with the target leading to the erosion of target particles. These target atoms are deposited on the substrate forming a thin film. An inert gas (Ar is most widely used) is used as the medium for plasma generation. Ar^+ ions have a very small mean free path (~ 52 nm under standard temperature and pressure). So, a magnetic field across the target is maintained in order to enhance the number of high energy ions bombarding the target. This traps secondary electrons in the discharge for a longer duration, increasing the probability of ionising argon during their travel from cathode to anode [3].

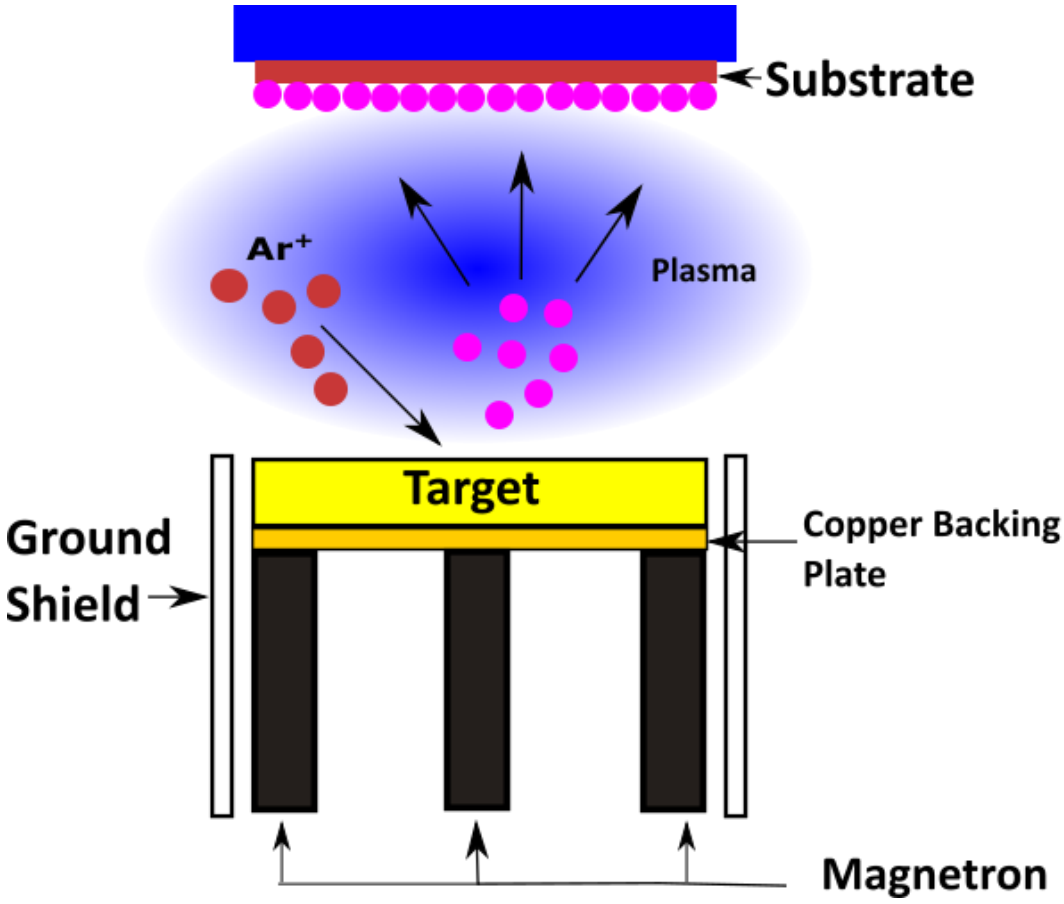

Fig. 3.1 Thin film growth by the sputter deposition in a vacuum chamber: During the deposition, a high voltage (By DC or RF power supply) is applied between the target (Cathode) and the ground and a plasma is ignited in the process chamber; being trapped close to the magnetron, high energy plasma ions collide with the target and ejected target material atoms are deposited on the substrate.

A new sputter deposition system has been installed in the James Watt Nanofabrication Centre, University of Glasgow in April 2014. The system was manufactured by Plassys Bestek, France (http://www.plassys.com). Here, we have presented the detailed description of the sputter deposition system.

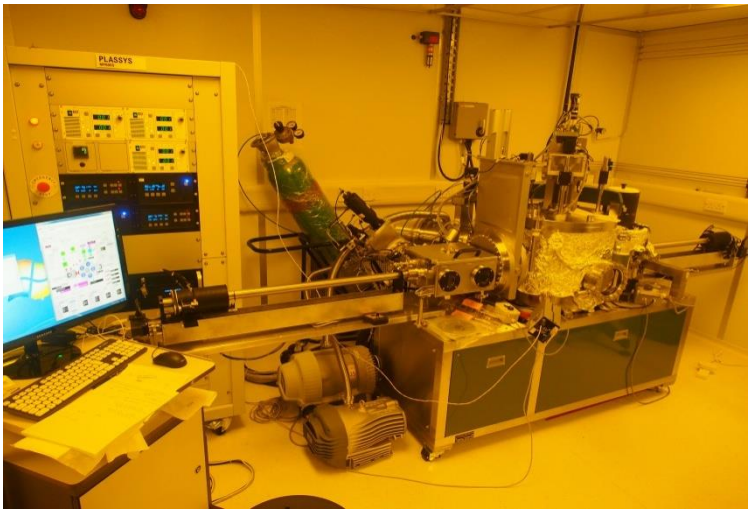

Fig. 3.2 Plassys VI Sputter deposition system.

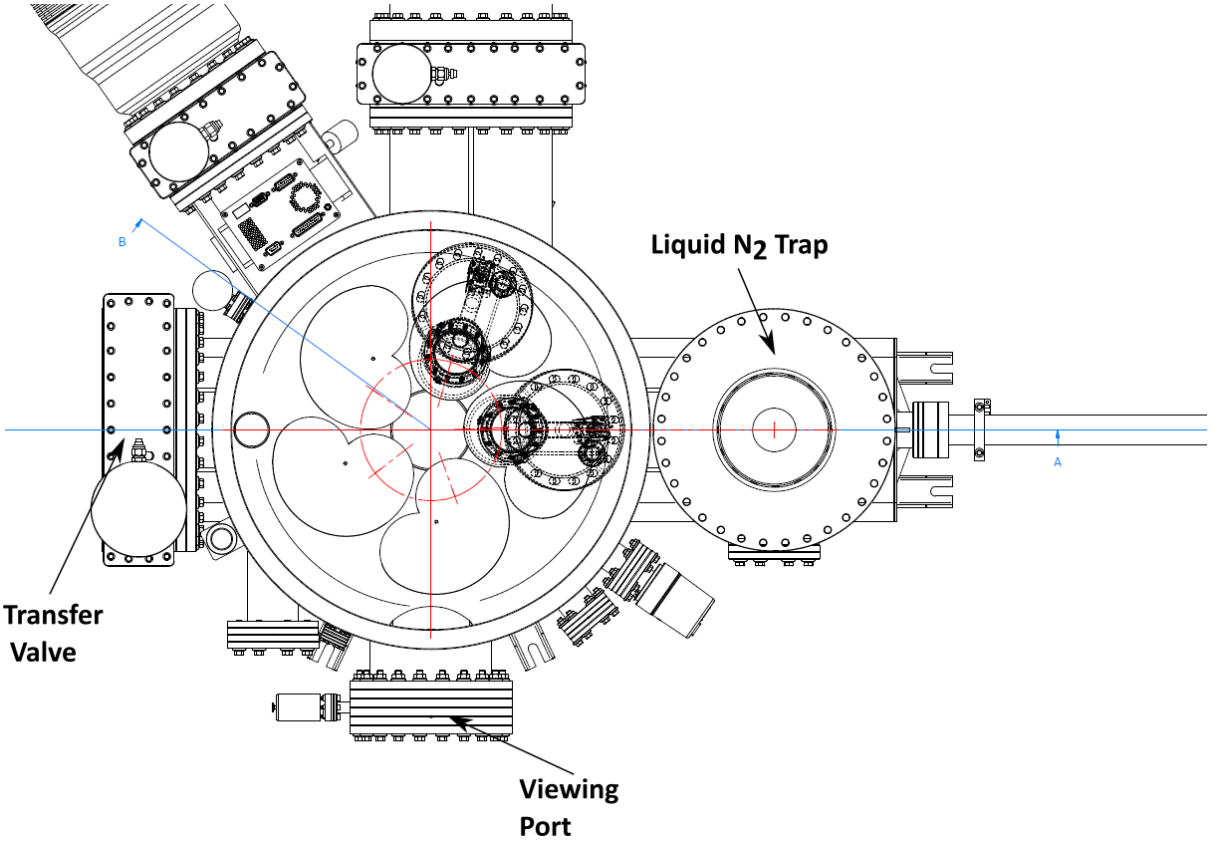

Fig. 3.3 Technical drawing of the cross-section of the deposition system.

Figure 3.2 shows an image taken from the front of the system. The instrument has a 340 litre sputtering chamber made of electro polished stainless steel. The main process chamber is 400 mm high and has an inner diameter of 600 mm. The substrate holder is attached to the

removable top plate of the chamber. This plate is linked to an electrical hoist which may be used to lift and swivel the substrate holder away from the chamber. The hoist is secured with an atmospheric pressure membrane switch. The bottom plate of the chamber is equipped with a cluster of cathodes. There are five confocal magnetron sputter guns (manufactured by Meivac USA). Each gun can accommodate a 3" diameter sputter target with 0.25" or 0.125" thickness. Cathodes are tilted by 5°with respect to the vertical axis of the chamber. All the guns are connected to a power supply (three of them are connected to DC supply and two are to RF supply). A switching arrangement in the power supply allows safe and rapid interchange between sputter guns. (RF sputtering is very useful to remove charge accumulated on the dielectric or non-conducting target materials.) The power supplies are configured to enable co-sputtering from two or more sputter targets simultaneously. All the cathodes are supplied with cooling water to reduce the temperature rise due to the heat generation during sputtering. The sputtering chamber also has a view port covered with protective glass.

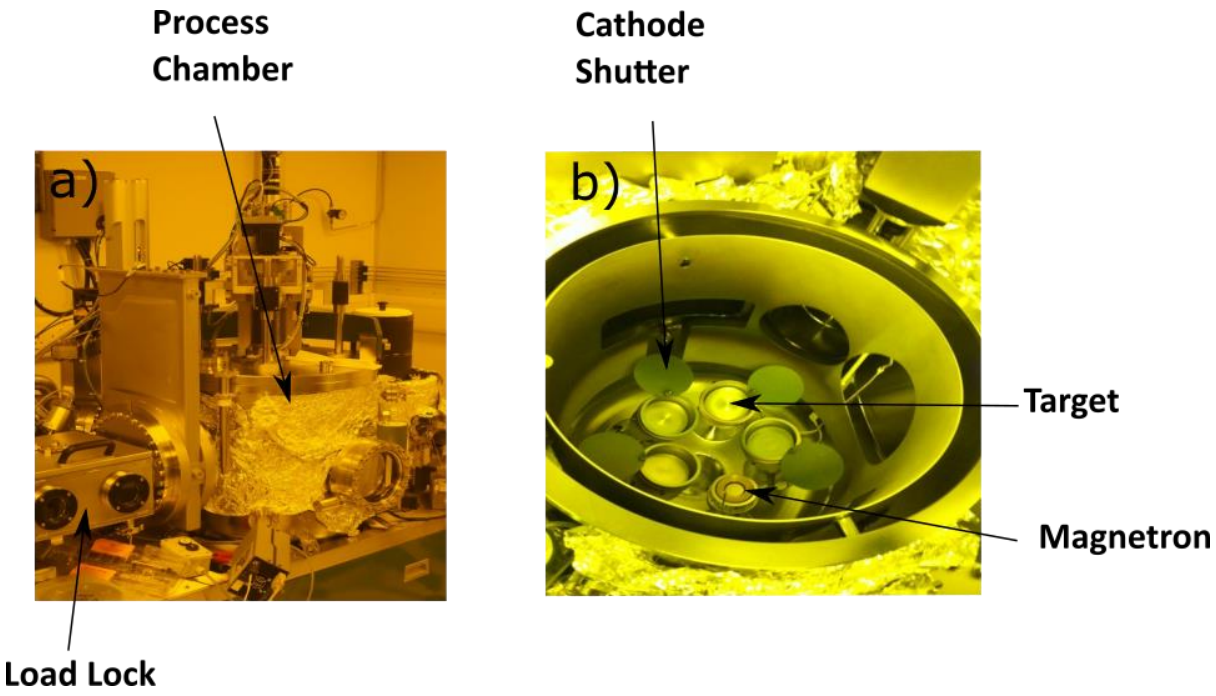

Fig. 3.4 (a): Main process chamber of the deposition system (b): Targets and the sputter gun inside the chamber.

The substrates are inserted into the system through a load lock mounted on the left side of the chamber. The substrate carrier has an adapter mount for up to nine 10 mm x 10 mm or

15 mm x 15 mm square samples. A specific substrate carrier made of molybdenum is to be used when substrates need to be heated. The load lock is a stainless steel chamber with a hinged top lid and viewport. A transfer valve separates the main process chamber from the load lock, allowing the sputter chamber to be kept at high vacuum at all times and to prevent contamination. Before being transferred to the main chamber, the substrates can be cleaned with argon plasma in the load lock. A motor driven, magnetically coupled transfer arm is used to insert the samples in the chamber and to transfer the samples back to the load lock at end of film growth.

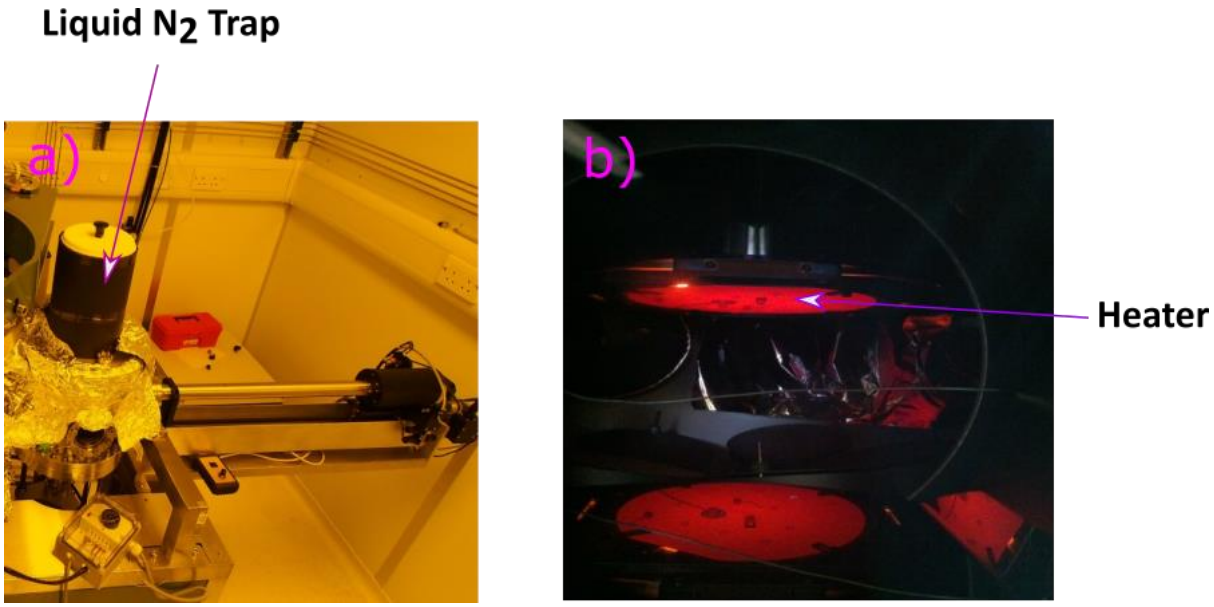

Fig. 3.5: (a) Liquid nitrogen trap. (b): Substrate heater glowing (note: the lower image is a reflection).

The substrate holder is mounted on a magnetically coupled feedthrough. Its distance from the magnetron cathodes can be adjusted by a motorised controller. The target-substrate distance can be adjusted over a range of 10 cm. According to the specifications provided by the system manufacturer, at a distance of 100 mm the film growth is most uniform over a large area (maximum wafer diameter 150 mm). The substrate holder can be rotated up to a speed of 200 rpm during thin film deposition to provide better uniformity. There is a PID controlled resistive heater attached to the holder, which can heat the substrates up to 800°C. The heater has a factory calibrated thermocouple to measure the substrate temperature.

Besides substrate heating, this deposition system also has the capability of cooling substrates before film growth. The process chamber is connected to a liquid N_2 trap mounted on a flange. This trap is manually filled before film deposition. The substrate carrier is transferred from the main chamber to an elevator mounted on the base plate. This motor driven elevator pushes the substrate carrier against the LN_2 trap to cool it down. Once the carrier has been cooled down, it is transferred to the substrate holder. A magnetically coupled transfer arm will move the substrate from the LN_2 position to the deposition position inside the main chamber.

The sputtering chamber is connected to two high vacuum pumping assemblies (viz. cryo and turbo pumping system). Pumping ports are mounted on the sidewall of the chamber. They maintain an ultra-high vacuum (with a base pressure of less than 5 X $10^{\wedge-9}$ Torr) in the process chamber. [Oxford Instruments model 8/8LP cryo pump, pumping speed: 1500 l/sec for Air, 4000 l/s for H_2O water cooled compressor; Edwards model STPA 803c turbo pump, pumping speed: 800 l/sec.] The base pressure of the chamber is monitored through a hot-filament ionisation gauge (manufactured by Kurt-J-Lesker).

The instrument is connected to four gas lines (Ar, N_2, O_2 and CH_4). Each line is equipped with a digitally controlled mass flow controller and a pneumatic stop valve. During the execution of any process in the chamber, the cryo pump line is closed with a gate valve (Mode CF 200) as reactive gases are not safe for cryo pumping and the turbo pump is throttled with a butterfly valve (VAT model 612). The position of this throttle valve, along with the flow rate of incoming gas, controls chamber pressure during any process.

The following table gives an overview of the sputter targets we have used for thin film deposition in our instrument.

Table 3.1 Detailed Descriptions of the Sputter Targets

Material	Mode of Power Supply	Purity	Manufacturer	Thickness
Niobium	DC	99.95%	Materion Microelectronics and services	0.250''
Titanium	DC	99.995%	International Advanced Materials	0.250''
Molybdenum	DC	99.99%	International Advanced Materials	0.250''
Silicon	RF	99.999%	Kurt J. Lesker Company Ltd.	0.250''
Germanium	RF	99.99%	International Advanced Materials	0.250''

3.1.2 Atomic Layer Deposition System

ALD is a chemical reaction based deposition technique. During the ALD process, chemical precursors (usually of gaseous phase) are pulsed in sequentially inside a reaction chamber. These precursors undergo self limiting chemical reactions on the surface of the substrate leading to the formation of thin film. Inductively coupled plasma may be ignited in the process chamber using some reactive gases (e.g. N_2 or H_2) to assist the film growth. The substrate can be heated to promote the chemical reaction. At the end of each pulse step, the reaction chamber is purged with argon to clean remaining precursors and reaction by-products [4].

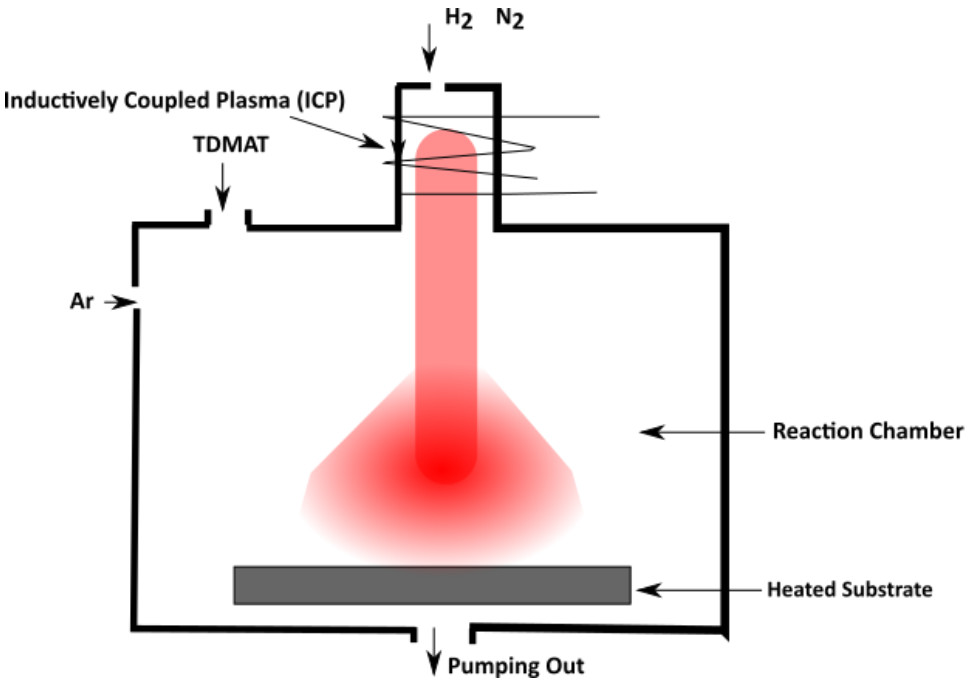

Fig. 3.6: Schematic diagram of the process chamber of Atomic layer deposition (ALD): formation of thin film by surface limiting chemical reaction on the substrate surface.

We have used a FlexAL®II ALD system manufactured by Oxford Instruments for TiN thin film deposition. This system is integrated into a cluster tool installed in the James Watt Nanofabrication Centre, University of Glasgow. The system can accommodate a wafer size with a diameter of up to 200 mm (8”). There is a load lock attached to the main process chamber, which allows substrate transfer without venting the main chamber. To increase the efficiency of the deposition process, the wafer carrier can be electrically heated up to a temperature of 500°C. The temperature of the substrate is monitored with the help of a PLC controller during the deposition. The main chamber is pumped with the help of a turbo pump. An inductively coupled plasma source (ICP 65) has been used in this system to generate plasma during film deposition (a RF generator and AMU has served the purpose of power supply). There is a precursor delivery module adjacent to the system to deliver necessary precursors for the film growth. The flow of the precursors is controlled by pneumatic valves.

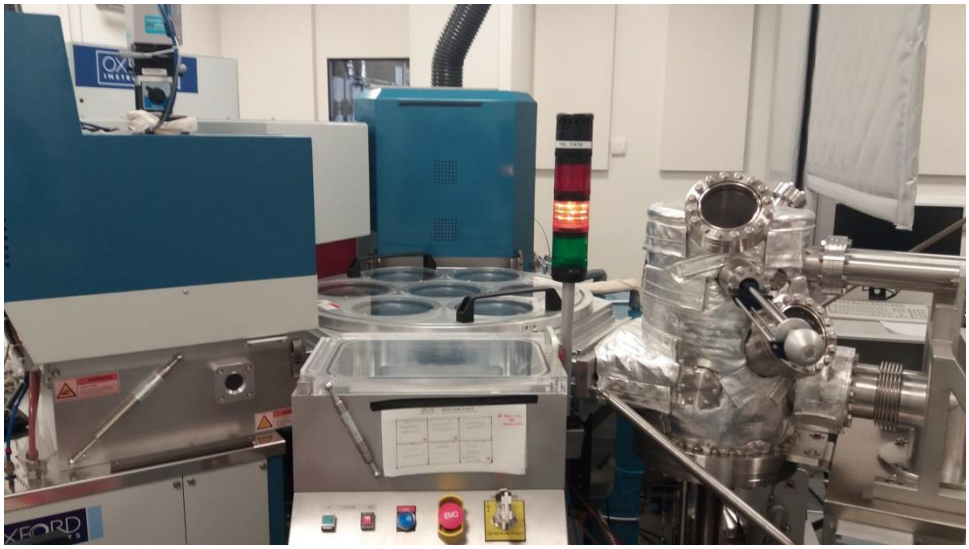

Fig. 3.7: Atomic layer deposition chamber as a part of the cluster tool installed in the James Watt Nanofabrication Centre, University of Glasgow, manufactured by Oxford Instruments.

3.2 Cryogen free Thin Film Testing Station[1]

Until the end of last century, the most common method for cooling down a superconducting sample was to immerse it in liquid helium. Usually, liquid helium is stored in a cryogenic storage dewar, but no dewar can provide perfect thermal insulation. Thus, the cryogenic liquid slowly boils away and the liquid helium storage needs to be refilled regularly. This makes the use of liquid helium dewars very expensive. Moreover, regular use of liquid helium may lead to several safety hazards, and this demands trained personnel for proper use. Recently developed refrigeration systems based on closed cycle cooling offer a solution to this problem. Over the past decade, commercially available closed cycle cryo-coolers have improved it to a large extent so far as attainable base temperature is concerned.

A closed cycle cryostat has been developed to measure the superconducting transition temperature of the thin films. This thin film testing system is based on a Sumitomo RDK101D coldhead and a Sumitomo CNA-11C compressor unit. The compressor and the coldhead are connected with a two way gas line. This system runs through a 13 A electrical outlet (with 1 kW power consumption) and requires only air cooling. The operation of this cold head is based on Gifford-McMahon (GM) closed cycle cooling. High purity helium is

[1] **The cryogen-free thin film testing set up was designed by the author and built up by Kleanthis Erotokritou as a part of his master thesis.**

circulated through the cold head and compressor. The cyclic operation of the GM cryo-cooler consists of 4 steps [5].

Step 1: At first, the high pressure inlet valve is open. The displacer is moved to the top of the coldhead. The gas flows through the regenerator to the bottom of the coldhead. The regenerator absorbs heat from the gas, reducing its temperature. This gas, in turn, reduces the temperature of the coldhead.

Step 2: The high pressure valve is then closed and the low pressure valve is opened with the position of the displacer fixed at the top. Part of the gas flows through the regenerator to the low pressure side of the compressor. Thus, gas in the cold head expands. This expansion cools down the gas further.

Step 3: The displacer is moved to the bottom of the coldhead forcefully (using a motor). This forces the cold gas to pass the regenerator while taking up heat from the regenerator. Gas flows to the low pressure outlet valve.

Step 4: The outlet valve is then closed and the inlet valve is opened with the displacer at a fixed position. The gas, now in the hot end of the coldhead, is compressed and heat is released to the surroundings. At the end of this step, we are back to Step 1.

Sub-helium temperature can easily be achieved by building multi stage cryo-coolers. As shown in the following figure, the coldhead we have used has two stages: One warmer stage and another colder stage which reach a base temperature of ~3-4K during cool-down.

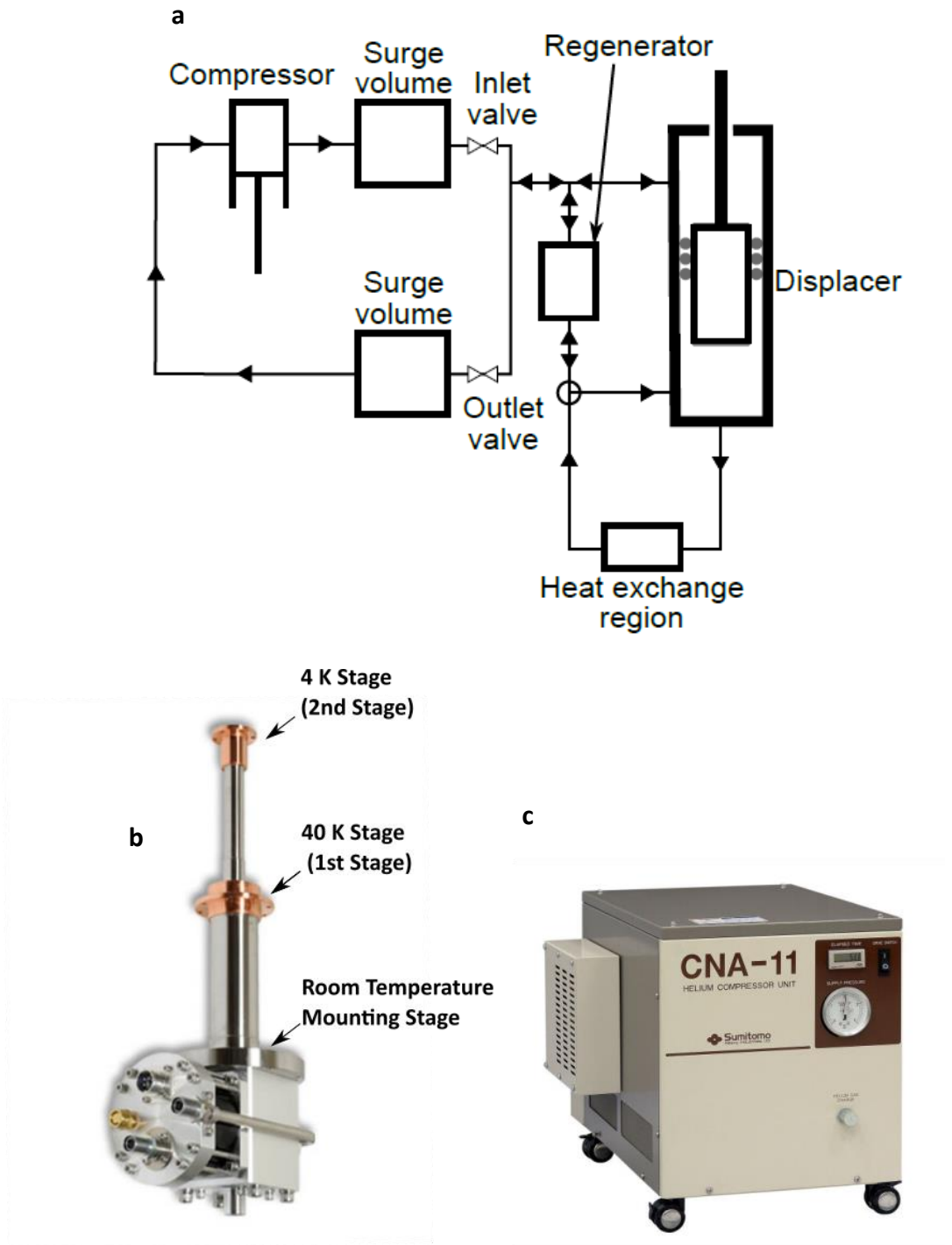

Fig. 3.8: (a) Heat flow diagram of Gifford-McMahon (GM) cryo-cooler. (b) Sumitomo RDK101D coldhead. (c) Sumitomo CNA-11C compressor unit.

In the thin film testing set-up, we aim to measure the resistance of eight samples at a time (using four pogo pins for each sample) as a function of temperature. The samples are mounted on the 4 K stage, which is the second stage (or the sample stage) of the cryo-cooler. As shown in the figure below, we have placed a circular metal disc at 4 K stage of the

coldhead. Around this disc there are 8 rectangular holes with steps at their boundary to place pogo pin holders (as shown in Figure 3.10(a)). In each holder (made of Tufnol laminated plastic) we have inserted four pogo pins by press fitting. On the top of this, we placed another circular metal disc. This disc has eight slots to accommodate eight 15 mm x 15 mm square samples (Figure 3.10(b)). Our samples (thin films sputtered on different substrates) are to be placed in these slots. An insulating carrier is used for this purpose to avoid shortage between the edge of samples and the metal stage. This disc is to be placed on the metal stage with pogo pins in such a way that all the pogo pins can touch the samples. Oxygen-Free High Conductivity (OFHC) copper has been used for these metallic parts as it has a very high thermal conductivity.

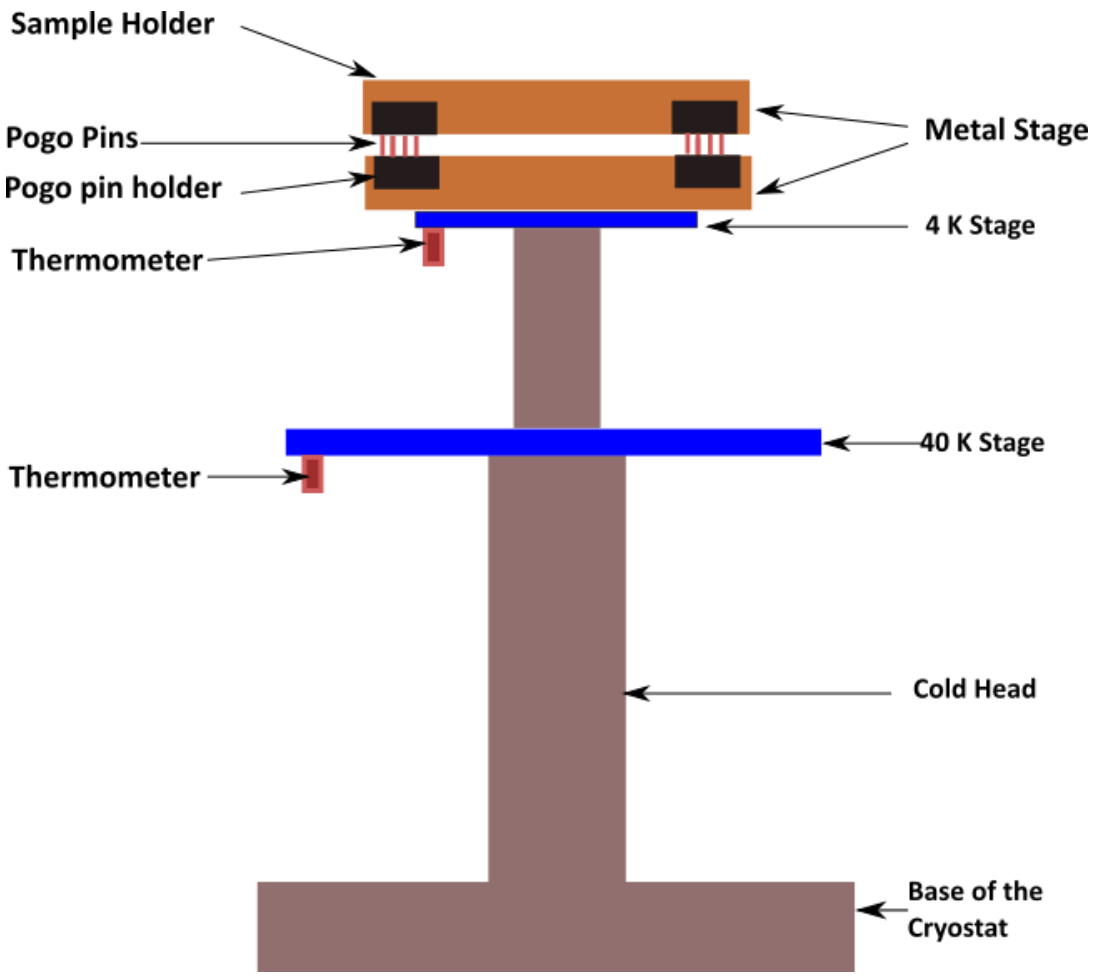

Fig. 3.9: Block diagram of the cryogen free thin film testing set up.

The coldhead needs to be encapsulated in a vacuum can and sealed off before cool-down because cold surfaces act as a trap for any residual gases remaining inside the chamber after the cool-down, and this can lead to a serious hazard. We have attached a hexagonal base at the bottom of the cold head (Fig. 3.10 (c)). A vacuum can with commercially available O-rings and flanges have been placed over the hexagonal base. Before every cool-down, the system has been pumped down and sealed off using an isolation valve.

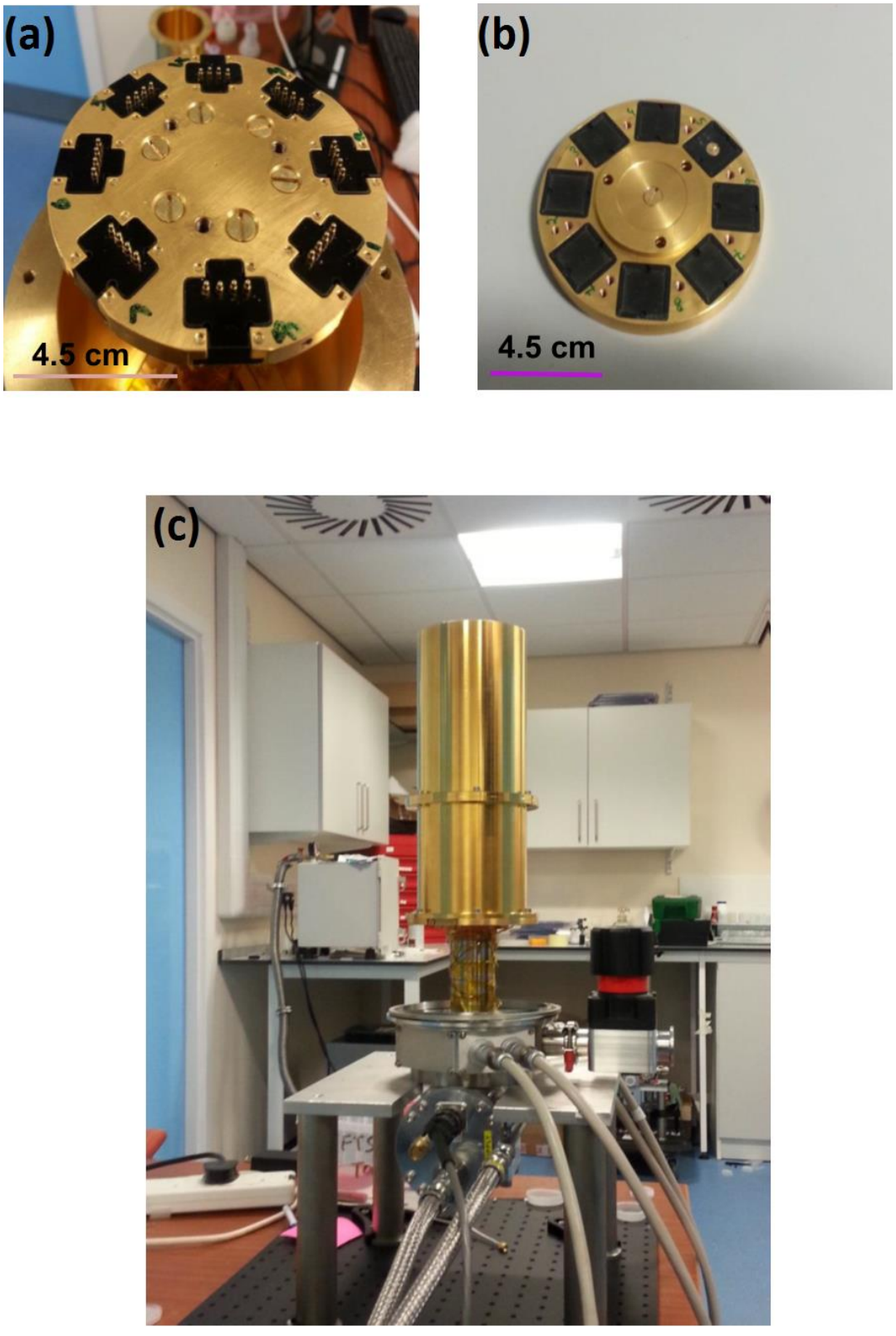

Fig. 3.10: Different parts of the cryogen free T_c testing set up. (a): Metal disc placed on the 4 K stage of the coldhead, pogo pins are press fitted in the insulating holders. (b) Metal disc to hold the samples (Both the discs are made of oxygen free high conductivity copper). (c) Radiation shields made of gold plated aluminium.

One of the primary requirements for our cryostat design is to reach a stable base temperature of below 4 K for a long period of time so that it can be employed in the electrical characterisation of superconducting thin films. For that purpose, it is necessary to reduce the heat load in the cryostat as much as possible. Radiative heat load can be a significant problem in reaching very low temperatures due to the huge difference between ambient temperature and temperature in the coldhead. Therefore, we have mounted a radiation shield on the 40 K stage of the cold head. Metals with highly reflective surfaces can be used for this purpose since these have very low radiation emissivity. Emissivity can be further reduced by polishing the metals' surfaces. We have used gold plated aluminium for the radiation shield.

For the electronics read-out we have used an isolated voltage source (SRS SIM928) in series with a resistor to provide a constant amount of current through the outer pair of pogo pins at each individual sample. At the same time, we have measured the voltage difference across each sample with the help of an inner pair of pins as a function of cryostat temperature (four point resistance measurement). We have introduced a programmable Labjack switch which is connected to a computer through a RS-232 cable. The purpose of the Labjack is to record the applied current and measure potential difference values across each sample and then calculate their individual resistance by the use of a home built Python program. Additionally, an electronic switching circuit (relay) is connected through the Labjack to the computer in order to swap between the connected samples. The isolated voltage source, digital voltmeter and temperature sensors are installed in an SRS SIM900 mainframe.

For temperature measurement, we have used a silicon diode thermometer manufactured by Lake Shore which can be used in a cryogenic environment. The thermometer is attached to the 4 K stage of the coldhead. Since the accuracy of temperature measurement is crucial for this set-up, this thermometer is individually calibrated by the manufacturing company. It is calibrated from 1.4 K to 325 K with a tolerance of ±12 mK. The calibrated curve has been loaded to the SRS temperature sensor by a Python program. In order to connect the pogo pins of each sample to the electronic controlling circuit, we have used twisted pairs of a 110 micrometre diameter polyester insulated constantan wire. This wire was chosen mainly due to the fact that low thermal conductivity of constantan would help to decrease conductive heat load on the system. These wires connect the pogo pins and the hermetically sealed

electrical connectors attached to the rectangular panels of the hexagonal base of the cryostat. Through the Python program, we can monitor and record *R* versus *T* data of superconducting thin films during cool-down or warming up.

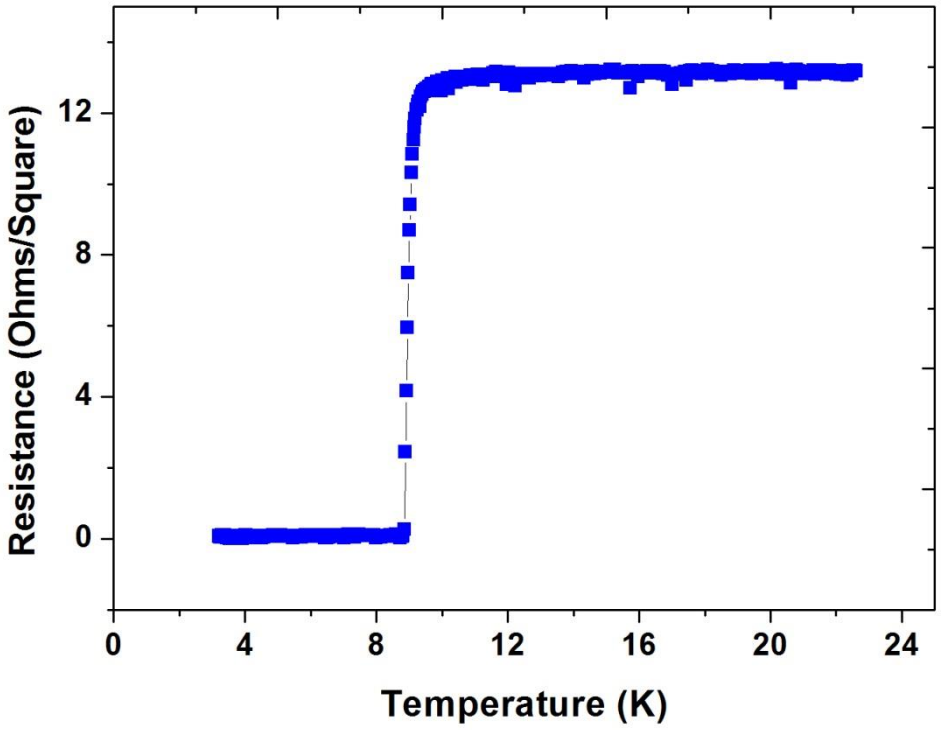

Fig. 3.11: Resistance versus Temperature curve of a superconducting thin film measured in the thin film testing set up.

3.2.1 Measurement of Critical Current Density[2]

Towards the end of this study, we have modified the programming of the thin film testing system so that we can measure the critical current density of superconducting thin films at the base temperature of the cryostat (~3 K) which have been deposited in our system. We have designed a mask to pattern a nanostrip on the thin films. The following figure 3.12 shows the design of the mask. The strip is 6 µm wide and 300 µm long. It is connected to four contact pads in such a way that if we place the patterned sample in the sample holder of the above described T_c testing set-up, the pogo pins with connect contact pads and the

[2] **The photolithography mask for critical density measurement was designed by Umberto Nasti and the modification in the programming has been done by Christopher Gough as a part of his 1st year postgraduate research project.**

current-voltage characteristic of the nanostrip can be measured using a SIM 970 voltmeter and a SIM 928 voltage source.

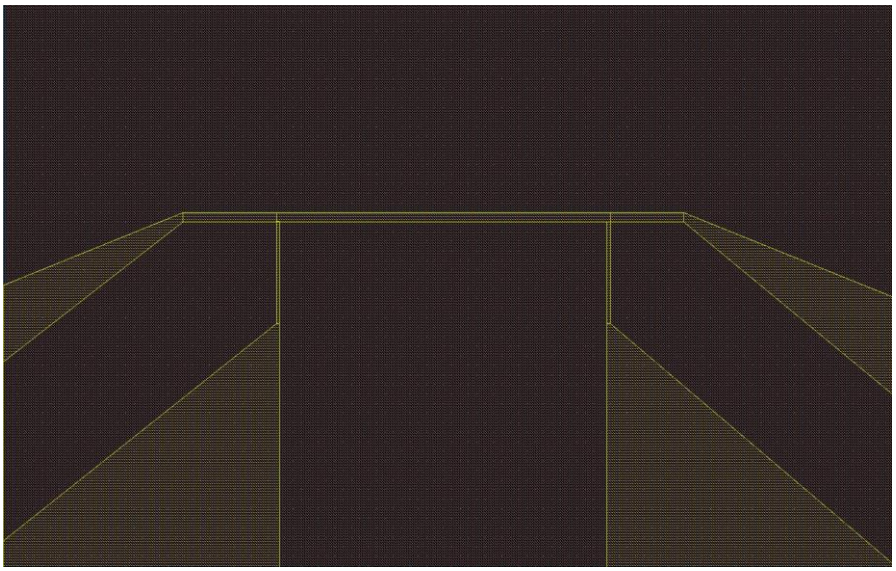

(a)

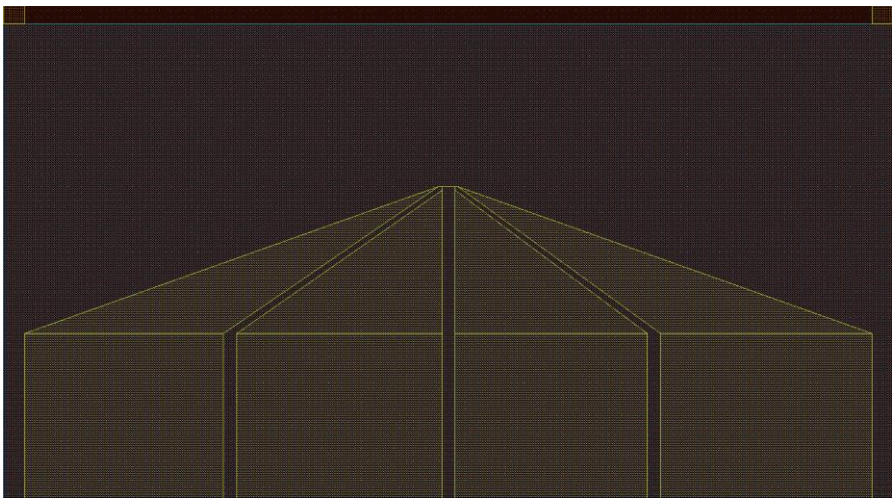

(b)

Fig. 3.12: Mask used to pattern the nanowire on the superconducting thin film to measure critical current density.

3.3 Thickness Measurement

The sputter deposition tool which has been used for the growth of superconducting materials does not have any real time thickness monitor inside its chamber. However, an accurate estimation of film thickness and growth rate is essential for each process. Hence, we had to measure the thickness of the films after deposition. Initially, while executing the process

optimisation for different materials, we followed a simple process to measure thickness. Before deposition, we drew a line across the substrate with an ink gel pen. After that, the substrate is inserted into the chamber and film is deposited on the top of it. At the end of deposition cycle, we etched the ink with acetone. Finally, the step created in the etch process can be scanned in atomic force microscopy (AFM). From this AFM scan, we can measure the thickness of the film.

Later on, several films have been analysed in high resolution transmission electron microscopy (HRTEM) and variable angle spectroscopic ellipsometry (VASE). We have extracted film thickness from these techniques and compared it with AFM measurements.

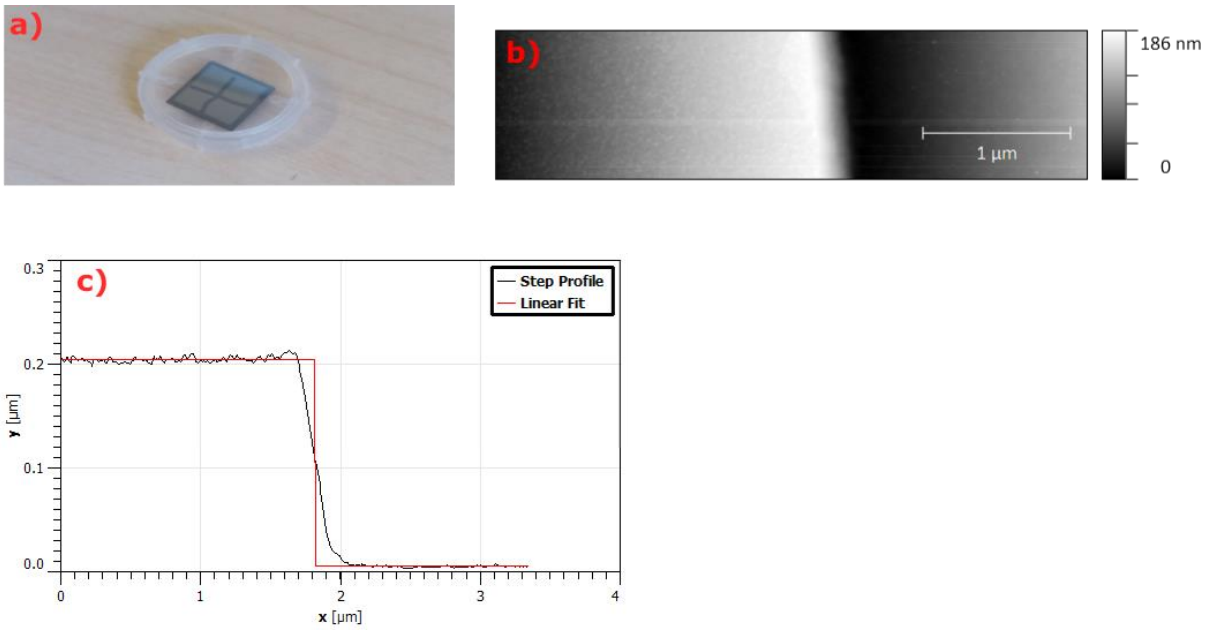

Fig. 3.13: Thickness measurement: (a) Step created by making a cross mark on the substrate with help of an ink pen prior to film growth and etching the film in acetone after deposition. (b) AFM scan across the step created. (c) Thickness measurement from the step profile.

3.4 Transmission Electron Microscopy[3]

We have analysed chemical composition and structural characteristics of superconducting thin films in high resolution transmission electron microscopy (HRTEM). The transmission electron microscope facilities available in the School of Physics and Astronomy, University of Glasgow (JEOL ARM200cF and FEI Tecnai T20 microscope) have been used for this

[3] **Transmission electron microscopy analysis has been carried out in collaboration with the research group led by Dr. Ian MacLaren, School of Physics and Astronomy, University of Glasgow.**

purpose. Before the HRTEM analysis, electron transparent cross sections have been prepared using a dual beam focussed ion beam (FIB) system [6].

3.4.1 Sample Preparation for HRTEM Analysis

At the beginning of the sample preparation, a conductive layer is deposited on the top of the film as a protection against the potential damage during FIB processing. For our samples, Gold has been used as the protective layer. After that, the sample is inserted in the FIB system. A metal strip (Pt for our films) is deposited on the region of interest using ion beam (Fig. 3.14 (b)). Then, material surrounding the region of interest is removed with the help of a focussed ion beam. As shown in Fig. 3.14 (c), a large stair-step FIB trench is cut on one side of the area of interest and a rectangular trench is made on the other side. After this step, the sample holder is tilted to an angle of >45° and then the bottom, left side and a portion of the right side of the specimen is cut so that the sample is partially released. Then, the holder is tilted back to its original position and the specimen is thinned to electron transparency. For HRTEM analysis, a final thinning is performed at an angle of ∼1–2° with respect to the plane of the sample surface. The thinnest portion of the sample lies in the area of interest for HRTEM analysis (usually ~50 nm). Finally, a micromanipulator is used to lift the sample cross section from the trench and transfer to a copper TEM mesh grid (Fig. 3.14 (d)).

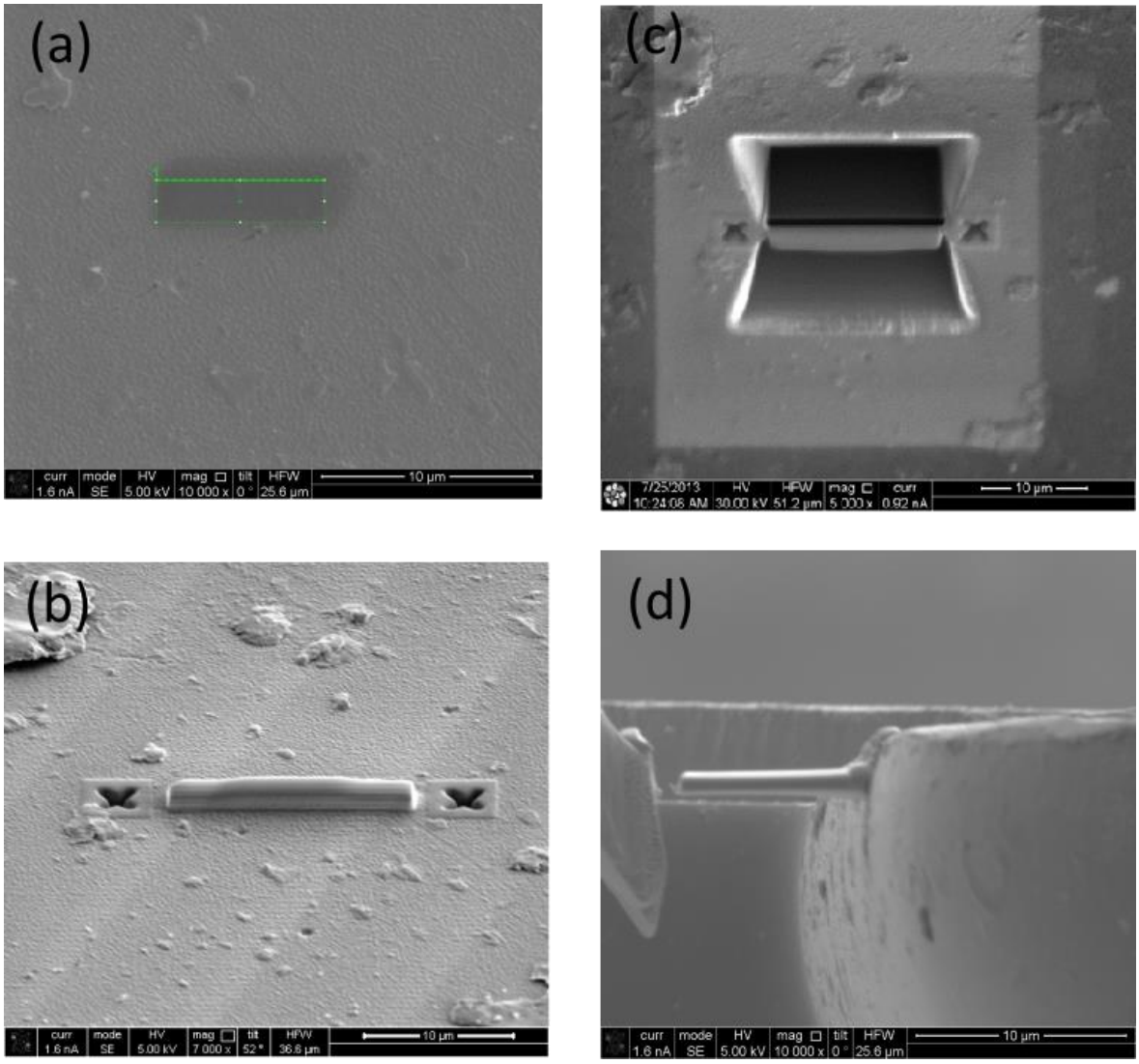

Fig. 3.14: Sample preparation for high resolution transmission electron microscopy analysis. (a) Area of interest on the sample. (b) Metal strip (Pt) deposited on the area of interest. (c) Material removed surrounding the area of interest to create trench so that (d) Electron transparent thin sample cross section is lifted to TEM grid through a micromanipulator.

3.4.2 Working principle of Transmission Electron Microscopy

In transmission electron microscopy, a high energy electron beam is used to analyse material properties of samples. Due to a smaller wavelength of electron beam (3.7 pm for a 100 keV electron beam), it is possible to obtain a much higher resolution with TEM in comparison to an optical microscope. In our set up, JEOL ARM200cF has a cold field emission gun and Tecnai T20 uses a LaB_6 filament as the electron source [7].

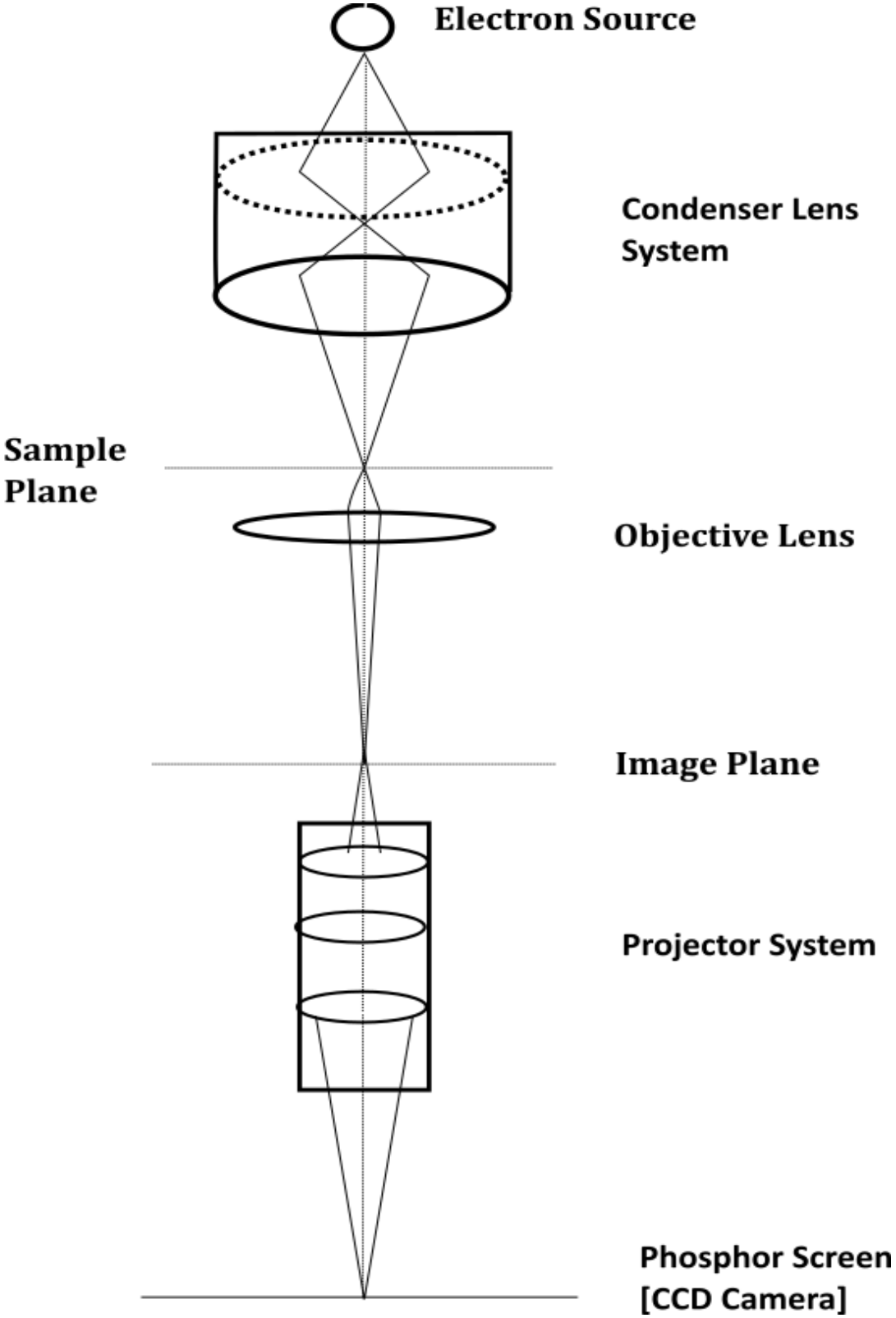

Fig. 3.15: Basic schematic diagram of transmission electron microscopy demonstrating its working principle.

As shown in the above figure, the electron source of the microscope generates a high energy electron beam. A two stage condenser lens system is used to focus the electron beam on the sample. There is an aperture immediately after the condenser lens system. The 'brightness' of the image is controlled by the condenser system. The objective lens forms an inverted image (with a small degree of magnification) of the sample by focussing the transmitted electron beam in a virtual image plane. The focal length of the lens can be changed by adjusting the current passing through the electromagnetic coil that makes up the objective lens. An objective aperture may be inserted to select electrons which will form the image (selecting specific diffraction spots for dark field imaging). The projection system forms a magnified image in the recording device. The magnification of the microscope can vary from a few hundred to several hundred thousand depending on the setting of the strength of the projector lenses.

By adjusting the projection lens system, we can also image the diffraction pattern formed due to the interaction between the electron beam and the sample at the back focal plane of the objective lens. The diffraction pattern can reveal much useful information about the structural properties of the sample under investigation.

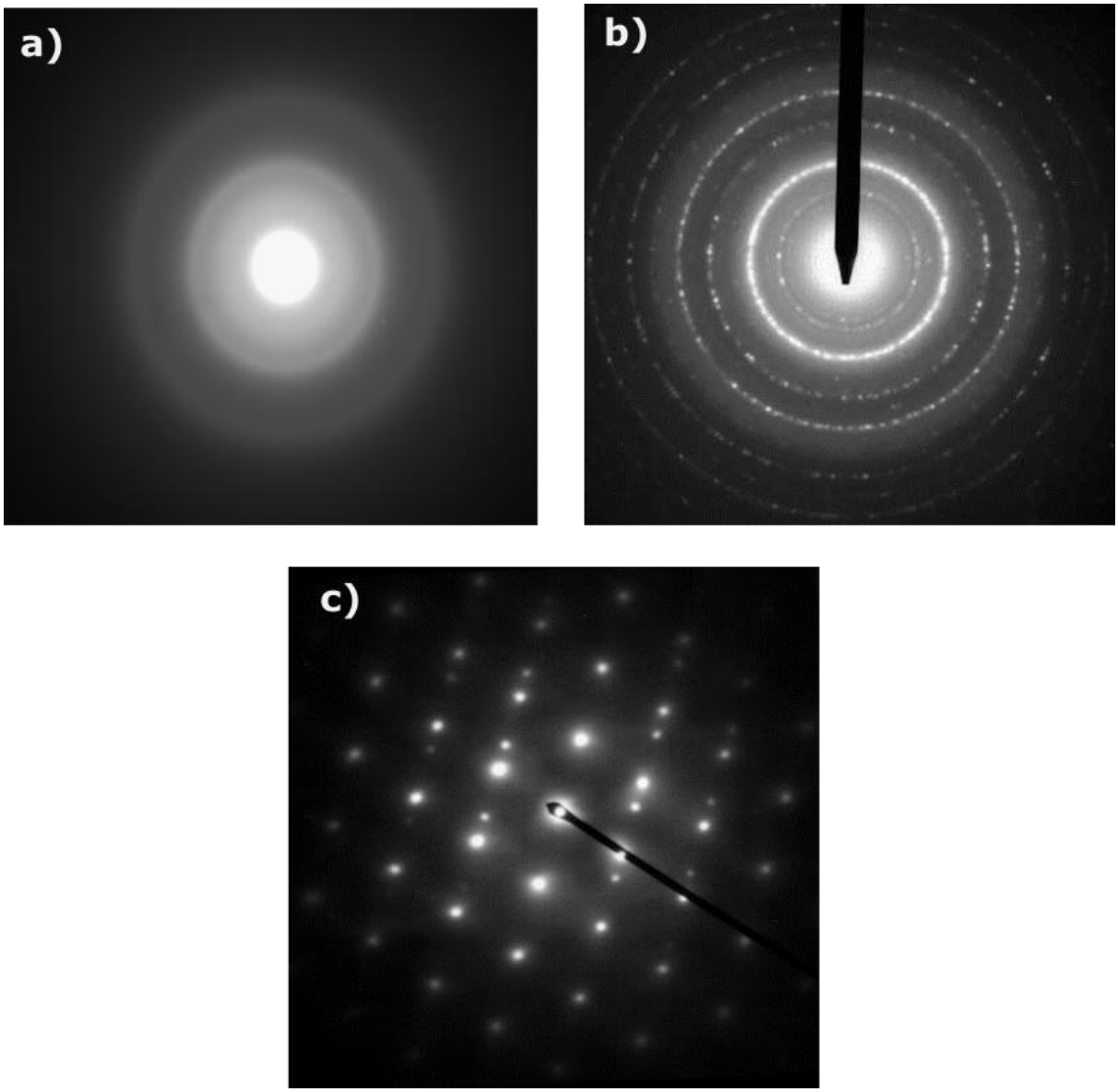

Fig. 3:16: Diffraction pattern recorded in transmission electron microscopy: (a) Diffused rings amorphous materials (Diffraction pattern recorded from amorphous MoSi films grown by our group). (b) Diffuse patterns with polycrystalline grains (Polycrystalline Zr/Ni/Cu-based alloy, *Image taken from* *http://www.ammrf.org.au/myscope/images/tem/diffraction-sad.jpg*) (c) Single crystalline diffraction pattern (Zone axis diffraction pattern of austenite crystal, *Image taken from* *https://commons.wikimedia.org/wiki/File:Austenite_ZADP.jpg*).

3.5 Variable Angle Spectroscopic Ellipsometry (VASE)

The optical properties of superconducting thin films have been analysed by variable angle spectroscopic ellipsometry techniques. A J K Woollam's spectroscopic ellipsometer (spectral range: 270 nm to 2200 nm, Si/AlGaAs detector) has been used for this study.

Ellipsometry is a nondestructive optical characterisation technique. It measures the state of polarisation of the incident light while being reflected (or transmitted) by the sample surface. Optical properties of the sample determine how it influences the incident electromagnetic radiation [8], [9].

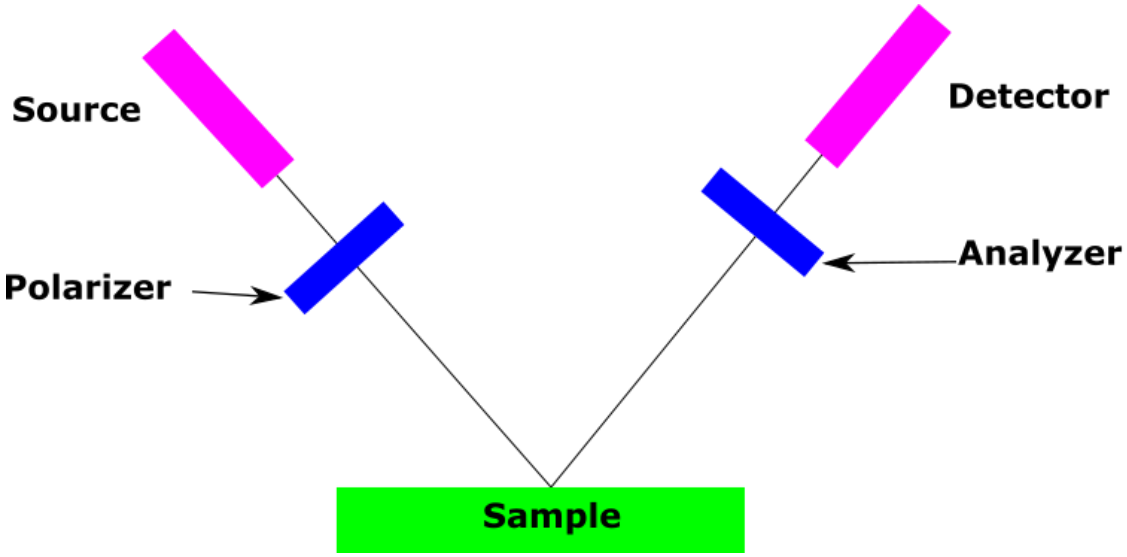

Fig. 3.17: Variable Angle Spectroscopic Ellipsometry (VASE): a linearly polarised light is incident on the sample surface and a change in the state polarisation upon reflection off of the sample is measured with the help of the analyser and the photo detector.

As shown in the above figure, during the ellipsometric analysis, a linearly polarised light is directed on the sample at a user defined angle of incidence. A monochromator is attached to the source. After being reflected at the sample surface, the polarisation of light changes and, in general, it becomes elliptically polarised. This change in the state of polarisation is analysed by the second polariser (called 'analyser') and a photodetector. From the signal detected after the analyser, ellipsometry measures the ratio of the Fresnel reflection coefficients for the p and s polarised components as shown in the following equation.

$$\rho = \frac{r_p}{r_s} = \tan(\psi)\exp(i\Delta_v) \quad (3.1)$$

The above equation is the fundamental equation of ellipsometry. Here, r_p and r_s denote the Fresnel reflection co-efficient for the p and s polarised components. $\tan(\psi)$ and Δ_v are the amplitude change and phase shift of the incident light upon reflection. (p polarised light denotes light polarised parallel to the plane of incidence and s polarised light denotes light polarised perpendicular to the plane of incidence.) Measured data is usually expressed as a function of ψ and Δ_v as shown in equation 3.1. The angle of incidence is usually kept close to the Brewster angle so that the measured ratio can be maximised.

To retrieve important information (e.g. thickness, refractive index, etc.) from the ellipsometric measurement, we need to construct a model which is suitable for the sample which is being measured. After constructing the model, we take the help of different fitting algorithms of the analysis software provided with the instrument (WVASE32 version 3.840) to fit the theoretical model with the ψ and Δ_v measurement data. It is to be noted that ellipsometric measurement strongly depends on the modelling as we cannot extract useful optical or physical parameters only from the measured data. For the superconducting thin films we have used a combination of Drude and Lorentz oscillator models to describe their optical properties.

3.6 Nanowire patterning of superconducting thin films

The transport properties, including the temperature dependence of the critical current density of amorphous superconducting thin films, have been measured from the low temperature measurements of nanowires patterned on the films. Electron beam lithography (EBL) and reactive ion etching (RIE) have been used for this purpose. Here, we have given a brief overview of the fabrication procedure which has been followed to fabricate the nanowires.

At the beginning, amorphous MoSi film (~ 10 nm thick) is grown on the top of the silicon substrate. Then, ZEP 520 A (a positive tone electron beam resist) is spun at 4000 rpm for 60 seconds and baked for four minutes (leading to a thickness of 110 nm). EBL is used to define the patterns for alignment markers and contact pads. A Vistec VB6 UHR EHF EBL tool at 100 keV has been used for all the EBL patterning. Then the chip is developed in Oxylene (at 23°C temperature), leaving only the unexposed resist. 15nm Ti and then 75 nm Au is deposited on the device by electron beam evaporation. The Ti layer works as an adhesive layer between the Au layer and the Si substrate. The resist along with the unwanted Au is

removed by putting the chip in a 1165-Stripper solvent overnight. After that, the nanowires are patterned over the thin film. A second round of the EBL process is performed in a similar way to steps 2–4 to create the pattern. Reactive Ion Etching (RIE) removes the thin film unshielded by the resist (CF_4 gas). The remaining resist is stripped using Shipley 1165 microposit remover.

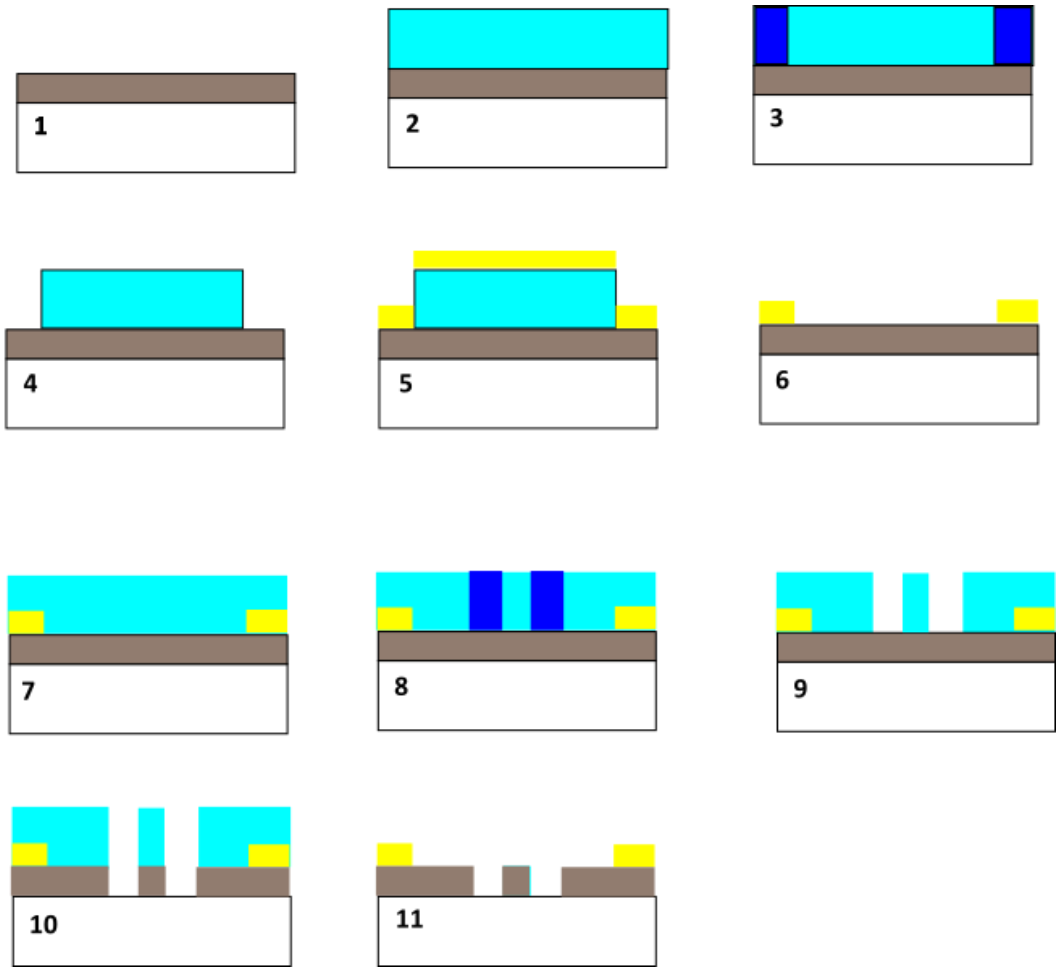

Fig. 3.18: Nanowire fabrication: 1: Deposition of superconducting thin film on Silicon substrate. 2. Spinning of ZEP 520 A (a positive tone electron beam resist) at 4000 rotations per minute (rpm) for 60 seconds and baked for four minutes. 3. Exposure to the electron beam to define patterns for contact pads and alignment markers. 4. Development in Oxylene (at 23°C temperature) for 60 seconds. 5. Deposition of 15 nm Ti and then 75 nm Au using electron beam evaporation. 6. Removal of resist along with the unwanted Au by putting the chip in 1165-Stripper solvent overnight. 7-9. Nanowire patterns are defined using a second round of EBL. 10. Reactive Ion Etching (RIE) removes the thin film unshielded by the resist (CF_4 gas). 11. The remaining resist is stripped using Shipley 1165 microposit remover.

References

[1] J. George, *Preparation of thin films*. M. Dekker, 1992.

[2] M. Leskela and M. Ritalä, “Atomic layer deposition (ALD) : from precursors to thin film structures,” *Thin Solid Films*, vol. 409, pp. 138–146, 2002.

[3] E. Alfonso, J. Olaya, and G. Cubillos, “Thin Film Growth Through Sputtering Technique and Its Applications,” in *Crystallization - Science and Technology*, InTech, 2012, pp. 397-432.

[4] R. W. Johnson, A. Hultqvist, and S. F. Bent, “A brief review of atomic layer deposition: from fundamentals to applications,” *Mater. Today*, vol. 17, no. 5, pp. 236–246, Jun. 2014.

[5] W. E. Gifford and R. C. Longsworth, “Surface Heat Pumping,” in *Advances in Cryogenic Engineering*, Boston, MA: Springer US, 1966, pp. 171–179.

[6] L. A. Giannuzzi and F. A. Stevie, “A review of focused ion beam milling techniques for TEM specimen preparation,” *Micron*, vol. 30, no. 3, pp. 197–204, 1999.

[7] D. B. Williams and C. B. Carter, *Transmission Electron Microscopy*. Boston, MA: Springer US, 2009.

[8] J. A. Woollam and P. G. Snyder, “Fundamentals and applications of variable angle spectroscopic ellipsometry,” *Mater. Sci. Eng. B*, vol. 5, no. 2, pp. 279–283, Jan. 1990.

[9] J. A. Woollam, P. G. Snyder, and M. C. Rost, “Variable angle spectroscopic ellipsometry: A non-destructive characterization technique for ultrathin and multilayer materials,” *Thin Solid Films*, vol. 166, pp. 317–323, Dec. 1988.

Chapter 4

Optimisation of Niobium (Nb), Niobium Nitride (NbN) and Niobium Titanium Nitride (NbTiN) Thin Film Growth

Since the fabrication of superconducting nanowire single photon detectors (SNSPDs) begins with superconducting thin film deposition, the quality of the films plays a vital role determining device performance. Nb based refractory metal nitrides (NbN & NbTiN) are the most widely used traditional thin film material for SNSPD applications. In this chapter, the growth and optimisation of NbTiN thin films have been reported (Section 4.2). Structural and optical characterisation of NbTiN films have also been discussed (Section 4.4 & 4.5). The acceptance test of the sputter deposition system (Section 4.1) and the process developed for NbN has been reported (Section 4.3). The chapter concludes with a short discussion on the SNSPD device fabrication based on the films deposited following the optimised process described in this chapter (Section 4.6).

4.1 Acceptance test of sputter deposition system

Immediately after the installation of the sputter deposition system, we started with the optimisation of thick superconducting niobium film. A 300 nm thick niobium film was deposited in our sputtering system (at 0.2 Pa chamber pressure, 0.9 A discharge current) and transition temperature was measured in the thin film testing set-up. The following figure presents resistance versus temperature data (Fig. 4.1). The film has a transition temperature of 9.1 K, which is close to the transition temperature of bulk niobium. This was a part of the acceptance test for the sputter deposition system.[4]

[4] **In the literature, there are several definitions of T_c. We define it as the temperature at which resistance of the film disappears or falls to zero in the R vs. T curve.**

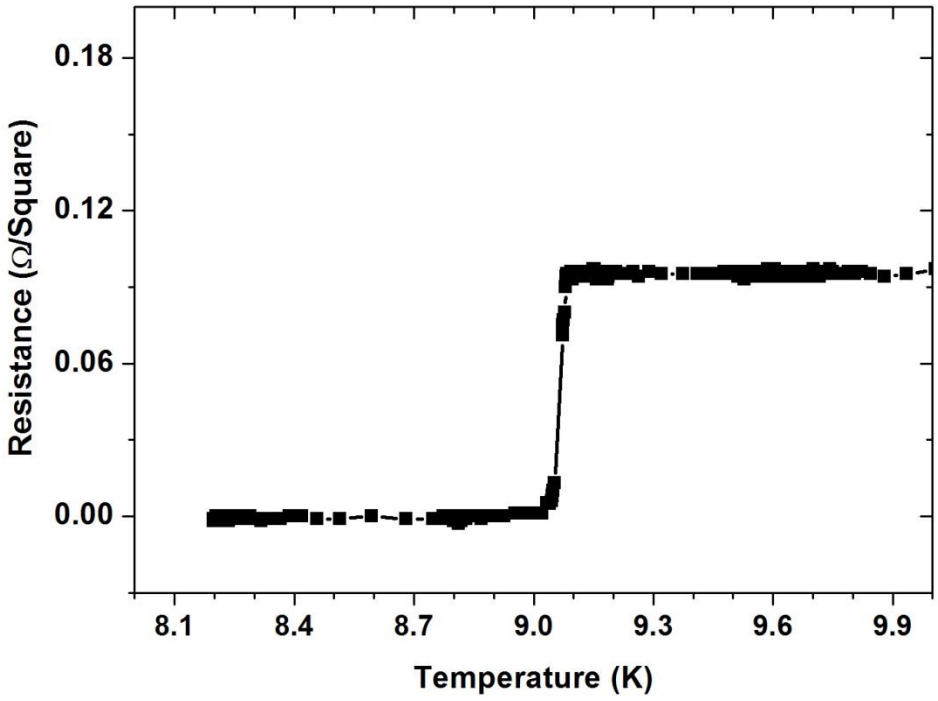

Fig. 4.1: Resistance versus Temperature curve of 300 nm thick niobium film deposited on a silicon substrate (zoomed in view) demonstrating a T_c of 9.1 K.

It is observed from the *R* vs *T* curve (Fig. 4.2) that resistance of the niobium film steadily decreases with temperature during the cool-down process. Hence, the film is purely metallic in nature. The residual resistivity ratio (*RRR*) of the film is 4.4.

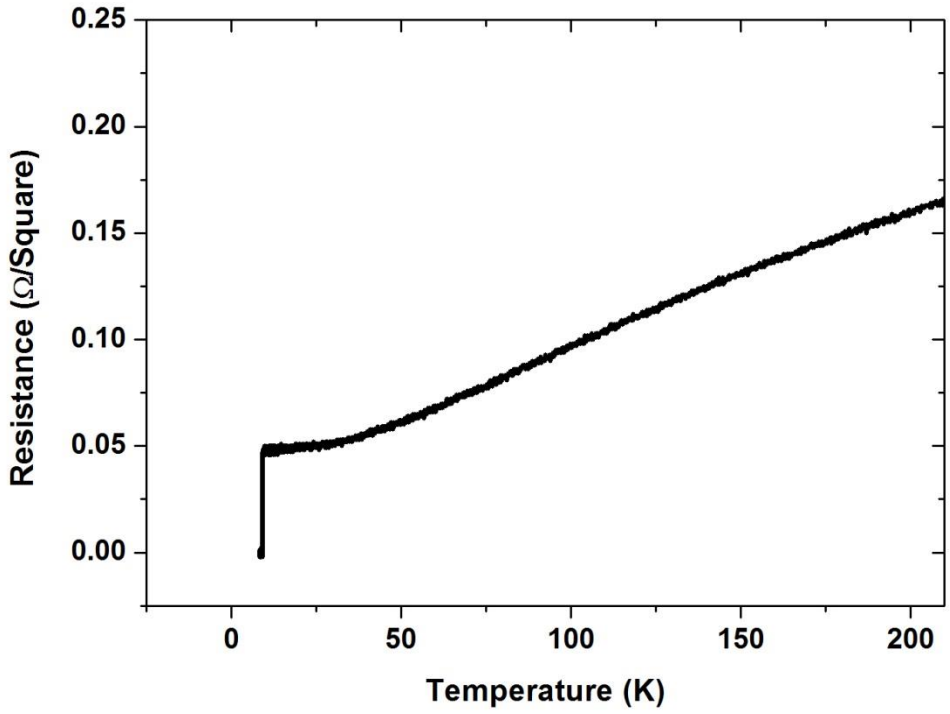

Fig. 4.2: Resistance versus Temperature curve of 300 nm thick niobium film deposited on a silicon substrate.

4.2 Niobium Titanium Nitride Growth and Characterisation

As discussed in the Section 2.4 of Chapter 2, the fabrication process of a superconducting nanowire single photon detector (SNSPD) initiates with superconducting thin films growth. For the operation of an SNSPD, ultrathin superconducting films (with a thickness of < 10 nm) are required which can be cooled down below their transition temperatures using a 2 stage cryo-coolers (to avoid expensive and hazardous cryogenic liquids). Gol'tsman *et al.* used NbN film in their initial SNSPD devices [1]. Until now, NbN & NbTiN are the most extensively used base materials for SNSPD fabrication (due to their higher bulk critical temperature and shorter coherence length) [2]. Hence, we have started our thin film optimization with NbTiN and NbN.

4.2.1 Choice of substrate and deposition conditions

At first, NbTiN film growth has been optimised in terms of desirable thickness, uniformity and superconducting properties. As was stated earlier in Section 2.4 of Chapter 2, since the

lattice parameters of MgO or sapphire are very close to that of NbTiN, they have been widely used as substrates for NbN or NbTiN based SNSPDs. However, this limited choice of substrates restricts the potential application of SNSPDs. That is why we chose silicon as our substrate for optimisation. Silicon is an attractive substrate material for various applications at telecommunication wavelength. It also has an advanced and mature fabrication technology. Single side polished silicon wafers with <001> crystalline direction have been diced into 15 mm x 15 mm sized substrates and have been used for NbN & NbTiN growth optimisation.

Before deposition, the substrates have been cleaned in an ultrasonic bath with RO water, acetone and IPA for 5 minutes. Then, the substrates are inserted in the loadlock of the sputter deposition tool. Prior to the film deposition, substrates were etched into the loadlock with argon plasma for 2 minutes. After that, they are transferred to the main chamber with the automated transfer arm. NbTiN films are grown by the co-sputtering of confocal Nb and Ti targets in an argon environment and introducing a small amount of nitrogen in the chamber as the reactive gas. The distance between the substrate and the target is kept at 100 mm. The substrate holder was rotated at a speed of 60 rpm during deposition for better uniformity of the film growth. While executing the deposition process, the cryo gate valve of the chamber is closed. The turbo pump is throttled with a butterfly valve to maintain the desired pressure in the chamber.

4.2.2 Choice between Current and Voltage Controlled Deposition

Thin film growth process in DC magnetron sputtering can be controlled by the constant current mode, constant voltage mode or constant power mode. Yagoubov *et al.* [3] have discussed a potential approach to monitoring the NbN sputtering process and avoiding the hysteresis formation. According to their study, if NbN (or NbTiN) films are sputtered at a constant voltage or power mode, there is a possibility of the formation of a hysteresis loop in the *I-V* curve due to the unstable state of the discharge plasma. Fig. 4.3 depicts such a curve (I-V curve during reactive sputtering of NbN in the constant voltage mode).

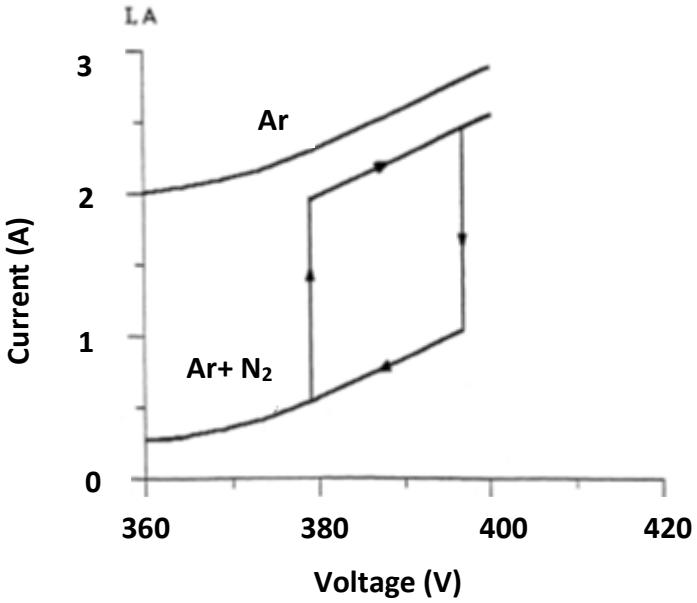

Fig. 4.3: Current versus Voltage curve of the plasma during the reactive sputtering of NbN in the constant voltage mode as reported by Yagoubov *et al.* [3].

It is to be noted that besides deposited material, reactive nitrogen also reacts with the Nb (and Ti in case of NbTiN growth) target to form NbN there. At low discharge voltages and when the sputtering rate is very low, nitrogen mainly reacts with the target. Hence, the target becomes totally covered with NbN. As discharge voltage gradually increases, the sputtering rate of NbN on the substrate increases. At a certain critical voltage, the sputtering rate of the target becomes higher than the rate of formation of NbN on the target. Thus, the NbN layer on the target surface is partially eroded. The sputtered Nb atoms absorb more nitrogen leading to a further decrease of the NbN formation on the target surface and, hence, the target is further depleted of NbN. Since Nb has a larger secondary electron emission factor than that of NbN, discharge current rises sharply and discharge characteristics approach the I-V curve of pure argon. Then, if discharge voltage is afterwards gradually reduced, the nitrogen will still be almost completely absorbed by the sputtered niobium to form NbN on the substrate. But at a critical point, the target sputtering rate decreases to such an extent that NbN deposition on the target surface is renewed. As a result, the current drops abruptly, and the target is instantly coated with NbN.

Let us now consider the *I-V* characteristics under constant current mode (Fig. 4.4). It clearly shows that there is no hysteresis in the curve. This is due to the fact that discharge voltage is compensated once it is deviated from the equilibrium position. If the sputtering rate increases, an additional part of the target surface is depleted of NbN leading to decrement in

nitrogen partial pressure. This will reduce discharge voltage (since the presence of nitrogen enhances impedance of argon plasma in the discharge). Hence, the sputtering rate returns to its initial value. The converse will occur if the sputtering rate decreases. Hence, it is possible to obtain a one-to-one correspondence between discharge voltage and nitrogen flow at constant current mode operation. Therefore, the change in discharge voltage due to the introduction of nitrogen into the chamber may be used as a suitable parameter to control nitrogen partial pressure in the system.

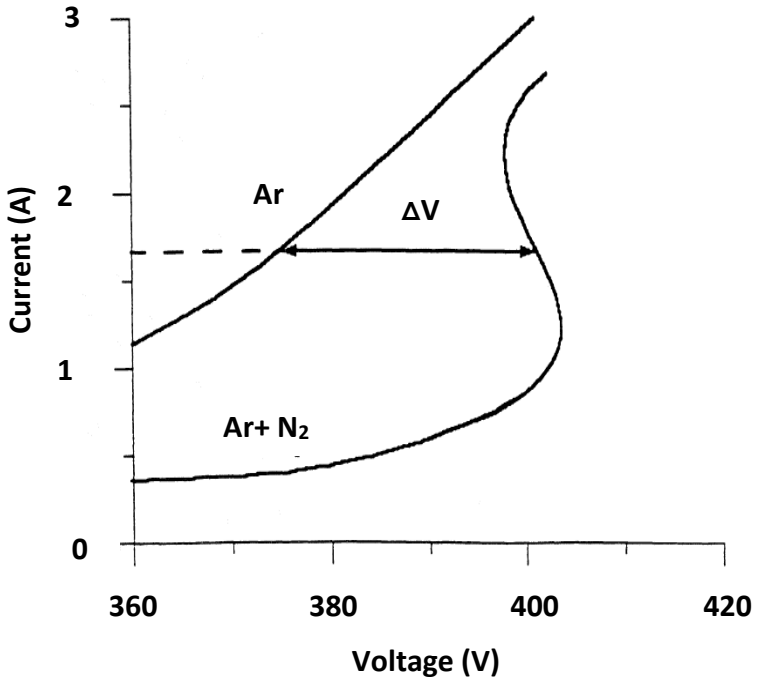

Fig. 4.4: Current-Voltage curve when NbN is deposited in constant current stabilisation condition [3].

Later on, many other groups (for instance Marsili *et al.*, Matsunaga *et al.*, etc.) have utilised this concept to optimise NbN or NbTiN thin film deposition in reactive sputtering [4], [5]. In this study, we have also used a constant current controlled approach.

4.2.3 Characterisation of Plasma

At the beginning of the film growth, we have explored the target voltage vs nitrogen flow curve of niobium plasma in order to set a starting value of nitrogen flow for optimisation.

To determine this curve, 18 sccm of argon has been introduced in the process chamber and the throttle valve was set at 75° (setting total chamber pressure at 0.14 Pa). At first, the Nb target has been pre-sputtered for 5 minutes, keeping the shutters closed to remove any contamination on the target surface. Then, Nb target was sputtered with a 0.9 A discharge current and nitrogen was introduced into the chamber. A flow rate of N_2 has been increased at a step of 0.5 sccm. For each nitrogen flow target, a voltage has been recorded once plasma is stabilised. After the target had become totally covered with nitrogen (operating above the hysteresis portion of the curve), the downward portion of the hysteresis curve has been determined by decreasing the N_2 flow in 0.5 sccm steps. Fig. 4.5 shows the target voltage versus N_2 flow curve. A 5 sccm nitrogen flow was chosen as the starting point (midpoint of hysteresis region of the curve) for the NbN or NbTiN growth optimisation. As discussed in the previous section – and suggested by Vaneldik *et al.* or Glowacka *et al.* – target voltage is an indicator of the state of nitridation of the target, and consequently also of the film stoichiometry. The mid-point of the top elbow of the hysteresis curve can be a good starting point for optimisation (5 sccm) [6], [7].

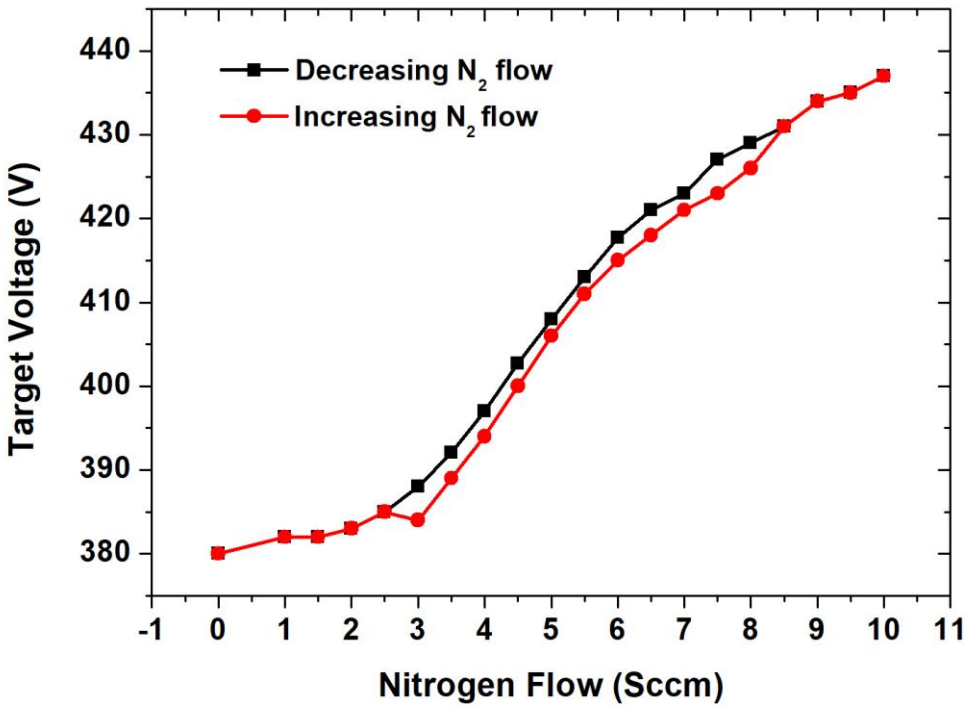

Fig. 4.5: Characterisation of plasma: Target voltage versus nitrogen glow curve for niobium target.

4.2.4 Optimisation of Process Parameters

We started the optimisation with bulk NbTiN film growth. Nb target has been sputtered with a discharge current of 0.9 A and Ti has been sputtered with a 0.450 A current. The discharge current has been chosen in such a way that composition of the film would have been around 80% Nb and 20% Ti by weight. 100 nm thick NbTiN films have been grown at various chamber total pressure. (Chamber total pressure is varied by controlling argon flow in the process chamber keeping the throttle valve at a fixed angular position of 75° keeping nitrogen flow fixed at 5 sccm.) Fig. 4.6 shows the variation of T_c with total argon flow in the chamber. All the depositions have been done at room temperature. Both the Nb and Ti targets were pre-sputtered prior to deposition for 5 minutes to stabilise the deposition conditions. The substrate holder has been rotated with a speed of 60 rpm.

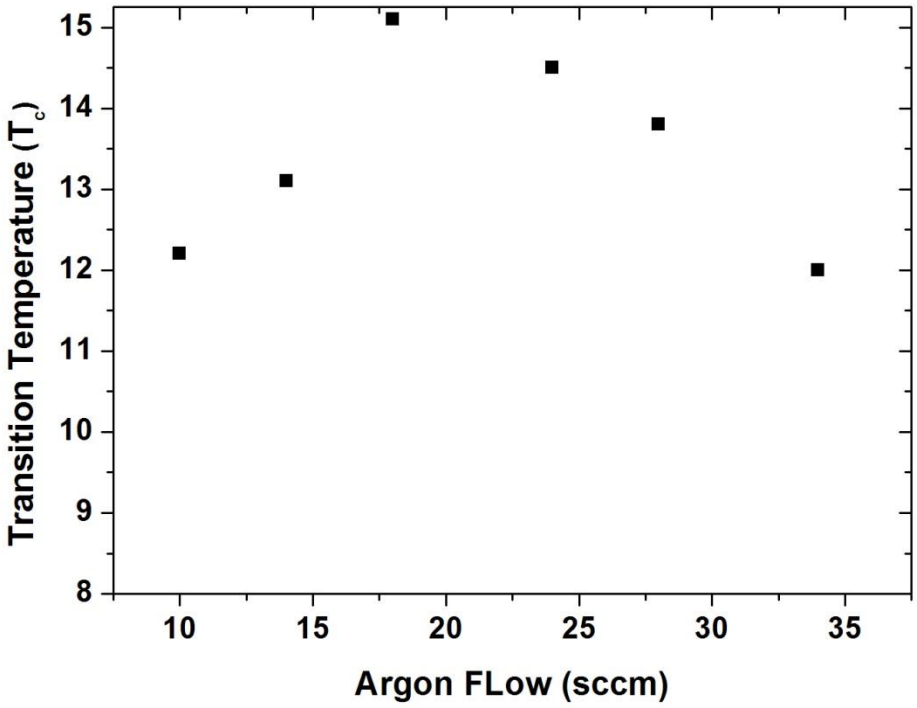

Fig. 4.6: Superconducting transition temperature of 100 nm thick NbTiN films deposited on unheated silicon substrates by co-sputtering from Nb and Ti target in an Ar/N_2 environment as a function of different argon flow rates.

From the Fig. 4.6 it can be clearly seen that a maximum T_c of 15.1 K is achieved if NbTiN is grown with 18 sccm Ar and 5 sccm N_2. (This corresponds to a total chamber pressure of 0.14 Pa.) A deposition time of 6 minutes has been used to deposit 100 nm thick films.

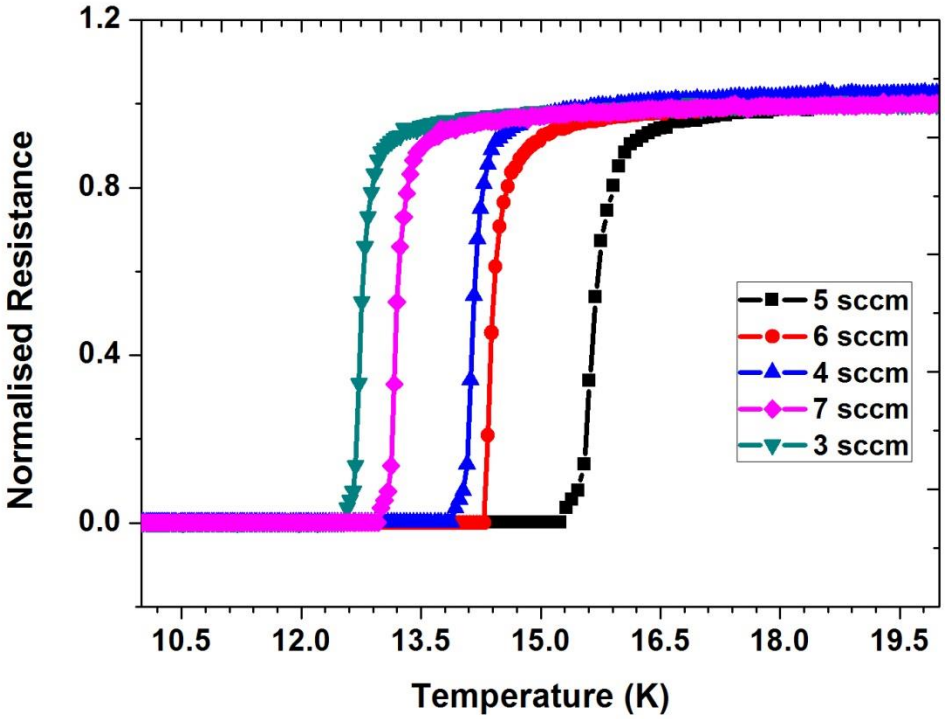

Fig. 4.7: Normalised Resistance versus Temperature of 100 nm thick NbTiN film deposited at various nitrogen flows keeping the total chamber pressure constant at 0.14 Pa.

After that, the total chamber pressure has been fixed at 0.14 Pa and 100 nm thick NbTiN film was deposited at different nitrogen flow rates when other deposition parameters were kept unchanged. As it can be seen from the Fig. 4.7, a maximum T_c of 15.1 K can be achieved from a film grown with 5 sccm N_2 flow. We have also checked the influence of other deposition parameters (e.g. Nb:Ti ratio or substrate holder rotation) on superconducting property of the film. The above mentioned process parameters give an optimum T_c for 100 nm thick NbTiN film deposited at room temperature.

Table 4.1: Optimised Recipe for NbTiN Deposition

Nb	0.9 A (356 W, 398 V)
Ti	0.450 A (179 W, 399 V)
Target Substrate Distance	100 mm
Substrate Holder Rotation	60 Rotation per minute
Ar Flow	18 sccm
N_2Flow	5 sccm
Throttle Position	75°
Chamber Pressure	0.14 Pa

4.2.5 Process Optimisation for ultrathin NbTiN Films (thickness <10 nm)

As mentioned in Chapter 2, decreasing film thickness results in the degradation of superconducting and electrical properties of thin films. To explore this thickness dependence, NbTiN films ranging from 100 to 5.5 nm in thickness were deposited on silicon substrates under the same optimised deposition conditions. The thickness of the films has been reduced by decreasing the deposition time.

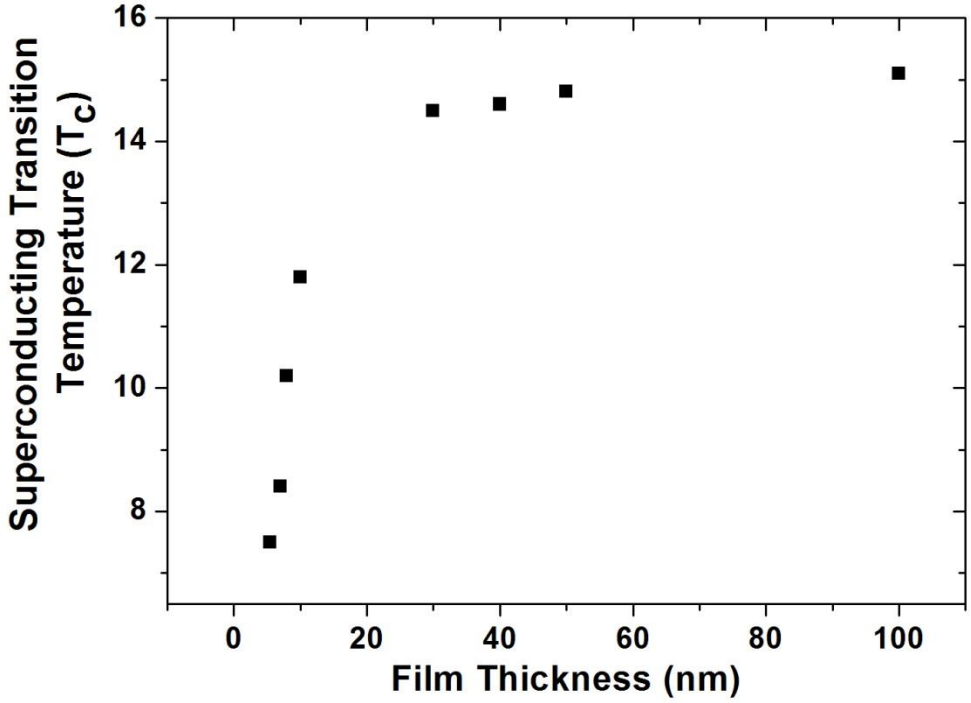

Fig. 4.8: Variation of superconducting transition temperature of NbTiN films with film thickness.

Fig. 4.8 shows that T_c sharply degrades as the film thickness decreases below 10 nm. For a 5.5 nm thick film, we have obtained a T_c of 7.3 K with an *RRR* of 0.88. The deposition rate of this process was 0.275 nm/sec, meaning it took 20 seconds of deposition time to grow a 5.5 nm thick film. The substrate temperature during thin film deposition has been found to be a crucial factor influencing the superconducting properties of NbTiN films since the crystalline structure of thin films changes with deposition temperature. There is a resistive heater in our sputter deposition tool attached to the deposition stage which can heat the substrates up to 800°C. A substrate holder made of molybdenum has been used for this purpose. 5.5 nm thick NbTiN films have been deposited at various substrate temperatures and a significant improvement of T_c has been observed as a result of substrate heating. If we heat the substrate to 800°C for 20 minutes before deposition, the T_c improves to 10.4 K (with *RRR*= 0.91). Higher *RRR* indicates that films deposited on a heated substrate are more metallic and have better crystalline quality and a larger grain size.

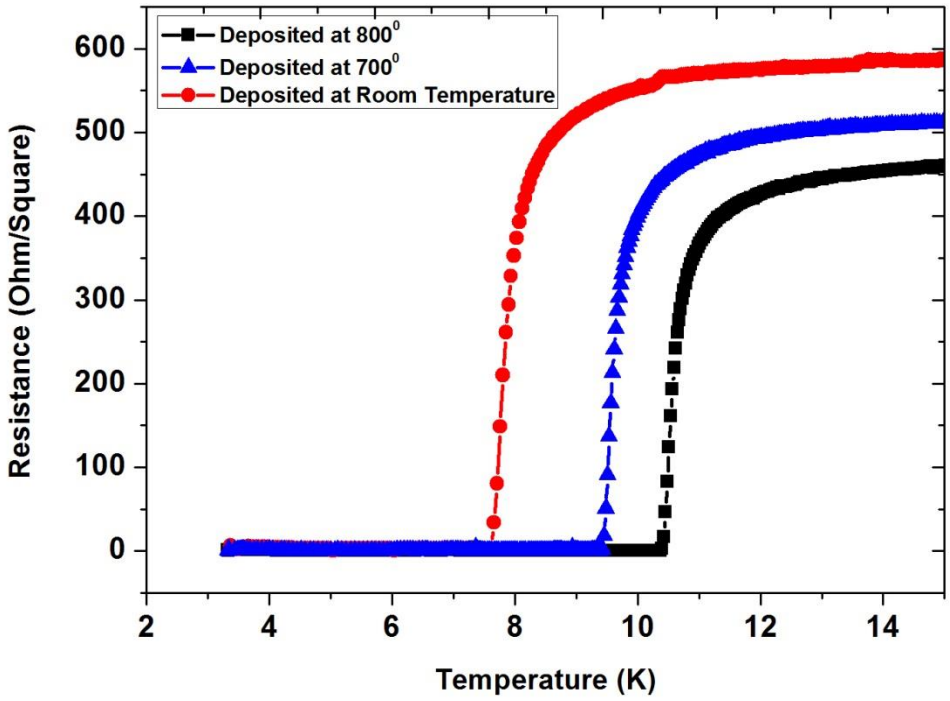

Fig. 4.9: Effect of substrate heating: substrate heating improves the superconducting property of NbTiN films. T_c of 5.5 nm thick NbTiN film increases from 7.2 K to 10.4 K.

As we can see from Fig. 4.9, films grown on heated substrates have lower sheet resistance and higher T_c. As stated in Section 2.3.2 of Chapter 2 and according to Thornton's structure zone model, films deposited at room temperature have poor crystalline structures (Zone 1). When films are grown on a heated substrate, improved crystalline structures can be observed consisting of columns having tight grain boundaries between them (Zone 2). In the following Section 4.3, we have verified through transmission microscopy analysis that substrate heating improves structural properties of the NbTiN films.

In order to verify how the crystalline property of substrates influences the superconducting property of NbTiN films, we have deposited a 5.5 nm thick film following the same optimised recipe on a silicon on insulator substrate (a popular substrate for integrated quantum photonics). As it can be seen from the Fig. 4.10, the film deposited at room temperature demonstrates a clear degradation of the transition temperature (6.3 K T_c, 0.9 K less than the film deposited on the standard silicon substrate). For the films deposited on the heated substrate, superconducting properties improve and the difference in the T_c decreases

to 0.2 K. Hence, it can be inferred that due to its polycrystalline nature, superconducting properties of NbTiN can be highly influenced by substrates.

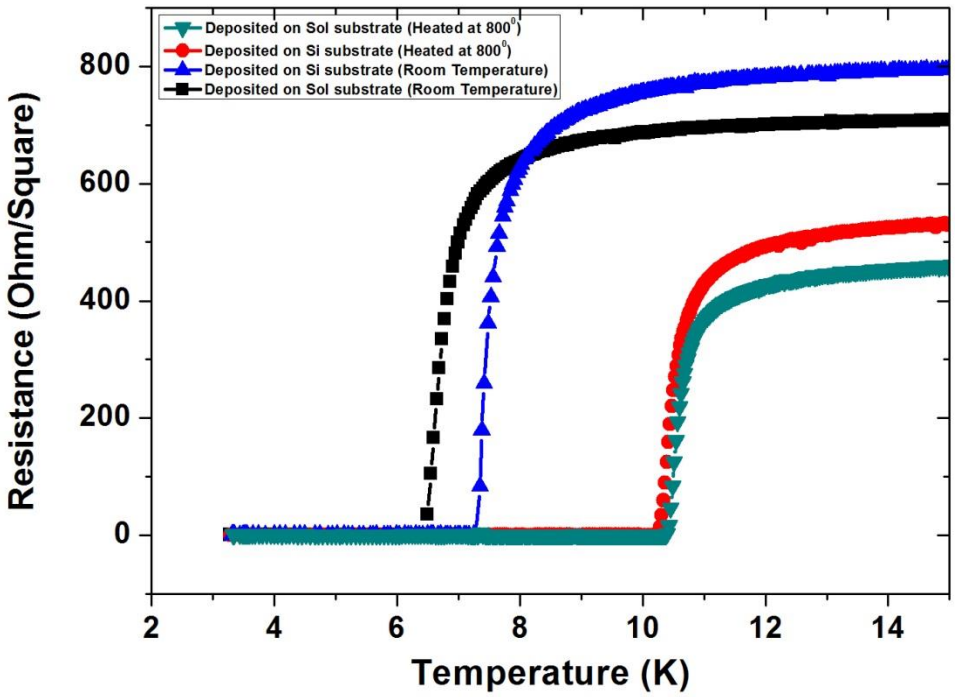

Fig. 4.10: Superconducting property of 5.5 nm thick NbTiN film deposited on silicon and silicon on insulator (SoI) substrates with and without heating.

4.2.6 Comparison with Theoretical Models

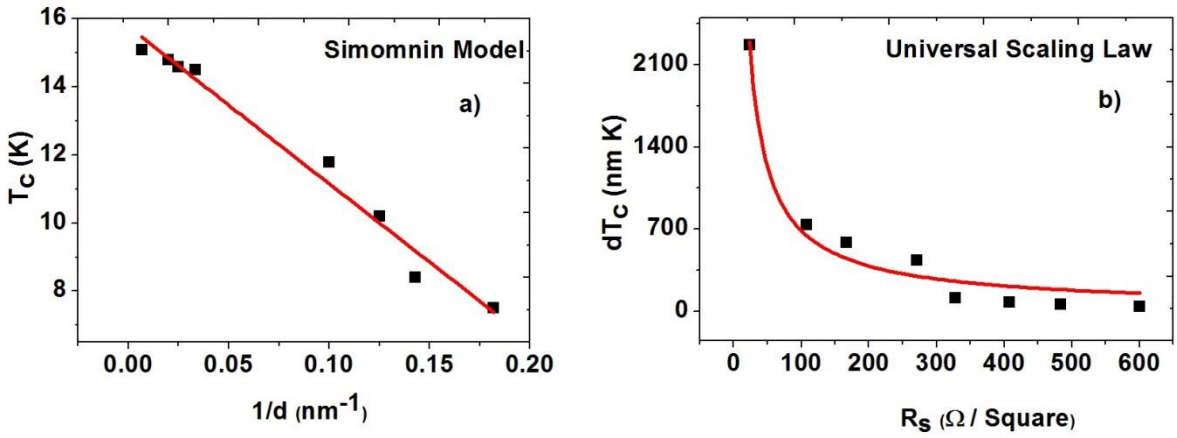

Fig. 4.11: Comparison of the superconducting properties of NbTiN films with theoretical models: (a) Simonin model fit with T_c versus 1/d curve [$T_c=T_{co}(1-d_c/d)$; T_{co}=15.76 K ± 0.3 and d_c = 2.92 ± 0.2 nm. (b) T_cd vs R_s curve with its fit to the universal scaling law proposed by Ivry [$T_cd=AR_s^{-B}$]; A= 31408 and B=0.83 ± 0.1.

To explore the correlation between the superconducting property and material parameters we have compared the T_c measurement data of the NbTiN films with the theoretical models described in Section 2.3.1 of Chapter 2. Fig. 4.11 (a) shows how the Simonin model fits with the T_c versus *1/d* data. All the data points fit with the model with the fitting parameter T_{co}=15.76 K ± 0.3 and d_c = 2.92 ± 0.2 nm. The fitted value of T_{co} is close to the bulk transition temperature of NbTiN reported in the literature (17 K). Fig. 4.11 (b) demonstrates how the universal scaling law proposed by Ivry *et al.* fits with the NbTiN measurement data. A= 31408 and B=0.83 ± 0.1 have been used as the optimised value of the fitting parameters to fit the scaling law with the NbTiN growth data. As mentioned by Ivry *et al.*, for polycrystalline materials, the free parameter B assumes a value which is expected to be less than one.

4.3 Process optimisation for Niobium Nitride growth

We emphasised on NbTiN as the refractory metal nitride material for optimisation since it has few advantages. Due to its polycrystalline nature, NbTiN is more forgiving towards lattice mismatched substrates (e.g. Silicon). Based on the optimised recipe for NbTiN, we have designed a recipe for NbN. In this process, we have sputtered from the Nb (instead of co-sputtering Nb & Ti) target introducing a fixed amount of nitrogen flow in the argon

plasma environment. As shown in Fig. 4.12, 5.5 nm thick NbN film deposited on silicon substrate shows a T_c of 7 K when the film is deposited at room temperature.

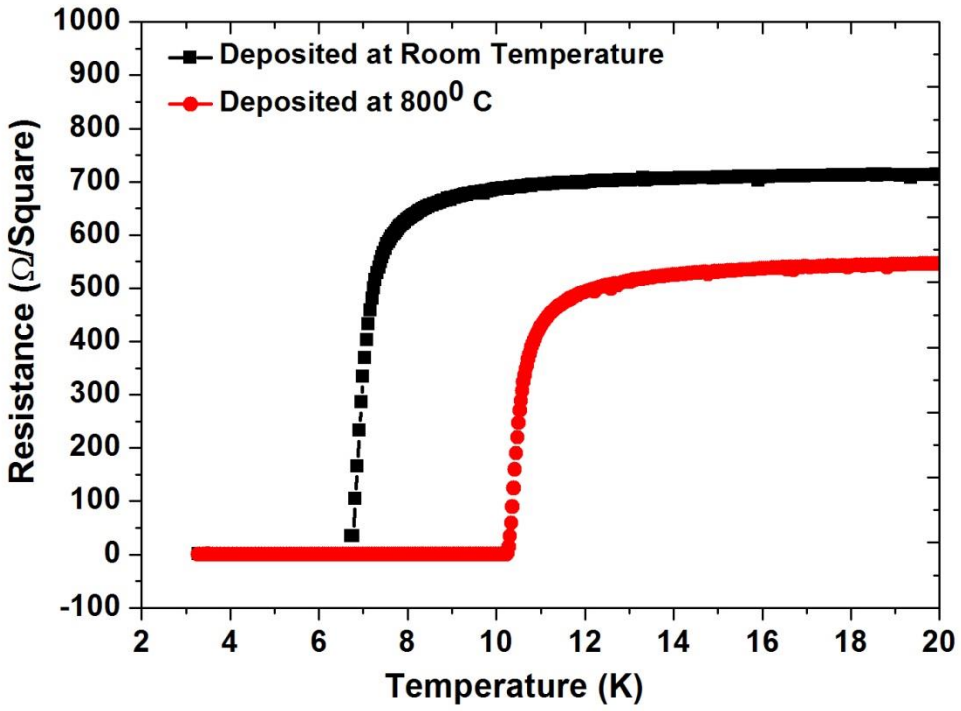

Fig. 4.12: *R* versus *T* curve of 5.5 nm thick NbN film grown on silicon substrate following the process described in table 3.2 .

Table 4.2: Optimised Recipe for NbN Deposition

Nb	0.9 A (356 W, 398 V)
Target Substrate Distance	100 mm
Substrate Holder Rotation	60 Rotation per minute
Ar Flow	18 sccm
N_2Flow	5 sccm
Throttle Position	75°
Chamber Pressure	0.14 Pa

4.4 High resolution scanning transmission electron microscopy analysis

We have analysed a specific selection of NbTiN films in high resolution TEM. Samples have been prepared for TEM analysis following the process described in Section 3.4 of Chapter 3. A JEOL ARM200cF microscope has been used for this analysis. Fig. 4.13 shows the TEM images (400 KX) of a 6.5 nm thick NbTiN film deposited at room temperature and at 800°C. The ordered structure of the crystalline silicon substrate is seen on the left hand side of the cross section image. Between the film and the substrate, there is a native oxide layer. The cross section also shows epitaxial growth of films with a smooth and sharp interface. We have measured the thickness of the layers at several locations for both the films. NbTiN and native oxide layers have a thickness of 6.7 nm (± 0.2 nm) and 2.5 nm (± 0.3 nm) respectively. Line profile analysis of digital micrograph software has been used to extract thickness of all the layers. As can be seen from the line profiles for the film deposited at room temperature and the film deposited on the heated substrate, the substrate heating does not affect film thickness or deposition rate.

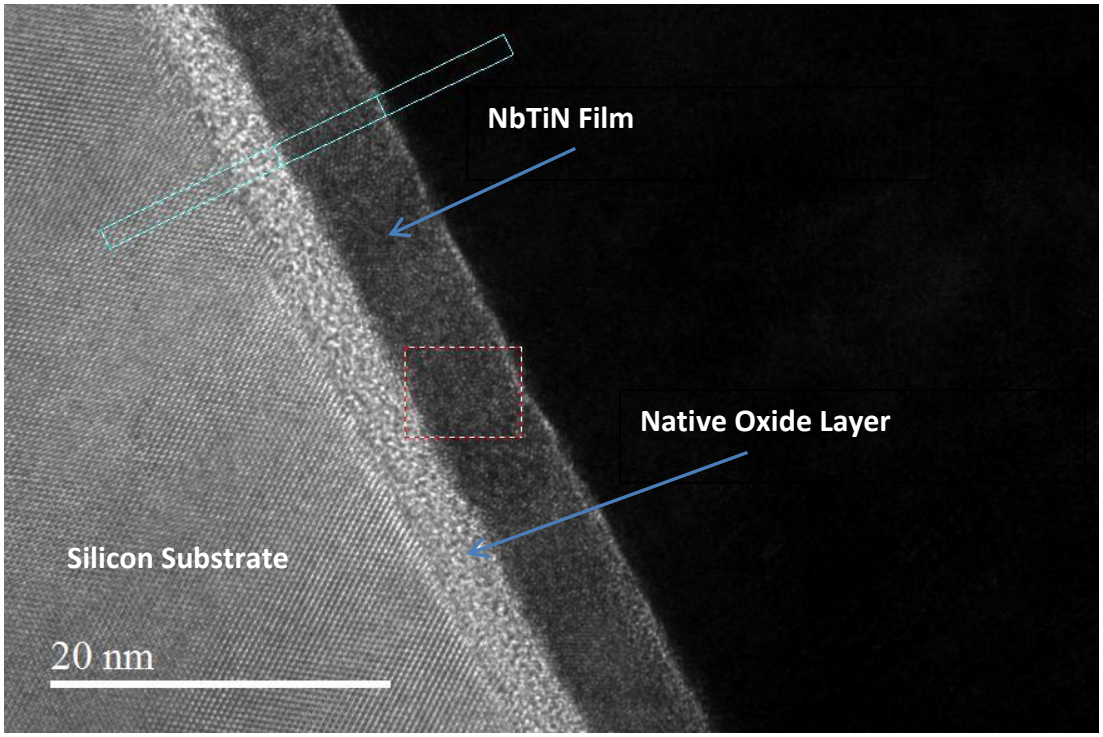

Fig .4.13 TEM cross-section image of a 6.5 nm thick NbTiN film deposited at room temperature.

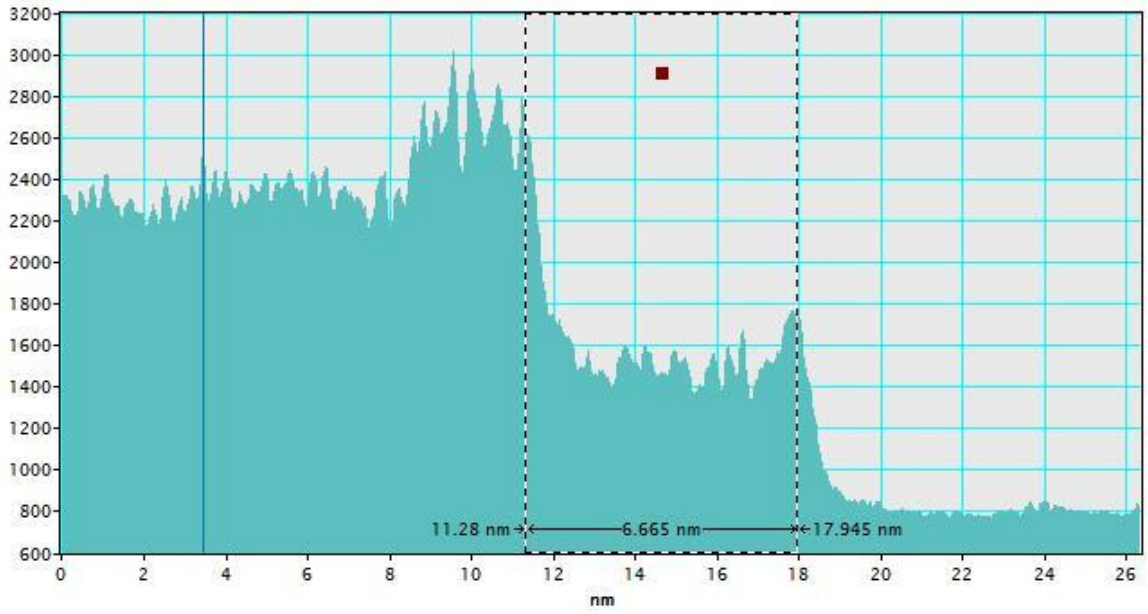

Fig. 4.14: Line profile analysis and thickness measurement of the room temperature deposited NbTiN film from image shown in the Fig. 4.13.

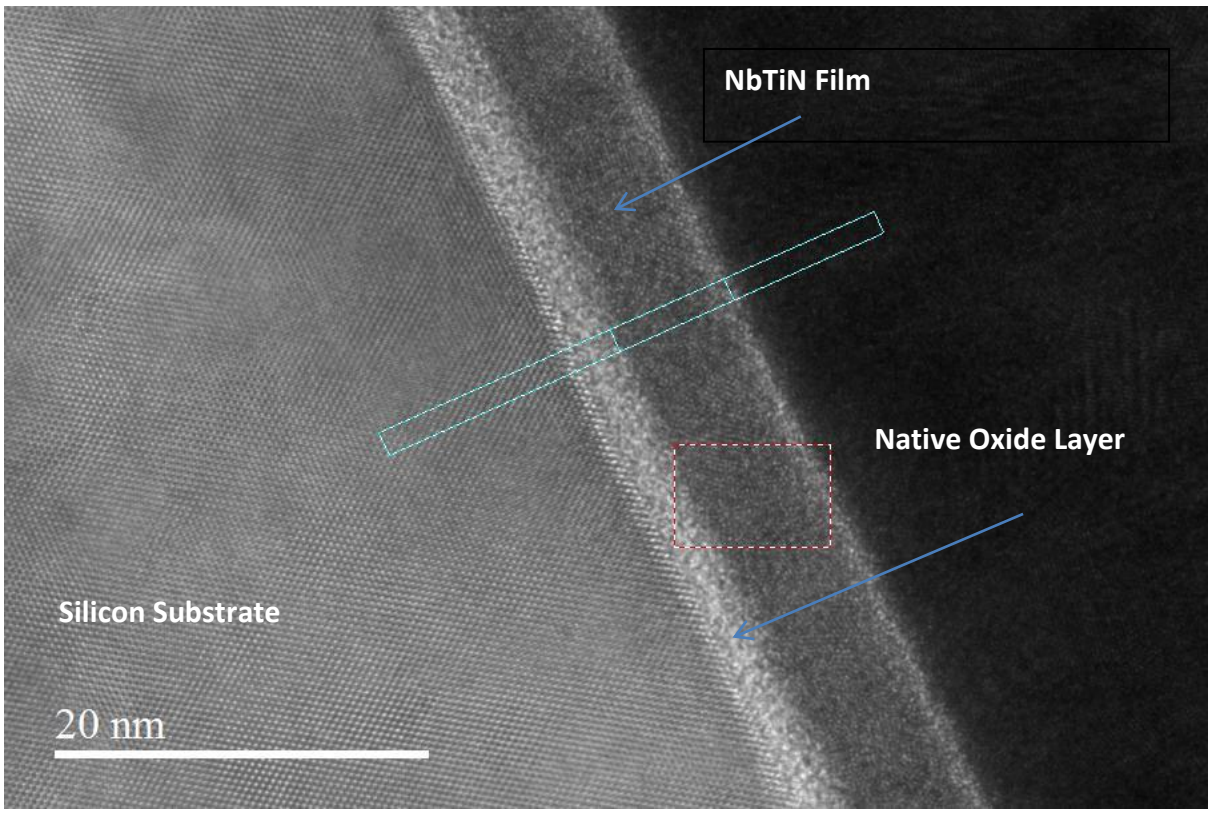

Fig. 4.15: TEM cross-section image of 6.5 nm thick NbTiN film deposited on the substrate heated at 800˚C.

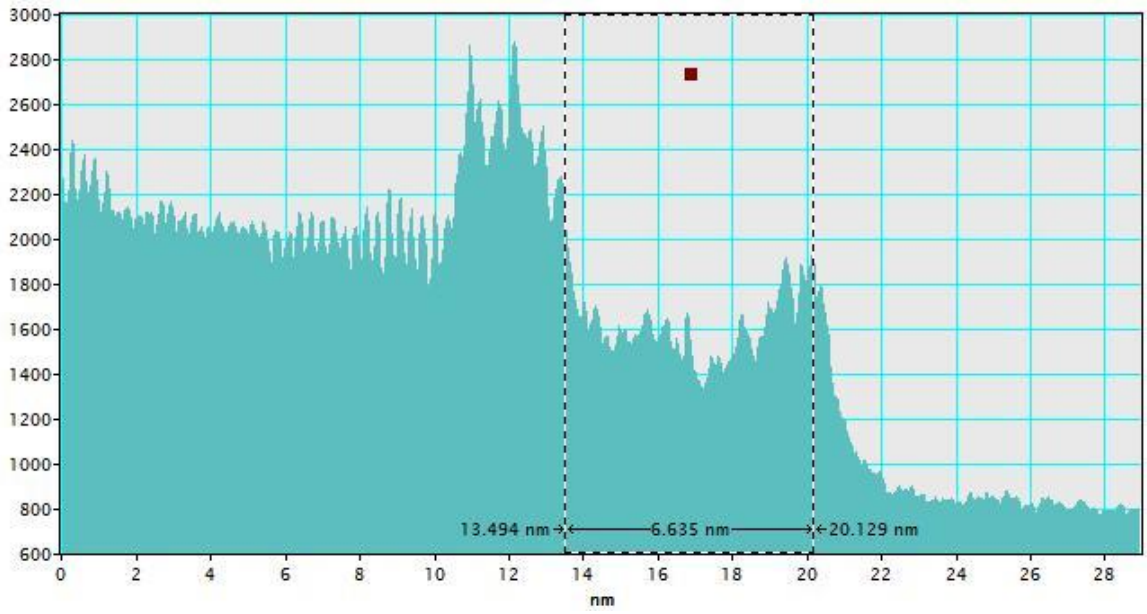

Fig. 4.16: Line profile analysis and thickness measurement of NbTiN film deposited on the heated substrate from image shown in the Fig. 4.15 .

The following figure shows the fast Fourier transform (FFT) views extracted from different selected areas of the image. The area selected is marked by a red square.

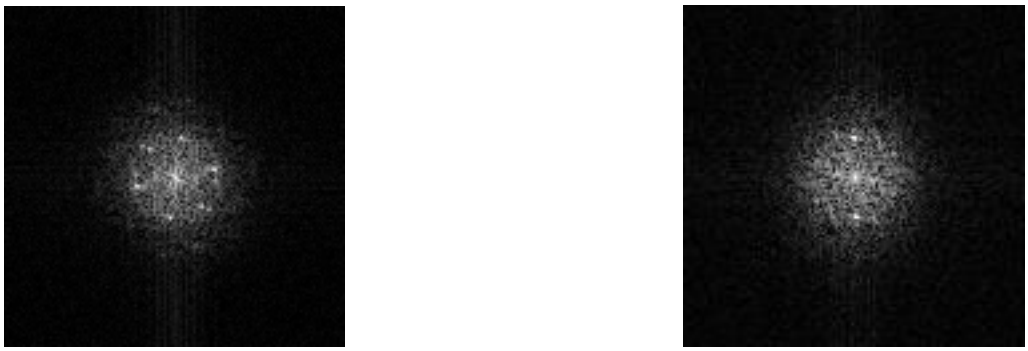

(a) (b)

Fig. 4.17: Fast Fourier transform (FFT) view extracted from the selected area of the TEM images. (a) FFT view of film deposited on the heated substrate. (b) FFT view of film deposited at room temperature (selected areas of the images are marked by the red square).

As we see from the FFT view of the films, substrate heating improves structural quality of the films. For the film deposited at room temperature, no proper ordering is observed in the FFT pattern. Hence, we can say that film deposited at room temperature is quite disordered.

However, for the film deposited on a heated substrate, we can see a clear improvement in structural ordering. This improved crystalline quality can explain the enhanced superconducting transition temperature of NbTiN films when deposited on a heated substrate.

We have also carried out stoichiometric analysis of the films using the energy dispersive x-ray spectrometer (EDX) detector attached inside the TEM. Fig. 4.18 shows the x-ray spectrum of the film deposited at room temperature. While passing through the sample, the electron beam may eject an electron from an inner shell of the sample atom, creating a hole where the electron was situated. An electron from an outer shell then fills the hole, and the difference in energy between the higher energy shell and the lower energy shell is released in the form of an x-ray photon. As the energy of the x-ray photon is characteristic of the difference in energy between the two shells, and of the atomic structure of the element from which it is emitted, this allows the elemental composition of the specimen to be measured.

As we see from the x-ray spectrum, there are strong peaks indicating the existence of silicon, copper (used as sample mount during TEM analysis), niobium and titanium. In EDX analysis, it is easier to detect heavier elements. On the other hand, it is very difficult to detect lighter elements (such as N or O or C) which may play a crucial role in controlling superconducting properties of the thin film samples. As nitrogen is a light element, it is hard to get a proper signal regarding nitrogen although we can locate its existence on the extreme left side of the spectrum. There is no indication of oxygen or carbon impurities in the spectrum. However, this may be due to the limitation of EDX analysis.

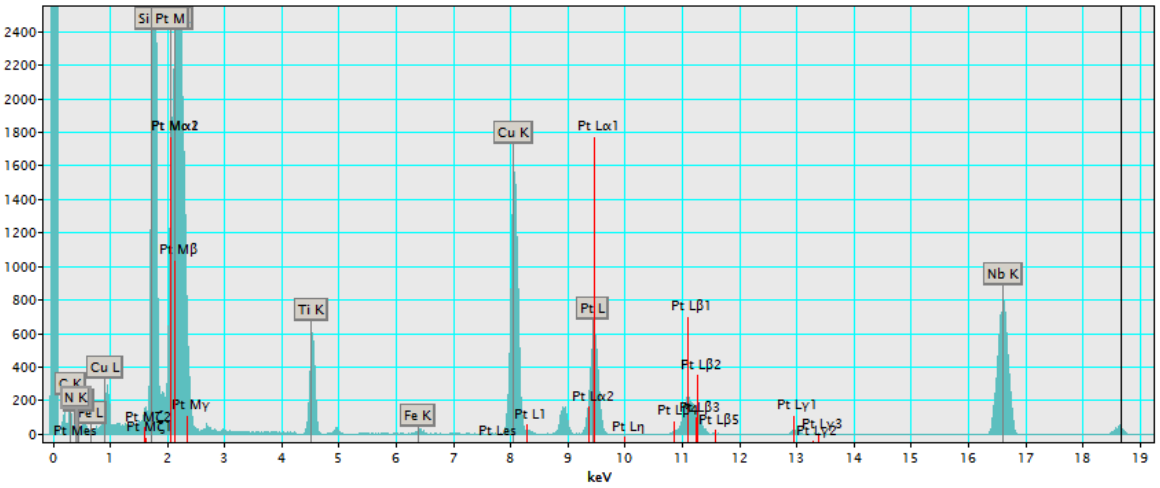

Fig. 4.18: Energy dispersive x-ray (EDX) spectrum recorded from the 6.5 nm thick NbTiN film during HRTEM analysis; the peaks of the spectrum indicate the existence of Nb, Ti, Pt (deposited as capping during the FIB cross-section) and Si (Substrate).

4.5 Measurement of optical constants for NbN & NbTiN

Accurate measurement of optical constants is crucial to the simulation of optical absorption in SNSPDs and is a key to integrating these devices with complex optical structures (such as cavities, nanoantennas and waveguides). The complex refractive index of NbN & NbTiN films (deposited following the optimised recipe) has been evaluated at room temperature using a J.A. Woollam & Co. VASE (variable angle spectroscopic ellipsometry) instrument. We used plasma-enhanced chemical vapour deposition (PECVD) to deposit a 390 nm thick layer of SiO_2 on several silicon substrates. 5.5 nm thick NbN & NbTiN films have been grown on the top of that at room temperature.

Spectral range of the VASE measurement is from a 270 nm to 2200 nm wavelength (with a wavelength resolution of 10 nm). Since both the films are optically absorbing all over the measurement range, it could be difficult to find a unique solution for both the film thickness and optical parameters due to strong correlations between them. This is why a transparent layer of SiO_2 has been added between the NbN or NbTiN films and substrates. The SiO_2 layer underneath the thin films helps to break parameter correlation between optical constants and film thickness by interference enhancement during the VASE measurement [8]. The data obtained from ellipsometric measurement has been modelled with a combination of several Lorentz oscillators. In the following figures, we have shown refractive index (n) and extinction co-efficient (k) measured from 5.5 nm thick NbN and NbTiN films. It can be clearly seen that NbTiN film has a higher extinction co-efficient

(~10% higher at 1550 nm) than that of NbN film. In a previous study, Anant *et al.* have reported optical constants of 12 nm thick NbN film [9]. Their measured values of *n* & *k* at 1550 nm were 5.23 and 5.82, which is ~1.5 times higher than our measured value (4.22 and 3.50). This higher value might be due to thicker films they used for VASE measurements.

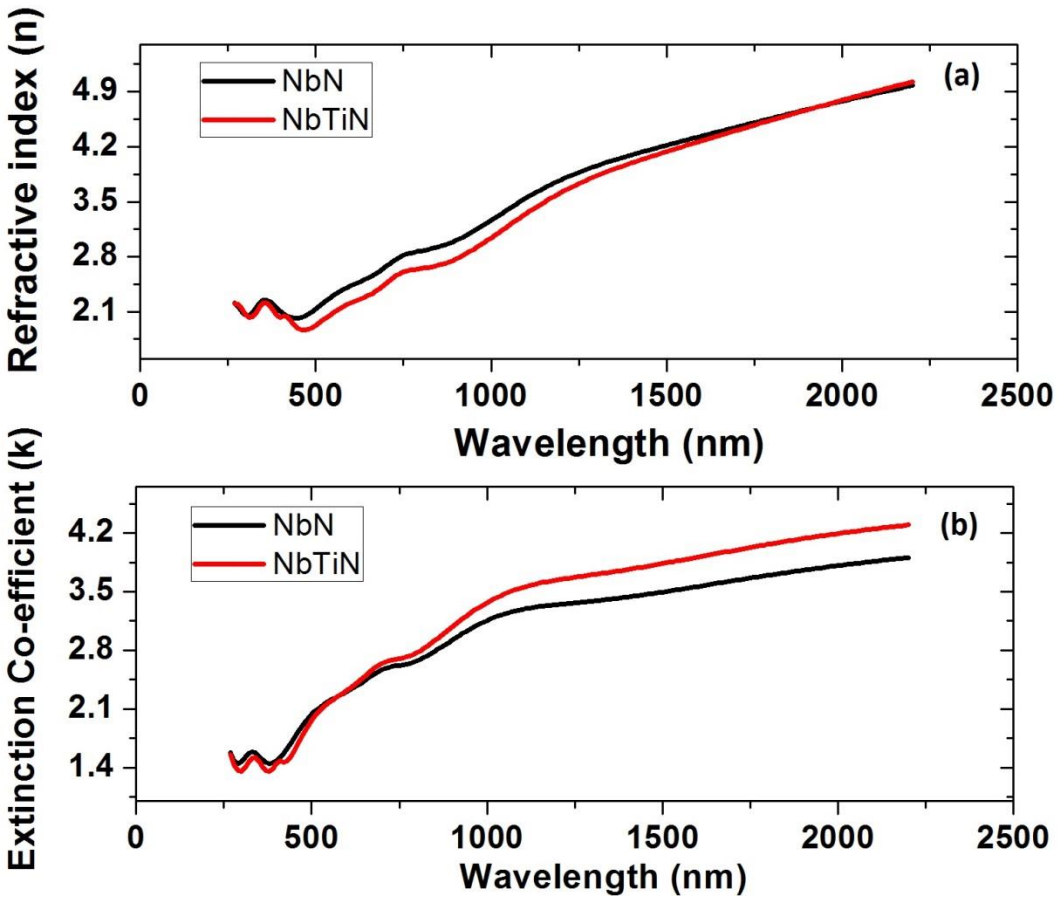

Fig. 4.19: Complex refractive index measurement of 5.5 nm thick NbTiN and NbN films using variable angle spectroscopic ellipsometry (VASE) (Both the films have been grown at room temperature on the silicon substrate).

4.6 Device fabrication[5]

The NbTiN films optimised in this chapter have been used for multi-pixel SNSPD array fabrication by Dr Alessandro Casaburi. Fig. 4.20 demonstrates a 4 pixel array (60 X 60 um^2) fabricated based on NbTiN film being deposited following the optimised recipe described in Table 4.1. 7 nm thick films were deposited on Si/SiO_2 based DBR substrates at room temperature for device fabrication. After fabrication, the device shows a T_c of 8 K. Fig. 4.20 (b) shows current versus voltage characteristic curves of all the four pixels measured at 3.6 K. It can be seen that one pixel has a critical current (I_c) of 44 µA while others show I_c between 50-54 µA. At 1550 nm, the best performing pixel has shown 35% system detection efficiency at 1 kHz dark count rate.

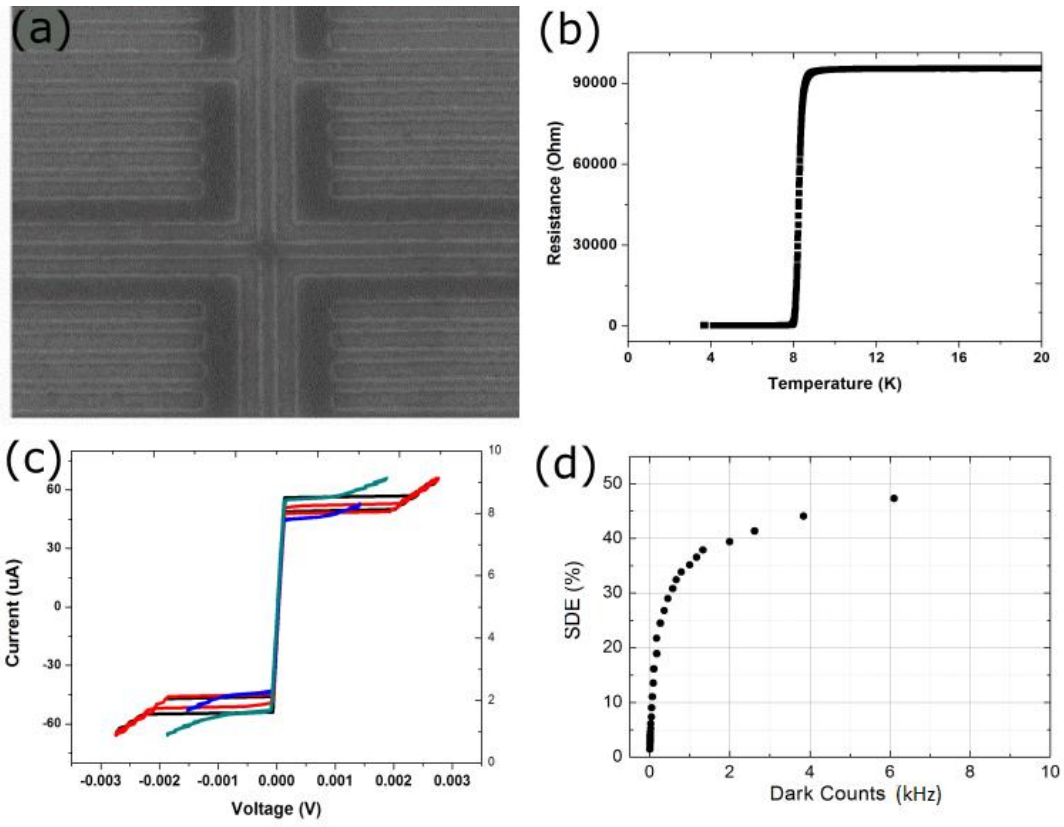

Fig. 4.20: Superconducting device fabrication based on the films grown following the optimised process described in this chapter: (a) SEM image of a 4 pixel array (60 X 60 μm^2) fabricated based on 7 nm thick NbTiN film. (b) *R(T)* curve of the device indicating a T_c of 8 K (c) Current-Voltage curves of all the four pixels measured at 3.6 K. (d) System Detection Efficiency versus dark counts measured at 1550 nm.

[5] **SNSPD device fabrication based on NbTiN thin film and its characterisation has been performed by Dr. Alessandro Casaburi.**

4.7 Summary

In this chapter, we have reported the growth and optimisation of refractory metal nitrides with an emphasis on NbTiN. Following the optimised process, a T_c of 7.2 K has been achieved for a 5.5 nm thick NbTiN film grown on a silicon substrate. When we heat the substrate up to 800°C, a NbTiN film with the same thickness shows a transition temperature of 10.4 K. Higher T_c and a lower sheet resistance of the films grown on the heated substrate indicate that films deposited at higher temperatures have larger grains and better crystalline structures. Comparison of T_c measurement data with the theoretical models (Ivry and Simonin) indicates polycrystalline nature of NbTiN films. HRTEM analysis shows that film thickness or deposition rate is independent of substrate temperature and the structural property of the thin films improves with substrate heating. Elemental mapping using EDX analysis confirms that composition of the films consists of Nb, Ti and N_2 as expected.

References

[1] G. N. Gol'tsman, O. Okunev, G. Chulkova, A. Lipatov, A. Semenov, K. Smirnov, B. Voronov, A. Dzardanov, C. Williams, and R. Sobolewski, "Picosecond superconducting single-photon optical detector," *Appl. Phys. Lett.*, vol. 79, no. 6, p. 705, Aug. 2001.

[2] C. M. Natarajan, M. G. Tanner, and R. H. Hadfield, "Superconducting nanowire single-photon detectors: physics and applications," *Supercond. Sci. Technol.*, vol. 25, no. 6, p. 63001, Jun. 2012.

[3] P. Yagoubov, G. Gol'tsman, B. Voronov, L. Seidman, V. Siomash, and S. Cherednichenko, "THE BANDWIDTH OF HEB MIXERS EMPLOYING ULTRATHIN NbN FILMS ON SAPPHIRE SUBSTRATE," Proc. of the 7th Int. Symp. on Space Terahertz Tech, pp. 290–302, March 1996.

[4] T. Matsunaga, H. Maezawa, and T. Noguchi, "Characterization of NbTiN thin films prepared by reactive DC-magnetron sputtering," *IEEE Trans. Appiled Supercond.*, vol. 13, no. 2, pp. 3284–3287, Jun. 2003.

[5] F. Marsili, D. Bitauld, A. Fiore, A. Gaggero, F. Mattioli, R. Leoni, M. Benkahoul, and F. Lévy, "High efficiency NbN nanowire superconducting single photon detectors fabricated on MgO substrates from a low temperature process," *Opt. Express*, vol. 16, no. 5, p. 3191, 2008.

[6] J. F. Vaneldik, K. L. Westra, D. Routledge, and M. J. Brett, "Target hysteresis and film properties of sputtered NbN," *J. Phys. D. Appl. Phys.*, vol. 22, no. 11, pp. 1788–1790, Nov. 1989.

[7] D. M. Glowacka, D. J. Goldie, S. Withington, H. Muhammad, and G. Yassin, "Development of a NbN Deposition Process for Superconducting Quantum Sensors," Jan. 2014.

[8] J. N. Hilfiker, N. Singh, T. Tiwald, D. Convey, S. M. Smith, J. H. Baker, and H. G.

Tompkins, “Survey of methods to characterize thin absorbing films with Spectroscopic Ellipsometry,” *Thin Solid Films*, vol. 516, no. 22, pp. 7979–7989, 2008.

[9] V. Anant, “Engineering the optical properties of subwavelength devices and materials,” *P.hD Thesis*, Dept. of Electrical Engineering and Computer Science, Massachusetts Institute of Technology, U.S.A, 2007.

Chapter 5

Amorphous Superconducting Thin Films: Molybdenum Silicide (MoSi) and Molybdenum Germanium (MoGe)

The crystalline nature of NbN or NbTiN makes the substrate choice for SNSPD very limited, which sometimes restricts their range of applications. So, amorphous superconducting films like MoSi or MoGe can be very useful for superconducting detector applications. Amorphous films do not set strict requirements on substrate choice as there is no issue of lattice matching. This chapter describes the growth, characterisation and optimisation of amorphous MoSi and MoGe thin films deposited by co-sputtering in an Ar plasma environment (Sections 5.1 and 5.2). The correlation between superconducting transition temperature (T_c), sheet resistance (R_s) and thickness of the films has been compared to several theoretical models for disordered superconducting films (Section 5.3). Superconducting and optical properties of amorphous materials must be very sensitive to short (up to 1 nm) or medium-range order (~1-3 nm) in the atomic structure. Fluctuation electron microscopy (FEM) studies (an HRTEM analysis technique) showed that the films assumed an A15 like medium-range order. Electron energy loss spectroscopy (EELS) indicates that the film stoichiometry was close to $Mo_{83}Si_{17}$, which is consistent with reports that many other A15 structures with the nominal formula A_3B show a significant non-stoichiometry with A:B > 3:1 (Section 5.4). Optical properties from ultraviolet (270 nm) to infrared (2200 nm) wavelengths were measured via variable angle spectroscopic ellipsometry for 5 nm thick MoSi films and have been compared with the optical properties of polycrystalline NbN and NbTiN (Section 5.5).

5.1 Molybdenum Silicide deposition

Molybdenum silicide (MoSi) films have been grown on various substrates in the sputter deposition system (Chapter 3.1). We have co-sputtered from confocal molybdenum (Mo) and silicon (Si) targets in an argon plasma environment. The distance between the targets and the substrate is kept at 100 mm. The substrate holder has been rotated at a speed of 60 rotations per minute during the deposition for better uniformity of the film growth. At the beginning of each deposition cycle, 30 sccm of Argon was introduced into the process chamber keeping the throttle valve fixed at 80^o (setting the total chamber pressure at 0.2 Pa). Film growth has been initially optimised on a silicon substrate.

We have sputtered from the Mo target with a DC power supply at a constant current mode and silicon target with an impedance matched RF power supply. At first, the discharge current of the Mo target was fixed at a specific value. Then, the RF power of Si targets was varied keeping other deposition conditions unchanged to tune the composition of the MoSi films. Prior to each sample deposition, both the targets were pre-sputtered keeping the shutters closed for one minute to stabilise the deposition conditions. After that, the same process had been repeated at several fixed discharge current values for the Mo target, keeping other chamber parameters unchanged.

Fig. 5.1(a) summarises the variation of T_c of 20 nm thick MoSi films deposited on silicon substrates as a function of applied power at the Si target for several different Mo discharge currents. Deposition time was adjusted for each deposition cycle in such a way that the film thickness remains constant. All the depositions were carried out at room temperature. Fig. 1(b) shows the normalised resistance versus temperature curves for the 20 nm thick MoSi films deposited with a 0.3 A discharge current applied at a Mo target. Both the figures indicate that an optimal film composition has been achieved, with a T_c of 7.3 K (and an *RRR* of 0.95) for a 0.3 A Mo target discharge current and 125 W Si target RF power. Later on, the influence of other chamber variables (e.g. substrate holder rotation etc.) on film property was also checked, which indicates that these deposition parameters are optimum in terms of film quality. For this optimised growth condition, the film deposition rate was 0.122 nm/sec, meaning that 2 minutes and 45 seconds of deposition time was used to grow the 20 nm thick film.

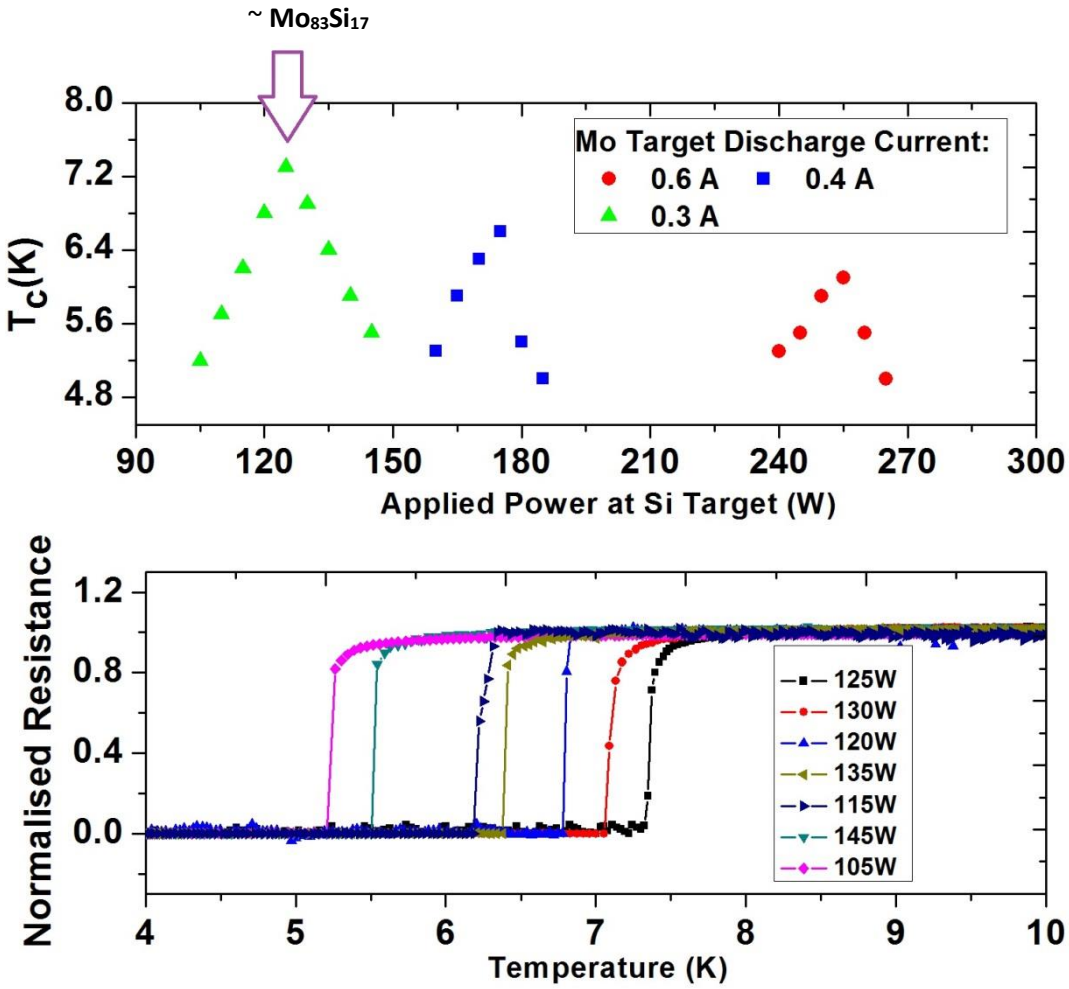

Fig. 5.1: MoSi growth optimisation. a) T_c of 20 nm thick MoSi films deposited on a silicon substrate as a function of power applied at the silicon target. b) Normalised Resistance versus Temperature Curve of 20 nm thick MoSi films deposited with a 0.3 A discharge current applied at Mo target of the deposition system.

The details of the optimised recipe for MoSi thin film deposition is as follows:

Table 5.1 Optimised Recipe for MoSi growth

Mo	0.3 A (105 W, 400 V)
Si	125 W
Target Substrate Distance	100 mm
Substrate Holder Rotation	60 Rotation per minute
Ar Flow	30 sccm
Throttle Position	80°
Chamber Pressure	0.2 Pa

As discussed in the Section 2.5 of Chapter 2, few nm thick ultrathin (<10 nm) superconducting films are required for SNSPD fabrication. Otherwise, superconducting detectors will not be able to generate an output signal upon photon absorption. Fig. 5.2 shows the variation in the superconducting transition of MoSi films with film thickness (Here, all the films have been grown following the optimised recipe described in Table 5.1). A 5.5 K T_c (*RRR*= 0.8) is obtained from a 5 nm thick film. *RRR* increases with film thickness. Thinner films also have a greater sheet resistance as expected.

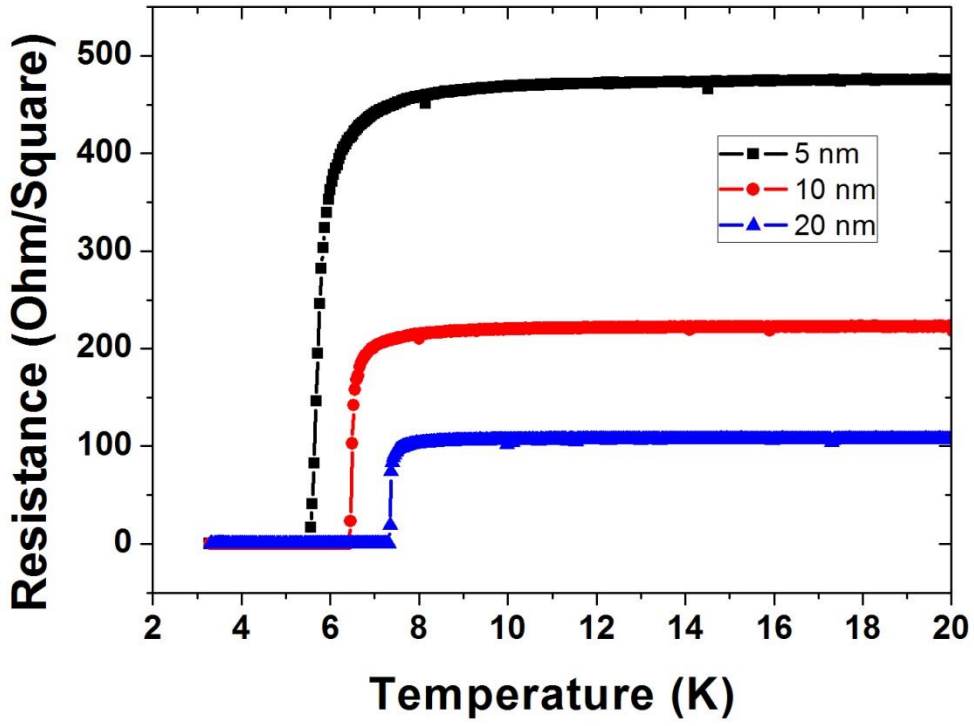

Fig. 5.2: *R* versus *T* curve of MoSi film with three different thicknesses deposited at room temperature on a silicon substrate.

5.2 Optimisation of Molybdenum Germanium thin film growth

MoGe is another amorphous TM based superconducting material which can be used for SNSPD fabrication. Deposition of MoGe superconducting thin films has also been optimised following a similar process as MoSi. MoGe films have been co-sputtered from confocal Mo and Ge targets in the argon plasma environment of the UHV deposition system. The distance between the targets and the substrate is kept at 100 mm. We introduced 30 sccm of argon in the process chamber keeping the butterfly throttle valve fixed at 80° (total chamber pressure: 0.2 Pa). Molybdenum target have been sputtered with a DC power supply at a constant current mode and germanium target with an impedance that matched the RF power supply. The discharge current of Mo target was fixed at a specific value. Then, the RF power of the Ge target has been varied while other deposition conditions are kept unchanged to tune the composition of MoGe films.

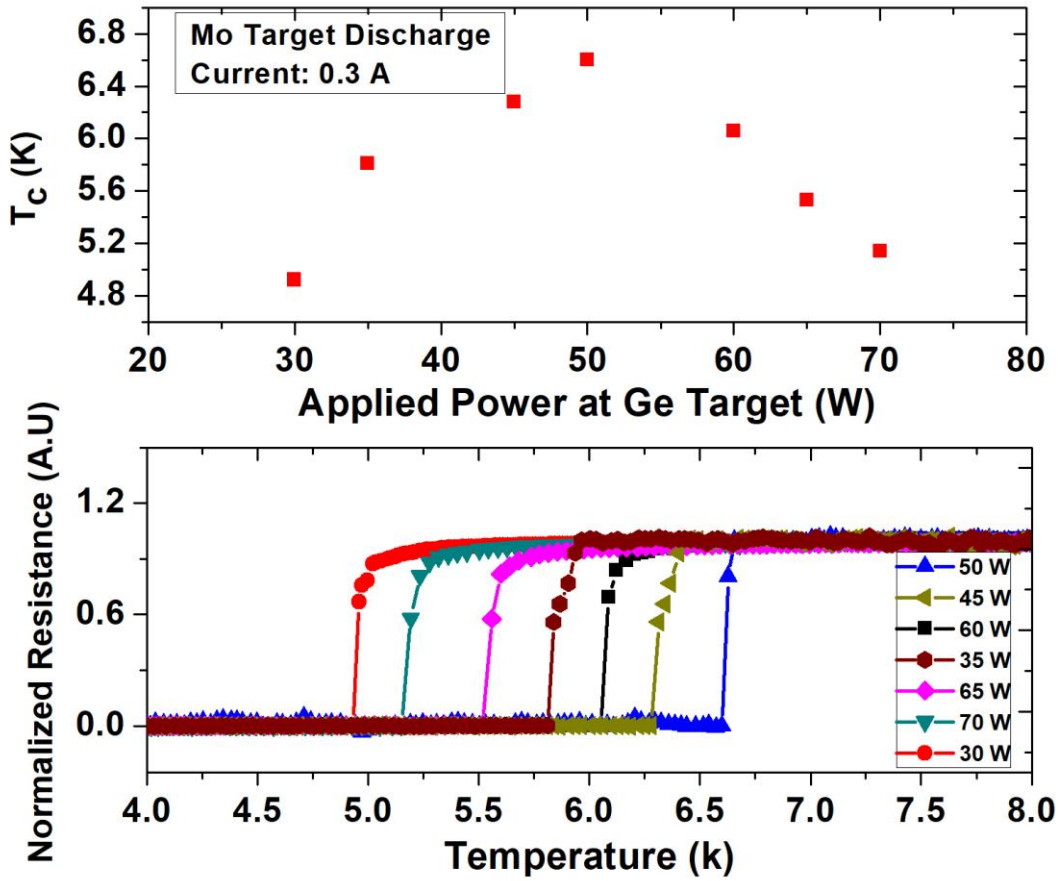

Fig. 5.3: Optimisation of MoGe thin film growth: a) T_c of 30 nm thick MoGe films deposited on a silicon substrate as a function of power applied at the germenium target. b) Normalised Resistance versus Temperature Curve of 30 nm thick MoSi films deposited with a 0.3 A discharge current applied at Mo target of the deposition system.

.

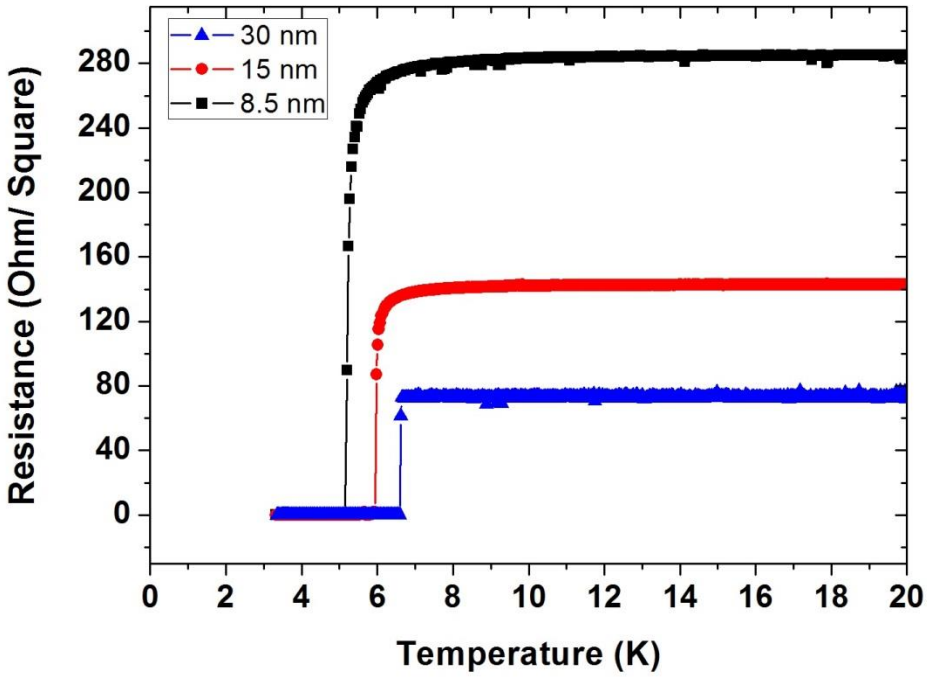

Fig. 5.4: *R* versus *T* curve of MoGe films with three different thicknesses deposited at room temperature.

The above Fig. 5.3 shows the normalised resistance versus temperature curve of 30 nm thick MoGe film deposited on a silicon substrate at room temperature for various values of RF power applied at the Ge target. 2 minutes and 40 seconds (160 seconds) of deposition time was used when we deposited with a 0.3 A of discharge current at the Mo target. Before deposition, both Mo and Ge targets were pre-sputtered for one minute with the shutter closed. Fig. 5.3 shows we get a T_c of 6.6 K (with *RRR* 0.95) if we deposit a 30 nm thick MoGe film with a 0.3 A discharge current at a Mo target and 50 W RF power at a Ge target.

Table 5.2 Optimised Recipe for MoGe Growth

Mo	0.3 A (105 W, 400 V)
Ge	50 W
Target Substrate Distance	100 mm
Substrate Holder Rotation	60 Rotations per minute
Ar Flow	30 sccm
Throttle Position	80°
Chamber Pressure	0.2 Pa

Fig. 5.4 demonstrates how superconducting properties of MoGe films degrade with film thickness. If we compare with MoSi, we can clearly see that the T_c of MoGe films decreases much more sharply with thickness. From an 8 nm thick MoGe film we have measured a 5.2 K T_c whereas even for a 5 nm thick MoSi film a 5.5 K T_c has been achieved. Hence, MoSi is more advantageous as a base material for high performance SNSPDs which can be operated at a temperature of >2 K using relatively cheap, less complex closed-cycle cryogenic systems.

5.3 Variation of transition temperature with film thickness and comparison with theoretical models

To better understand the interplay between superconducting properties and empirical material parameters, a variation of the T_c of MoSi films with sheet resistance and thickness has been compared with the theoretical models (Section 2.5, Chapter 2).

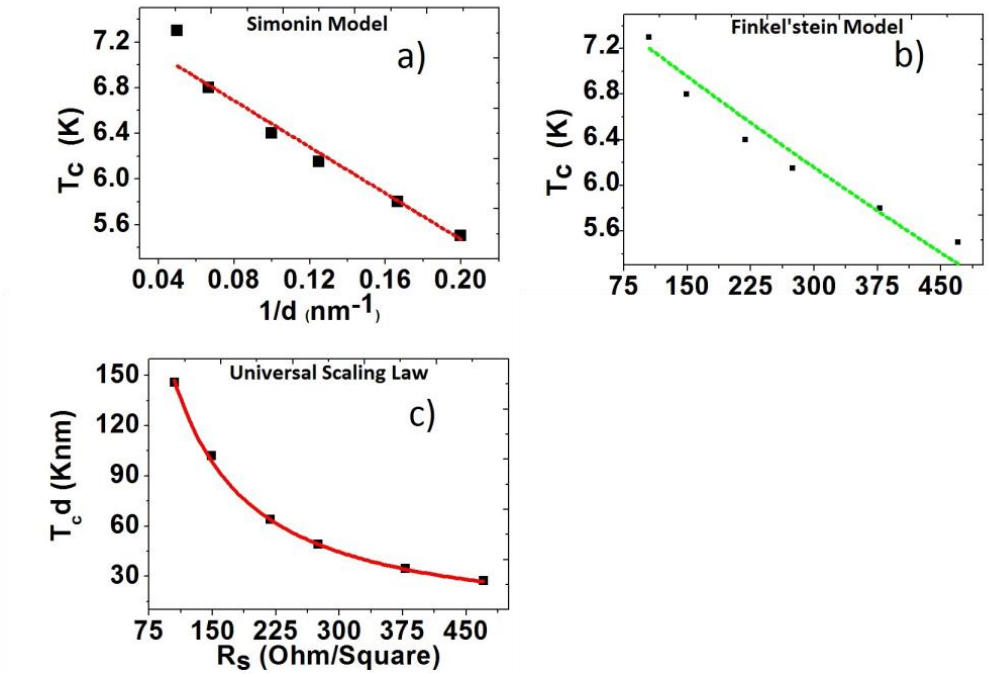

Fig. 5.5: Variation of superconducting transition temperature with film thickness and comparison with theoretical models: a) Simonin model fit for T_c versus 1/d curve [$T_c=Tco(1-d_c/d)$] ;T_{co}=7.5±0.2 K & d_c=1.46±0.2 nm b) T_c versus R_s curve and its fit with Finkel'stein model [$\frac{T_c}{T_{co}}=\exp(\gamma)[\frac{1+X}{1-X}]^{1/\sqrt{2r}}$]; T_{co}=7.8 K & γ=7.66±0.1 c) T_cd vs R_s curve with its fit to the universal scaling law proposed by Ivry [$T_cd=AR_s^{-B}$] ; A=29436 & B=1.14 ±0.1.

Fig. 5.5(a) shows T_c vs 1/d plot and how equation 2.11 (Simonin Model) is fitted with the data [1]. The data point related to 20 nm thick film (thickest of the set) deviates from the fit. The rest of the data set fits well with a least squares fit using T_{co}=7.5±0.2 K and d_c = 1.46 ± 0.2 nm. These values are in good agreement with literature. Critical thickness is related to BCS interaction potential by $d_c = 2a/N(0)V_{BCS}$. From Osofsky *et al.*, we get for MoSi $N(0)V_{BCS}$= 0.086 and a ~0.06 nm. Hence, d_c ~1.4 nm [2].

In Fig. 5.5(b) we have compared the T_c vs R_s plot of the MoSi films we have grown with Finkel'stein model (equation 2.10) [3]. The fit was obtained by optimising T_{co} and γ. The T_c data fits in Finkel'stein model with T_{co}=7.8 K and γ= 7.66 ±0.1. Such a high value of fitting parameter γ is an indication of a strongly disordered film. (For amorphous MoGe, Graybeal *et al.* have reported a value of 8.2 for the same parameter [4].) This means that the suppression of superconductivity due to the fluctuation of Cooper pairs can be neglected because of the amorphous nature of the film.

From these values of T_{co} and γ we obtain a mean scattering time of τ= 4.61 X 10^{-16} sec (as we saw in the equation 2.10, $\gamma = Ln[\hbar/\tau T_{co} k_B]$). For the 5 nm thick MoSi film, the measured resistivity is 235.2 μΩ cm. Using this value of mean scattering time, we can estimate an electron density n_e=3.24 X 10^{22} /cm^3 ($\sigma = n_e(e^2/m_e)\tau$), diffusion constant D = 0.21 X 10^{-4} m^2/sec($D = \frac{\mu k_B T}{e}$) and a mean free path of 0.2 nm (assuming free electron mass equals the rest mass of the electron). The free electron density is about 10 times lower than that of the NbN reported in literature (for 6 nm NbN 1.26 X10^{23} /cm^3 [5]) as expected for MoSi. Ioffe-Regel parameters ($k_f l$) calculated based on a free electron model [$k_f l = \hbar(3\pi^2)^{\frac{2}{3}} n_e^{-\frac{1}{3}} (e^{-2}\rho_n^{-1})$] gives a value of 5.25, which is another indication of a homogeneously disordered film. However, our estimated value of $k_f l$ is slightly higher in comparison to the measurements of IR parameters which have been reported for strongly disordered films in literature (2.6 for 5 nm thick TiN [6]). This higher value may be due to inaccuracy in the approximation of electron density from our data fit (we have not measured it directly). Also, Graham *et al.* have shown that for some amorphous materials, a metal-insulator transition may be observed at a much higher value (around $k_f l$~ 5.2 for indium oxide) [7]. Instead of $k_f l$ ~ 1, they proposed $k_f l$~ π as the Ioffe-Regal criteria. We also note

in the following table that both the free electron concentration and Ioffe-Regel parameter show a slowly increasing trend with film thickness.

Table 5.3: Free Electron Concentration *n* , Ioffe-Regel parameter ($k_f l$) and T_c of MoSi film with four different thicknesses, *d*

d (nm)	T_c (k)	*n* (10^{22}/ cm^3)	$k_f l$
5	5.5	3.24	5.25
6	5.8	3.36	5.34
8	6.15	3.46	5.49
10	6.4	3.49	5.54

Although comparison of T_c versus R_s data with the Finkel'stein model has given realistic values for various physical parameters of MoSi films, this model was actually initially proposed for two-dimensional films (film thickness below the mean free path of the electron). For films having a thickness larger than their mean free path (which is the case here) it includes a correction factor in the expression on mean scattering time $\tau^* = (d/l)^2\tau$; for film thickness d=5 nm, assuming a mean free path of l= ~0.2 nm, we obtain τ =0.1844 X 10^{-16} sec and D=0.0084 X 10^{-4} m^2/sec. This value of the diffusion co-efficient is much smaller than the value reported in literature [8]. Therefore, we did not take into consideration the correction factor here. Extraction of selected physical parameters from alternate measurements and comparing them may be helpful for more accurate modelling.

Fig. 5.5 (c) depicts how the university scaling law (proposed by Ivry *et al.*) fits to the MoSi growth data [9]. Values of the fitting parameters are A=29435 and B= 1.14±0.1. As discussed by Ivry *et al.*, for amorphous films, B is higher than one.

One can see a clear and accurate trend if we plot $T_c d$ as a function of R_s (Fig. 5.5 (c)). For amorphous films, dependence on sheet resistance dominates over the thickness dependence. That is why the data points corresponding to the thickest film deviates from the Simonin model fit. At the same time, the Finkel'stein model fits quantitatively with all the data points. Universal scaling law takes into consideration both the effects of sheet resistance and thickness. Hence, it provides a far more accurate fit for our MoSi data. A higher value of the fitting parameter B also indicates the amorphous nature of the film and the dominating sheet resistance dependence.

5.4 Influence of variations in deposition conditions and choice of substrate

We have also explored the effects of various small modifications in the deposition conditions on the superconducting properties of amorphous MoSi films. Bosworth *et al*. showed that substrate cooling may promote amorphous character in superconducting MoSi films and hence enhance their superconducting characteristics [10]. We have cooled a silicon substrate under the liquid nitrogen trap (77 K) of our deposition system for three hours and then immediately deposited a 10 nm thick MoSi film on it. Fig. 5.6 shows that the film deposited on the cooled substrate has a sheet resistance slightly lower than that of the film deposited at room temperature. The film deposited on the cooled substrate has a slightly lower T_c (~0.2K < room temperature deposited film) however the film deposited at a low temperature shows a sharper superconducting transition (transition width of 55 mK) in comparison to the film grown at room temperature (376 mK transition width). This narrower transition can be explained by an improvement in film homogeneity due to deposition on a liquid nitrogen cooled substrate. In our chamber, the target-substrate distance is large (100 mm). So, there is unlikely to be significant radiative heating of the substrate holder during deposition. Hence, even the films we deposited at room temperature are amorphous. (Later on, we checked this fact using TEM observation.)

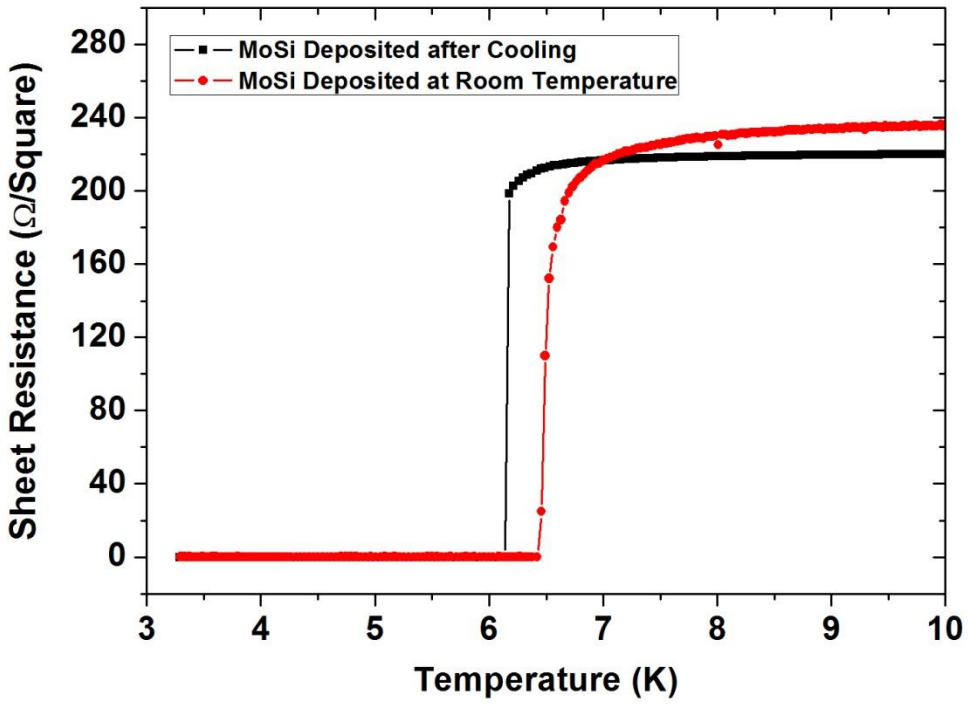

Fig. 5.6: Effect of substrate cooling on the superconducting transition in MoSi Films: *R* vs *T* curves of 10 nm thick MoSi films deposited at room temperature and deposited on a liquid N_2 cooled substrate.

We have also investigated the effect of various substrates on the superconducting properties of MoSi films. 10 nm thick MoSi films were grown on 3 different types of substrates following the same optimised deposition parameters. Resulting superconducting properties are shown in Table 5.4.

Table 5.4: Superconducting Transition Temperature and RRR of 10 nm thick MoSi Film grown on various substrates

Substrates	T_c	*RRR*
Silicon	6.4	0.8
SOI	6.32	0.83
HF-Treated Silicon	6.22	0.85

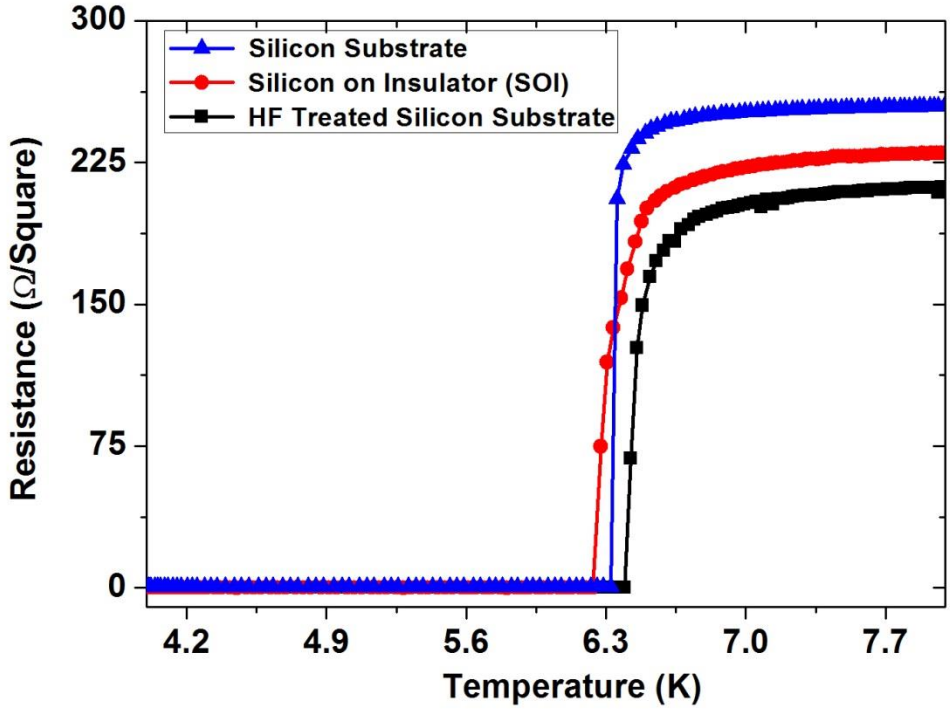

Fig. 5.7: *R(T)* curve of 10 nm thick MoSi films grown on three different kinds of substrate.

As we have discussed in Section 3.1 of Chapter 3, we can accommodate wafer sizes up to a 6 inch (150 mm) diameter in the substrate holder of our sputter deposition system. So, it is possible to deposit superconducting thin films on large area wafers for the fabrication of large area focal plane arrays or complex superconducting quantum photonic circuits. The substrate carrier has an adapter mount which can accommodate nine 10 mm x 10 mm or 15 mm x 15 mm substrates (as shown in Fig. 5.8 (a)) in each deposition cycle. To determine how the superconducting properties change if we deposit a thin film on a large area wafer, we deposited 10 nm MoSi films on all the nine positions of the substrate holder and examined the T_c of three films which were positioned diagonally across the holder. From Fig. 5.8 (b) it is evident that the T_c of these three films differs by only ± 0.15 K with a mean T_c of 6.3 K. It indicates that large area deposition in our system is quite uniform.

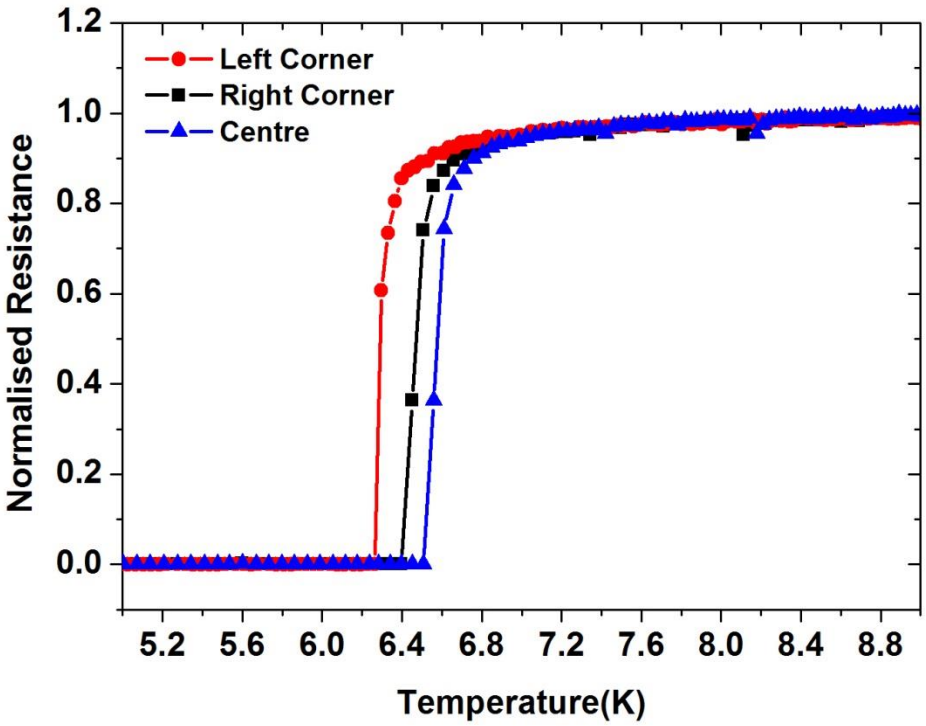

(a)

(b)

Fig. 5.8: Large area deposition. (a) Normalised resistance versus temperature curve of three 10 nm thick MoSi films which were positioned diagonally across the substrate holder. (b) Photograph of substrate holder with the adapter.

During the process of optimisation, to prevent possible degradation of MoSi films due to surface oxidation, a thin capping layer of amorphous silicon (~ 4 nm) was deposited on the

top of the film. During the device fabrication process, environmental contact may affect the superconducting property of the films by surface oxidation. For this reason, we have used a protective silicon capping layer which was deposited on the MoSi film in the same chamber without breaking the vacuum.

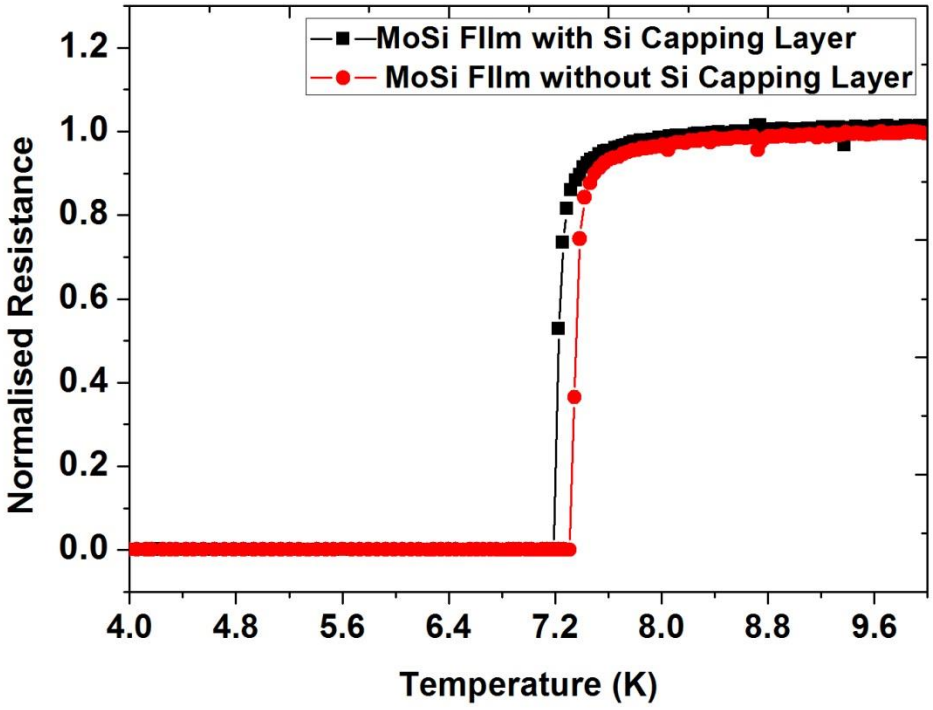

Fig. 5.9: Effect of Silicon Capping Layer: Normalised Resistance versus Temperature curve of 20 nm thick MoSi films (One film with a silicon capping layer and the other film without any capping layer).

As we can observe from the above figure, the T_c of a 20 nm thick MoSi film with an Si capping layer is almost the same as that of the MoSi film without any Si capping layer. They differ by 0.1 K, which may be ignorable for SNSPD applications. Later on, during device fabrication, we checked that the SNSPD devices that were fabricated from MoSi films without any protective capping layer do not work at all due to the degradation in superconducting properties during fabrication and atmospheric exposure.

From the measurements carried out in this section, it can be seen that slight modification of optimised deposition conditions (e.g. substrate cooling or HF treatment of substrates) may

measurably affect superconducting properties of amorphous films in various ways. It can be predicted that these small changes in the deposition process influence the short range structural ordering of the amorphous film. Based on resistivity measurements, Bieger *et al*. have shown that the superconducting properties of amorphous materials are quite sensitive to short range order [11]. That is why it is crucial to carry out a proper investigation of the local structural ordering of amorphous MoSi films although preferably with more direct methods. In the crystalline state, Mo_3Si assumes an A15 structure and has a very low bulk T_c (~1.3 K) [12]. Lattice disorder enhances its superconducting properties [13], [14]. Amorphous MoSi has a bulk T_c of around 7.5 K [15]. The effect of material properties on the superconducting transition temperature can be described by McMillan's Parameter (given by $\lambda_M = \frac{N(0)<J^2>}{M<w^2>}$; where *N(0)* is the density of states at the Fermi level, $< w^2 >$ denotes average phonon frequency, *M* is ion mass and $< J^2 >$ is the average electron-phonon coupling matrix) [16]. McMillan proposed the following numerical relationship between T_c and λ based on generalised BCS theory.

$$T_c = \frac{\theta_D}{1.45} \exp\left[-\frac{1.04(1+\lambda_M)}{\lambda_M - \mu^*(1+0.62\lambda_M)}\right] \qquad (5.1)$$

A15 structured crystalline alloys like Mo_3Si or Mo_3Ge which have very low bulk T_c have a low density of states. Lattice disorder increases T_c due to an enhancement in *N(0)* and the weakening of the phonon mode. The electron-phonon coupling matrix $< J^2 >$ is a function of structure factor. Hence, any modification in short range structural order or 'amorphous' nature will change it and influence the McMillan's parameter and the superconducting properties.

5.5 High resolution scanning transmission electron microscopy analysis of structure and composition[6]

We have analysed the atomic structure and composition of MoSi films with the help of advanced high resolution transmission electron microscopy (TEM) techniques. A standard

[6] **High resolution scanning transmission electron microscopy analysis has been carried out in collaboration with Professor Ian MacLaren and Alastiar Doye (School of Physics and Astronomy, University of Glasgow).**

focussed ion beam (FIB) technique has been used to prepare samples for TEM analysis. The following figure shows a TEM image (600 KX magnified) of a 5.5 nm thick MoSi film without a Si capping layer.

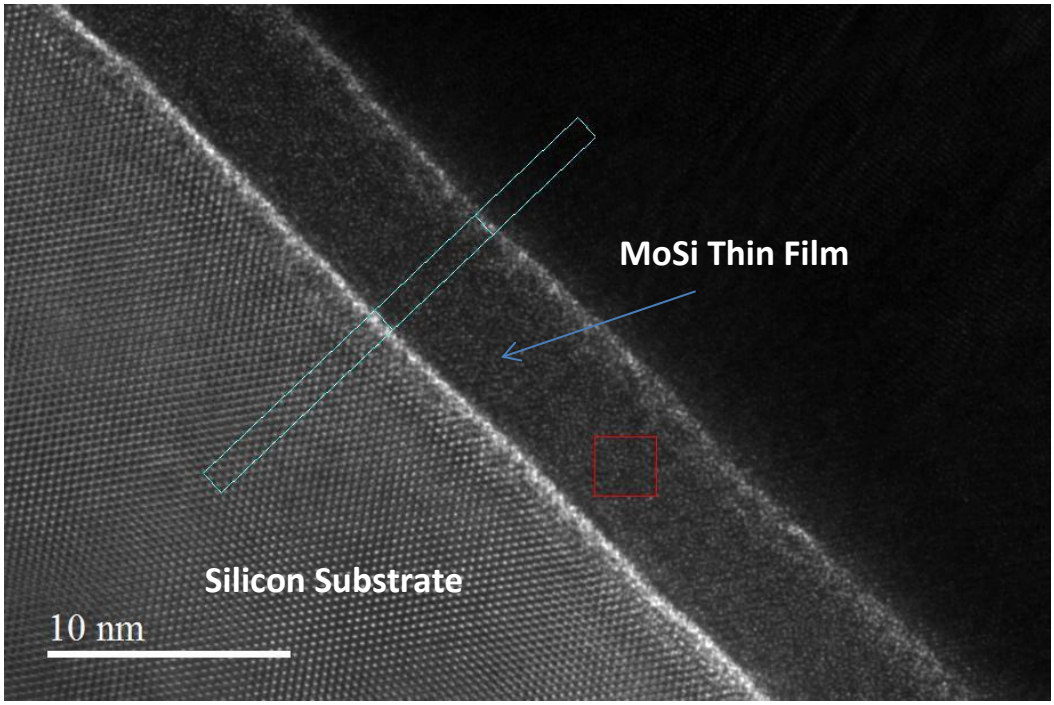

Fig. 5.10: Cross section of 5.5 thick MoSi Film without any Si cap.

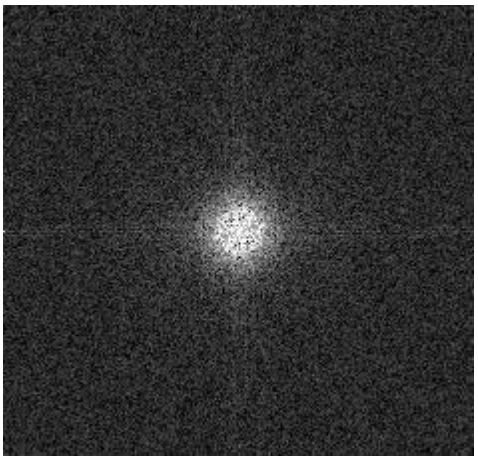

Fig. 5.11: FFT View of the selected area of the film (marked by a red line in Fig. 5.10).

The ordered structure of crystalline silicon substrate is seen in the lower left hand region of the image. Since it is high resistivity silicon, the substrate does not have a native oxide layer. The cross section also shows the epitaxial growth of films with a flat surface and sharp interface. The FFT view extracted from a selected area of the film (marked by the red square in the figure) shows an amorphous ring. Since this FFT view was extracted from the TEM image, with the help of an image processing software package, it looks very noisy. We have measured film thickness at several locations by using line profile analysis. Figure 5.12 shows the line profile extracted from the blue coloured rectangular box marked in the figure 5.10. It seems our deposition is quite uniform and thickness of the film measured from line profile analysis is 5.5 ± 0.2 nm.

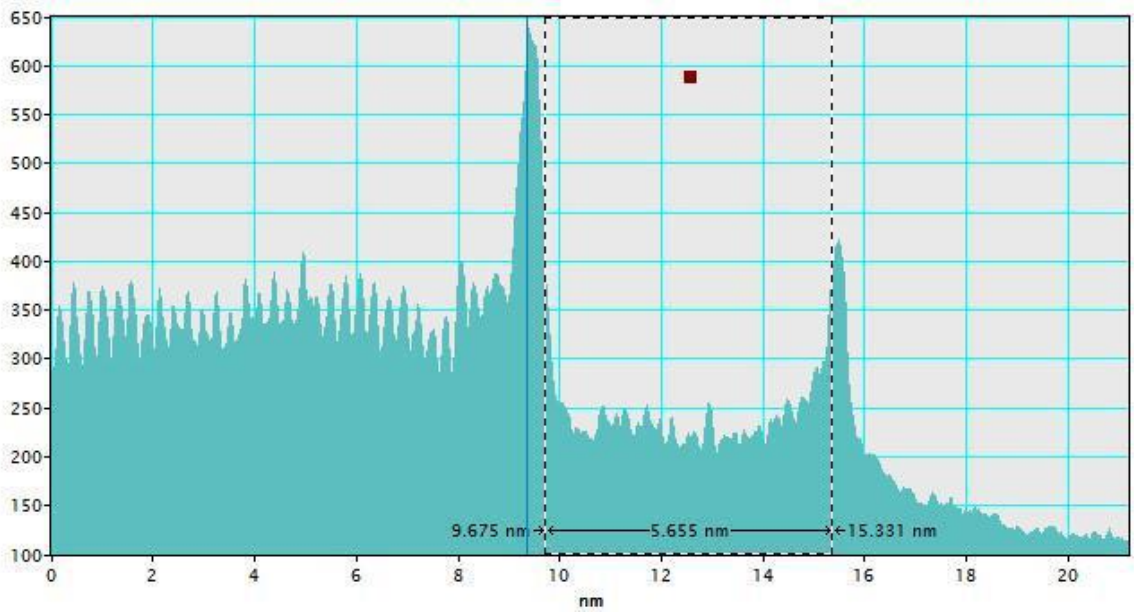

Fig. 5.12: Line profile analysis and thickness measurement of the MoSi film without any Si cap.

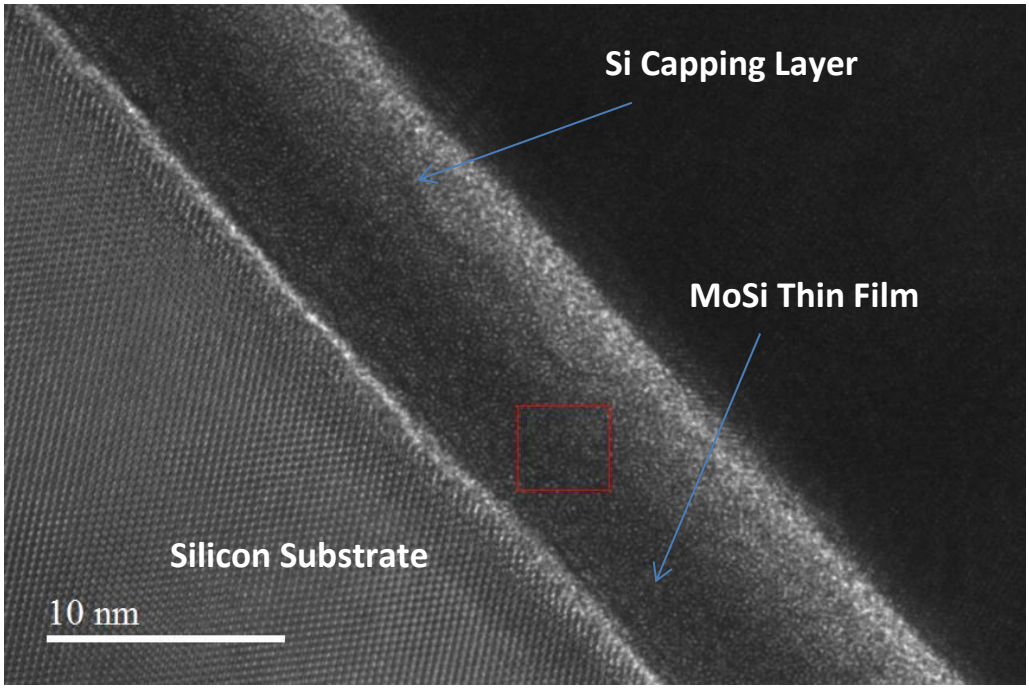

Fig. 5.13: Cross section of 5.5 nm MoSi film with a Si Cap.

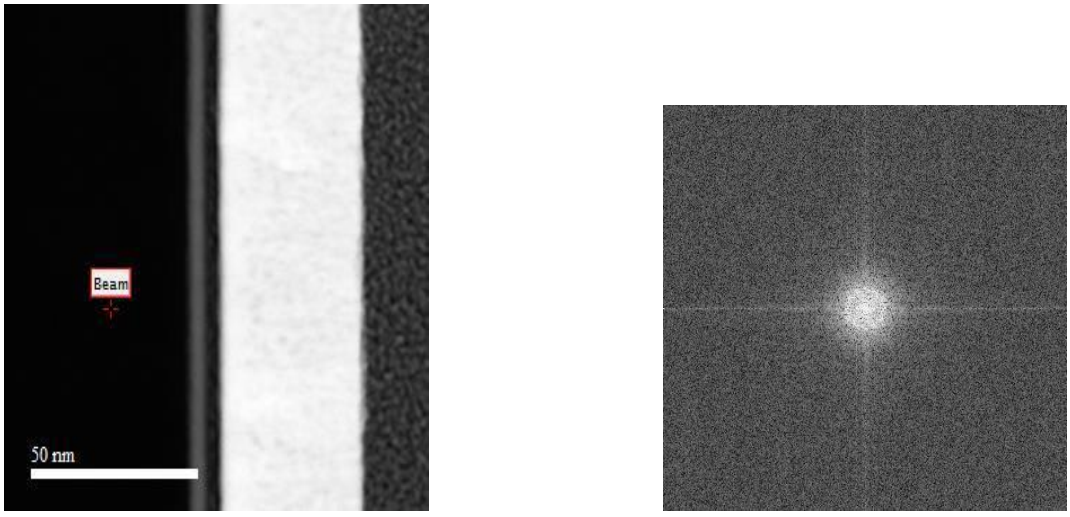

(a) (b)

Fig. 5.14: (a) Annular dark field image of 5.5 thick MoSi film with a Si Cap. (b) FFT view of the selected area (marked by red) of the same film.

Figure 5.13 shows the cross section of a 5.5 nm thick MoSi film with a silicon capping layer. Here also, the FFT view confirms the amorphous nature of the film. However, in the high resolution TEM image it is difficult to differentiate between the silicon capping layer and the film as both the layers are amorphous (meaning there is no proper structure or orders in the two layers). But, in the annular dark field (ADF) image shown above (Fig.5.14), we can clearly see the MoSi film and silicon capping layer on the top of it. Both the layers show a

sharp edge and maintain a uniform thickness showing consistent film deposition in our system.

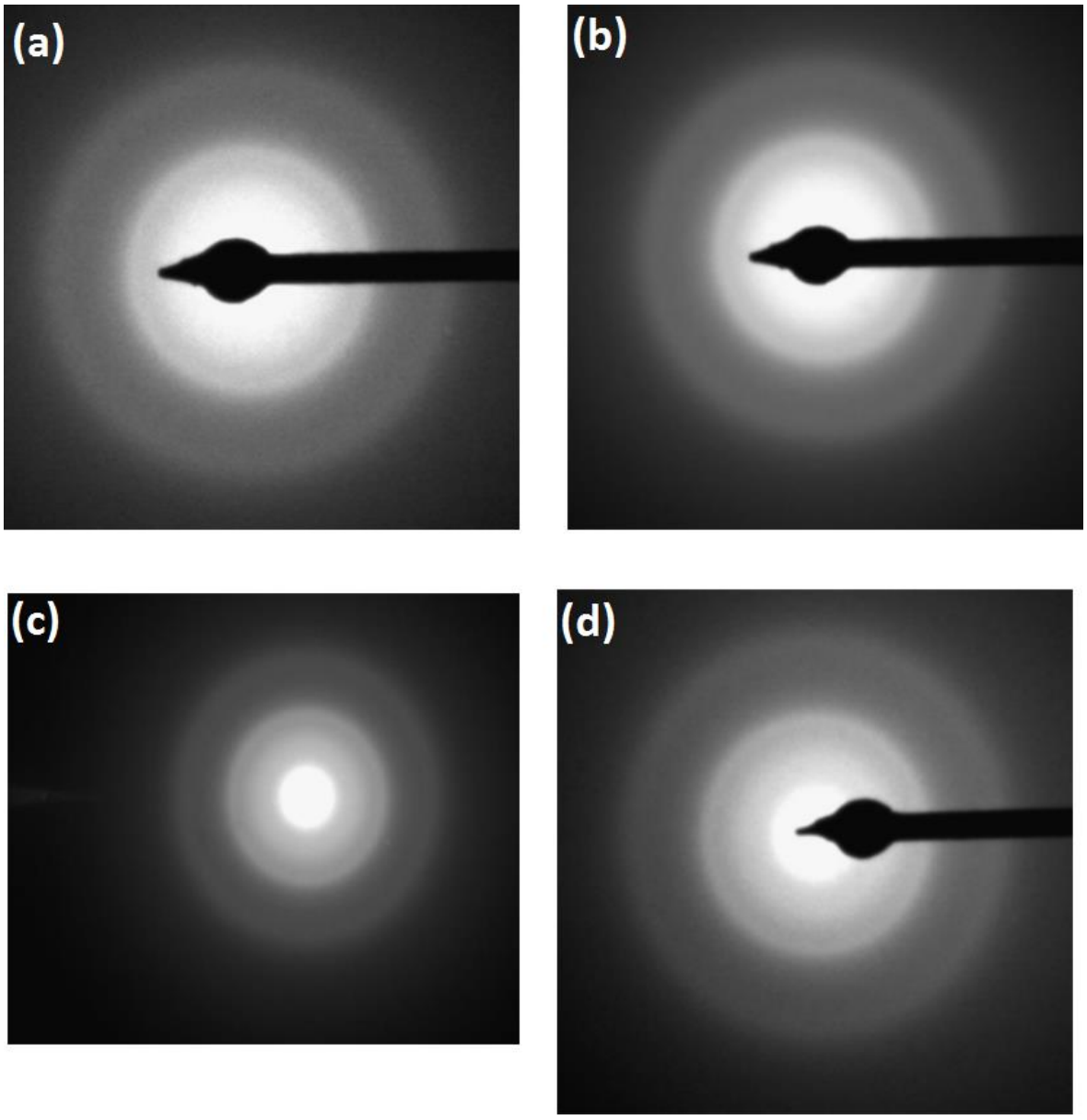

Fig. 5.15: Diffraction patterns recorded from the plan view image of 5 nm thick MoSi film deposited on a SiN membrane.

We have also deposited a selection of 5 nm thick MoSi thin films on a SiN membrane (200 nm thick) and imaged them in a Technai T20 TEM. Fig. 5.15 shows the diffraction patterns we recorded from the plan view image of the films. The images in the figure (b), (c) and (d) show diffraction patterns obtained from different regions of a 5 nm thick MoSi film

deposited without any Si capping layer. Figure (a) shows the diffraction pattern when a selected area aperture is inserted in the TEM. Hence, these images clearly show the amorphous nature of MoSi film. Our optimised recipe thus promotes the amorphous nature of MoSi thin films.

As we have stated in Section 5.3, the superconducting properties of amorphous materials must be very sensitive to short or medium range ordering. We have employed the Fluctuation Electron Microscopy (FEM) technique to explore local structural ordering of MoSi films. FEM is a diffraction based analysis to investigate the medium range ordering (~1-3 nm) in the atomic structure of disordered materials. This method was initially proposed by Gibson and Treacy [17]. In this technique, a small sample volume was scanned with a probe size of the order of 1-2 nm, and a large data set of diffraction patterns were collected (thousands of diffraction patterns). We have carried out this analysis in a JEOL ARM200F microscope using the Medipix-3 camera. The illumination of the microscope was adjusted by turning the objective lens off and working in the aberration-corrected Lorentz mode to produce small probe convergence angles to increase resolution in reciprocal space.

In this analysis, a qualitative idea about short or medium range ordering (SRO/MRO) in the sample can be achieved from the fluctuations in the diffracted intensity. The magnitude of such fluctuations is measured by computing the normalised variance of the diffracted intensity.

$$V(k_s, r) = \frac{<I^2(r,k_s)>}{<I(r,k_s)>^2} - 1 \qquad (5.2)$$

Here, k_s is the scattering vector and r denotes the position in sample space.

In the following figure 5.16, we have shown the diffraction pattern recorded from the MoSi film. The speckle ring indicates the existence of nano crystalline structures embedded in the amorphous film. The variance of all the diffraction patterns from the central portion of the film was calculated as a function of $q=2\pi k_r$ (k_r denotes the interplaner distance in reciprocal lattice space) using the method described by Hart *et al.* [18]. As we can see in the figure 5.17, the variance plot of the MoSi film has several small and large peaks. A small peak occurs at a q value of around 1.8 $Å^{-1}$, while larger peaks are visible at ~2.85 $Å^{-1}$ and ~4.6 $Å^{-1}$. We have compared these peak locations with diffraction peaks of A15 structured Mo_3Si (shown in the same figure). The similarity between them clearly indicates that our films consist of A15-like nanoscale structures over a short range evolving to a long range disorder.

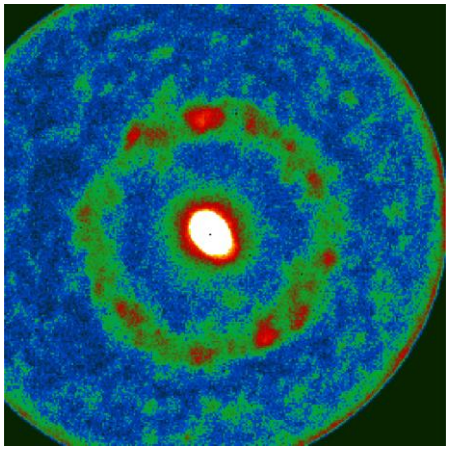

Fig. 5.16: Speckle pattern indicating the existence of short or medium range order in the MoSi film.

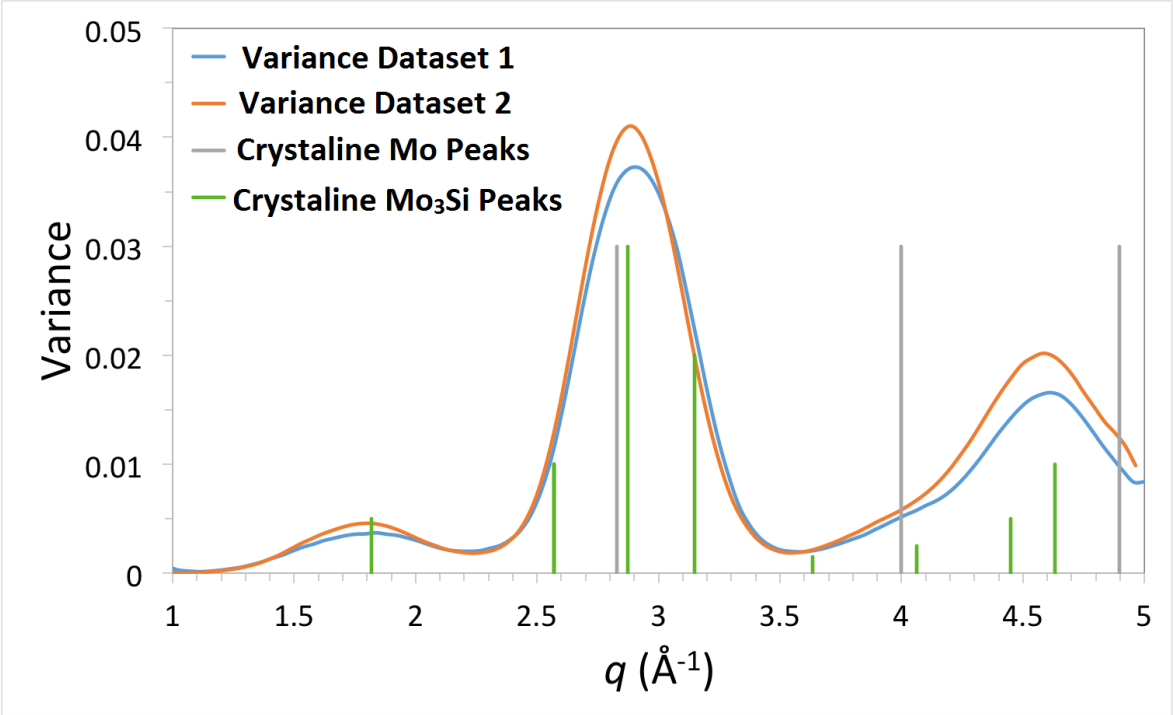

Fig. 5:17: Variance plot of diffracted intensity obtained from the FEM analysis of 5 nm thick MoSi film, peaks of the variance plot match with the diffraction peak of Mo_3Si crystal structure.

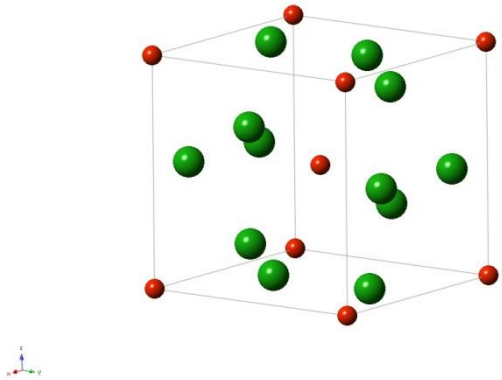

Fig. 5.18: Model of A15 crystal structure: in the cubic unit cell, 2 Si atoms (Red) occupy (0,0,0) and (1/2,1/2,1/2) positions whereas 6 Mo atoms (Green) are situated at (1/4,0,1/2); (1/2,1/4,0); (0,1/2,1/4); (3/4,0,1/2); (1/2,3/4,0); and (0,1/2,1/4) positions.

The chemical composition of the films has been investigated through electron energy loss spectroscopy spectrum imaging (EELS-SI). This analysis was also performed using the JEOL ARM200F microscope that is equipped with a cold field emission gun and operated at 200 kV. This microscope is fitted with a probe aberration corrector and a Gatan GIF Quantum ER spectrometer/energy filter. The probe convergence semi-angle was 29 mrad (with a probe current of 400 pA) and the spectrometer acceptance semi-angle was 36 mrad. All the acquisitions were carried out in DualEELS mode. The energy range for the high loss EELS spectrum was fixed in such way that it includes both Si-K and Mo-$L_{2,3}$ edges. The resulting data has been analysed using the *Elemental Quantification* plugin of Digital Micrograph software. The cross sections for EELS quantification were the Hartree-Slater cross sections provided by Gatan. In the following Figure 5.19, we have shown the elemental quantification map of Mo and Si (scan area indicated by a black box). Also, we have shown the atomic percent of Mo and Si in a line trace from the substrate into the film. It is clearly seen that the Mo content in the film peaks at the centre at about 83%, with a little excess Si being found at the surface.

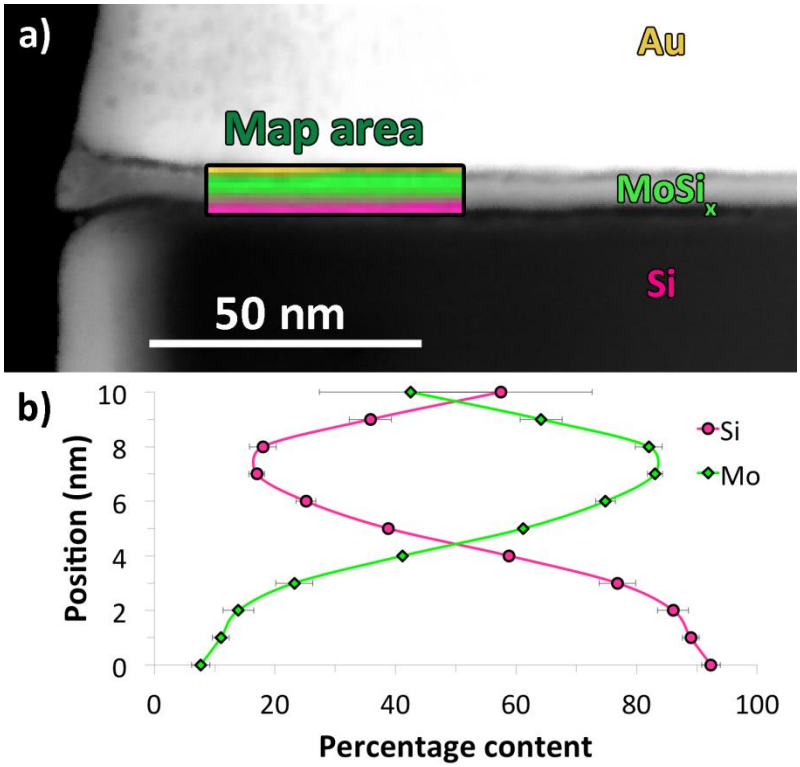

Fig. 5.19: Investigating the composition of uncapped co-sputtered MoSi films via Electron Energy Loss Spectroscopy (EELS): (a) dark field image of the Focused Ion Beam (FIB) cross section of MoSi film, with the scan area indicated by the black box (coloured elemental map shows the silicon substrate, MoSi film and gold layer deposited on top of the film). (b) Averaged elemental percentage composition from bottom to top (substrate across the film).

Hence, we can say that in contrast to the existence of A15 nano structures (as shown by FEM analysis), the composition of the film is closer to 83:17 rather than 75:25. As shown by Nunes *et al.* and Aindow *et al.*, this small variation in composition is quite common in A15 structured materials [19], [20]. This may be due to either a significant vacancy in the population on the corner of B (Si) sites of A_3B (Mo_3Si) structure or alternatively substitution of A (Mo) atoms on some of the B (Si) sites.

5.6. Measurement of optical constants for MoSi

Optical constants of two of our MoSi films have been measured at room temperature using the VASE. Following the same process used in the case of nitride films, a 390 nm thick layer of SiO_2 has been deposited on silicon substrates. Two 5 nm thick MoSi films have been grown on the top of them. For one MoSi film, we have grown a protective Si capping layer (~4 nm thick) on top of it.

In the following figure 5.20, we have shown the optical constants evaluated from a 5 nm thick MoSi film and a 5 nm film thick MoSi film with a Si capping layer. The presence of the Si capping layer slightly enhances the extinction co-efficient. The enhancement of absorption co-efficient due to the Si capping layer is more pronounced at $\lambda < 600$ nm. This wavelength range is well above the gap energy of Si, so the Si is acting as an additional absorbing layer. Over the IR range, a slight enhancement in *k* for the Si capping is still noticeable. We have also compared these measurements with VASE measurements carried out on 5.5 nm thick polycrystalline NbN and NbTiN thin films. It can be easily seen that MoSi films have a much higher extinction coefficient (*k*) in comparison to NbN or NbTiN over the whole spectral range, which means that at any specific wavelength the MoSi thin films are more favourable in terms of optical absorption. We can also see that the *k(λ)* curve of MoSi shows a continuous sharp increase even in the higher wavelength region (1500nm -2200nm). But for NbN or NbTiN, *k(λ)* shows a saturation and very slow increment in that wavelength region. Hence, MoSi can serve as a more suitable material for mid-infrared SNSPDs in terms of optical properties.

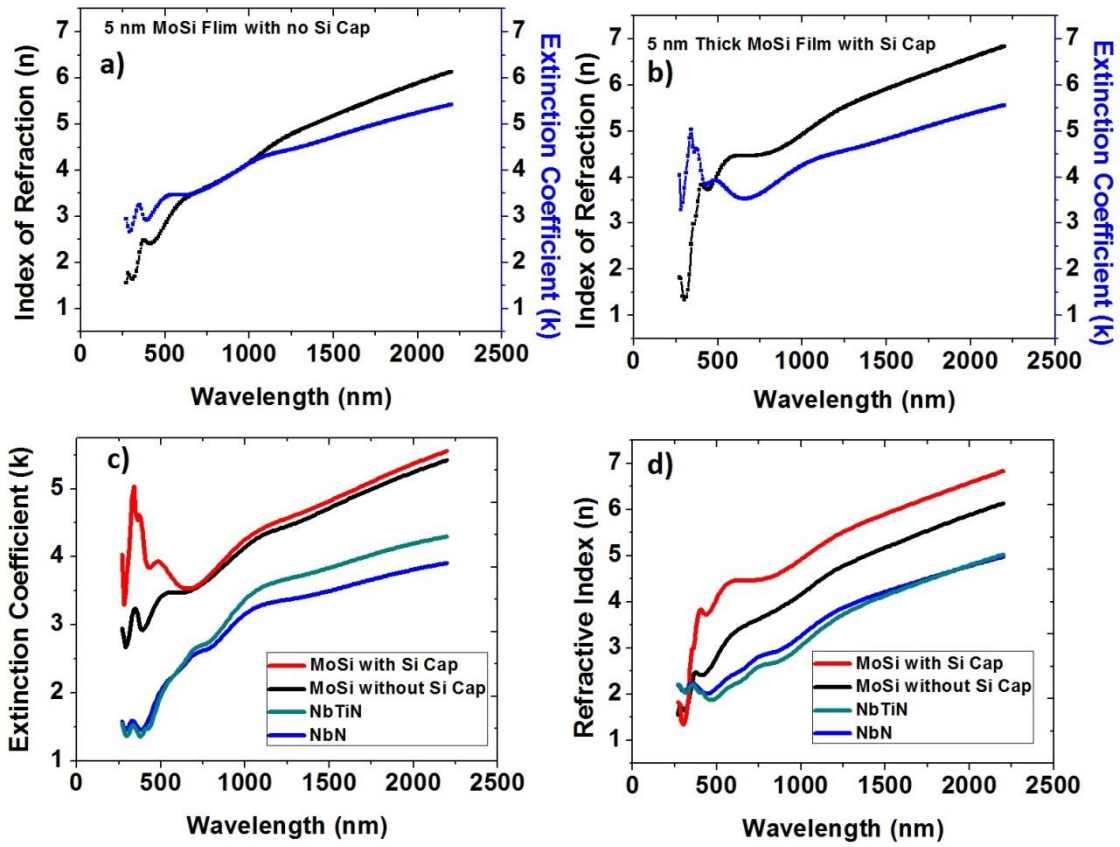

Fig. 5.20: Complex refractive index measurement for uncapped and capped MoSi films using variable angle spectroscopic ellipsometry (VASE) and comparison with optical constants (index of refraction *n* and extinction co-efficient *k*) measurements of NbN and NbTiN films. a) *n* & *k* data for a 5 nm MoSi film. b) *n* & *k* data for a 5 nm thick MoSi film with 5 nm Si cap. c) extinction co-efficient measurement of MoSi film with Si cap, MoSi film without a Si cap, NbN film and NbTiN film. d) refractive index measurement of MoSi film with Si cap, MoSi film without a Si cap, NbN film and NbTiN film.

5.7 Transport properties of patterned superconducting MoSi nanowires[7]

Along with the superconducting transition temperature, the critical current (I_c) is also another crucial parameter influencing the performance of superconducting devices. Typically, an optimal operation point for an SNSPD is set by the application of a bias current just below the critical current value of the specific device at the given operating temperature. Hence,

[7] **All the nanowire patterning and low temperature transport measurements have been performed by Luke Baker**

higher critical current density (j_c) is desirable for high sensitivity, low noise photon detection. In this section, the temperature dependence of critical current density has been explored in the nanowires patterned from MoSi thin films. A 10 nm thick MoSi film has been patterned into nanowires of various widths from 200 nm to 2 μm using a two-step EBL process. Methods used for nanowire fabrication has been discussed in Section 3.6 of Chapter 3. Transport properties of MoSi nanowires have been investigated in a pulsed tube cooler based closed cycle-cryostat. The base operating temperature of the cryostat is 3.5 K.

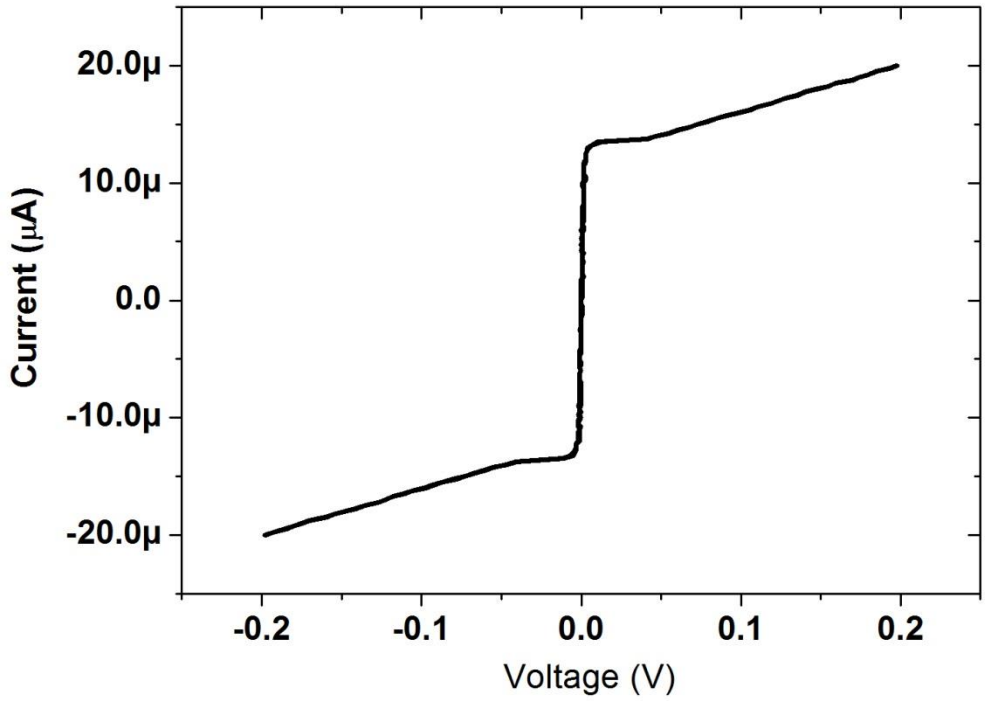

Fig. 5.21: Current- Voltage curve recorded from the 390 nm wide nanowire measured at 4 K .

I-V curves of the device have been recorded using a 4 point measurement setup. A Keithley 238 current source has been used to bias the device. The device is connected to the measurement circuit by SMA coaxial cables. While recording current-voltage characteristics, the compressor of the cryostat was turned on and off, allowing the cryostat temperature to vary between 3.5 K – 6.5 K. The cryostat took 2 minutes and 35 seconds to warm up from the base temperature to 6.5 K. Fig. 5.22 (a) shows the variation of critical current with nanowire width at three different measurement temperatures. Critical current is increasing with wire width as expected. Critical current density has been calculated using a cross section area of each nanowire. Fig. 5.23 depicts the variation of critical current density

with measurement temperature for different wire widths. Scanning Electron Microscopy (SEM) has been used to measure the accurate wire width after fabrication. The 2003 nm wide wire shows a critical current density of 0.36 MA/cm^2 at 3.6 K.

Critical current versus temperature data of MoSi nanowires have been fitted to the equation (2.7) and (2.8) described in Chapter 2 using $I_c(0)$, T_C and $2\Delta(0)$ as the fitting parameters. Table 5.5 shows the values of energy gap obtained from the curve fitting.

Table 5.5: Transition Temperature (T_c), Critical Current measured at 4K ($I_c(4K)$), the extracted critical current at 0 K ($I_c(0)$) and Superconducting energy gap $2\Delta(0)$

Nanowire Width (nm)	T_c (K) [Measured]	I_c(0) (μA) [Extracted]	$2\Delta(0)$ (meV) [Extracted]	I_c (uA) at 4K [Measured]
2003	6.23	79.60 ±0.16	1.868 ± 0.001	69.89
957	6.26	33.95±0.2	1.868 ± 0.002	29.75
458	6.15	14.81±0.05	1.856 ± 0.001	12.77
364	5.99	12.051±0.04	1.798 ± 0.001	10.22
264	5.94	7.91±0.06	1.788 ± 0.001	6.71
173	5.94	4.07±0.02	1.766 ± 0.001	3.41

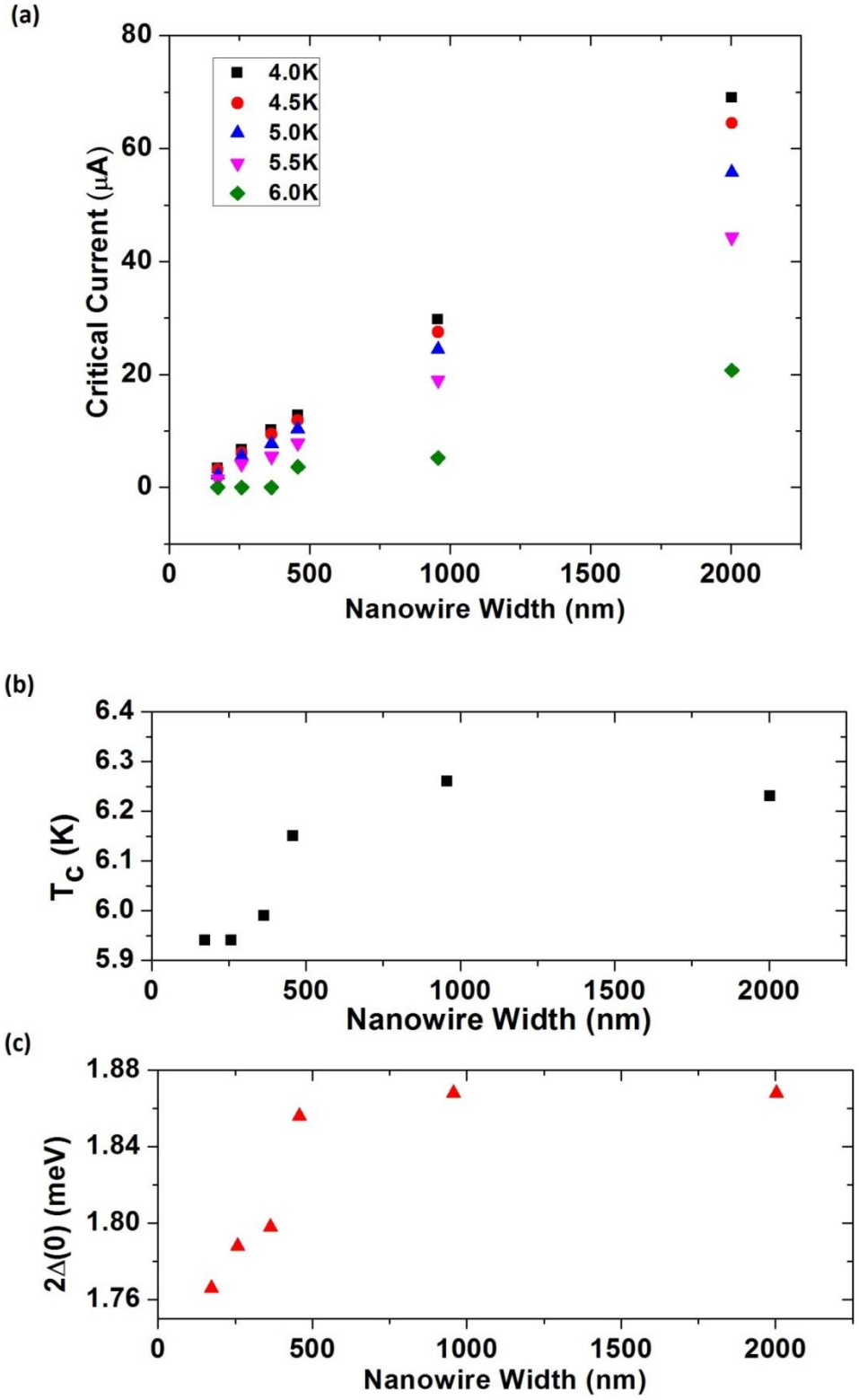

Fig. 5:22: Transport measurement of nanowires patterned in a 10 nm thick MoSi thin film. (a) Variation of critical current with nanowire width at five different temperatures. (b) and (c) Variation of transition temperature and superconducting energy gap with nanowire width.

It is evident that all the nanowires (2003-173 nm width) show a similar trend of superconducting transport properties. T_c is slightly depressed with decreasing wire width (from 6.23 K to 5.94 K). Fig. 5.22 (b) and 5.22 (c) demonstrate how T_c and the values of superconducting energy gap obtained through the curve fitting vary over the nanowire width. Though critical current decreases consistently with wire width (as expected), all the nanowires show a common trend of variation in critical current density with temperature (Fig. 5.23). Also, at any specific measurement temperature, there is a slow reduction in critical current density values of the nanowires with decreasing wire width. The nanowire of 2003 nm width shows a critical current density of 0.36 MA/cm^2 measured at 3.6 K. The thinnest nanowire (173 nm wide) shows a comparatively lower J_c of 0.2 MA/cm^2. This deviation along with the fluctuation in values of J_c in the rest of the nanowires can be explained by inhomogeneity caused during the nanowire fabrication. Close SEM inspection indicates the edges of the nanowires may be damaged with redeposition of etch debris and e-beam resist which would lead to a reduction in the superconducting cross section. This effect would be strongest (proportionately to the width) in the narrowest wires. The superconducting energy gaps of the nanowires based on our thin films are much smaller than the bulk energy gap of MoSi (~ 2.26 meV) reported in the literature. The wire width > 458 nm $2\Delta(0)$ assumes a value of ~ 1.87 meV; for the 173 nm wide nanowire, it drops to 1.77 meV.

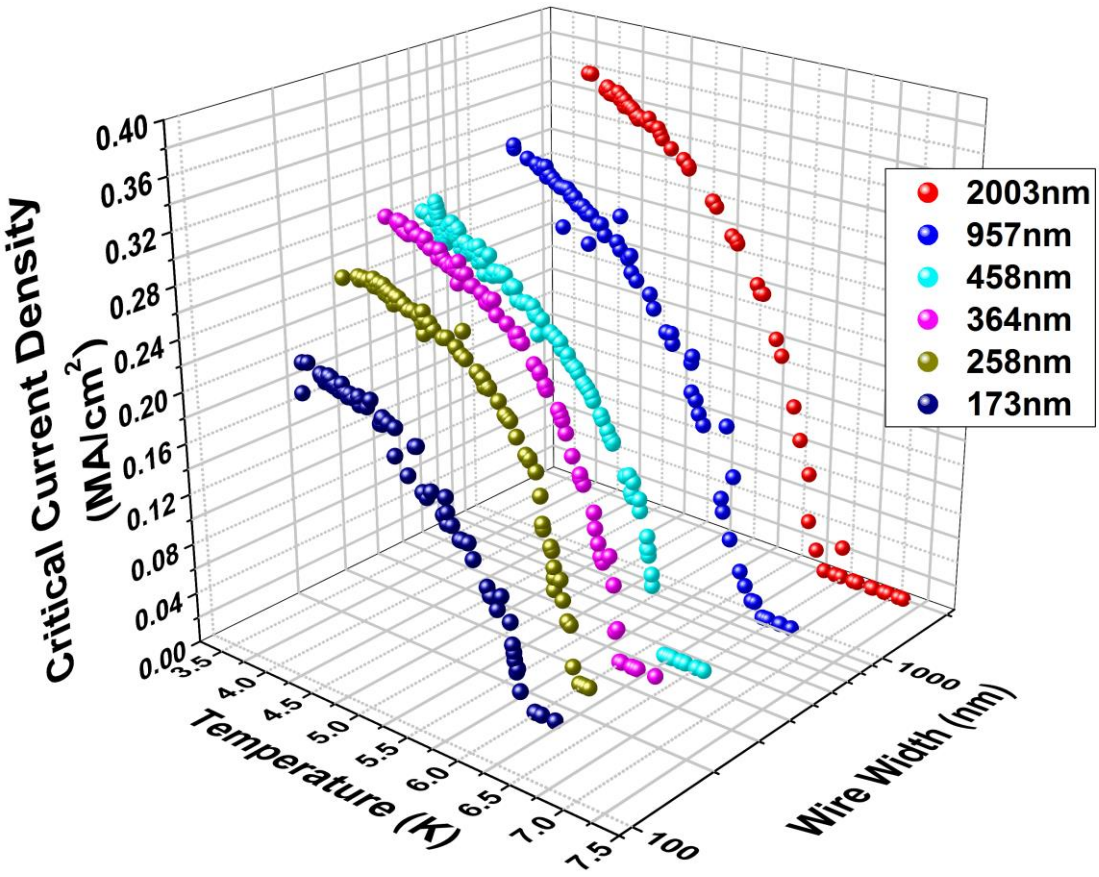

Fig. 5.23: Critical current density versus temperature curve of MoSi nanowires with widths ranging from 90 nm to 2003 nm (widths of the nanowires have been corrected from SEM inspection).

Lita *et al.* [15] have reported a critical current density of ~1.3 MA/cm^2 at 250 mK for a 1μm wide nanowire patterned on a 6.3 nm thick MoSi film. Korneeva *et al.* [21], [22] have shown critical current density varies from 1.1-2.5 MA/cm^2 for nanowire patterned meander devices on 4 nm thick MoSi films measured at 1.7 K. In comparison, the lower critical current densities observed in the nanowires fabricated from our film can be explained by a higher measurement temperature range.

Table 5.6: Comparison of Critical Current density data with previous reports

Operating Temperature (K)	Film Thickness (nm)	Critical Current Density (MA/cm^2)	
3.6	10	0.36 (for 2003 nm wide nanowire)	Our Study
0.250	6.3	1.3	Lita *et al.*
1.7	4	1.1-2.5	Korneeva *et al.*

5.8 Summary

In this chapter, growth and optimisation of amorphous MoSi thin films have been explored in terms of the desirable superconducting properties for SNSPD fabrication. The variation of superconducting properties with sheet resistance and film thickness has been compared with several theoretical models. The material parameters extracted from these models concur with the amorphous and homogeneously disordered nature of these films.

FEM analysis shows that the films deposited in accordance with the optimised growth recipe (leading to the maximum T_c) assume an A15-like structure over the range of a few atomic spacings while there is no long range crystallographic order. Electron energy loss spectroscopy (EELS) analysis was also performed, indicating the film stoichiometry was close to $Mo_{83}Si_{17}$.This indicates that some Si sites in the Mo_3Si A15 structure may be vacant. Moreover this stoichiometry differs from the compositions reported by other groups studying this material as a candidate for SNSPD fabrication: $Mo_{80}Si_{20}$ or $Mo_{75}Si_{25}$. The measurement of the complex refractive index shows that MoSi films have a higher extinction co-efficient in comparison to NbN and NbTiN films. Hence, MoSi is a more advantageous material in terms of optical absorption.

References

[1] J. Simonin, “Surface term in the superconductive Ginzburg-Landau free energy: Application to thin films,” *Phys. Rev. B*, vol. 33, no. 11, pp. 7830–7832, Jun. 1986.

[2] M. S. Osofsky, R. J. Soulen, J. H. Claassen, G. Trotter, H. Kim, and J. S. Horwitz, “New Insight into Enhanced Superconductivity in Metals near the Metal-Insulator Transition,” *Phys. Rev. Lett.*, vol. 87, no. 19, p. 197004, 2001.

[3] A. M. Finkel’stein, “Suppression of superconductivity in homogeneously disordered systems,” *Phys. B Condens. Matter*, vol. 197, no. 1, pp. 636–648, 1994.

[4] J. M. Graybeal and M. R. Beasley, “Localization and interaction effects in ultrathin amorphous superconducting films,” *Phys. Rev. B*, vol. 29, no. 7, pp. 4167–4169, Apr. 1984.

[5] A. Semenov, B. Günther, U. Böttger, H.-W. Hübers, H. Bartolf, A. Engel, A. Schilling, K. Ilin, M. Siegel, R. Schneider, D. Gerthsen, and N. A. Gippius, “Optical and transport properties of ultrathin NbN films and nanostructures,” *Phys. Rev. B*, vol. 80, no. 5, p. 54510, Aug. 2009.

[6] N. Hadacek, M. Sanquer, and J.-C. Villé, “Double reentrant superconductor-insulator transition in thin TiN films,” *Phys. Rev. B*, vol. 69, p. 24505, 2004.

[7] M. R. Graham, C. J. Adkins, H. Behar, and R. Rosenbaum, “Experimental study of the Ioffe-Regel criterion for amorphous indium oxide films,” *J. Phys. Condens. Matter*, vol. 10, no. 4, pp. 809–819, Feb. 1998.

[8] X. Zhang, A. Engel, Q. Wang, A. Schilling, A. Semenov, M. Sidorova, H.-W. Hübers, I. Charaev, K. Ilin, and M. Siegel, “Characteristics of superconducting tungsten silicide $W_x Si_{1-x}$ for single photon detection,” *Phys. Rev. B*, vol. 94, 2016.

[9] Y. Ivry, C. S. Kim, A. E. Dane, D. De Fazio, A. N. McCaughan, K. A. Sunter, Q. Zhao, and K. K. Berggren, “Universal scaling of the critical temperature for thin films near the superconducting-to-insulating transition,” *Phys. Rev. B*, vol. 90, no. 21, p. 214515, 2014.

[10] D. Bosworth, S.-L. Sahonta, R. H. Hadfield, and Z. H. Barber, “Amorphous Molybdenum Silicon Superconducting Thin Films,” *AIP Adv.*, vol. 5, no. 8, p. 87106, 2015.

[11] J. Bieger, H. Adrian, P. Müller, G. Saemann-Ischenko, and E. L. Haase, “Superconductivity and electrical resistivity of amorphous Nb75Ge25 and Nb80Si20 after heavy ion irradiation at low temperature,” *Solid State Commun.*, vol. 36, no. 11, pp. 979–982, 1980.

[12] H. M. Tütüncü, S. Bağcı, and G. P. Srivastava, “Electronic structure, phonons, and electron-phonon interaction in Mo 3 Si,” *Phys. Rev. B*, vol. 82, no. 21, p. 214510, Dec. 2010.

[13] M. Lehmann, G. Saemann-Ischenko, H. Adrian, and C. Nölscher, “Disordered A15 compounds from the Matthias-Valley: Mo_3Ge and Mo_3Si,” *Phys. B+C*, vol. 107, no. 1, pp. 473–474, 1981.

[14] A. E. Kar’kin, V. I. Voronin, T. V. D’yachkova, N. I. Kadyrova, A. P. Tyutyunik, V. G. Zubkov, Y. G. Zainulin, M. V. Sadovskii, and B. N. Goshchitskii, “Superconducting properties of the atomically disordered MgB_2 compound,” *J. Exp. Theor. Phys. Lett.*, vol. 73, no. 10, pp. 570–572, 2001.

[15] A. E. Lita, V. B. Verma, R. D. Horansky, J. M. Shainline, R. P. Mirin, and S. Nam, “Materials Development for High Efficiency Superconducting Nanowire Single-Photon Detectors,” *MRS Proc.*, vol. 1807, pp. 1–6, 2015.

[16] W. L. McMillan, “Transition Temperature of Strong-Coupled Superconductors,” *Phys. Rev.*, vol. 167, no. 2, pp. 331–344, Mar. 1968.

[17] M. M. J. Treacy and J. M. Gibson, “Variable coherence microscopy,” *Acta Crystallogr. Sect. A Found. Crystallogr.*, vol. 52, no. 2, pp. 212–220, 1996.

[18] R. Bassiri, M. Hart, R. L. Byer, K. B. Borisenko, K. Evans, M. M. Fejer, A. C. Lin, I. MacLaren, A. S. Markosyan, I. W. Martin, R. K. Route, and S. Rowan, "Investigating the medium range order in amorphous $Ta_2 O_5$ coatings," *J. Phys. Conf. Ser.*, vol. 522, no. June, p. 12043, 2014.

[19] C. A. Nunes, G. C. Coelho, and A. S. Ramos, "On the invariant reactions in the Mo-rich portion of the Mo-Si system," *J. Phase Equilibria*, vol. 22, no. 5, pp. 556–559, Oct. 2001.

[20] M. Aindow, L. S. Smith, J. Shyue, M. H. Loretto, and H. L. Fraser, "On the origins of 'forbidden' 100-type spots in electron diffraction patterns from the A15 compounds Nb $_3$ AI, Cr $_3$ Si and V $_3$ Si," *Philos. Mag. Lett.*, vol. 69, no. 1, pp. 23–30, Jan. 1994.

[21] Y. P. Korneeva, M. Y. Mikhailov, and Y. P. Pershin, "Superconducting single-photon detector made of MoSi film," *arXiv:1309.7074v1*.

[22] Y. P. Korneeva, M. Y. Mikhailov, Y. P. Pershin, N. N. Manova, A. V Divochiy, Y. B. Vakhtomin, A. A. Korneev, K. V Smirnov, A. G. Sivakov, A. Y. Devizenko, and G. N. Goltsman, "Superconducting single-photon detector made of MoSi film," *Supercond. Sci. Technol.*, vol. 27, no. 9, p. 95012, Sep. 2014.

Chapter 6

Titanium nitride (TiN) Growth for Microwave Kinetic Inductance Detector Applications

Microwave Kinetic Inductance Detector (MKID) is a cryogenic detector technology which is quickly gaining importance in the field of astronomical instruments. The main advantages of MKIDs are that they are simple to fabricate and easy to multiplex into a large detector array using the concept of frequency domain multiplexing [1]. As stated in Section 2.6 of Chapter 2, basic operating principle of any MKID device is to measure the change in the complex impedance of the superconducting film upon photon absorption. Any photon with an energy of $h\nu > 2\Delta$ if absorbed will break the Cooper pairs resulting in an increase in the kinetic inductance (L_k). This change in L_k is very small; so we need to pattern the superconducting films in to a high quality factor microwave resonance circuit to detect this variation.

Traditionally, MKIDs have been fabricated into superconducting quarter-wavelength or half-wavelength resonator elements capacitive coupled to a co-planar feed line. The change in kinetic inductance is detected from the resulting shift in the resonant frequency of the resonant circuit. This approach requires the quasi-particles generated by photon absorption to be concentrated at the high current density region of the circuit. This can be achieved by antenna coupling or quasi-particle trapping. For the detectors to work at a terahertz frequency range (approximately 0.3 to 3 THz or 1 mm to 100 μm in terms of wavelength), where antenna coupling can introduce a significant loss of efficiency, then a direct absorption method needs to be considered. The concept of Lumped Element KID (LEKID) has been proposed to solve this problem of coupling terahertz radiation to kinetic inductance detectors. In this design, there is no requirement of antenna coupling or quasi-particle trapping [2], [3].

We have explored the potential of TiN as an alternate base material for superconducting lumped element kinetic inductance detector (LEKID) fabrication. Titanium nitride (TiN) has been demonstrated to work as a useful material for MKIDs [4]. It offers several advantages over the more traditionally available material (e.g. Al) for this purpose. The superconducting property of TiN is tuneable with the nitrogen content of the film. So, we can engineer detector material accordingly to our need. TiN also has higher normal state resistivity. There

is less possibility of formation of surface oxide on the top of TiN film. Moreover, due to its higher T_c, TiN based MKID devices can be operated at a comparatively higher base temperature which is within the reach of modern close cycle cryogenic cooling technology.

6.1 Optimisation of TiN thin film growth in sputter deposition system

TiN thin films have been grown by reactive sputtering (Chapter 3.1.1). Double sized polished high resistivity silicon wafers have been used as substrates for this purpose. TiN films are deposited by the sputtering of Ti targets and by introducing a small amount of nitrogen into the chamber as the reacting gas. The distance between the substrate and the target is kept at 100 mm. We introduced 18 sccm of argon into the chamber with a fixed position of the throttle valve (75°). The following Fig. 6.1 shows the *R* versus *T* curve of 90 nm thick TiN film grown with several nitrogen flows. It can be seen that a T_c of 2.9 K can be achieved if we grow the film with a 10 sccm N_2 flow. When the substrate is heated up to 500°C before deposition, a 4 K T_c can be achieved. For these deposition parameters, a deposition time of 40 minutes was required to grow the 90 nm thick films (meaning the deposition rate was 2.25 nm/minute). Before deposition, we have cleaned the substrates in an ultrasonic bath with RO water, acetone and IPA for 5 minutes. Also, the substrates have been etched with diluted hydro fluoric (HF) acid immediately prior to film growth in order to remove the native silicon oxide layer grown on the top of the substrate. The film grown on the heated substrate has less sheet resistance indicating a larger grain size and improved structural property of the film grown at higher temperature.

Table 6.1 Recipe used for sputtered TiN growth

Ti:	0.6 A (238 W, 397 V when deposited at room temperature; 242 W, 404 V after heating substrate)
Ar Flow	18 sccm
Total Pressure	0.18 Pa
Target Substrate Distance	100 mm
Substrate Holder Rotation	60 rpm

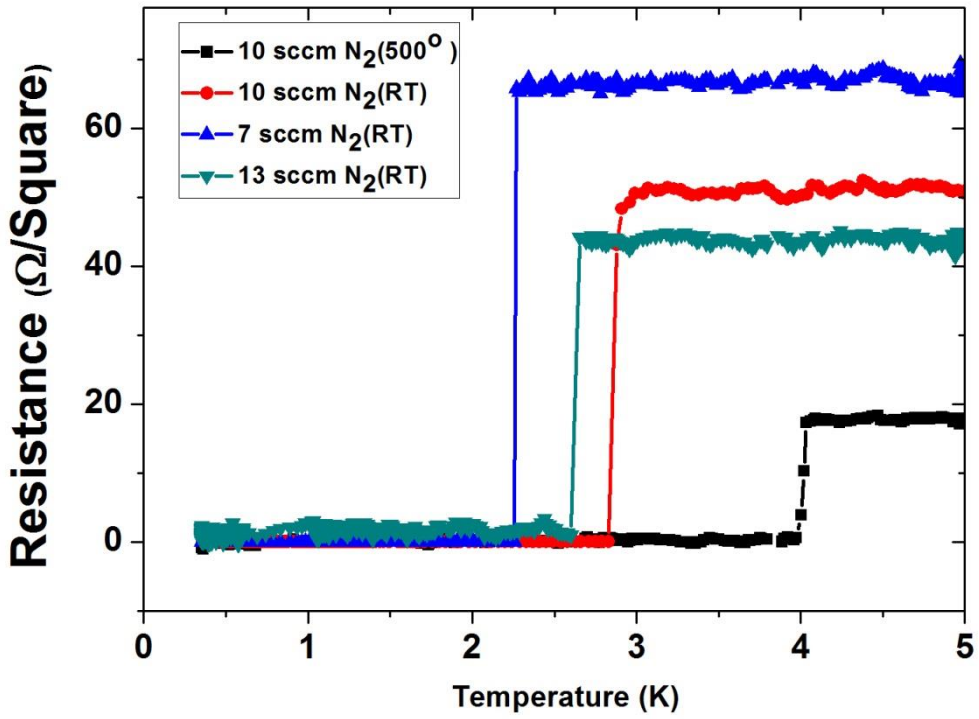

Fig. 6.1: *R(T)* Curve of 90 nm thick TiN films deposited in the sputter deposited system.

6.2 TiN thin film growth in Atomic Layer Deposition system

We have also grown TiN films in the atomic layer deposition (ALD) system installed in our clean room. At the beginning of film growth, substrates are inserted into the process chamber and pumped down with the help of a turbo and a roughing pump. After that, the substrates are pre-heated at a temperature of 350°C for 30 seconds. During the pre-heating, 100 sccm of N_2 and 200 sccm of Ar has been introduced in the chamber and the total chamber pressure has been kept at 200 mTorr. TiN films are grown by using TDMAT (*tetrakis dimethylamino titanium, $Ti(N(CH_3)_2)_4$*) as the precursor and H_2/N_2 plasma as the reactant gas. Each deposition cycle consists of 1 second of exposure to precursors, 5 seconds of purging, 15 seconds of exposure to reactive gas and plasma and finally 10 seconds of post plasma purging. TDMAT has been delivered from a remote reservoir. 20 sccm of Ar has been used as the carrier gas. The Ar purge flow rate has been fixed at 200 sccm. The following table 6.2 describes the process parameters which have been used for the TiN growth in ALD.

Table 6.2 Recipe used for TiN growth in Atomic Layer Deposition (ALD)

Pre-Heat (at 350°C)	100 sccm N_2 , 200 sccm Ar Purge; Chamber Pressure: 200 mTorr Duration: 30 seconds
Pressure Set up	
TDMAT Dose	200 sccm Ar Purge, 20 sccm Ar Carrier; Chamber Pressure: 40 mTorr Duration: 1 seconds
TDMAT Purge	200 Sccm Ar Purge, 20 Sccm Ar Carrier; Chamber Pressure: 40 mTorr Duration: 5 seconds
Plasma Gas stabilisation	5 sccm H_2, 15 or 30 sccm N_2, 200 sccm Ar Purge, 20 sccm Ar Carrier; Chamber Pressure: 10 mTorr Duration: 5 seconds
H_2/N_2 Plasma	5 sccm H_2, 30 or 15 sccm N_2, 200 sccm Ar Purge, 20 sccm Ar Carrier; Chamber Pressure: 10 mTorr Duration: 5 seconds Plasma Power: 200 W Duration: 15 seconds
Post Plasma Purge	200 sccm Ar Purge, 200 sccm Ar Carrier; Chamber Pressure: 40 mTorr Duration: 10 seconds

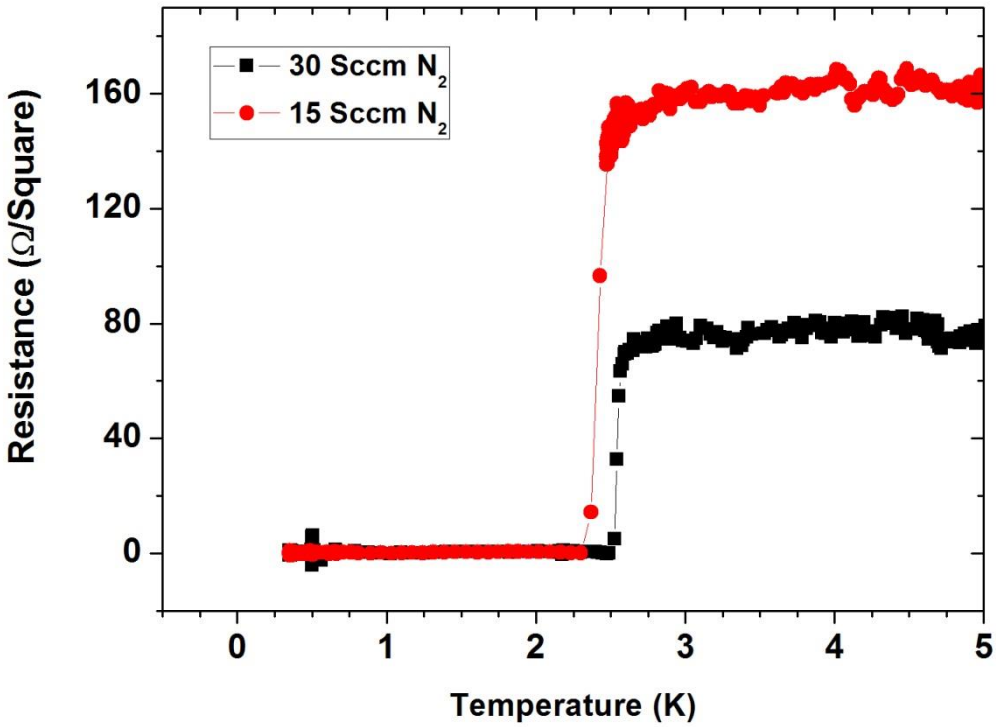

Fig. 6.2: *R(T)* Curve of 30 nm thick TiN films deposited in the atomic layer deposition system (Nitrogen flow rate in the reactive plasma has been varied).

Fig. 6.2 presents the T_c measurement of the 30 nm thick TiN films deposited following the process described in Table 6.2. Two different N_2 flow rates in the reactive plasma have been used during TiN film growth. As it can be seen from the above figure, for the film grown with 30 sccm N_2, a 2.4 K T_c can be obtained. In this recipe, a total of 240 minutes (4 hours) of deposition time was used to grow a 30 nm thick TiN film (meaning the film deposition rate was 0.125 nm/minute).

A set of thicker TiN film (60 nm) grown by the ALD process have shown reduced T_c (2.2 K) which is contrary to the common trend found in the literature for TiN films [5]. This anomalous behaviour may be explained by growth of impurities from the precursor in the film as the film thickness is increased, degrading the superconducting properties.

6.3 Transmission Electron Microscopy analysis

The structural properties of the TiN films have been analysed in HRTEM. Samples have been prepared for TEM analysis following the process described in Section 3.4.1 of Chapter 3. A JEOL ARM200cF microscope has been used for this analysis. Fig. 6.3 shows the TEM images (400 KX) of 30 nm thick TiN film deposited in the atomic layer deposition system. Since high resistivity silicon has been used as the substrate and all the substrates were processed with HF dip before the film growth, there is no native oxide layer between the film and the substrate. The TEM image also demonstrates a smooth film substrate interface indicating the uniformity of film growth. Film thickness has been measured at several locations with help of line profile analysis. TiN film has a thickness of 31.9 (± 0.2 nm) nm.

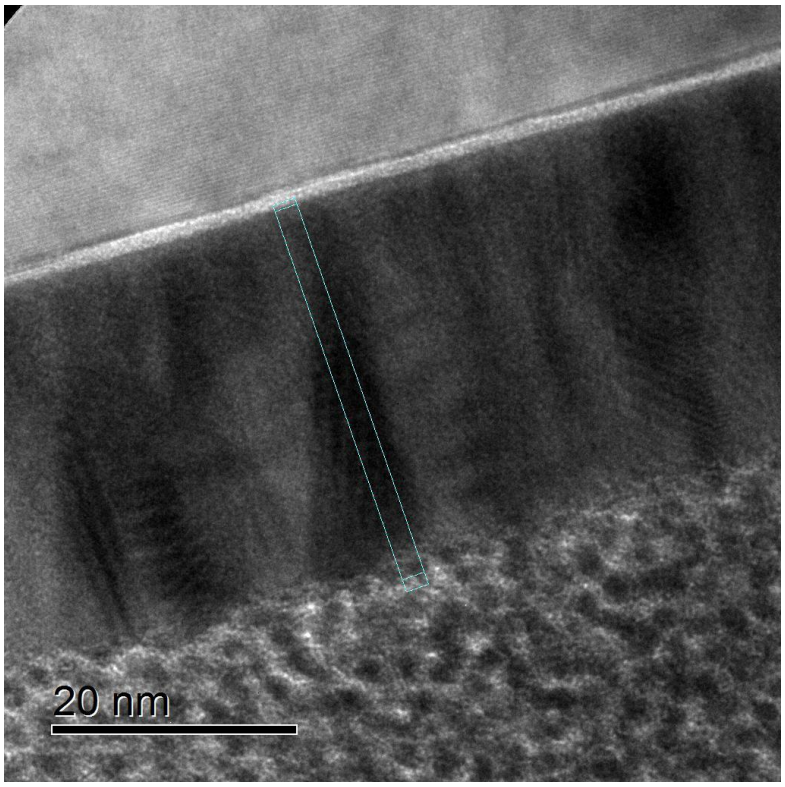

Fig. 6.3: TEM cross section image of 30 nm thick TiN film deposited in the ALD system.

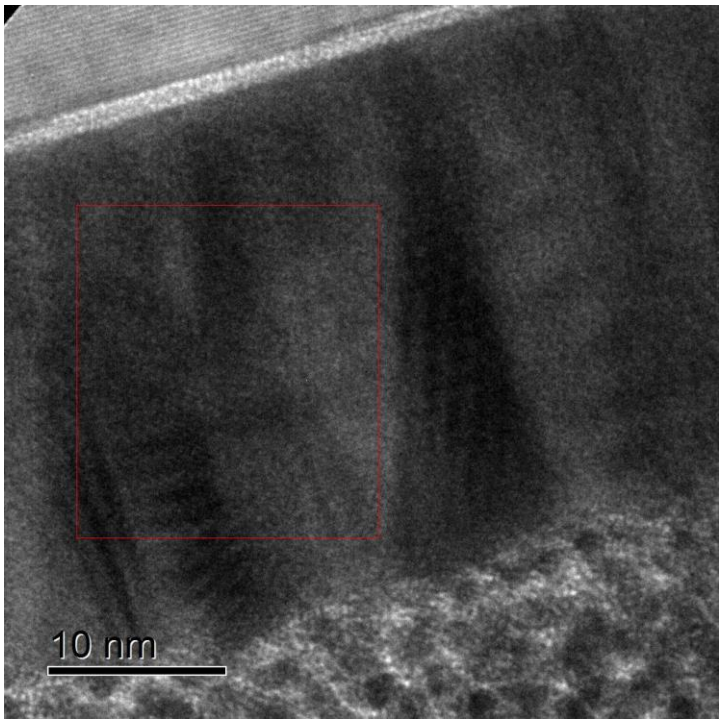

Fig. 6.4: Higher magnification view of the TEM cross section image of 30 nm thick TiN Film deposited in the ALD system showing the columnar structure and tight grain boundaries.

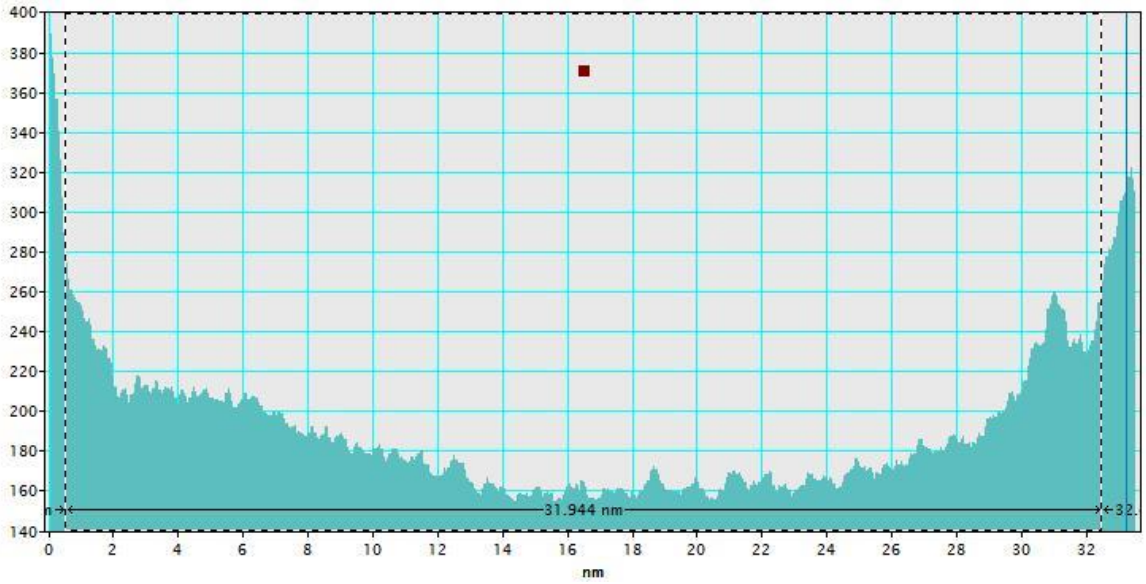

Fig. 6.5: Line profile analysis and thickness measurement of TiN film deposited in ALD (cross section has been shown in Fig. 6.4).

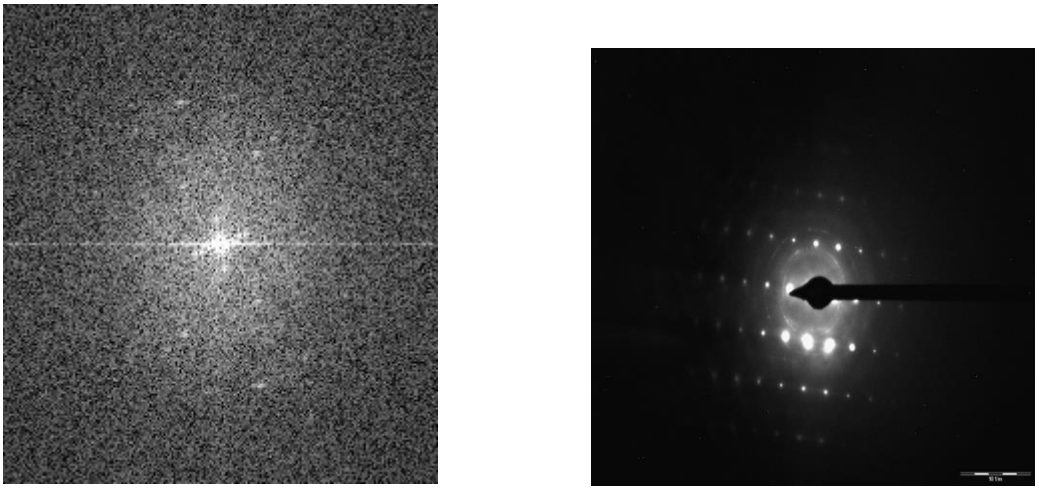

(a) (b)

Fig. 6.6: Structural properties of ALD deposited TiN film: (a) FFT view extracted from the area marked by the red square in Fig. 6.5; (b) Convergent beam electron diffraction image of the TiN film.

Both Fig. 6.3 and Fig. 6.4 show columnar film growth and tight grain boundaries (grains have a horizontal dimension of ~ 15 -20 nm). In Fig. 6.6 (a), an FFT view extracted from the area marked by the red square in Fig. 6.4 has been shown. Though the image is very noisy, the existence of structural order can be seen. In Fig. 6.6 (b), we have shown a convergent beam electron diffraction pattern recorded the TiN film. Fig. 6.7 shows a cross section image of 90 nm thick TiN film grown on a heated substrate in the sputter deposition system. The line profile indicates a thickness of 87.5± 0.3 nm. The crystalline structure and large grains of the sputter deposited film can be observed from the TEM image.

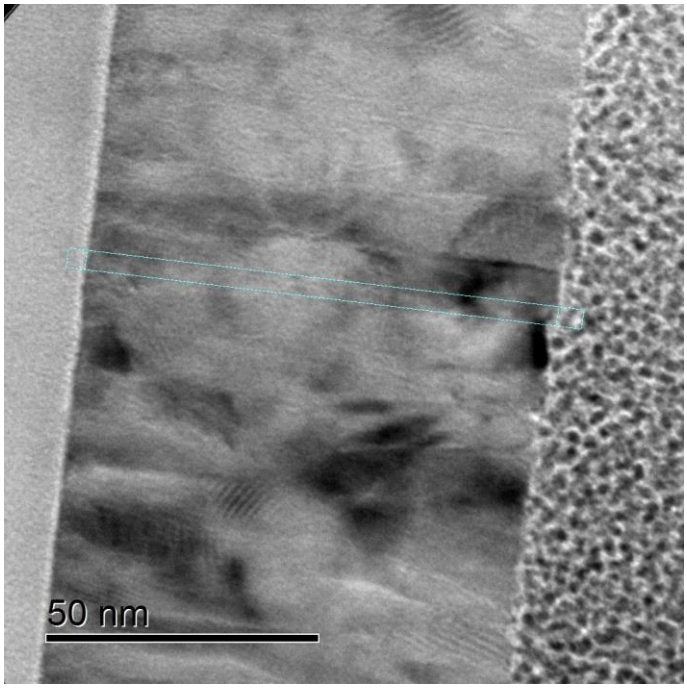

Fig. 6.7: TEM cross section image of 90 nm thick TiN Film deposited in the sputter deposition system.

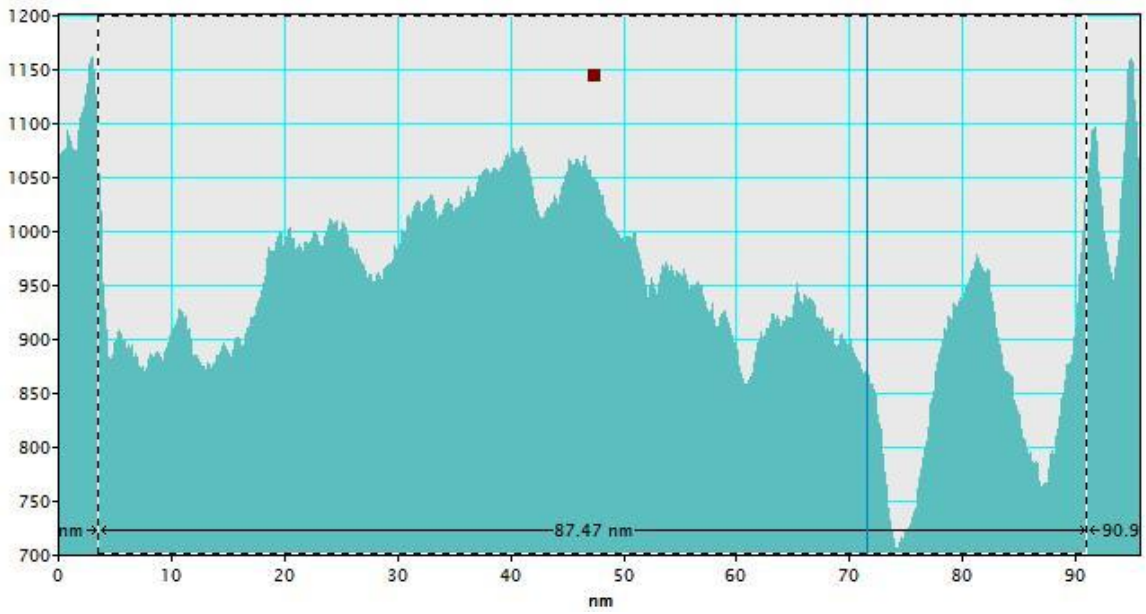

Fig. 6.8: Line profile analysis and thickness measurement of TiN film deposited in the sputter system (cross section has been shown in Fig. 6.7).

The following figure (Fig. 6.9) shows the chemical composition analysis of the ALD deposited TiN thin film. The elemental mapping clearly indicates that the film consists of titanium and nitrogen. We have also shown a mapping of oxygen over the sample. It reveals that though there are oxygen impurities in the substrate as expected, there is no noticeable oxygen contamination in the film.

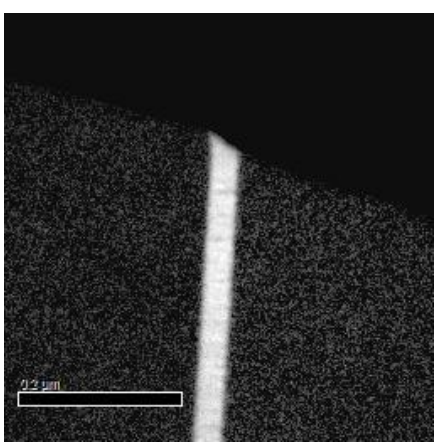

(a)

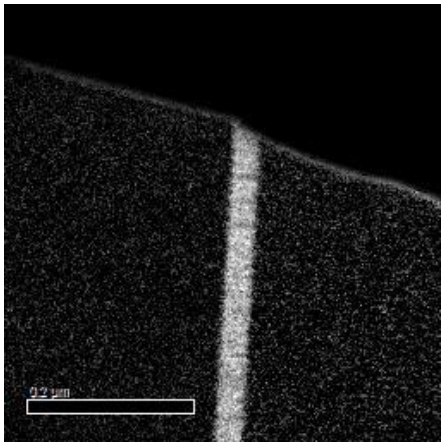

(b)

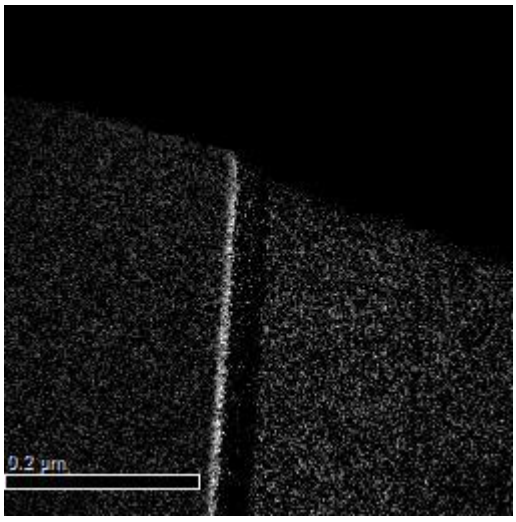

(c)

Fig. 6.9: Composition analysis of 30 nm thick TiN Film deposited in atomic layer deposition system: (a) Ti map. (b) N_2 map. (c) O_2 map.

6.4 Device fabrication and testing[8]

MKID devices have been fabricated based on the TiN thin films deposited following the optimised recipes described in this chapter. The device fabricated based on the 90 nm thick sputter deposited film showed a resonance. However, the resonance curve of the device was unresponsive to any optical radiation. On the other hand, the device fabricated from 30 nm thick ALD deposited film has shown a proper response. As shown in the following figure, the resonant frequency of the MKID device shifts towards left with the increase in optical power while the depth of the resonance decreases. Fig. 6.10 demonstrates the design and the optical microscope image of the device.

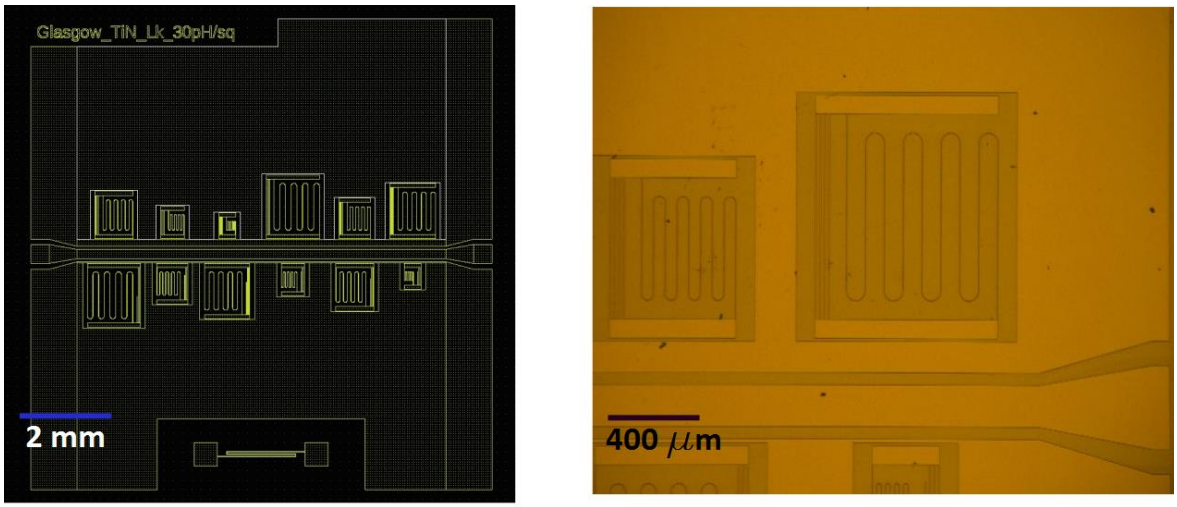

Fig. 6.10: Design and optical microscope image of the MKID device fabricated from the 30 nm thick ALD deposited TiN film.

[8] **MKID device fabrication and low temperature characterisation have been performed by Dr. Dmtry Morozov using facilities at the University of Cardiff.**

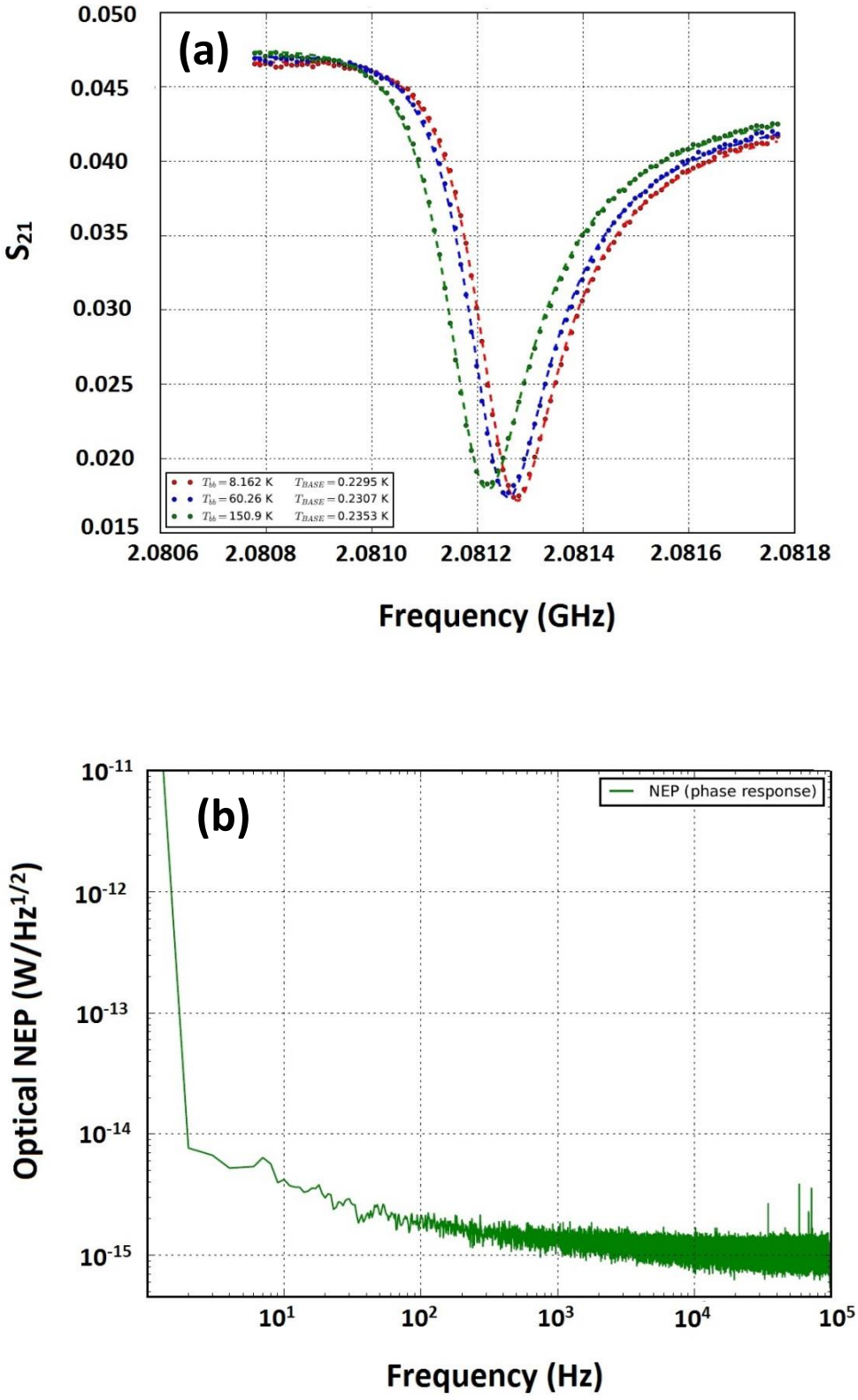

Fig. 6.11: Low temperature characterisation of the MKID device: (a) Resonance curve of the device with different blackbody radiation. (b) Optical NEP of the phase response of the device at T_{base} = 230 mK.

From the Fig. 6.11 (a), it is clear that the device is responsive to blackbody radiation. At the lowest blackbody temperature (8.16 K), the resonant frequency of the device is 2.0812 GHz. The internal quality factor of the device is 21783.22. Base temperature of the device is maintained below 0.3 K. Fig. 6.11 (b) shows optical NEP data of phase response of the device at a 350 mK temperature. It is of the order of ~10^-15. As stated in Chapter 2, this NEP value is sufficient for the application in passive terahertz imaging.

6.5 Summary

In this chapter, optimisation of TiN thin film growth for MKID applications has been reported. 30 nm thick ALD deposited film has shown a T_c of 2.4 K and 90 nm thick sputter deposited film has shown a maximum T_c of 4 K. The deposition rate of the ALD process is much slower (~18 times) in comparison to the sputter deposition. HRTEM analysis reveals that TiN films are highly crystalline in nature with large grain size. A prototype MKID device has been fabricated from the TiN film that was grown following recipes described in this chapter. The difference in the optical response of devices fabricated from the sputtered and ALD deposited films is still unknown, but a slower deposition rate and higher uniformity of ALD films can be a crucial reason behind this.

References

[1] P. K. Day, H. G. LeDuc, B. A. Mazin, A. Vayonakis, and J. Zmuidzinas, "A broadband superconducting detector suitable for use in large arrays," *Nature*, vol. 425, no. 6960, pp. 817–821, Oct. 2003.

[2] S. Doyle, P. Mauskopf, J. Naylon, A. Porch, and C. Duncombe, "Lumped Element Kinetic Inductance Detectors," *J. Low Temp. Phys.*, vol. 151, no. 1–2, pp. 530–536, Apr. 2008.

[3] S. Rowe, "Passive terahertz imaging with lumped element kinetic inductance detectors," *PhD Thesis*, Department of Physics and Astronomy, School of Physics and Astronomy, Cardiff University, U.K, 2015.

[4] G. Coiffard, K.-F. Schuster, E. F. C. Driessen, S. Pignard, M. Calvo, A. Catalano, J. Goupy, and A. Monfardini, "Uniform Non-stoichiometric Titanium Nitride Thin Films for Improved Kinetic Inductance Detector Arrays," in *Journal of Low Temperature Physics*, 2016, vol. 184, no. 3–4, pp. 654–660.

[5] E. F. C. Driessen, P. C. J. J. Coumou, R. R. Tromp, P. J. de Visser, and T. M. Klapwijk, “Strongly Disordered TiN and NbTiN s -Wave Superconductors Probed by Microwave Electrodynamics,” *Phys. Rev. Lett.*, vol. 109, no. 10, p. 107003, Sep. 2012.

Chapter 7

Conclusion and Outlook

7.1 Summary of Thesis Work

In this thesis, we have carried out an extensive study on the growth and optimisation of superconducting thin films for next generation superconducting detector applications. Thin films have been grown in a newly installed load-locked ultra-high vacuum sputter deposition system and new atomic layer deposition unit in the James Watt Nanofabrication Centre at the University of Glasgow. A cryogen free low temperature testing set-up has been built to characterise superconducting properties of thin films.

At the beginning of this thesis, we started with the acceptance test of the sputter deposition system (a T_c of 9.1 K has been reported for a 300 nm thick Nb film). NbN and NbTiN are the most extensively used conventional thin film materials for SNSPD application. We have optimised NbTiN thin films in terms of superconducting properties. Films have been grown by the co-sputtering of Nb and Ti in an Ar environment. Nitrogen has been used as the reactive gas. The amount of nitrogen in the chamber has been controlled by the throttle valve position and the mass flow controller determining incoming gas flow. A T_c of 7.2 K has been demonstrated by our optimised recipe for a 5.5 nm thick NbTiN film grown on a silicon substrate at room temperature. When we heat the substrate up to 800°C during deposition, a NbTiN film with the same thickness shows a transition temperature of 10.4 K. High resolution transmission electron microscopy (HRTEM) analysis demonstrates the polycrystalline nature of the NbTiN thin films. It also shows that substrate heating improves the superconducting properties of the films.

The lattice-matching requirements between NbN or NbTiN films and the substrate create a major constraint on high efficiency SNSPD fabrication or in integrating SNSPDs in complex circuits. Amorphous superconducting materials such as MoSi, MoGe or WSi offer a potential solution to this problem. Amorphous films do not set strict requirements on substrate choice as there is no issue regarding lattice matching. In Chapter 5, we have presented optimisation of MoSi film growth and demonstrated a T_c of 5.5 K for a 5 nm thick film. A comparison of T_c measurement between MoGe and MoSi thin films indicates that

MoSi is a more suitable material for SNSPDs which can be operated at an elevated temperature. By comparing our transition temperature measurement data with several theoretical models (Finkel'stein, Simonin and Ivry) we find that the room temperature sheet resistance is strongly linked to the resulting T_c of the amorphous film. We have employed advanced TEM techniques, including FEM, to reveal that the film consists of a short range nano crystalline structure which is similar to an A15 Mo_3Si structure. Based on the sputter deposition rates, the composition of the film is closer to 83:17 than 75:25. This is typical of A15 structures and could be due to either a significant vacancy population on the corner of B (Si) sites of an A_3B (Mo_3Si) structure or alternatively due to the substitution of A (Mo) atoms on some of the B (Si) sites. VASE studies have also been carried out to determine the complex refractive index of uncapped and Si capped MoSi films. This data is critically important for integrating MoSi SNSPDs into advanced optical structures such as waveguides and cavities, and it can also be crucial for tailoring devices to specific wavelengths in the future. The refractive index properties of MoSi have been compared with NbTiN and NbN, indicating that MoSi has superior optical absorption at mid infrared wavelengths. Finally, transport properties including critical current and its dependence on temperature have been evaluated after nanowire patterning (in range of 2003 nm width down to 173 nm width) in a 10 nm thick film. The critical current density measured at 3.6 K (in the range 0.36 to 0.2 MA/cm^2, diminishing with wire width) indicates nanowires are suitable for SNSPD operation at an elevated temperature (> 2 K). This study has implications for the optimisation of MoSi films for next generation SNSPDs, for the realisation of uniform large area SNSPD focal plane arrays and for the integration with advanced optical architectures such as quantum photonic waveguide circuits.

To date, we have reported a low temperature photoresponse map recorded at 350 mK (corresponding to a maximum system detection efficiency of approximately 5% at a 1550 nm wavelength under the perpendicular illumination condition) from a waveguide integrated SNSPD fabricated on a 10 nm thick MoSi thin film deposited at the University of Cambridge with a similar composition ($Mo_{83}Si_{17}$) [1]. Presently, the optical response of full SNSPD devices fabricated based on the MoSi films that have been optimised in this study are being explored.

In Chapter 6, we have described the process optimisation of TiN thin film growth for MKID applications. Two different deposition techniques (sputtering and atomic layer deposition) have been used to grow TiN films. Hydro fluoric (HF) acid cleaned, double side polished silicon substrate has been used for the film growth. For the sputtered deposited films, a T_c of

2.9 K has been achieved for the 90 nm thick film grown at room temperature. Substrate heating during deposition enhances T_c up to 4 K. A 30 nm thick TiN film in the ALD system deposited following the optimised process shows a T_c of 2.4 K. HRTEM analysis shows that ALD deposited films are uniform. Their cross-section images exhibit columnar film structure and tight grain boundaries (with a grain size of ~ 15 -20 nm). Sputtered deposited films also show a crystalline structure. Elemental mapping using TEM shows the existence of Ti and N_2 in the TiN thin film samples. The existence of oxygen impurities can be observed in the silicon substrate. However, there is no noticeable oxygen contamination in the TiN thin film samples.

7.2 Outlook

Since the initial demonstration of SNSPD and MKID technology, there has been a considerable amount of effort made to improve the optimisation of superconducting thin film materials for specific superconducting detector applications. For SNSPDs, amorphous superconductors have evolved as potential alternatives to substitute traditional materials like NbN or NbTiN. In case of MKID, TiN based devices have shown promising results. My view on the further lines of research in this area has been summarised below.

A combination of deposition technique consisting of ALD and sputtering can be useful to enhance the uniformity of superconducting thin film growth. Thin film growth in the ALD chamber is very slow (~few Å/minute) and uniform. At first, a seed layer of a few nm thick film can be grown using the atomic layer deposition system. Immediately after that, samples can be taken out of the ALD chamber and inserted in the sputter deposition system. In the sputter system, the same material can be sputtered until the desired thickness is reached. The ALD deposited layer will help to promote uniformity and crystalline structure of the thin film.

A bilayer of amorphous and polycrystalline superconducting thin film can be used as a base material for SNSPDs. As discussed by Ivry *et al.* [2], both crystalline metal nitrides and amorphous alloys have certain material properties which promote the specific performance parameters of SNSPDs (e.g. NbN based devices are much faster with <35 ps timing jitter and < 3ns reset timing; on the other hand, WSi based detectors show over 90% system detector efficiency). Use of a hybrid thin film system consisting of both crystalline and amorphous material can be a novel approach to optimising performance parameters of SNSPDs.

Two-dimensional materials have recently gained huge interest in the scientific community due to their unique properties. These materials have many exceptional applications in real life [3]. Although the theoretical aspects of two-dimensional superconductivity are being explored since past several decades, it remains extremely challenging to fabricate two-dimensional superconducting material. Due to recent advances in nanofabrication (especially after the discovery of graphene), the experimental investigation of 2D superconductors is going to be an important field of research. Ugeda *et al.* have shown that $NbSe_2$ remains even in single atomic layer form and shows a T_c of 1.9 K (whereas its bulk T_c is 7.2 K) [4]. Further exploration of superconducting properties in novel 2D materials may lead to new concepts in superconducting detector technology.

The performance of superconducting detectors strongly depends on cryogenic technology. At present, a base temperature at least below 2 K is required for the operation of high efficiency SNDPDs. The fabrication of detectors based on the materials with higher transition temperatures may elevate the operating temperature of detectors. MgB_2 has a bulk T_c of 39 K (discovered in 2001) [5]. In recent years, there have been consistent efforts to fabricate nanowire based superconducting devices from MgB_2. Arpaia *et al.* have reported photoresponse of nanowires fabricated based on YBCO (a high temperature superconductor) [6]. However, it is extremely challenging to fabricate uniform nanoscale devices on these high T_c materials since they have complicated structural properties and are frequently degraded during nanopatterning. Exploration of nanofabrication techniques and superconducting properties of these materials may provide some new solution to the issues of cooling power related to the operation of SNSPDs.

One of main disadvantage of the SNSPD is that its needs to be packaged in a complicated cryogenic system which demands a lot of space and cooling power. Recently, there is some research being done regarding the miniaturisation of cryo-coolers and the packaging of SNSPDs into them [7], [8]. Since the base temperature of these smaller cryo-coolers is comparatively high (~4.2 K) SNSPD devices which show excellent performance at lower temperatures may not show high efficiency if integrated into such a system. It would be interesting to optimise thin films for such a specific device operating temperature.

Since the past few years, several groups are investigating the detection process of SNSPD devices and the hotspot growth mechanism in different superconducting materials [9], [10]. Further exploration on the microscopic process involved in the photon detection by SNSPDs will give us a sound understanding of how material parameters influence superconducting

detector properties. This will also be useful for optimizing superconducting materials for any specific detector application.

References

[1] J. Li, R. A. Kirkwood, L. J. Baker, D. Bosworth, K. Erotokritou, A. Banerjee, R. M. Heath, C. M. Natarajan, Z. H. Barber, M. Sorel, and R. H. Hadfield, "Nano-optical single-photon response mapping of waveguide integrated molybdenum silicide (MoSi) superconducting nanowires," *Opt. Express*, vol. 24, no. 13, p. 13931, Jun. 2016.

[2] Y. Ivry, J. J. Surick, M. Barzilay, C.-S. Kim, F. Najafi, E. Kalfon-Cohen, A. D. Dane, and K. K. Berggren, "Superconducting-superconducting hybridization for enhancing single-photon detection," *arXiv: 1703.08034*, Mar. 2017.

[3] S. Qin, J. Kim, Q. Niu, and C.-K. Shih, "Superconductivity at the two-dimensional limit.," *Science*, vol. 324, no. 5932, pp. 1314–7, Jun. 2009.

[4] M. M. Ugeda, A. J. Bradley, Y. Zhang, S. Onishi, Y. Chen, W. Ruan, C. Ojeda-Aristizabal, H. Ryu, M. T. Edmonds, H.-Z. Tsai, A. Riss, S.-K. Mo, D. Lee, A. Zettl, Z. Hussain, Z.-X. Shen, and M. F. Crommie, "Characterization of collective ground states in single-layer NbSe2," *Nat Phys*, vol. 12, no. 1, pp. 92–97, Jan. 2016.

[5] J. Nagamatsu, N. Nakagawa, T. Muranaka, Y. Zenitani, and J. Akimitsu, "Superconductivity at 39 K in magnesium diboride," *Nature*, vol. 410, no. 6824, pp. 63–64, Mar. 2001.

[6] R. Arpaia, M. Ejrnaes, L. Parlato, F. Tafuri, R. Cristiano, D. Golubev, R. Sobolewski, T. Bauch, F. Lombardi, and G. P. Pepe, "High-temperature superconducting nanowires for photon detection," *Phys. C Supercond. its Appl.*, vol. 509, pp. 16–21, Feb. 2015.

[7] V. Kotsubo, R. Radebaugh, P. Hendershott, M. Bonczyski, B. Wilson, S. W. Nam, and J. N. Ullom, "Compact 2.2 K Cooling System for Superconducting Nanowire Single Photon Detectors," *IEEE Trans. Appl. Supercond.*, vol. 27, no. 4, pp. 1–5, Jun. 2017.

[8] N. R. Gemmell, M. Hills, T. Bradshaw, T. Rawlings, B. Green, R. M. Heath, K. Tsimvrakidis, S. Dobrovolskiy, V. Zwiller, S. N. Dorenbos, M. Crook, R. H. Hadfield "A miniaturized 4 K platform for superconducting infrared photon counting detectors," (*Sumbitted in Supercond. Sci. Technol.)*, 2017.

[9] F. Marsili, M. J. Stevens, A. Kozorezov, V. B. Verma, C. Lambert, J. A. Stern, R. D. Horansky, S. Dyer, S. Duff, D. P. Pappas, A. E. Lita, M. D. Shaw, R. P. Mirin, and S. W. Nam, "Hotspot relaxation dynamics in a current-carrying superconductor," *Phys. Rev. B*, vol. 93, no. 9, p. 94518, Mar. 2016.

[10] A. GKozorezov, C. Lambert, F. Marsili, M. J. Stevens, V. B. Verma, M. D. Shaw, R. P. Mirin, and S. Woo Nam, “Fano fluctuations in superconducting nanowire single-photon detectors,” *arXiv:1702.02813v1,* Feb.2017.

Appendix

List of Publications

[1] A. Banerjee, L. Baker, A. Doye, M. Nord, R. Heath, K. Erotokritou, D. Bosworth, Z. Barber, I. MacLaren, and R. Hadfield, “Characterisation of amorphous molybdenum silicide (MoSi) superconducting thin films and nanowires,” *Supercond. Sci. Technol.*,vol. 30, no. 8, p. 84010, Jun. 2017.

[2] J. Li, R. A. Kirkwood, L. J. Baker, D. Bosworth, K. Erotokritou, A. Banerjee, R. M. Heath, C. M. Natarajan, Z. H. Barber, M. Sorel, and R. H. Hadfield, “Nano-optical single-photon response mapping of waveguide integrated molybdenum silicide (MoSi) superconducting nanowires,” *Opt. Express*, vol. 24, no. 13, p. 13931, Jun. 2016.

[3] D. Morozov, S. Doyle, A. Banerjee, T. Brian, R. H. Hadfield, D. Hemakumara, I. Thayne “Design and characterization of titanium nitride subarrays of Kinetic Inductance Detectors for passive terahertz imaging, ” (Under Preparation)

Conference presentations

1. A.Banerjee, K. Erotokritou, R. Heath, A. Casaburi, R.H. Hadfield, " Large area superconducting thin film deposition for single photon detector focal plane arrays," Applied Superconductivity Conference, September 4-9 2016 Denver USA (Poster)

2. L.J. Baker, J. Li, R.Kirkwood, D. Bosworth, K. Erotokritou, A. Banerjee, R. Heath, C.Natarajan, Z. Barber, R.H. Hadfield , "Nano-optical single-photon response mapping of waveguide-integrated molybdenum silicide," Applied Superconductivity Conference, September 4-9 2016 Denver USA (Poster)

3. A.K. Doye, A. Banerjee, M. Nord, R.H. Hadfield, I. MacLaren, "Determining local structural and chemical ordering in amorphous MoSix for superconducting nanowire

single-photon detectors" Microscopy & Microanalysis July 24-28 2016 Ohio USA (Poster)

Detailed drawings and designs of the sputter deposition system

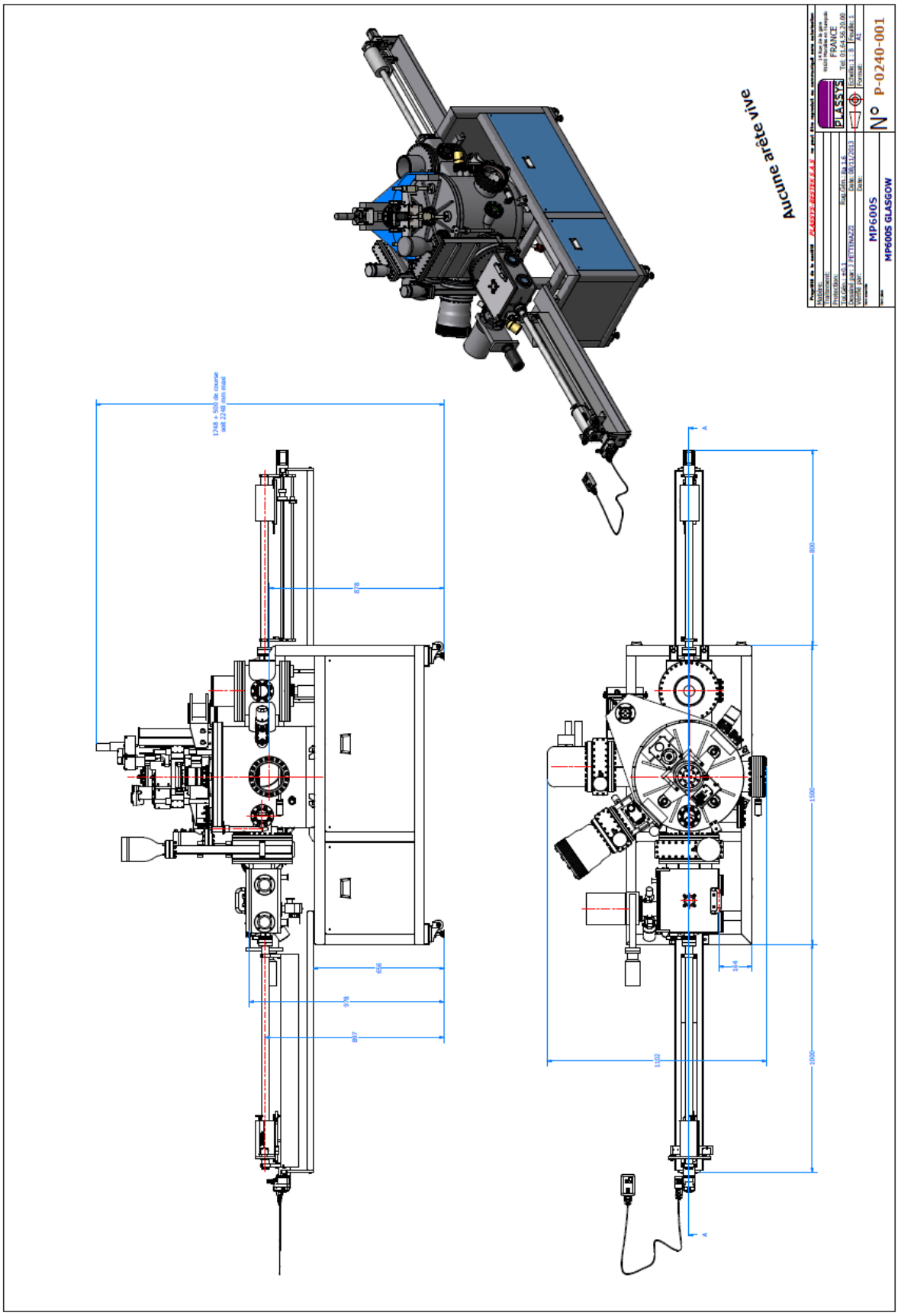

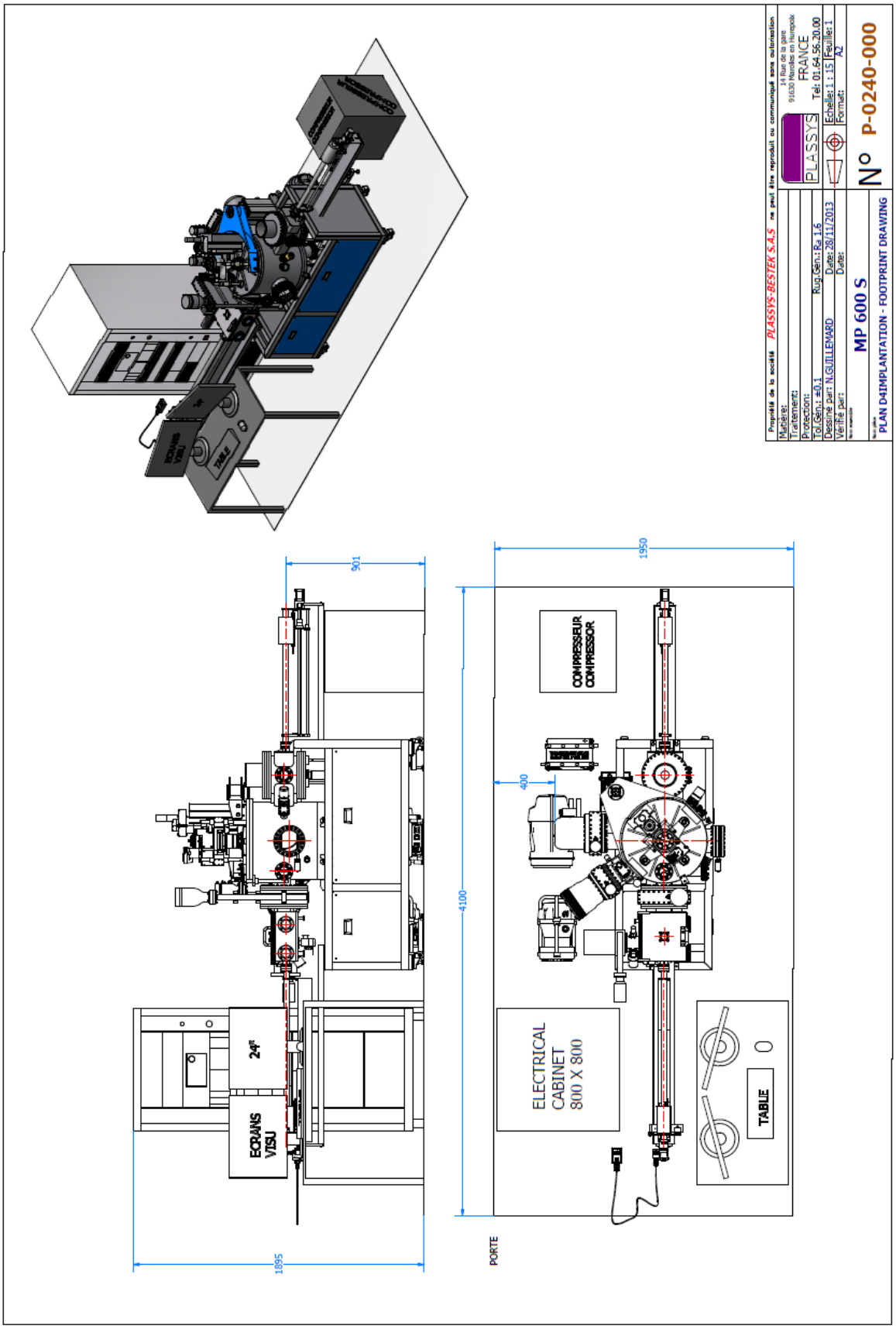
Propriété de la société PLASSYS-BESTEX S.A.S ne peut être reproduit ou communiqué sans autorisation
Matière:
Traitement:
Protection:
Tol.Gén.: ±0.1
Rug.Gen.: Ra 1.6
Dessiné par: N.GUILLEMARD
Date: 28/11/2013
Vérifié par:
Date:
PLASSYS
14 Rue de la paix
91630 Marolles en Hurepoix
FRANCE
Tél: 01.64.56.20.00
Echelle: 1 : 15
Feuille: 1
Format: A2
N° P-0240-000
MP 600 S
PLAN D4IMPLANTATION - FOOTPRINT DRAWING
ECRANS VISU
24"
TABLE
ELECTRICAL CABINET 800 X 800
COMPRESSEUR COMPRESSOR
PORTE
901
1095
1950
4100
400

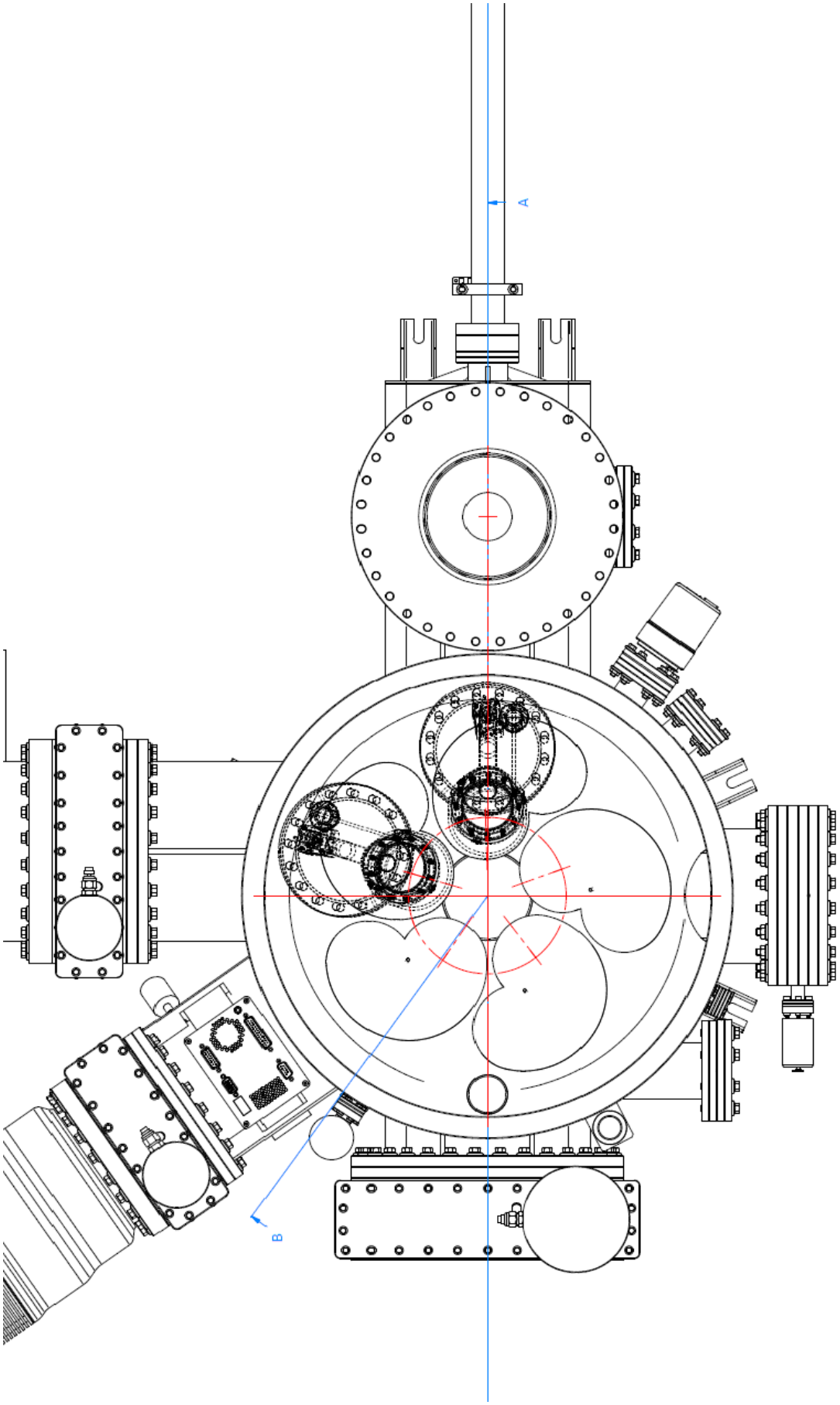
A
B

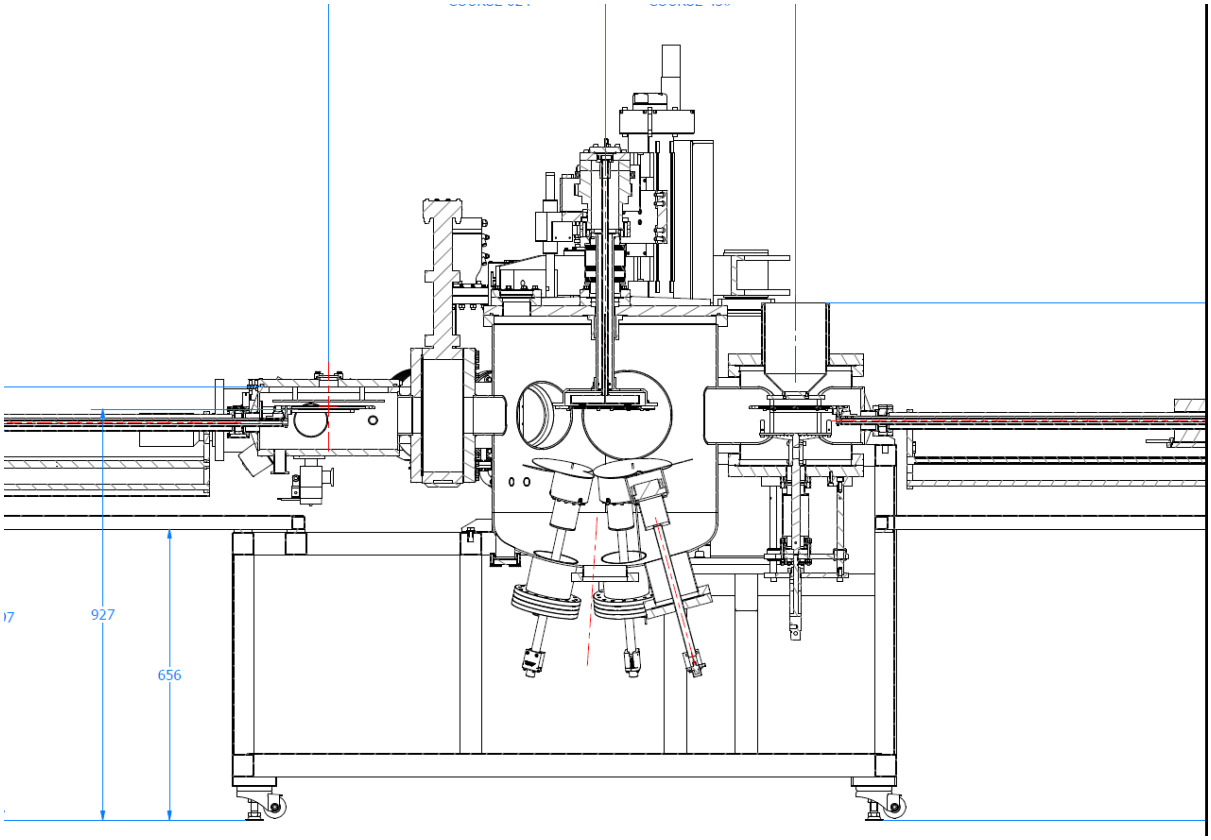

Timeline of superconducting materials grown in the sputter deposition system

Materials Growth in the Sputter System		
Materials	**START DATE**	**END DATE**
Niobium	01/05/2014	30/09/2014
Niobium Titanium Nitride and Nibium Nitride	01/09/2014	31/03/2015
Molybdelum Silicide	01/02/2015	30/09/2015
Molybdelum Germenium	01/11/2015	31/01/2016
Titanium Nitride	01/12/2015	